Electromagnetic Model-Based Measurement, Sensing, and Detection for Wireless Power Transfer

by

Sung Yul Chu

A dissertation submitted in partial fulfillment
of the requirements for the degree of
Doctor of Philosophy
(Electrical and Computer Engineering)
in the University of Michigan
2021

Doctoral Committee:

Assistant Professor Al-Thaddeus Avestruz, Chair
Professor Heath Hofmann
Dr. Jason Pries
Associate Professor Alanson Sample

Sung Yul Chu
sungyul@umich.edu
ORCID iD: 0000-0002-5901-6408

ACKNOWLEDGMENTS

First, I would like to express my deepest gratitude to my advisor, Professor Al-Thaddeus Avestruz, for his endless guidance and support. He has taught me everything about conducting research: setting up a research problem, solving it, and having completeness and craftsmanship. I will never forget all the days and long nights that we spent on discussion and writing, and especially our first oral presentation at 2017 IEEE COMPEL is my special memory. I am grateful to have had you as my advisor.

I would like to thank all my committee members. Professor Heath Hofmann, thank you for giving me all your advice and support. I especially thank you for giving me the opportunity to be a lab instructor of the 2019 Electrify Tech Summer Camp, one of my best memories in ECE, where I could broaden educational perspectives. I thank Dr. Jason Pries for giving me general and technical support and advice, as well as recommendations, where I could explore diverse opportunities. I thank Professor Alanson Sample for providing guidance and comments, which make me have a broader perspective of the research.

I also thank Professor Stéphane Lafortune, Professor Achilleas Anastasopoulos, and Professor Vijay Subramanian. It was a great pleasure working with you as an EECS 216 GSI throughout multiple semesters.

I will miss you all my friends and our group, PEERS (Power Electronics and Energy Research Studios at the University of Michigan). Akshay, Alireza, Xiaofan, and Xin! It has been a great pleasure doing many things together with pleasant memories at conferences. You are special to me, and I have felt powerful bonds with you during my graduate life. I also thank Yanqiao, Yingying, Michelle, Madeleine, Stephen, Veronica, Haochen, Jack, James, Daniel, and Austin for sharing a great experience at PEERS. I also thank my fellow graduate students and friends: Jake, Sunho, Fanny, Yuanying, Ziyou, Salman, Morteza, Sijia, Bowen, Mengqi, Kang, Omar, Navid, Myungjoon, Jongyup, Kyumin, Li, Hyungjoo, Hyunsoo, Jihun, Hyochan, and many others. It has been a pleasure meeting with you in EECS. Il Yong and Hanpyo, thank you for having coffee breaks with me, one of the best refreshers. I also wanted to thank ECE staff: Anne, Kristen, John, Silvia, Shelly, Judi, Kathy, Robert Giles, and Joel for their kind support.

Special thanks to my mother in heaven. You gave me the best memories and encouragement for anything always. I thank my family members: Dong Keon, Kibok, Young Ja, Eunsik, Kyungsik, Ah-Yul, Do-Young, Taein, Yein, Daejoo, Sewon, Joshua, Seowon, and Seojin, for your support.

I want to express my special gratitude to my wife, Yejin, for her endless love and support. You are always there and encourage me to have confidence in whatever I am doing. Thank you, my son, my energy, Teo. Let's start a new bright journey!

TABLE OF CONTENTS

LIST OF FIGURES

FIGURE

LIST OF TABLES

TABLE

LIST OF APPENDICES

ABSTRACT

Advances in measurement, sensing, and detection are the basis of technological development, which drives or hampers innovation, technology adoption, confidence in the value services, and security. As electric vehicles (EVs) become one of the dominant means of transportation in the next few decades with wireless power transfer for charging, the accuracy and fairness of energy metering and charging safety become prominent.

This dissertation aims to develop smart electromagnetic measurement and detection systems integrated for wireless charging. A small number of sensors sample the electromagnetic field to reconstruct the information needed for power measurement for fair metering and foreign object detection for safe wireless charging. This electromagnetic model-based measurement, sensing, and detection provide accurate solutions for receiver coil misalignment and power level variations.

First, Faraday coil transfer-power measurement (FC-TPM) is presented for fair metering and transactions of wireless charging in electric vehicles. The transfer-power is defined from the Poynting vector, which is the directed power density. The winding losses in the transmitter and receiver coils are derived and decomposed based on heat dissipation to show how the measurement of transfer-power demarcates the losses and imposes the costs for power losses to each coil based on physical power dissipation, resulting in fair metering. FC-TPM employs non-contact, open-circuited sense coils to calculate the transfer-power. The information obtained from the sense coils (e.g., sense coil voltages) is combined uniquely for the power reconstruction, which is accurate despite receiver coil misalignment without explicitly measuring the misalignment. The coupling coefficient variations to the misalignment are approximated by quadratic functions, explaining why a linear combination of multiple sense coil voltages results in accurate power reconstruction across the variation. Furthermore, this method is accurate over other types of variations (e.g., operat-

ing frequencies, different types of wires) since polynomials can generally approximate variations. FC-TPM was demonstrated in hardware accurately within 0.1% errors despite a receiver coil misalignment of up to 10 cm using a 1kW wireless power transfer system.

Second, Electromagnetic Model-Based Foreign Object Detection (EM-FOD) is presented for safe wireless power transfer, where foreign objects neighboring wireless power transfer systems are fire hazards. The same electromagnetic physics model, constructed by the transmitter, receiver, and sense coils, is the normal model and can be used to detect the hazardous objects by excluding them from the original normal model. A target information (e.g., the transmitter coil current) reconstruction by the normal model becomes inaccurate when there is a foreign object. The detection metric is a sequent error in the information reconstruction compared to the true information obtained by an independent measurement simultaneously. The detection metric is invariant to receiver coil misalignment and power level, allowing less risky pre-startup low-power detection. Hardware demonstrations show that a 2 cm diameter U.S. nickel coin can be detected using only 9 W regardless of a receiver coil misalignment of up to 10 cm.

This dissertation is concluded by presenting a calibration-transfer strategy to consider the practical deployment of the wireless charging models for FC-TPM to energy service stations. Open-circuited sense coils are chosen as transfer standards that convey accurate data obtained from the certified standard in standards laboratories to the transmitter and sense coils in energy service stations.

CHAPTER 1

Introduction

1.1 Motivation

Trust in technology is essential for its adoption. We accept what is efficient, fair, safe, and secured, where accurate measurement and sensing provide the discernment of those values. This dissertation presents an advanced measurement, sensing, and detection method that can be used to improve wireless vehicle charging in two ways: (i) providing fair metering for customers and providers; (ii) detecting foreign objects to prevent fires and improve safety. Broadly, this method works by using a small number of sensors to sample an electromagnetic field to reconstruct two essential pieces of information: (i) real power flow through the intervening space, which demarcates and imposes the costs of electrical losses to a transmitter and receiver based on physical heat dissipation resulting in fair metering; (ii) existence of a foreign object, which is a fire hazard in wireless power transfer.

Wireless power transfer (WPT) is an emerging technology that enables overcoming range anxiety in electric vehicles. User convenience, energy flexibility, and suitability for advanced electrified transportation such as autonomous vehicles are also what wireless charging can bring. Power levels, charging speed, air-gap, and efficiency that were big question marks have been achieved to the practical numbers and keep improving rapidly [2; 3; 4; 5; 6; 7; 8] with continuing achievements in maximum power transfer and high efficiency [9; 10; 11; 12; 13; 14; 15] along with kilowatt level high power wireless charging [16; 17; 18; 19; 20; 21], effective coil de-

sign [22; 23; 24; 25; 26; 27; 28; 29], and electromagnetic exposure safety [11; 30; 31; 32]. A bi-directional wireless charging for ac grid and electric vehicle fleet has also been demonstrated with 20 kW across an 11-inch air gap at 92% efficiency, where electric vehicles' batteries can be used for energy storage to support the electric grid [33].

While many challenges related to wireless charging have been addressed, two questions remain unanswered: (i) how to provide a metering system that is fair to consumers and providers; (ii) how to create a wireless charging system that is safe for widespread consumers usage. Wireless charging has unique concerns regarding fair power metering and safety: (i) transmitter and receiver coils are physically separated, where power can be measured at either coil terminal, which necessarily incorporates coil losses. Metering based on the coil terminal power measurement can be unfair to one side when the other side causes the incorporated loss. This unfairness can be exacerbated when the power is measured as a dc power at the front- or rear- end of the wireless power transfer system, which includes power electronics losses; (ii) a strong time-varying electromagnetic field for power transfer can threaten passenger safety. Foreign objects near magnetic wireless power transfer systems are one fire hazard because they can heat from eddy currents and cause a fire.

Fairness in metering wireless power transfer has an integral significance to providers and consumers of energy as an arbiter in their competing financial interests. By 2030, EVs will consume over 1,000 terawatt-hours of electricity every year worldwide; even a 1% misrepresentation in metering will cost energy consumers and providers over $ 1 billion[1] [34; 35; 36; 37]. For fairness, the cost of lost energy must be appropriately assigned among the stakeholders. Transmitter losses must be disaggregated from receiver losses for the equitable metering of wireless power transfer. Energy station owners and EV owners will then be individually motivated to improve their efficiency and hence reduce their financial losses.

The proper demarcation line for the "point of sale" in wireless charging had been posited to be physically between the transmitter (Tx) and vehicle receiver (Rx) coil by [38].[2] Transfer-power

[1] Based on EV projections: (i) 250 million EVs by 2030 [34]; (ii) 4,500 kWh/year/EV [35]; (iii) $ 0.1/kWh, the 10-years average price of electricity to ultimate customers in the transportation category [36].

[2] Subgroup in the U.S National Work Group on Measuring Systems for Electric Vehicle Fueling and Submetering, sponsored by the National Institute of Standards and Technology (NIST).

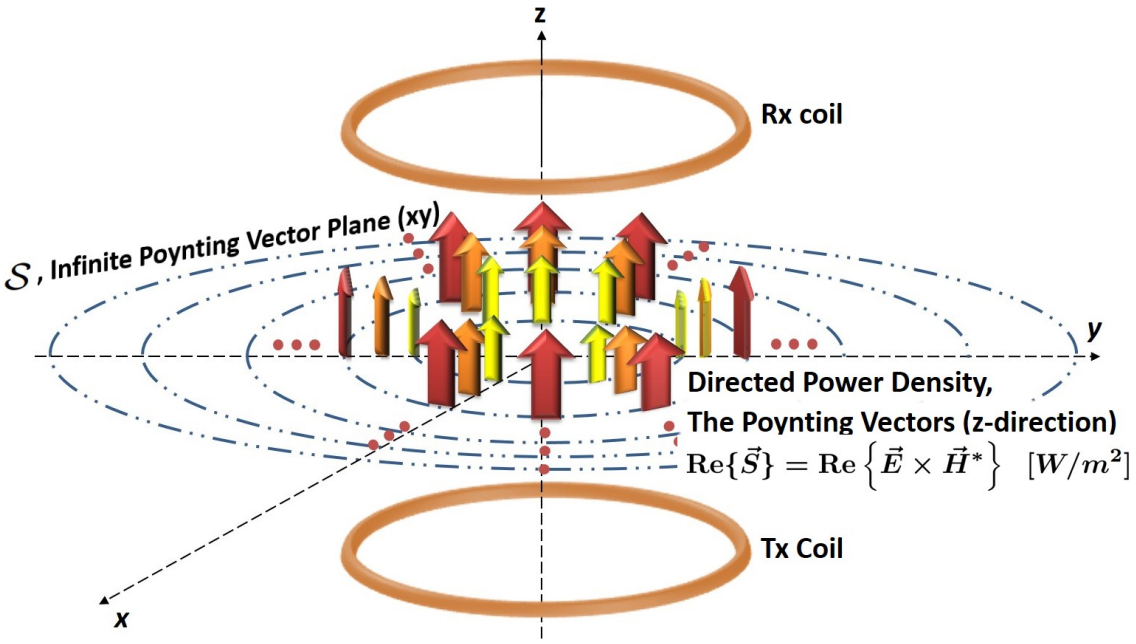

Figure 1.1. The Poynting vector is the directed power density. Transfer-power is equivalent to the surface integration of the components of the Poynting vectors that are normal to a surface S between the transmitter (Tx) and receiver (Rx) coils.

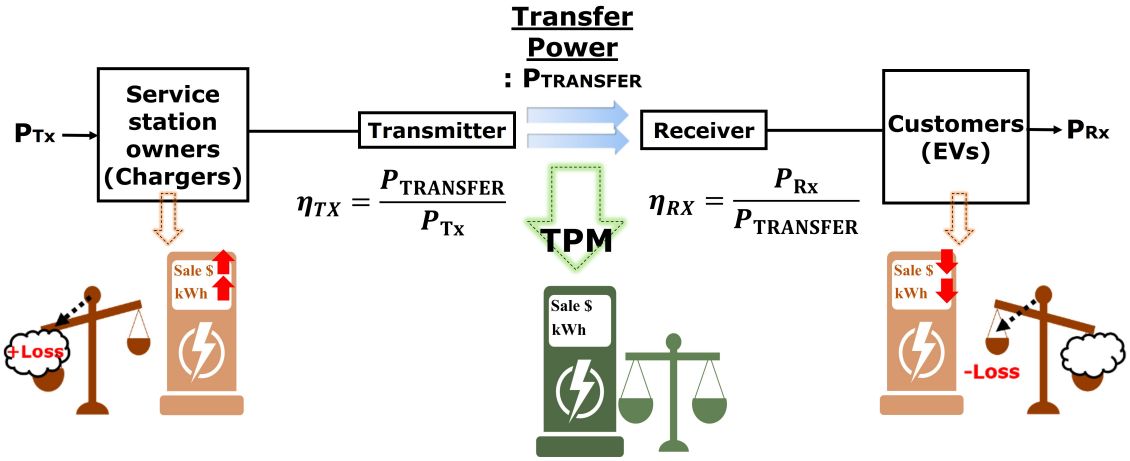

Figure 1.2. Transfer-power measurement results in fair metering and accurate diagnostics by disaggregating the efficiency of the transmitter (Tx) and receiver (Rx).

(P_{Transfer}) is the missing link. It is the real power through the air gap, purely dispensed from the Tx coil to the Rx coil. This real power can be represented electromagnetically through the Poynting vector illustrated in Fig. 1.1.

At first glance, there appeared to be no direct way to measure the quantity of power transfer; rather, what had been available were only the voltages and currents at the Tx and Rx electrical terminals with which to calculate the Tx input (P_{Tx}) and Rx output (P_{Rx}) power, which had been performed to varying degrees of accuracy and robustness in [39; 40]. The shortcoming of these methods is that Tx input and Rx output power necessarily incorporate aggregated losses from both sides, including those from winding resistance and eddy currents [41; 42].

Except for the unlikely case that the losses are symmetric in Tx and Rx, the correct attribution of power inefficiency is not possible. Fig. 1.2 illustrates the conundrum: input or output power measured at the Tx or Rx electrical terminal imposes the cost of the aggregated losses to one side or the other unilaterally; for example, if power is measured at the Tx terminal (P_{Tx}), metering adds Tx losses to the evaluation of transferred power, which ought to have been excluded in pricing, and thus customers are overcharged. Likewise, metering at the customer (Rx) terminal (P_{Rx}) subtracts Rx losses from the evaluation of transferred power and hence represents an undercharge. These inequities are exacerbated in systems where low efficiency from cost-cutting in design, production, installation, or maintenance is incentivized without proper metering, with another potential for abuse when there is physical access to the measurement terminals. Even if power efficiency is legislated, a robust way to validate disaggregated efficiencies is still needed.

These flaws can be overcome by measuring the transfer-power through the air-gap between the Tx and Rx coils, as shown in Fig. 1.2. Not only will this provide fair metering, but will also disaggregate individual Tx and Rx efficiencies, $P_{\text{Transfer}}/P_{\text{Tx}}$ and $P_{\text{Rx}}/P_{\text{Transfer}}$, respectively. As a diagnostic, it can financially incentivize the decisions and behaviors of providers and customers.

Wireless power transfer (WPT) is predicted to emerge as the primary mode of electric vehicle (EV) charging with safety as the main concern to adoption [43]. A foreign object near WPT, as shown in Fig. 1.3, should be detected for safety because it can cause a fire; an eddy current

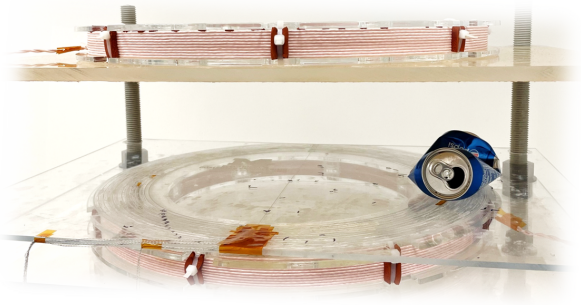

Figure 1.3. Wireless power transfer system is disrupted by an aluminum can.

is induced by the time-varying electromagnetic field in the foreign object, where Joule heating from the eddy current can cause a fire in the foreign object itself [44] or near a flammable liquid. Regulatory standard SAE J2954 mandates foreign object detection (FOD) [45].

This dissertation presents electromagnetic model-based transfer-power measurement and foreign object detection to address the fairness and safety concerns in wireless power transfer, which can contribute to accelerating the wireless charging technology adoption.

1.2 Electromagnetic Physics Model

A sparse electromagnetic measurement is used to recover high fidelity information; an electromagnetic physics model is constructed by employing a set of open-circuited sense coils to reconstruct the information needed for power measurement (transfer-power measurement) and foreign object detection. Wireless charging system can then be decomposed and modeled as separate winding such as a Tx, Rx, and sense coils, which are electromagnetically coupled to each other. Fig. 1.4 shows the electromagnetic physics model, which consists of a Tx, Rx, and sense coils. The sense coil voltages are induced by the Tx and Rx coil currents, corresponding to the electromagnetic coupling between the Tx and Rx coils to each sense coil. The sensor information (e.g., sense coil voltages) is transformed through the electromagnetic model to reconstruct the target information (e.g., transfer-power or existence of foreign objects).

The electromagnetic model is mainly derived from the geometric configuration of coils, which

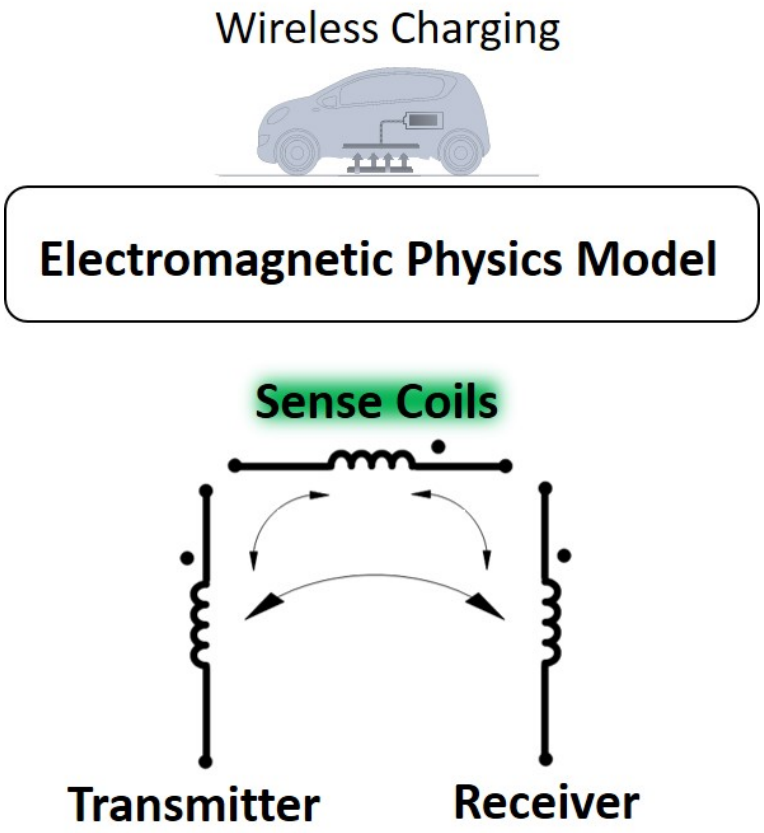

Figure 1.4. Electromagnetic physics model consists of the transmitter, receiver, and sense coils.

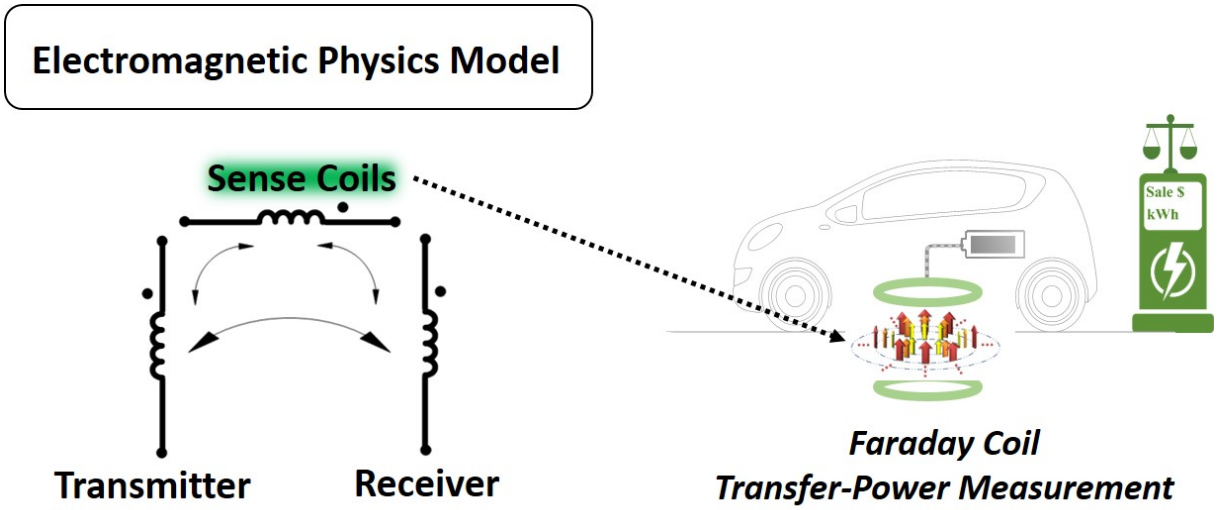

Figure 1.5. A power flow in the wireless power transfer can be reconstructed by the sense coil voltages through the electromagnetic physics model.

is independent of power level, driving circuits (e.g., compensating power electronics for wireless charging [12]), and output loads. Furthermore, the electromagnetic model can be accurate despite geometrical variations such as coil misalignment, presented in Chapter 3. The advantages of using the electromagnetic physics model include the following.

- Minimal electromagnetic and physical perturbation; the sensor is non-contact, open-circuited, and extremely thin single-turn coils.
- Smart; the reconstructed information is accurate over possible disturbances or variations (e.g., coil misalignment) without requiring any auxiliary systems.
- Multi-functional and hence cost-effective; the same sensors can be used for transfer-power measurement and foreign object detection.
- Enabling safe diagnostics at low-power, where the electromagnetic model-based solution is invariant to power level.
- Undemanding systems to users; information from the receiver sides (users) is not required for decisions.

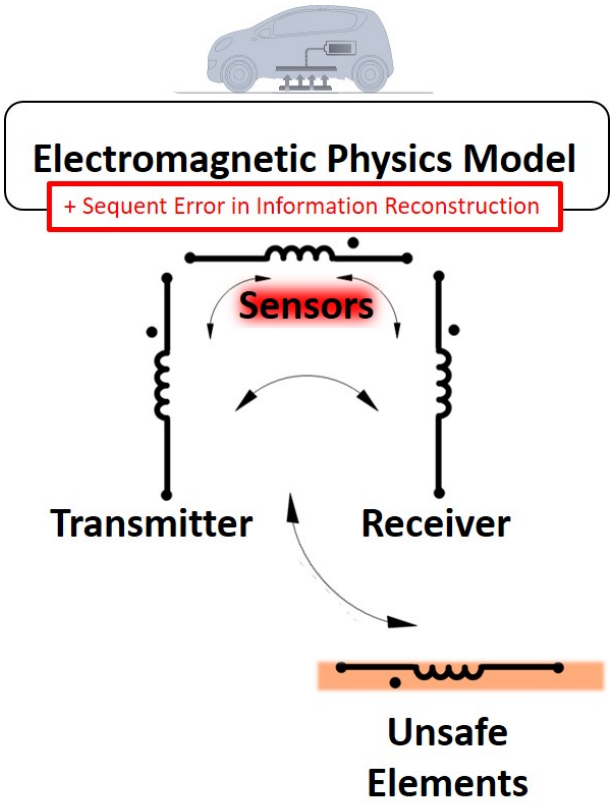

Figure 1.6. Unsafe elements such as foreign objects can be detected by a sequent error in information, which is reconstructed by an electromagnetic physics model.

Fig. 1.5 shows the diagram of *Faraday Coil Transfer-Power Measurement* (FC-TPM). Using sense coil voltages, the transfer-power, which is the power flow in the intervening space between the Tx and Rx coil, is reconstructed through a predefined electromagnetic physics model.

Fig. 1.6 shows that hazardous foreign objects can be detected using electromagnetic physics model; the target information, which is reconstructed by sense coil voltages through the electromagnetic model, becomes inaccurate when there is a foreign object, which does not exist when the model is defined. In the electromagnetic physics model, the foreign object can be modeled as a single winding coupled to the original model, consisting of the Tx, Rx, and sense coils. When an independent sensor separately measures the target information (e.g., a current sensor), and the measured value is compared to the reconstructed target information, a sequent error between the measured and reconstructed value can be a metric for the foreign object detection. The sequent error is only caused by an additional coupling brought by the foreign object. Thus, the detection metric for the *Electromagnetic Model-Based Foreign Object Detection* (EM-FOD) is invariant to power level, enabling low-power detection, which is less risky than a detection that requires high power.

1.3 Dissertation Outline and Contributions

This dissertation presents the fundamentals of the electromagnetic model for wireless power transfer, which consists of the Tx, Rx, and sense coils, in theory, numerical analysis, simulation, and hardware for the *Faraday Coil Transfer-Power Measurement* (FC-TPM). Information from the sense coils is uniquely combined to provide an accurate reconstruction of the target information (e.g., transfer-power) over geometric variations (e.g., coil misalignment). Using the same fundamentals of the electromagnetic model, *Electromagnetic Model-Based Foreign Object Detection* is also presented and demonstrated. A deviation in the model due to foreign object's additional couplings is an effective detection metric.

The organization and main contributions of each chapter are as follows.

Chapter 2 presents *Faraday Coil Transfer-Power Measurement* (FC-TPM). Transfer-power is defined from the Poynting vector, which is the directed power density. The transfer-power is also derived in lossy wireless charging coils from a winding loss model, where heat dissipation-based loss assignment of FC-TPM to the Tx and Rx sides can be manifested as fair metering. The mapping of the sense coil voltages to the Poynting vector is derived to validate FC-TPM as a measurement of electromagnetic power.

Chapter 3 presents accurate FC-TPM over misalignment between the Tx and Rx coils. The variations of coupling coefficients over the misalignment are approximated by quadratics, where non-varying geometric parameters over the misalignment can be derived. The transfer-power can be reconstructed accurately regardless of misalignment without needing explicit measurement of misalignment. The chapter also verifies that a greater number of sense coils can maintain FC-TPM accuracy despite the variations from different types of wire (e.g., litz wire) and operating frequencies.

Chapter 4 discusses how sense coils can be designed to be both physically and electromagnetically unobtrusive. The eddy current losses, which are dissipated in thin sense coils, are negligible, where there is no ohmic-loss from zero open-circuited sense coil current. A multi-objective optimization problem is solved to show flat sense coils placed on a low-profile coplanar plane are a good candidate for FC-TPM.

Chapter 5 demonstrates accurate FC-TPM in hardware over a standardized Rx coil misalignment of up to 10 cm with a 1 kW wireless power transfer system. 1 kW wireless charging testbed, including Tx, Rx, and sense coils, and power converters, is built for the demonstration.

Chapter 6 presents *Electromagnetic Model-Based Foreign Object Detection* (EM-FOD). The target information is the Tx coil current, where the detection metric is a sequent error in the Tx coil current reconstruction due to the foreign object's additional electromagnetic coupling. The detection metric is power level and misalignment invariant, enabling low-risk pre-startup low power detection regardless of coil misalignment.

Chapter 7 describes the calibration-transfer strategy for the practical deployment of FC-TPM

to energy service stations. Open-circuited sense coils are chosen as transfer standards that convey accurate data, obtained from the certified standard in standards laboratories, to sense coils in energy service stations.

Chapter 8 concludes the dissertation and discusses a future research path.

CHAPTER 2

Faraday Coil Transfer-Power Measurement

2.1 Chapter Introduction

This chapter presents the fundamentals of *Faraday Coil Transfer-Power Measurement* (FC-TPM), which to our knowledge is a first among methods in directly metering wireless charging of EVs. The main contribution of this chapter is (i) providing a direct connection of transfer-power to the Poynting vector; (ii) a thorough decomposition and analysis of the power balance that includes eddy current losses from cross-coupled magnetic fields; (iii) FEM analyses for losses.

FC-TPM employs non-contact open-circuited sense coils electromagnetically coupled to the transmitter (Tx) and receiver (Rx) coils from which transfer-power is reconstructed. These sense coil voltages directly map to the Poynting vector, which is the directed power density, as shown in Fig. 1.1. FC-TPM is analogous to *trusted third party* gasoline fuel pump metering today from an arbitration perspective with inspection performed by an unbiased third party: for example, the Michigan Department of Agriculture's *Weights and Measures Program* as illustrated in Fig. 2.1.

This section is organized as follows. Section 2.2 defines the transfer-power from the Poynting vector and presents a formulation based on a transformer model. Section 2.3 presents the transfer-power in lossy WPT coils from a winding loss model. Section 2.4 presents Faraday coil transfer-power measurement (FC-TPM): we derive the mapping of the sense coil voltages to the Poynting vector to validate FC-TPM as a fundamental measurement of WPT's real power flow.

Figure 2.1. US Weights and Measure Program qualifies secured gas pump metering (left) with a seal (right). [Photo (left): Weights and Measures, Maryland Department of Agriculture]

2.2 Transfer-Power Defined From The Poynting Vector In Wireless Power Transfer

In wireless power transfer, we define *transfer-power* to be the real power propagated from a Tx coil to a Rx coil through the intervening space. In this section, the formulation for transfer-power is derived through both the Poynting vector and a transformer model; additionally, we show how these two formulations are equivalent and directly map to each other.

2.2.1 Transfer-Power from the Poynting Vector

P_{Transfer} or transfer-power can be defined from the Poynting vector, which is the directed electromagnetic power density and is determined by the cross product of the electric field $\vec{E}$ with the magnetic field $\vec{H}$ [46]. The average power p_{avg}, which is the real transfer-power, can then be obtained by a surface integral of the real part of the time-averaged complex Poynting vector $\vec{S}$,

$$P_{\text{Transfer}} \triangleq p_{\text{avg}} = \iint_{\mathcal{S}} \text{Re}\{\vec{S}\} \cdot d\vec{s}, \tag{2.1}$$

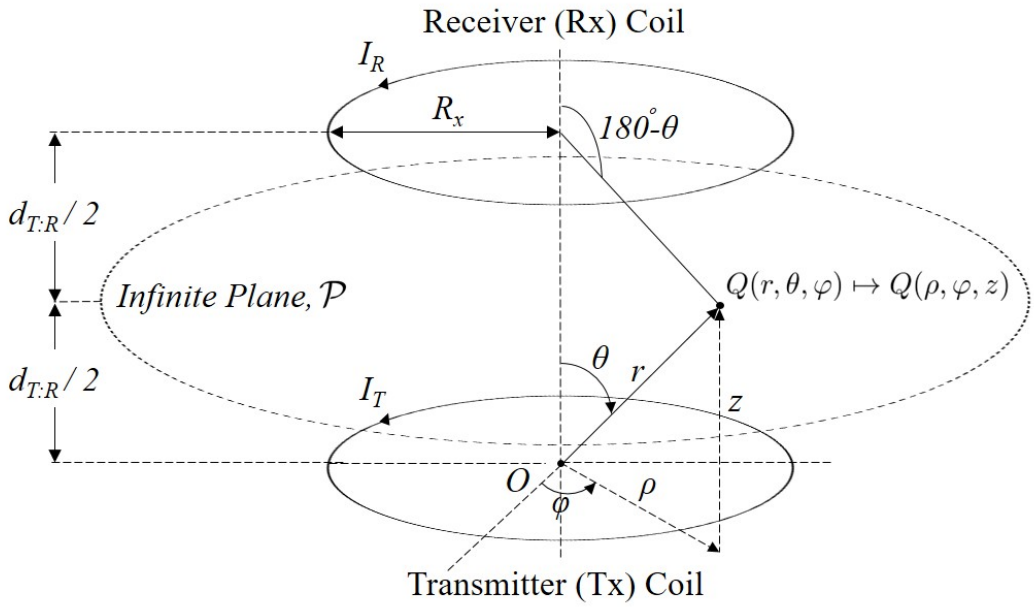

Figure 2.2. The fields from the Tx and Rx coil currents are modeled as magnetic dipoles. The magnetic and electric fields are calculated and then transformed from spherical to cylindrical coordinates to derive the Poynting vector in the wireless power transfer system.

where

$$\vec{S} = \vec{E} \times \vec{H}^*. \tag{2.2}$$

Note that $\vec{E}$ and $\vec{H}$ are phasors of time-harmonic fields whose magnitude is the rms value. $\mathrm{Re}\{\cdot\}$ indicates the real part and the asterisk (*) indicates the complex conjugate.

The Tx and Rx coils can be approximated as circular current loops whose basic physics can be illustrated by magnetic dipoles [47], as shown in Fig. 2.2 to derive the Poynting vector. The radii R_x of the Tx and Rx current loops are identical and assumed to be much smaller than the distance between the two coils $d_{T:R}$ ($R_x \ll d_{T:R}$). The Poynting vector through the point $Q : (r, \theta, \varphi)$ in spherical coordinates is analyzed on the infinite plane $\mathcal{P}$, which is located at $z = d_{T:R}/2$ between the Tx and Rx coil, as shown in Fig. 2.2, where the magnetic field $\vec{H}$ and electric field $\vec{E}$ created by the magnetic dipoles were formulated in [47; 48] in spherical coordinates. However, the Poynting vector and the resulting average power calculation can be represented more simply in cylindrical

coordinates; the Poynting vector is derived from $\vec{E}$ and $\vec{H}$

$$\vec{E} = -\ \hat{\varphi}\ \ j\omega\frac{\mu_0 A}{4\pi r^2}\sin\theta\,(I_T + I_R)\,, \tag{2.3}$$

$$\begin{aligned}\vec{H} = &\ \ \hat{\rho}\ \ \frac{3A}{8\pi r^3}\sin 2\theta\,(I_T - I_R)\\ &+\ \ \hat{z}\ \ \frac{A}{4\pi r^3}(3\cos^2\theta - 1)(I_T + I_R),\end{aligned} \tag{2.4}$$

where $A = \pi R_x^2$ is the Tx and Rx loop area, and I_T and I_R are the corresponding currents. Note that in cylindrical coordinates (ρ, φ, z)

$$r = \sqrt{\rho^2 + z^2},$$

$$\theta = \cos^{-1}\frac{z}{\sqrt{\rho^2 + z^2}}.$$

The real part of the time-averaged complex Poynting vector $\vec{S}$ is then,

$$\begin{aligned}\mathrm{Re}\{\vec{S}\} &= \mathrm{Re}\{S_z\}\\ &= \hat{z}\ \ \frac{3\mu_0 A^2}{16\pi^2 r^5}\ \sin 2\theta \sin\theta\ \ \mathrm{Re}\left\{j\omega I_R I_T^*\right\}.\end{aligned} \tag{2.5}$$

Note that only the $\hat{z}$ component of the Poynting vector contributes to the real power transfer, where both the Tx and Rx coil currents I_T, I_R determine the magnitude and direction of the Poynting vector. Fig. 2.3 shows the time-averaged Poynting vector field, simulated by the finite element method (FEM) in COMSOL; power is transferred from the Tx coil to the Rx coil when the Tx coil current leads the Rx coil current (i.e., the Tx and Rx coil current phase difference is positive, $\theta_T - \theta_R > 0$). Particularly, there is maximum power transfer when the phase difference is 90°.

The transfer-power P_{Transfer} is the average power, which is calculated from (2.1), applying the

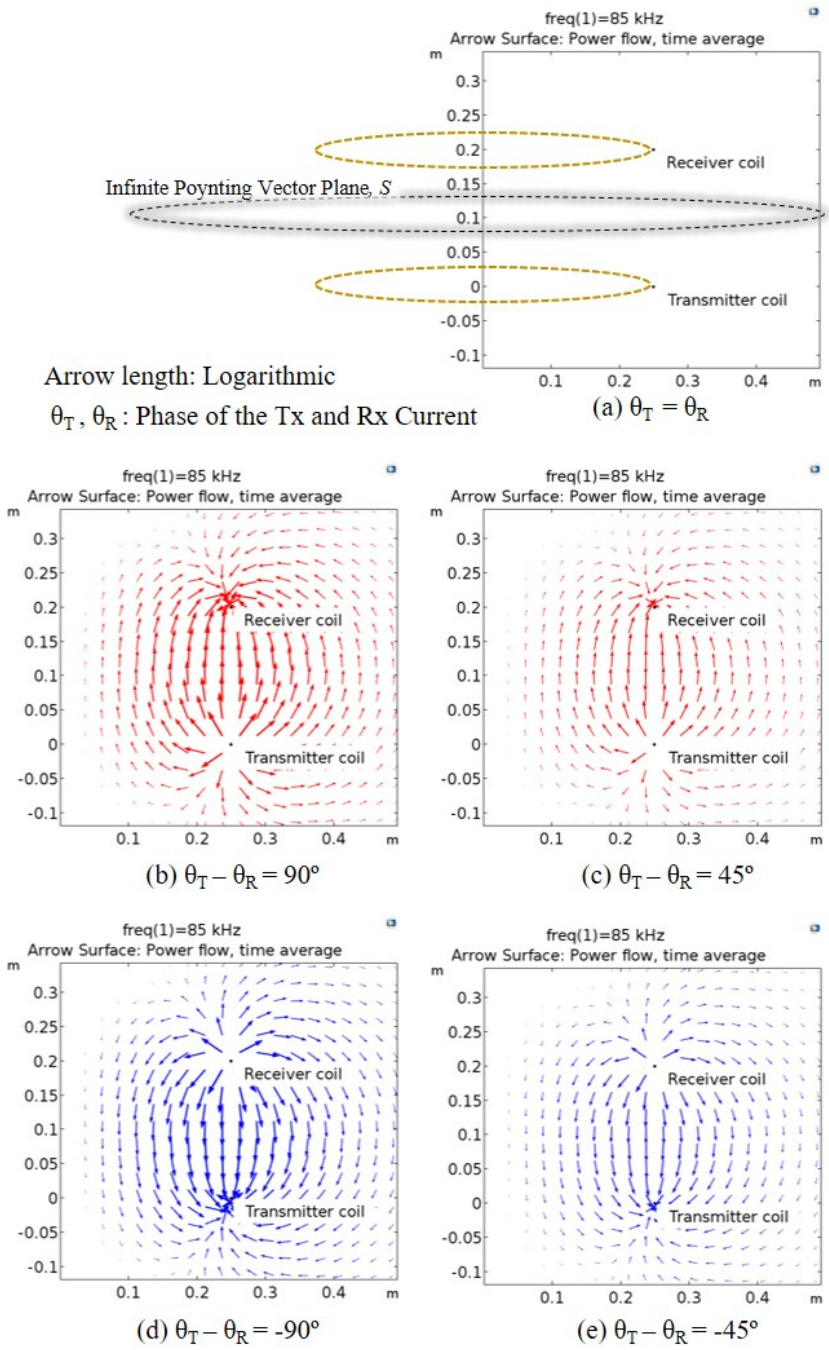

Figure 2.3. The time-averaged Poynting vector field [arrows] is plotted from 2D finite element method (FEM) simulations in COMSOL. The magnitude and direction of the power flow in WPT are represented by the Poynting vectors, which vary according to the Tx and Rx coil current phase differences ($\theta_T - \theta_R$): (a) there is no power transfer when the two coil currents are in phase; (b) maximum power transfer from the Tx to the Rx when the Tx current leads the Rx current by $90°$; (c) real power is transferred from the Tx coil to the Rx coil when the Tx current leads the Rx current. (d) maximum power transfer from the Rx to the Tx when the Rx current leads the Tx current by $90°$; (e) real power is transferred from the Rx coil to the Tx coil when the Rx current leads the Tx current.

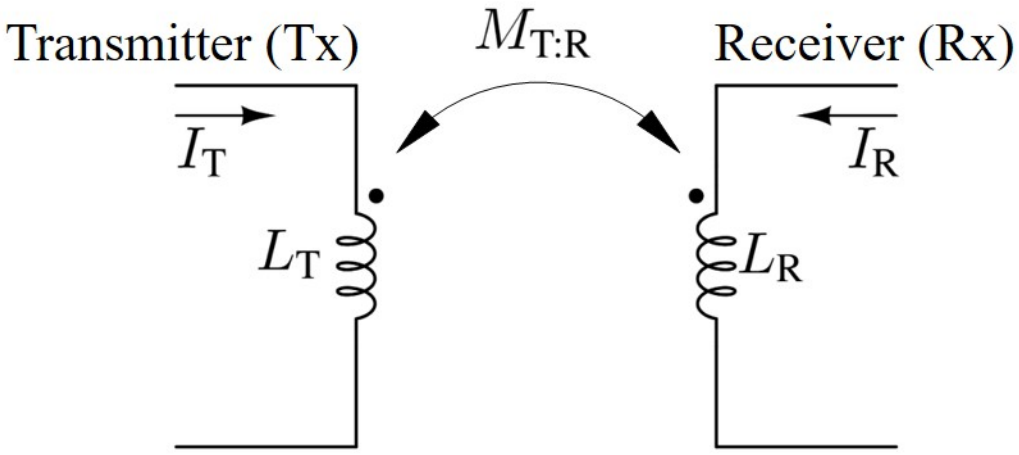

Figure 2.4. Equivalent transformer circuit model for wireless power transfer.

surface integral to (2.5) over the infinite plane $\mathcal{P}$,

$$P_{\text{Transfer}} = p_{\text{avg}} \tag{2.6}$$

$$= \text{Re}\left\{ j\omega \underbrace{\frac{\mu_0 A^2}{2\pi {d_{T:R}}^3}}_{\text{Geometric Factor}} I_R I_T^* \right\}. \tag{2.7}$$

P_{Transfer}, the real power leaving the transmitter, is the real part of the product of the complex conjugate of the Tx coil current I_T^* and induced voltage $j\omega M_{R:T} I_R$ (from the Rx coil current), where the geometric factor is the mutual inductance $M_{R:T}$ from the Rx to the Tx coil, which also appears in the transformer model. Detailed derivation of (2.7) is shown in Appendix B.

2.2.2 Transfer-Power in the Transformer Model

The Poynting vector illustrates how wireless power transfer operates. In practice, directly working with the Poynting vector is cumbersome; a transformer model is both elucidating and useful for the analysis and design of wireless power transfer.

Transfer-power can be formulated through a transformer model where losses are treated extrinsically. When a Tx and Rx coil pair are magnetically coupled through an air core, as shown in Fig. 2.4 and when there are no winding and eddy current losses, the Tx and Rx coil voltages (V_T

and V_R) are

$$V_T = j\omega L_T I_T + j\omega M_{R:T} I_R, \tag{2.8}$$

$$V_R = j\omega L_R I_R + j\omega M_{T:R} I_T, \tag{2.9}$$

where L_T and L_R are the self-inductances of each coil; $M_{X:Y}$ is the mutual inductance from coil X to coil Y; ω is the angular frequency; and $\{V_X, I_X\}$ are phasors whose magnitude is the rms value. Note that $M_{R:T} = M_{T:R}$ because of reciprocity.

In this dissertation, the subscripts attribute each variable to a particular coil: T (Transmitter), R (Receiver), natural numbers $1, 2, \ldots$ (sense coils); colons $(x : y)$ indicate a parameter relationship from coil x to coil y.

In a wireless power transfer system with lossless coils,[1] the transfer power is equal to the real power at the coil terminals. The real power at the terminals of the Tx coil in this case is

$$P_{\text{Transfer}} = \mathrm{Re}\left\{V_T I_T^*\right\} \tag{2.10}$$

$$= \underbrace{\mathrm{Re}\{j\omega L_T I_T I_T^*\}}_{\text{Zero}} + \underbrace{\mathrm{Re}\{j\omega M_{R:T} I_R I_T^*\}}_{\text{Transfer-power}} \tag{2.11}$$

$$= \mathrm{Re}\left\{j\omega M_{R:T} I_R I_T^*\right\}. \tag{2.12}$$

Note that the combination of the incident magnetic field from the Tx coil current I_T and the reflected electric field from the induced voltage $j\omega M_{R:T} I_R$ from the Rx coil current I_R comprises transfer-power [47; 49].[2] The geometric factor in (2.7) is the mutual inductance $M_{R:T}$. The transfer-power can also be similarly derived from the Rx side as $\mathrm{Re}\{j\omega M_{T:R} I_T I_R^*\}$, which results in a negative value of P_{Transfer}, indicating that power is consumed by Rx.

[1] Section 2.3 elaborates on the transformer model with winding losses.

[2] In this dissertation, the direction of the transfer-power is defined from the Tx side, meaning that the transfer-power is positive if power is transferred from the Tx coil to the Rx coil.

2.3 Transfer-Power in Lossy Wireless Power Transfer Coils: Winding Loss Breakdown

The principal transfer-power, which we denote $P_{\text{Tx:Rx}}$, corresponds to the directed real power from the terminal currents described in Section II. However, for metering, principal transfer-power may not offer a complete description of transfer-power when cross-coupled loss mechanisms are significant.

Winding losses decompose into ohmic and eddy current losses, which we derive in this section. These losses manifest as heat dissipation in either the Tx or Rx coil, which is formulated from the coil (Tx or Rx) currents. Assignment of losses based on heat dissipation is consistent with the Poynting vector definition of transfer-power, which is the power flow through the intervening space between the Tx and Rx coils. Transfer-power is saliently different from the black box notion of input and output electrical terminal power.

Fair metering using transfer-power means that costs for power losses are imposed on the transmitter (service station owner) and the receiver (EVs owner) equitably based on the amount of the each side's physical power dissipation, which manifests as heating. This heat dissipation-based demarcation of the loss penalizes stakeholders who use inferior quality coils, power electronics, or other system components that cause loss. In other words, fair metering motivates providers and customers to advance their system (e.g., by using better litz wire or winding methods) to reduce losses.

2.3.1 Winding Losses in the WPT Coils

2.3.1.1 Input and Output Terminal Power

The input power P_{Tx} and output power P_{Rx} that are measured at the coils' electrical terminals are

$$P_{\text{Tx}} = \text{Re}\left\{V_T I_T^*\right\}, \tag{2.13}$$

$$P_{\text{Rx}} = \text{Re}\left\{V_R I_R^*\right\}, \tag{2.14}$$

where

V_T, V_R : respective Tx, Rx coil terminal voltage;

I_T, I_R : respective Tx, Rx coil current.

The terminal voltage contains not only the induced coil voltages, represented by (2.8) and (2.9), but also the voltage drops that are related to winding losses, as shown in (2.24) and (2.25) in Section 2.3.1.2. From the perspective of power conservation,[3] the difference between the Tx coil input power and the Rx coil output power is the aggregate power loss within both the Tx and Rx coils.

2.3.1.2 Winding Losses

The main purpose of our winding loss derivation and ensuing loss breakdown is to identify the source of each loss and to clarify where each loss is dissipated. This is especially important for wireless power transfer metering in that the Tx and Rx coils are magnetically coupled, where each coil's current and hence magnetic field can generate a loss in the other's coil.

Using a winding loss model where eddy currents can be represented by an additional winding on a transformer, we can further show that the measurement of transfer-power disaggregates the losses between the Tx and Rx coils properly in contrast to the input and output terminal power, which lump both losses.

We decompose the winding losses into (i) ohmic losses due to ac and dc winding resistance and (ii) eddy current loss, which is the loss from eddy currents within a coil due to the external proximity effect, where the opposing coil generates an external magnetic field: for example, the external proximity effect loss in the Rx coil due to the Tx coil current and resulting magnetic field.[4] We refer to this external proximity effect loss as *eddy current loss* in this dissertation.

[3] If the power is transferred from Tx to Rx, P_{Tx} can be considered positive for power generated and P_{Rx} negative for power consumed, without loss of generality.

[4] The quantification of the loss can be confirmed by examining the difference in input power between the two cases when the Tx coil is driven by current source I_T: (i) when the Rx coil does not exist physically; and (ii) when the Rx coil is physically present, but open-circuited ($I_R = 0$).

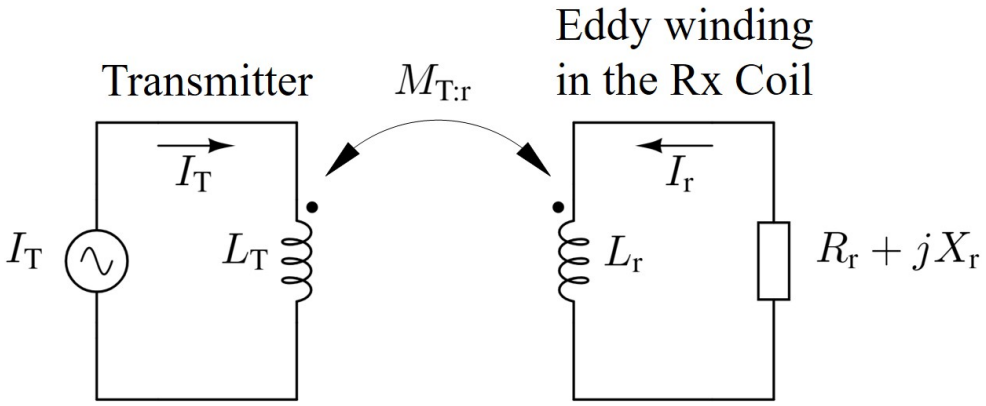

Figure 2.5. The equivalent circuit for the winding model of the eddy current; the Tx coil and eddy current winding in the Rx coil are magnetically coupled.

The eddy currents in the coils can be modeled as a transformer winding [50; 51]. For example, the eddy current in the Rx coil I_r, created by the Tx coil current I_T, is modeled as a winding to represent the eddy current loss in terms of the Tx coil current and effective resistance $R_{T:r}$. The equivalent circuit is shown in Fig. 2.5, resulting in the expression

$$- j\omega L_r I_r - j\omega M_{T:r} I_T = (R_r + jXr) I_r, \tag{2.15}$$

where $M_{T:r}$ is the mutual inductance between the Tx coil and Rx coil's eddy current winding; R_r and X_r are the equivalent resistance and reactance in the winding. From (2.15), the eddy current I_r can be represented in terms of the Tx current I_T

$$I_r = \frac{j\omega M_{T:r}}{-(R_r + jX_r + j\omega L_r)} I_T. \tag{2.16}$$

Transfer-power between two coils was defined in (2.12). The eddy current losses $P_{\text{Loss,eddy(Rx)}}$ can also be represented as a transfer-power:

$$P_{\text{Loss,eddy(Rx)}} = \mathrm{Re}\left\{ j\omega M_{T:r} I_r I_T^* \right\}. \tag{2.17}$$

Note that the eddy current loss is the power that is transferred from the Tx coil to the eddy winding.

The eddy current loss can also be found from (2.15) as the real power, dissipated by R_r

$$R_r \operatorname{Re}\{I_r I_r^*\} = \operatorname{Re}\{j\omega M_{T:r} I_r I_T^*\}, \tag{2.18}$$

confirming (2.17). Combining (2.16) and (2.17), the eddy current losses can be represented by

$$\begin{aligned} P_{\text{Loss,eddy(Rx)}} &= \operatorname{Re}\{R_{T:r} I_T I_T^*\} + \operatorname{Re}\{j\omega X_{T:r} I_T I_T^*\} \\ &= \operatorname{Re}\{I_T I_T^*\} R_{T:r}, \end{aligned} \tag{2.19}$$

where

$$R_{T:r} = \frac{\omega^2 M_{T:r}^2 R_r}{R_r^2 + (X_r + \omega L_r)^2}, \tag{2.20}$$

$$X_{T:r} = \frac{\omega M_{T:r}^2 (X_r + \omega L_r)}{R_r^2 + (X_r + \omega L_r)^2}. \tag{2.21}$$

The eddy current loss is represented in terms of the Tx coil current I_T and the effective resistance $R_{T:r}$.

Winding losses, which consist of the ohmic losses and eddy current losses, can be represented by the source currents

$$P_{\text{W,Tx}} = \operatorname{Re}\left\{I_T^* I_T + \gamma_{_R} I_T^* I_R\right\} R_T + \operatorname{Re}\{I_T^* I_T\} R_{T:r}, \tag{2.22}$$

$$P_{\text{W,Rx}} = \operatorname{Re}\left\{I_R^* I_R + \gamma_{_T} I_R^* I_T\right\} R_R + \operatorname{Re}\{I_R^* I_R\} R_{R:t}. \tag{2.23}$$

$P_{\text{W,Tx}}$ represents the Tx winding loss, measured at the Tx coil terminal as a part of the input power; R_T is the effective winding resistance, which is frequency-dependent and accounts for the skin and internal proximity effects when there is no external field. The discussion of $\gamma_{_R}$ is identical to that of $\gamma_{_T}$ because the transmitter and receiver can be interchanged (for example, (2.22) and (2.23) are symmetric in the sense that R can replace T in the subscripts or vice versa to obtain the other equation, hence also reflecting the symmetry of the physics). $\gamma_{_R}$ encapsulates the effect of

geometry in how the external field from the Rx coil affects the current density distribution in the Tx windings. The external field can reinforce or weaken the self-field depending on its magnitude and relative phase, which is represented in $I_T^* I_R$. The external field can also reinforce or weaken the self-field depending on the relative directions and relative strengths of the fields, which is represented in $\gamma_{_R}$ and therefore a factor which depends on geometry. $\gamma_{_T}$ and $\gamma_{_R}$ can be different because the Tx winding and the Rx winding are not necessarily identical; therefore, the geometric effect of the opposing external magnetic field is not necessarily symmetric.

The Tx coil current also contributes to the loss because of the external proximity effect, which is dissipated in the Rx coil; eddy currents are created in the Rx coil from the time-varying magnetic field from the Tx coil current. The eddy current loss is then a real power transferred from the Tx coil to the eddy winding and can be represented by the source current (Tx coil current) and the effective resistance $R_{T:r}$, which is the effective resistance that encapsulates: (i) the magnetic coupling between the Tx coil and an eddy current winding in the Rx coil and (ii) the effect of the impedance in the eddy current winding. $P_{\text{W, Rx}}$ represents the Rx winding loss, measured at the Rx coil's electrical terminal as a part of the output power, where R_R, $\gamma_{_T}$, and $R_{R:t}$ are defined in the same manner as for the Tx winding loss. Note that $\gamma_{_R} R_T$ and $\gamma_{_T} R_R$ are equal because of reciprocity.

The Tx coil terminal voltages V_T can be derived using (2.16), (2.20), (2.21), and (2.22)

$$\begin{aligned} V_T &= j\omega L_T I_T + j\omega M_{R:T} I_R + j\omega M_{T:r} I_r + R_T\big(I_T + \gamma_{_R} I_R\big) \\ &= j\omega(L_T - X_{T:r}) I_T + j\omega M_{R:T} I_R + R_T\big(I_T + \gamma_{_R} I_R\big) + R_{T:r} I_T. \end{aligned} \tag{2.24}$$

Similarly, the Rx coil terminal voltage V_R can represented by

$$V_R = j\omega(L_R - X_{R:t}) I_R + j\omega M_{T:R} I_T + R_R\big(I_R + \gamma_{_T} I_T\big) + R_{R:t} I_R. \tag{2.25}$$

Input power P_{Tx} in (2.13) and output power P_{Rx} in (2.14) can be formulated from the terminal

voltages (2.24) and (2.25) of the winding loss model

$$P_{\text{Tx}} = \text{Re}\left\{j\omega M_{R:T} I_R I_T^*\right\} + \text{Re}\left\{I_T^* I_T + \gamma_{_R} I_T^* I_R\right\} R_T + \text{Re}\left\{I_T^* I_T\right\} R_{T:r}, \tag{2.26}$$

$$P_{\text{Rx}} = \text{Re}\left\{j\omega M_{T:R} I_T I_R^*\right\} + \text{Re}\left\{I_R^* I_R + \gamma_{_T} I_R^* I_T\right\} R_R + \text{Re}\left\{I_R^* I_R\right\} R_{R:t}. \tag{2.27}$$

Fig. 2.6 shows the power flow in wireless power transfer. Observe that input and output terminal power commingle winding losses and therefore cannot disaggregate losses properly: (i) input power P_{Tx} aggregates winding losses, which are the ohmic losses dissipated in the Tx coil $P_{\text{Loss,ohmic(Tx)}}$ and the eddy current losses dissipated in the Rx coil $P_{\text{Loss,eddy(Rx)}}$ and (ii) output power P_{Rx} also aggregates winding losses, which are the ohmic losses dissipated in the Rx coil $P_{\text{Loss,ohmic(Rx)}}$ and the eddy current losses dissipated in the Tx coil $P_{\text{Loss,eddy(Tx)}}$. For example, when the Rx coil is open-circuited, the output power P_{Rx} is zero, but there is heat dissipation in the Rx coil from the Tx coil current, which should be attributed to the Rx coil. It is worth noting that the transfer-power that is useful for metering comprises the principal transfer-power and the eddy current losses,

$$P_{\text{Transfer}} = P_{\text{Tx:Rx}} + P_{\text{Loss,eddy(Rx)}} - P_{\text{Loss,eddy(Tx)}}. \tag{2.28}$$

For the purpose of fair metering, we can re-distribute power losses based on the Tx and Rx coils' dissipation $P_{\text{d,Tx}}$ and $P_{\text{d,Rx}}$

$$P_{\text{d,Tx}} = \text{Re}\left\{I_T^* I_T + \gamma_{_R} I_T^* I_R\right\} R_T + \text{Re}\left\{I_R^* I_R\right\} R_{R:t}, \tag{2.29}$$

$$P_{\text{d,Rx}} = \text{Re}\left\{I_R^* I_R + \gamma_{_T} I_R^* I_T\right\} R_R + \text{Re}\left\{I_T^* I_T\right\} R_{T:r}, \tag{2.30}$$

which are in contrast to (2.22) and (2.23). Note that what is dissipated in the coil is a combination of (i) the ohmic loss and (ii) the external proximity effect (eddy current losses). Equations (2.29) and (2.30) explain the eddy current losses in the Tx and Rx coils. This manifests in the example where despite the Rx coil being open-circuited ($I_R = 0$), $P_{\text{d,Rx}}$ is non-zero, yet with a loss generated by the Tx coil current.

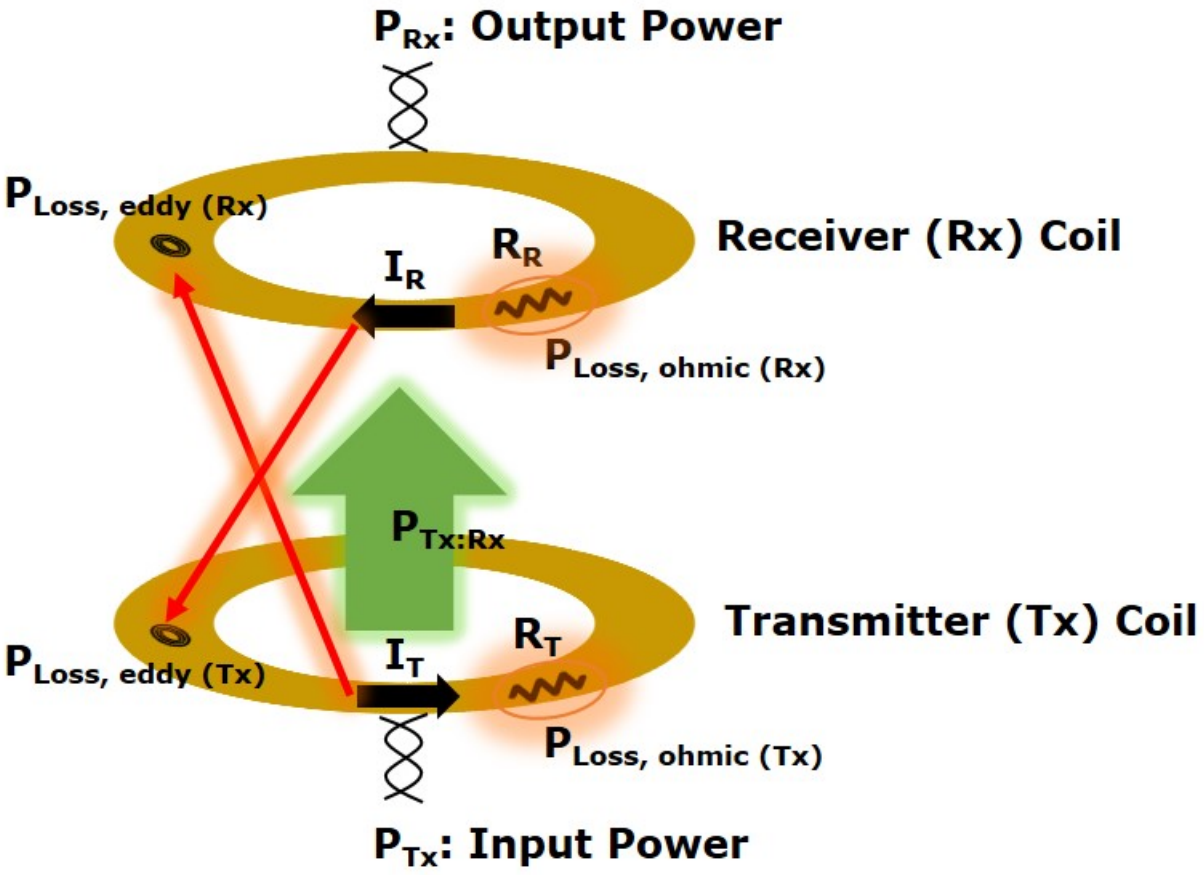

Figure 2.6. Power flow in wireless power transfer. Input power P_{Tx}, measured at the Tx coil terminal, is composed of: (i) $P_{\text{Tx:Rx}}$ in (2.12); (ii) $P_{\text{Loss, ohmic (Tx)}}$, ohmic losses due to the Tx coil winding resistance R_{T}; and (iii) $P_{\text{Loss, eddy (Rx)}}$, the external proximity effect loss, dissipated in the Rx coil, generated by the Tx coil current I_T. At the Rx coil, $P_{\text{Tx:Rx}}$ is received and losses are incurred, which are composed of: (i) $P_{\text{Loss, ohmic (Rx)}}$, ohmic losses due to the Rx coil winding resistance R_{R}; and (ii) $P_{\text{Loss, eddy (Tx)}}$, the external proximity effect loss, dissipated in the Tx coil, generated by the Rx coil current I_R. The output power P_{Rx} measured at the Rx coil terminal is then the difference between $P_{\text{Tx:Rx}}$ and the incurred loss.

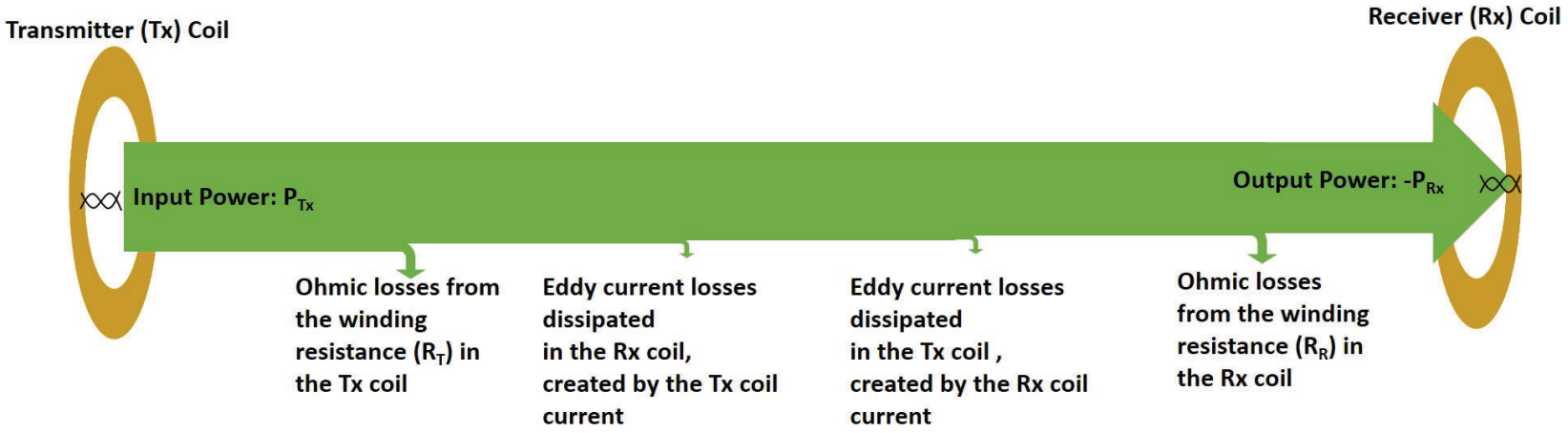

Figure 2. . Power conservation in a WPT system. Transfer-power can be obtained by disaggregating the winding losses from the input and output power.

Power conservation in wireless power transfer from the input power to the output power can be shown with an accounting of the winding losses

$$\begin{aligned}
\underbrace{P_{\text{Tx}}}_{\text{Input power at the Tx coil}} &= \underbrace{\text{Re}\left\{I_T^* I_T + \gamma_R I_T^* I_R\right\} R_T}_{\text{Ohmic loss from the Tx winding resistance } R_T} \\
&+ \underbrace{\text{Re}\left\{I_T^* I_T\right\} R_{T:r}}_{\text{Eddy current losses in the Rx coil, generated by } I_{\text{T}}} \\
&+ \underbrace{\text{Re}\left\{I_R^* I_R\right\} R_{R:t}}_{\text{Eddy current losses in the Tx coil, generated by } I_{\text{R}}} \\
&+ \underbrace{\text{Re}\left\{I_R^* I_R + \gamma_T I_R^* I_T\right\} R_R}_{\text{Ohmic loss from the Rx winding resistance } R_R} \\
&- \underbrace{P_{\text{Rx}}}_{\text{Output power at the Rx coil}}.
\end{aligned} \tag{2.31}$$

Note that the negative sign before P_{Rx} accounts for the power consumption in the Rx coil. Fig. 2.7 illustrates the conservation of power in wireless power transfer.

2.3.2 Transfer-Power Metering with Losses

In Section 2.2.1, transfer-power is defined from the Poynting vector, which is the electromagnetic power density through space. As shown in Fig. 2.6, the transfer-power P_{Transfer} for lossy coils is the sum of three power flows: (i) $P_{\text{Tx: Rx}}$: the real power transferred from the Tx to Rx coils, $\text{Re}\{j\omega M_{T:R} I_R I_T^*\}$ in (2.12), which is the principal transfer-power; (ii) $P_{\text{Loss,eddy(Rx)}}$: eddy current loss in the Rx coil; and (iii) $P_{\text{Loss,eddy(Tx)}}$: eddy current loss in the Tx coil, so that

$$P_{\text{Transfer}} = \text{Re}\left\{j\omega M_{R:T} I_R I_T^*\right\} + \left\{I_T^* I_T\right\} R_{T:r} - \left\{I_R^* I_R\right\} R_{R:t}. \tag{2.32}$$

Metering based on transfer-power explicitly attributes a particular coil's losses as the power it is dissipating as heat, which is consistent with the assertion of the Poynting vector definition.

Transfer-power is equal to transmitter coil terminal power minus the Tx coil power dissipation

$$P_{\text{Transfer (}\textit{Tx-referenced}\text{)}} = P_{\text{Tx}} - P_{\text{d,Tx}}. \tag{2.33}$$

In other words, transmitters Tx (providers) automatically pay for the cost of $P_{\text{d,Tx}}$ if metering is based on transfer-power. Similarly, receivers Rx (customers) automatically pay for their own power dissipation $P_{\text{d,Rx}}$ along with the power they receive for consumption. From the receiver side, the transfer-power can be represented by

$$P_{\text{Transfer (}\textit{Rx-referenced}\text{)}} = -P_{\text{Rx}} + P_{\text{d,Rx}}. \tag{2.34}$$

For example, a customer can reduce their dissipation (from ohmic and transmitter-induced eddy current loss), hence their cost of energy, by using a higher quality litz wire.

2.3.3 Extraction of Winding Loss Model from FEM Simulations

Winding losses can be determined from terminal measurement using different setups, which we show in FEM simulations. For example, the effective winding resistance of the Tx coil R_T can be extracted when the Tx coil is driven by the current I_T with the Rx coil physically removed; the input terminal power P_{Tx} is $\text{Re}\{I_T I_T^*\}R_T$. $R_{T:r}$, the effective resistance, which contributes to eddy current loss in the Rx coil due to the Tx coil current, can be extracted when the Rx coil is in place but open-circuited; the eddy current loss $P_{\text{Loss, eddy(Rx)}}$ is then the terminal input power minus what is dissipated in the Tx coil, $\text{Re}\{I_T I_T^*\}R_T$. Lastly, the electromagnetic parameter γ_R can be extracted from the ohmic loss in the Tx coil when the Tx and Rx coil currents are in phase, resulting in zero principal transfer-power $\text{Re}\{j\omega M_{T:R} I_R I_T^*\}$. R_R, $R_{R:t}$, and γ_T can be extracted in the same manner, as described in Appendix C.

From the simulation, we calculated how the power and loss distribute among the various mechanisms for various Tx and Rx coil configurations to study how, in practice, power partitions in WPT charging. Circular versions of wireless charging coils based on SAE J2954 [45] were evaluated

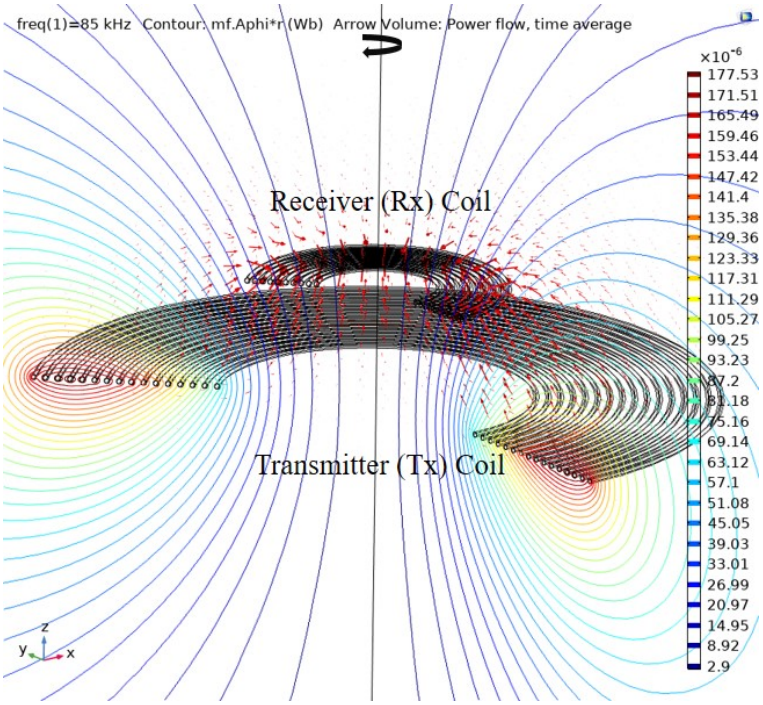

Figure 2.8. Multi-turn concentric solid wires were used for the Tx and Rx coils to emulate WPT2/Z1 class.

using finite element analysis using COMSOL. The specifications for the different coils are shown in Table 2.1. Different transmitter and receiver coil radii (r_T and r_R), air gaps ($d_{T:R}$), windings (N_T and N_R), and power classes, representing a wide range of standardized options, were selected.[5]

Two-dimensional axisymmetric simulations were performed with the Tx and Rx coils driven by current sources. Although in practice, litz wire is typical, solid wire was used in these analyses as worst-case examples. The Tx coil currents were chosen to be the maximum current for each power class, and the Rx coil currents were selected to satisfy the maximum power level for the class, both specified in [45]. Fig. 2.8 shows an example with 7.7 kW output power when the Tx-to-Rx coil air-gap is 100 mm, which emulates the WPT2/Z1 class; 2.5 mm radius wire was used, where the Tx coil and Rx coil diameters were 650 mm and 250 mm, respectively.

Table 2.2 shows the principal transfer-power $P_{\text{Tx:Rx}}$, ohmic losses ($P_{\text{ohmic,Tx}}$ and $P_{\text{ohmic, Rx}}$), and eddy current losses ($P_{\text{eddy, Tx}}$ and $P_{\text{eddy, Rx}}$) as a percentage of the input power for each coil spec-

[5]The Tx and Rx wire radii were identically 2.5 mm for all classes, except for the Rx wire radii for the WPT1/Z1 (1.57 mm) and WPT1/Z2 (2.02 mm).

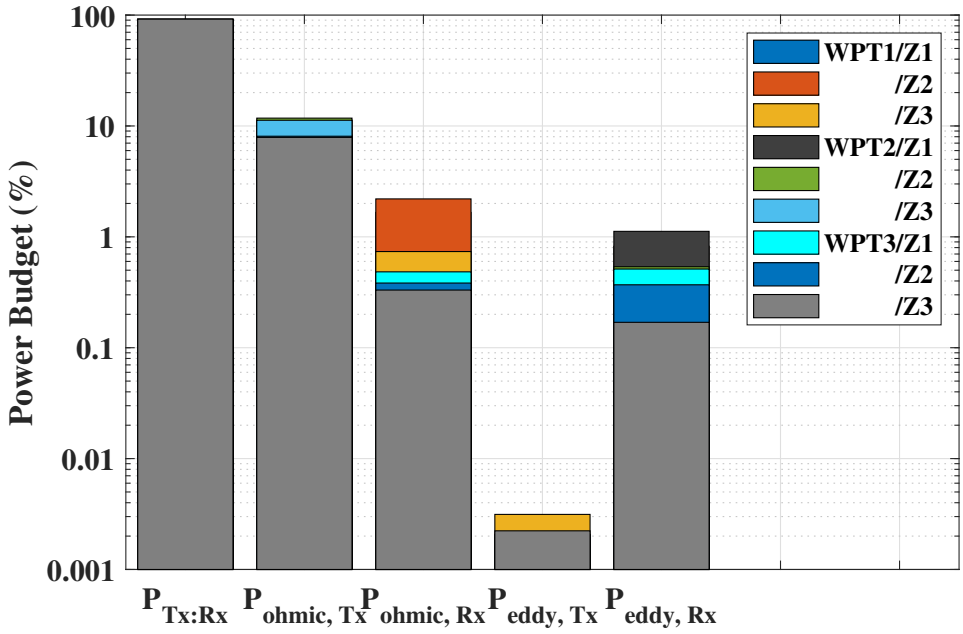

Figure 2.9. Budget for the transfer-power and loss as a percentage of the input Tx power P_{Tx} for various coil configurations and power levels.

ification. As expected (2.33) and (2.34) give identical results for each coil configuration.[6] The results are compared graphically in Fig. 2.9. The power flow from the Tx to Rx coil $P_{\text{Tx:Rx}}$ is the dominating quantity, while ohmic losses are the greatest portion of the winding losses. The worst case for the percentage eddy current loss was 1.12 %, dissipated in the Rx coil for the WPT2/Z1 class.

[6]Note that the values in the Table 2.2 are rounded to three significant digits.

TABLE 2.1
Loss Budget for Various WPT Coil Configurations (Solid Wire; Spiral Winding): Coil Specifications

Power Class	Z-Class	r_T	r_R	$d_{T:R}$	N_T	N_R	I_T	I_R	R_T	R_R	$R_{T:r}$	$R_{R:t}$	$\gamma_{_T} R_R = \gamma_{_R} R_T$
WPT1	Z1	290	130.1	100	15	9+8 (2-layers)	30	10.6	0.36	0.58	0.022	6.8E-04	0.042
	Z2		159.2	140		20		12		0.63	0.038	4.6E-04	0.095
	Z3		210	170		20		9.9		0.31	0.015	1.3E-03	0.048
WPT2	Z1	325	125	100	16	10	75	23.3	0.18	0.074	0.016	2.0E-04	0.016
	Z2		160	140		9		17.7		0.065	8.1E-03	3.5E-04	0.01
	Z3		190	170		8		20		0.045	3.8E-03	3.0E-04	5.7E-03
WPT3	Z1	325	135	100	16	10	75	33.9	0.18	0.054	0.012	2.3E-04	0.011
	Z2		160	140		9		26.9		0.065	8.1E-03	3.5E-04	0.01
	Z3		190	170		8		30.4		0.045	3.8E-03	3.0E-04	5.7E-03

Table 2.1 and 2.2 are FEM simulation results.
Power and Z-class are found in [45].
$r_{T,R}$ are the radii of the Tx and Rx coils. $d_{T:R}$ is the air-gap between the Tx and Rx coils. The unit of the length is mm.
N_T and N_R are the number of turns for the Tx and Rx coils, respectively.
I_T and I_R are rms values. All the phase angle differences between the Tx and Rx coil currents are maintained at 90°.
The unit of the effective resistances R_T, R_R, $R_{T:r}$, $R_{R:t}$, $\gamma_{_T} R_R$, and $\gamma_{_R} R_T$ is Ohms (Ω).

TABLE 2.2
Loss Budget for Various WPT Coil Configurations (Solid Wire; Spiral Winding): Power Budget

Power Class	Z-Class	P_{Tx}(kW)	$P_{\text{Tx:Rx}}(\%)$	$P_{\text{ohmic,Tx}}$ $(\%)$	$P_{\text{ohmic,Rx}}(\%)$	$P_{\text{eddy,Tx}}(\%)$	$P_{\text{eddy,Rx}}(\%)$	P_{Rx}(kW)	η $(\%)$
WPT1	Z1	3.91	91.2	8.30	1.67	1.94E-03	0.505	3.50	89.5
	Z2	4.11	91.3	7.89	2.20	1.62E-03	0.822	3.66	89.1
	Z3	4.08	91.7	7.96	0.737	3.14E-03	0.339	3.71	91.0
WPT2	Z1	8.83	87.8	11.3	0.454	1.23E-03	0.995	7.71	87.3
	Z2	8.44	87.7	11.8	0.241	1.29E-03	0.538	7.38	87.5
	Z3	8.83	88.5	11.3	0.215	1.45E-03	0.242	7.79	88.3
WPT3	Z1	12.9	91.8	7.70	0.483	2.07E-03	0.513	11.8	91.3
	Z2	12.3	91.5	8.08	0.383	2.05E-03	0.369	11.2	91.2
	Z3	12.6	91.9	7.89	0.331	2.23E-03	0.169	11.5	91.6

$P_{\text{Tx:Rx}}$, $P_{\text{ohmic,Tx}}$, $P_{\text{ohmic,Rx}}$, $P_{\text{eddy,Tx}}$, $P_{\text{eddy,Rx}}$ are percentages of the input power P_{Tx}.
η is the Tx-to-Rx coil efficiency in percent, $P_{\text{Rx}}/P_{\text{Tx}} \times 100$.

2.4 Faraday Coil Transfer-Power Measurement

Faraday Coil Transfer-Power Measurement (FC-TPM) is a non-contact electromagnetic method to measure *transfer-power* through an intervening space by making inferences based on sampling the electromagnetic fields using open-circuited Faraday sense coils. FC-TPM employs the voltages from open-circuited sense coils, as shown in Fig. 2.10, which are electromagnetically coupled to the Tx and Rx coils to reconstruct the transfer-power.

FC-TPM is the first among methods in EV charging to measure the power flow through space, resulting in fair metering. Advantages of FC-TPM include:

1. accuracy that is independent of self-inductance and ohmic loss of Tx and Rx coils, power electronics (e.g., compensation circuit topologies), and electrical loads of the Rx side.

2. accuracy that is insensitive to coil misalignment, operating frequencies, and various coil wire types (e.g., solid and litz wires).

3. small footprint with sense coils that are few in number and diminutive in size whose electromagnetic and physical disturbance is negligible.

This section shows how the sense coil voltages reconstruct the real power flow in wireless power transfer. First, we derive the Poynting vectors from the sense coil voltages to prove that FC-TPM directly measures the electromagnetic power flow through the air-gap. Then, we derive the transfer-power from the sense coil voltages using the transformer-model, which reveals the benefit of using geometric parameters and leads to calibration strategies for FC-TPM.

2.4.1 Mapping the Sense Coil Voltages to the Poynting Vector

The Poynting vector can be represented by sense coil voltages from which transfer-power can ultimately be derived.

Sense coils sample the electromagnetic field from which the Poynting vector can be reconstructed. If the sense coils are placed coaxially with the Tx and Rx coils, as shown in Fig. 2.11, a

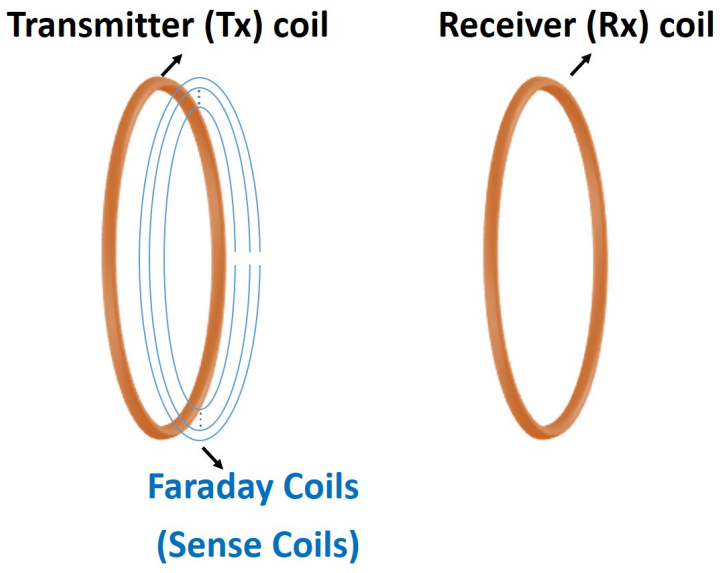

(a)

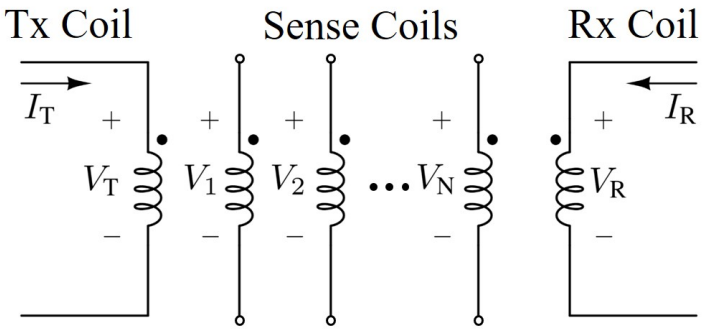

(b)

Figure 2.10. Non-contact and open-circuited Faraday sense coils are employed in the WPT system to measure the transfer-power. (a) The conceptual diagram. (b) The transformer equivalent circuit diagram.

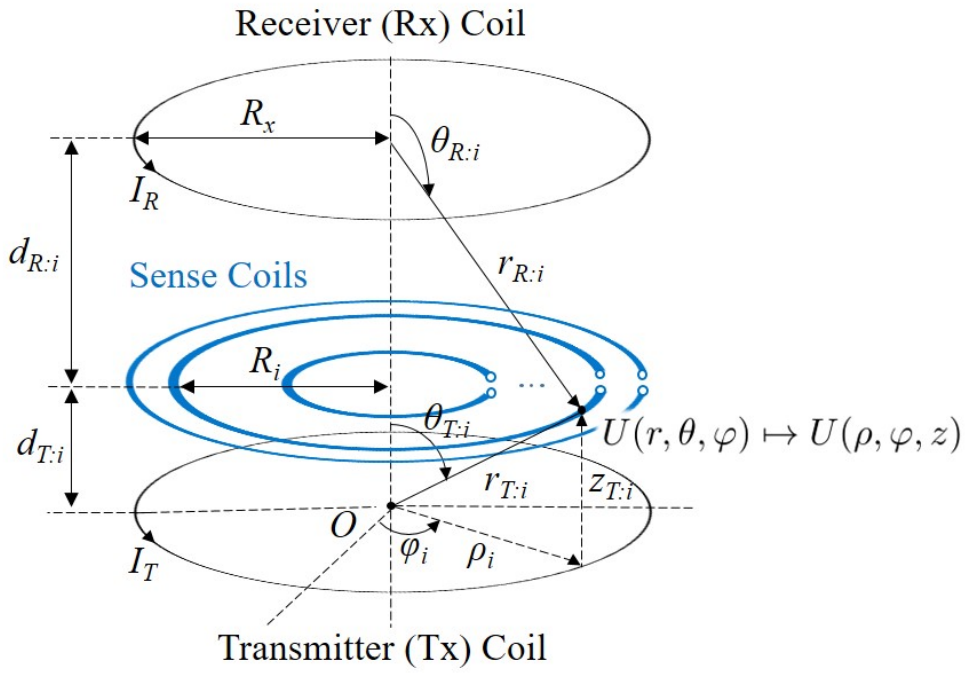

Figure 2.11. Non-contact open-circuited sense coils are placed between the Tx and Rx current loops. The sense coil voltages are induced by the magnetic fields from the Tx and Rx currents. The Poynting vectors can be mapped to the sense coil voltages.

sense coil voltage V_i is induced by the $\hat{z}$ component of the magnetic field from (2.4)[7]

$$V_i = -\oint \vec{E}_i \cdot d\vec{l} \tag{2.35}$$

$$= \frac{d}{dt} \iint_S B_z \hat{z} \cdot d\vec{s} \tag{2.36}$$

$$= g\left(d_{T:i}, R_i\right)\ j\omega I_T + g\left(d_{R:i}, R_i\right)\ j\omega I_R\,, \tag{2.37}$$

where

$$g\left(d_{X:i}, R_i\right) = \frac{\mu_0 A R_i^2}{2\left({d_{X:i}}^2 + R_i^2\right)^{\frac{3}{2}}}. \tag{2.38}$$

Note that $d_{X:i}$ is the distance between coil X and sense coil i; R_i is the radius of sense coil i; $A = \pi R_x^2$ is the Tx and Rx loop area, where R_x is assumed to be much smaller than the distance between the two coils $d_{T:R}$ ($R_x \ll d_{T:R}$) from the magnetic dipole approximation of the Tx and Rx

[7]Sign convention was chosen for more compact expressions, without loss of generality.

loops. What results from (2.37) and (2.38) is that the Tx and Rx coil currents (I_T and I_R) can be reconstructed by a linear combination of the pair of sense coil voltages (V_i and V_j)

$$I_T = \frac{g\left(d_{R:j}, R_j\right)}{\lambda}\frac{V_i}{j\omega} + \frac{-g\left(d_{R:i}, R_i\right)}{\lambda}\frac{V_j}{j\omega}, \tag{2.39}$$

$$I_R = \frac{-g\left(d_{T:j}, R_j\right)}{\lambda}\frac{V_i}{j\omega} + \frac{g\left(d_{T:i}, R_i\right)}{\lambda}\frac{V_j}{j\omega}, \tag{2.40}$$

where

$$\lambda = g\left(d_{T:i}, R_i\right) g\left(d_{R:j}, R_j\right) - g\left(d_{R:i}, R_i\right) g\left(d_{T:j}, R_j\right). \tag{2.41}$$

As shown in (2.5), the Poynting vector can be represented by the Tx and Rx coil currents. In other words, determining the Tx and Rx coil currents from the sense coil voltages in (2.39) and (2.40) enables one to find the Poynting vector.

The real part of the time-averaged complex Poynting vector is

$$\begin{aligned}
\mathrm{Re}\left\{\vec{S}\right\} &= \mathrm{Re}\left\{S_z\right\} && (2.42)\\
&= \mathrm{Re}\left\{E_\varphi \times H_\rho^*\right\} && (2.43)\\
&= \frac{m(r,\theta)}{\lambda}\frac{1}{\omega}\mathrm{Im}\left\{V_i V_j^*\right\}, && (2.44)
\end{aligned}$$

where

$$m(r,\theta) = \frac{3\mu_0 A^2}{16\pi^2 r^5}\sin 2\theta \sin\theta. \tag{2.45}$$

λ is the geometric parameter, determined by the sense coil positions. In summary, the real part of the Poynting vector at any point in the plane of interest can be mapped by the imaginary part of the complex conjugate pair of sense coil voltages $\mathrm{Im}\{V_i V_j^*\}$.

2.4.2 Theory of FC-TPM Using the Transformer Model

The sense coil voltages can represent transfer-power through the transformer model. In this and the following two sections (3.3 and 3.3.3), we neglect external eddy current losses.[8] Because there are no eddy current windings, the open-circuited sense coil voltages are induced only by the Tx and Rx coil currents.

The sense coil voltages V_i in the frequency domain are

$$V_i = j\omega M_{T:i} I_T + j\omega M_{R:i} I_R \,. \tag{2.46}$$

The Tx and Rx coil currents (I_T and I_R) can be derived from two sense coil voltages (V_i and V_j)

$$\begin{pmatrix} I_T \\ I_R \end{pmatrix} = \frac{1}{\mathcal{D}} \begin{pmatrix} M_{R:j} & -M_{R:i} \\ -M_{T:j} & M_{T:i} \end{pmatrix} \begin{pmatrix} \dfrac{V_i}{j\omega} \\ \dfrac{V_j}{j\omega} \end{pmatrix}, \tag{2.47}$$

$$\mathcal{D} = M_{T:i} M_{R:j} - M_{R:i} M_{T:j}, \tag{2.48}$$

where $M_{T:i}$ and $M_{R:i}$ are the mutual inductances from the Tx and Rx coils to the i^{th} sense coil.

The transfer-power in (2.12) is represented in terms of the mutual reactance $\omega M_{R:T}$ between the Tx and Rx coils, and the Tx and Rx coil currents (I_T and I_R). Sense coil voltages (V_i and V_j) can thus represent the transfer-power

$$P_{\text{Transfer}}(\omega) = \operatorname{Re}\left\{ j\omega M_{R:T} I_R(\omega) I_T(\omega)^* \right\} \tag{2.49}$$

$$= \frac{1}{\kappa} \operatorname{Im}\left\{ V_i(\omega) V_j^*(\omega) \right\}, \tag{2.50}$$

[8] This assumption elucidates the principle of accurate FC-TPM over the Rx coil's misalignment and corresponding calibration strategy in Section 3.3. The eddy current loss and hence the winding can be taken into account by increasing the matrix's dimension in (2.47) with four sense coils to include eddy currents I_t, I_r and corresponding mutual inductances, as shown in (3.38) in Section 3.4.2.

where

$$\kappa = \omega \sqrt{L_i L_j} \frac{k_{T:i} k_{R:j} - k_{T:j} k_{R:i}}{k_{R:T}}. \tag{2.51}$$

We denote $k_{m:n}$ as the coupling coefficient[9] between any two coils m and n. κ is a function of the coupling coefficients between coils and the self-inductances of the sense coils (L_i and L_j) at angular frequency ω.

2.4.3 Signal Processing

The power calculation is performed in the frequency domain because of several advantages over the time domain calculation. There are several advantages to processing in the frequency domain. These include accounting for frequency-dependent losses and nonlinearities through the integer harmonics of the fundamental. The prior knowledge that nonlinearities result in integer harmonics allows accurate frequency estimation. Besides, implementations of the Fast-Fourier Transform (FFT) both in software and digital hardware is efficient [52]. The geometric parameters at the fundamental can then be used. This is advantageous because the voltages at the fundamental are the largest compared to those from higher-order harmonics, hence representing the most reliable data with the biggest signal-to-noise ratio (SNR). Increasing measurements and data points can reduce measurement errors due to white noise. The processing of numerous data points, however, increases the data collection and computation time. Data reduction is therefore needed after measurements. Data reduction through the truncation of higher-order harmonics in the frequency domain does not incur phase error penalties in the remaining harmonics. This is not the case with non-aliasing decimation in the time domain.

In the frequency domain, the calculated component of transfer-power at each frequency point can be converted to the average power in watts (p_{Transfer}) through Parseval's theorem [52],

$$p_{\text{Transfer}} = \frac{1}{N} \sum_{\omega=0}^{N-1} P_{\text{Transfer}}(\omega), \tag{2.52}$$

[9] where $k_{m:n} = M_{m:n}/\sqrt{L_m L_n}$

where N is the number of data samples and P_{Transfer} is calculated from the discrete-time Fourier transform (DTFT) of the voltage and current signals. Total power in the time-domain is equal to that in the frequency domain.

2.4.3.1 Harmonic Bin Truncation Error

After the time domain signal is transformed to the frequency domain signal using discrete Fourier transform (DFT), each harmonic spectrum is a periodic sinc function, but not a perfect impulse due to the spectrum of a rectangular window used during the DFT process [53]. Additionally, spectral leakage can occur[10] when the frequency resolution Δf (i.e., bin spacing), defined by the sampling frequency f_s and the number of samples N_s as $\Delta f = f_s/N_s$, cannot represent the fundamental frequency and following harmonics by an integer multiple.[11] Although the spectral leakage, information at each frequency point, defined by a frequency resolution, can be processed individually for FC-TPM. One might attempt to define binning windows for corresponding harmonics. Information outside of each binning window is truncated, resulting in errors. Using the prior knowledge on the sinc function's envelopes, the window width can be chosen to bound the truncation error within a target accuracy. For a given binning window width ω_c, the truncation error ϵ can be derived from normalized periodic sinc function envelop [53]

$$\epsilon = \left(1 - \sum_{\omega=\omega_0-\frac{\omega_c}{2}}^{\omega=\omega_0+\frac{\omega_c}{2}} \frac{\sin\left(\frac{\omega}{2}N_s\right)}{\sin\left(\frac{\omega}{2}\right)N_s}\right) \times 100\,(\%) \tag{2.53}$$

Note that ω_0 is the center fundamental angular frequency (or harmonic angular frequency), where the binning window is symmetric around the center angular frequency, as shown in Fig. 2.12. For example, when f_s is 20 MHz, f_0 is 100.0005 kHz[12], N_s is 20 Mega-samples, and hence Δf is

[10] However, it is assumed that there is no too much spectral leakage and resulting broadening, such as if too few points are collected for a given sampling frequency.

[11] In the practical measurement condition, spectral leakage is likely to occur during the DFT process because; (i) there is an error in switching frequency in hardware (e.g., crystal oscillator or function generator); (ii) The first or last period of sinusoidal can be truncated by the rectangular window, resulting in imperfect sinusoidal waveform.

[12] f_0 is chosen not to be an integer to generate spectral leakage, where the frequency resolution is 1 Hz.

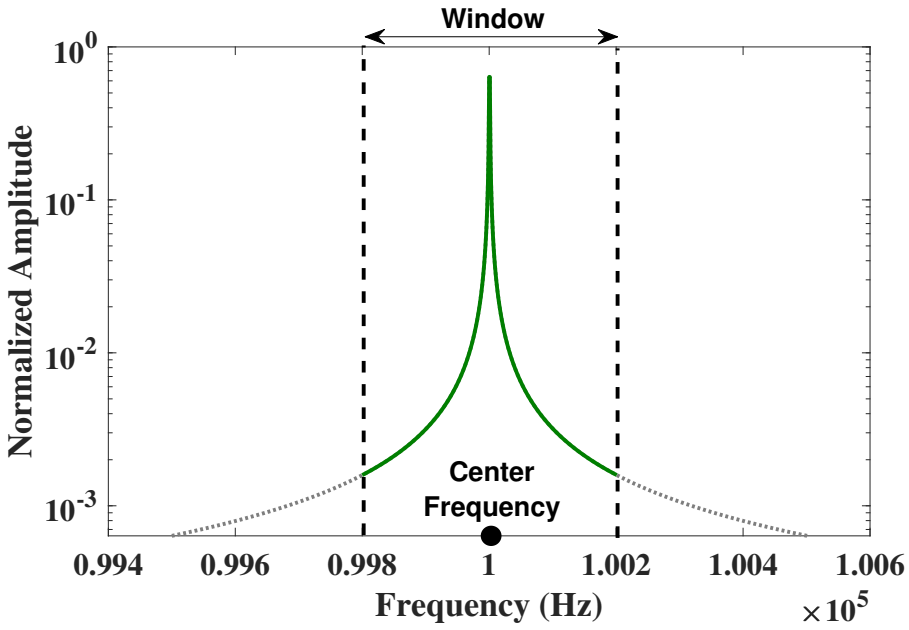

Figure 2.12. The binning window is determined to satisfy the target accuracy against losing data from the data truncation.

1 Hz, the binning window width of 400 Hz results in losing 0.1% of information.

CHAPTER 3

Accurate FC-TPM Over Geometric Variations

3.1 Chapter Introduction

Misalignment between the Tx (energy charging stations) and Rx coils (EVs), as illustrated in Fig. 3.1, is unavoidable; even an autonomous system can have a misalignment. In fact, SAE J2954 [45] certifies misalignment up to 10 cm for a 45 cm diameter coil. Misalignment between a vehicle and a charger degrades both power and efficiency. Misalignment of the order of the receiver coil radius can reduce the efficiency up to 40% [54]. For both sides, the misalignment of coils is an important factor in reducing efficiency and transfer and conversion losses, emphasizing the need to measure the transferred power throughout misalignment accurately. FC-TPM must therefore be accurate over that misalignment range.

FC-TPM as metering is practical for energy service stations in that only sense coil voltages are needed for measurement during charging. In the previous section 2.4.2, the corresponding geomet-

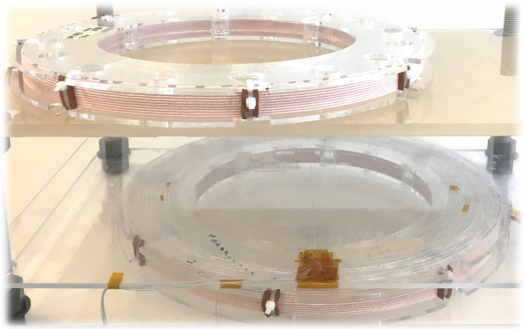

Figure 3.1. Misalignment between the transmitter and receiver coils

ric parameters were required to be constant so that they could be calibrated in advance. As detailed in (2.50) and (2.51), the geometric parameter κ is needed together with the sense coil voltages to determine transfer-power. In this chapter, the goals to make FC-TPM straightforward and accurate over misalignment is that (i) sense coil voltages are the only required measurements for metering during charging of EVs at stations; (ii) new geometric parameters, which is non-varying over misalignment, can be derived, enabling one time calibration of the parameters; (iii) the quantity of misalignment is not needed to be measured nor known so that no other auxiliary measurement system is needed. Additionally, this chapter presents the simulation results to show the accurate FC-TPM over multi-dimensional variations, including wireless charging coil's (i) misalignment; (ii) different types of wire (e.g., litz wire); and (iii) operating frequencies.

Section 3.2 analyzes the FC-TPM errors over Rx coil misalignment when only two sense coils and corresponding geometric parameters are used to reconstruct the transfer-power by (2.50). Section 3.3 presents how employing multiple sense coil voltages makes FC-TPM accurate over misalignment, where new geometric parameters are non-varying over misalignment. Section 3.4 verifies accurateness of FC-TPM over multi-dimensional variations when the Tx and Rx coils include proximity eddy current loss. Section 3.5 proposes potential safety diagnostics using the fundamental of accurate electromagnetic physics model across variations.

3.2 FC-TPM Errors with Two Sense Coils Over Rx Coil Misalignment

In this section, the transfer-power reconstruction error over lateral Rx coil misalignment is analyzed when two sense coils are used. Two sense coils are the minimum number to reconstruct the transfer-power in FC-TPM when the external proximity effect eddy current losses are neglected, as shown in (2.50). This error analysis gives an intuition of choosing the sense coil geometries (e.g., sizes and positions). In this dissertation, the shape of the Tx, Rx, and sense coils is defined as circular coils, one of the primary forms, from which theoretical and numerical analyses can be

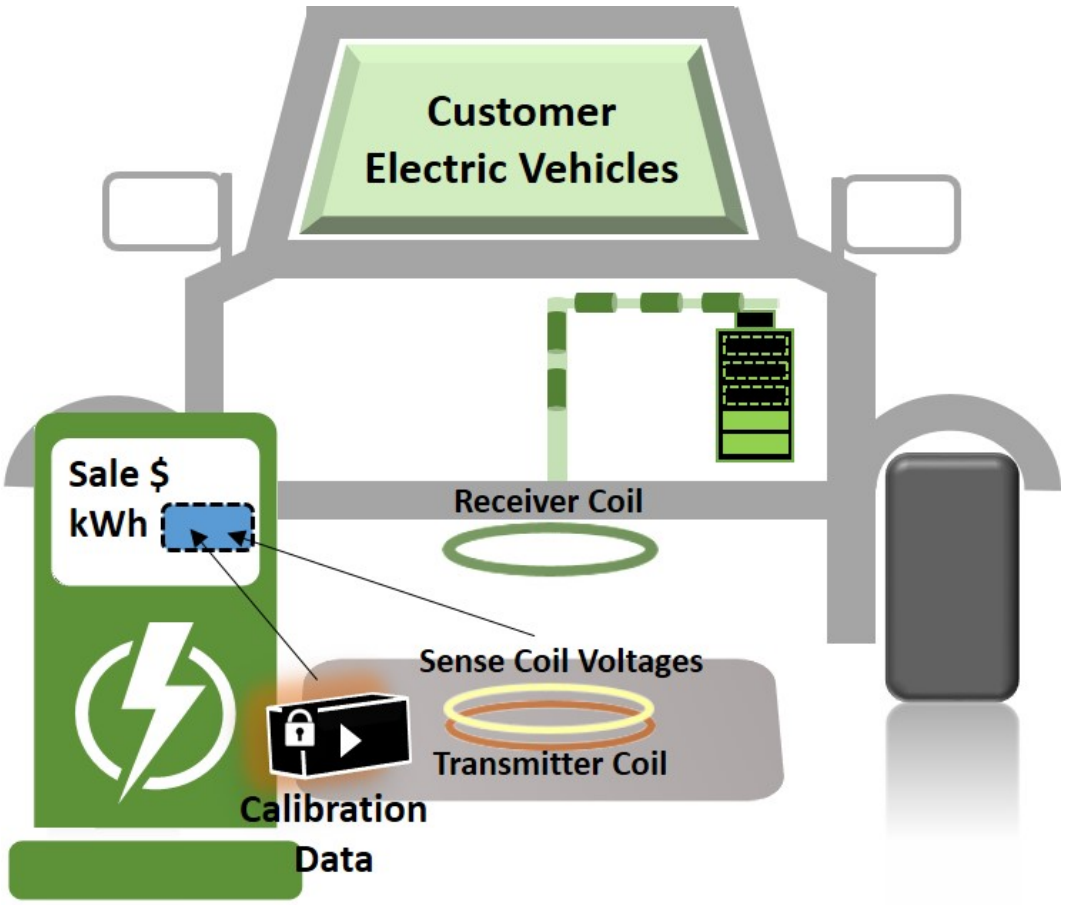

Figure 3.2. Conceptual Diagram: FC-TPM can be used as a metering for EVs at charging stations. The sense coil voltages and calibrated geometric parameters are used to reconstruct the transfer-power.

performed with tractability.[1] Ultimately, multiple sense coils are needed with a unique data combination for accurate FC-TPM over all eddy current losses as well as multi-dimensional variations (e.g., misalignment, operating frequency range, and different wire types), which will be shown in Section 3.3 and 3.4.

The first assumption for the FC-TPM as practical metering is that the geometric parameters should be calibrated initially and stored in the charging station. When EVs come to charge, only the sense coil voltages will be needed to calculate the transfer-power, where the initially calibrated geometric parameters are loaded, as shown in Fig. 3.2. Another assumption on the misalignment

[1]Numerical mutual inductance calculation between circular filament coils can be performed by [55], resulting in fast analysis with large data sets.

between the Tx and Rx coils is that there is no need to measure or know the misalignment information, which requires an additional misalignment measurement system and hence cost. Ultimate solutions for accurate FC-TPM over geometric variations which meet those assumptions are presented in Chapter 3.3.

When two sense coils are employed, calibration of the geometric parameter κ in (2.51) is performed when the Tx and Rx are assumed to be perfectly aligned. Subsequent misalignment from receivers result changes to $k_{T:R}, k_{R:1}$, and $k_{R:2}$, resulting in errors in transfer power reconstruction. Because the Tx coil and the sense coils are rigidly fixed by design[2], there is no subsequent misalignment among these; hence $k_{T:1}$ and $k_{T:2}$ do not change.

One can then conclude that sense coils (blue-coils in Fig. 2.10) should be placed closer to the Tx coil to maximize $k_{T:1}$ and $k_{T:2}$ so that the power calculation will be less sensitive to the position of the Rx coil. This positioning of coils minimizes the sensitivity of the FC-TPM to misalignment because changes of $k_{T:R}$ will be accompanied by changes in $k_{R:1}$ and $k_{R:2}$. Moreover, the self-inductance of the Tx (L_T) and Rx (L_R) coil cancel themselves to make the power calculation independent of these parameters. Only sense coil inductances (L_1 and L_2) matter, which are unaltered after calibration.

In this section, FC-TPM errors over Rx coil lateral misalignment are analyzed for two different sense coils geometries (positions and sizes). The lateral misalignment over *x* axis of the mobile Rx coil is considered,[3] as shown in Fig. 3.3.

3.2.1 Derivation of FC-TPM Errors Using Two Sense Coils Over Misalignment

Coupling coefficients between the Rx coil and other coils vary throughout misalignment. The variations of coupling coefficients cause FC-TPM errors. First, let the geometric parameter be κ_0,

[2]For the power metering in EV charging stations, the Tx coil and sense coils are fixed and buried underground. Vehicles (Rx coils) come to charge and can cause misalignment.

[3]This consideration can be expanded to any misalignment point on the *xy* plane because of the 360° symmetry of the coil configurations.

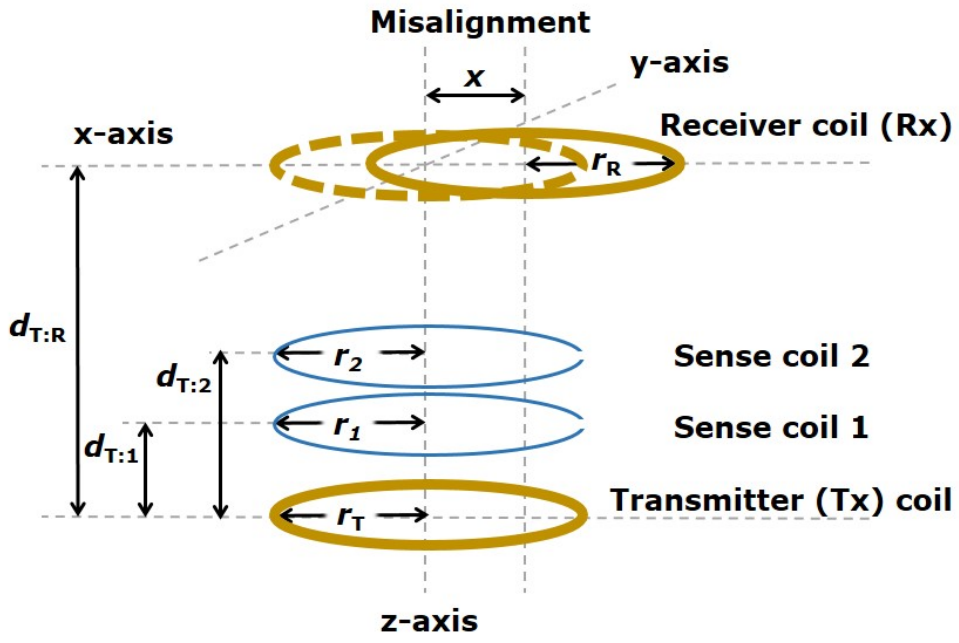

Figure 3.3. Configurations of the Tx, Rx, and two sense coils for misalignment analysis.

which is calibrated initially when the Rx coil is perfectly aligned ($x_0 = 0$). Then the transfer-power, $P'_{\text{Transfer}}(x)$, which is reconstructed by the κ_0 when the Rx coil is misaligned by x cm (Fig. 3.3) is

$$P'_{\text{Transfer}}(x) = \frac{1}{\kappa_0}\,\text{Im}\{V_1(x)V_2(x)^*\},$$

where,

$$\kappa_0 = \omega\sqrt{L_1L_2}\frac{k_{T:2}k_{R:1}(x_0) - k_{T:1}k_{R:2}(x_0)}{k_{T:R}(x_0)}. \tag{3.1}$$

Note that sense coil voltages, $V_1(x)$ and $V_2(x)$, are obtained when the Rx coil is positioned at x, while the geometric parameter k_0 was initially calibrated when the Rx coil was perfectly aligned, $x = 0$.

To calculate the reconstruction error in (3.1), the true value of the transfer-power (P_{Transfer}) at x is defined using κ_x as

$$P_{\text{Transfer}}(x) = \frac{1}{\kappa_x}\,\text{Im}\{V_1(x)V_2(x)^*\},$$

where,

$$\kappa_x = \omega\sqrt{L_1 L_2}\frac{k_{T:2}k_{R:1}(x) - k_{T:1}k_{R:2}(x)}{k_{T:R}(x)}. \tag{3.2}$$

From (3.1) and (3.2), we can find the FC-TPM error, ϵ_x, due to the misalignment, which only depends on the coupling coefficients and not inductances

$$\epsilon_x = 1 - \frac{P'_{\text{Transfer}}(x)}{P_{\text{Transfer}}(x)} = 1 - \frac{\kappa_x}{\kappa_0},$$

where, (3.3)

$$\frac{\kappa_x}{\kappa_0} = \frac{k_{T:R}(x_0)}{k_{T:R}(x)}\frac{\big(k_{T:2}k_{R:1}(x) - k_{T:1}k_{R:2}(x)\big)}{\big(k_{T:2}k_{R:1}(x_0) - k_{T:1}k_{R:2}(x_0)\big)}.$$

Note that the radii and positions of the sense coils can be chosen to minimize this error for a given the Tx and Rx coil configuration. This error is smaller when the sense coils are closer to the Tx coil than the Rx coil. This position is equivalent to choosing the Tx coil as the stationary reference frame and reducing the variation of the coupling coefficients from any of the coils to the misaligned Rx coil.

3.2.2 Error Analysis to Different Sense Coil Geometries over Misalignment

Using the error calculation in (3.3), one can analyze the sensitivity of the misalignment errors (ϵ_x) with respect to different distances ($d_{T:1}$ and $d_{T:2}$) or radii (r_1 and r_2) of the sense coils. Fig. 3.3 illustrates the configuration parameters for Tx, Rx, and the sense coils. The coils were approximated as circular filaments whose mutual inductance can be calculated [55]. The maximum Rx's misalignment was considered to 10 cm, which was specified as test points for WPT EVs in SAE TIR J2954 [45].

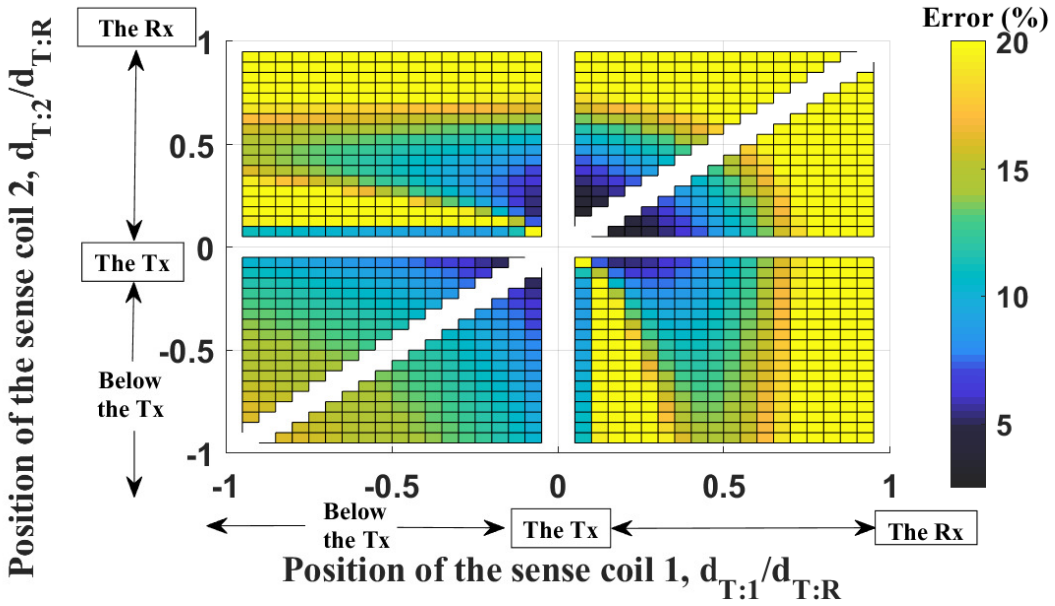

Figure 3.4. Transfer-power measurement error was plotted over $d_{T:1}/d_{T:R}$ and $d_{T:2}/d_{T:R}$ when all the coils had the same radii of 25 cm, and the Rx was misaligned by 10 cm to the Tx. Diagonal gaps represented the degenerate points, where the two sense coils are not separated. Vertical and horizontal gaps are physically excluded points, where either sense coil was overlapped with the Tx coil. The errors were bounded by 20% for better visualization.

3.2.2.1 Varying Sense Coil Distances

For a fixed misalignment of the Rx coil (x=10 cm) and the same radii of the coils ($r_{\text{T,R,1,2}}$=25 cm), $d_{T:1}$ and $d_{T:2}$ varied by 1 cm and tabulated with corresponding errors. The center of the Tx coil and the Rx coil were located and fixed at (0,0) and (10,20), respectively, using the (x, z) cm coordinate in Fig. 3.3. The sense coils' centers, (x, z) were varied from (0,-19) to (0,19). Fig. 3.4 shows the FC-TPM errors (color-map) under the misalignment with respect to the different ratios of $d_{T:1,2}$ to the $d_{T:R}$. As the sense coils were closer to the Tx coil, the FC-TPM errors are smaller (blue-region).

3.2.2.2 Varying Sense Coil Radii

Radii of the two sense coils ($r_{1,2}$) varied from 1 to 50 cm, at 1 cm intervals, and the power reconstruction errors were tabulated. The radii of the Tx and Rx were fixed to ($r_{T,R}$=25 cm), where the center of the Tx coil and Rx coil were (0,0) and (10,20), respectively. The fixed sense coil distances to the Tx coil were chosen as $d_{T:1} = 1$ and $d_{T:2} = 2$ cm for a small error. Fig. 3.5 illustrates the

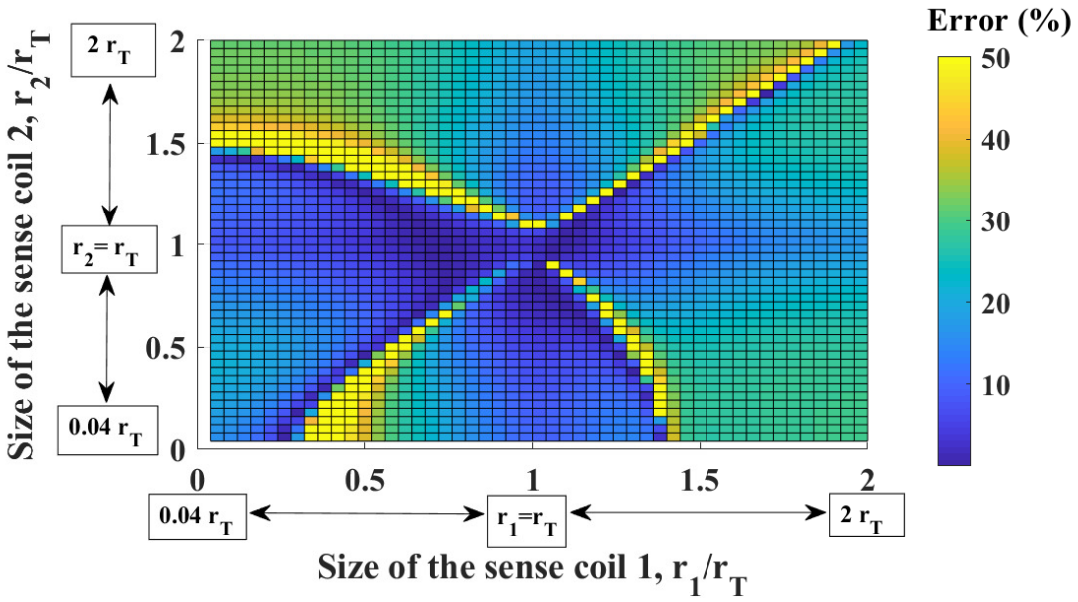

Figure 3.5. Transfer-power measurement error was plotted over r_1/r_T and r_2/r_T when the $d_{T:1}$=1 cm, $d_{T:2}$=2 cm, and the Rx was misaligned by 10 cm to the Tx. (The ill-conditioned cases where $k_{T:2}k_{R:1}(x_0) \approx k_{T:1}k_{R:2}(x_0)$ were bounded by 50% for the better visualization).

results of the numerical analysis. As the x-axis (r_1/r_T) and the y-axis (r_2/r_T) were closer to the center of the plot, meaning that the sense coils became similar size to the Tx coil (and the Rx coil), the FC-TPM errors were smaller (blue-region); the minimum error was 0.02% when (r_1, r_2) was $(25, 17)$ cm.

3.2.2.3 Lateral and Vertical Misalignment

Based on the results in Section 3.2.2.1 and 3.2.2.2, which reduce the errors across the lateral Rx coil misalignment, FC-TPM errors across the vertical Rx coil misalignment are also examined. This section shows how misalignment errors can be different from one sense coil geometry which shows particularly good performance for one axis (either x- or z-axis) misalignment. First, when $\{r_1, r_2, d_{T:1}, d_{T:2}\}$ are $\{25, 17, 1, 2\}$ cm, FC-TPM errors over vertical axis (z-axis) misalignment ϵ_z

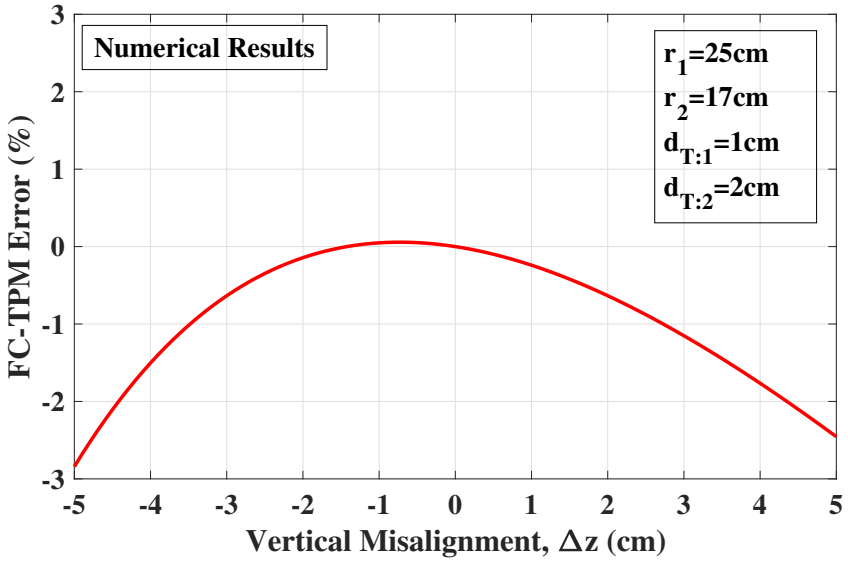

Figure 3.6. The FC-TPM errors were examined when the sense coils have the sizes and positions, which are found to have a good performance for the lateral misalignment.

is examined, where

$$\epsilon_z = 1 - \frac{P'_{\text{Transfer}}(z)}{P_{\text{Transfer}}(z)} = 1 - \frac{\kappa_z}{\kappa_0},$$

where, (3.4)

$$\frac{\kappa_z}{\kappa_0} = \frac{k_{T:R}(z_0)}{k_{T:R}(z)} \frac{\left(k_{T:2}k_{R:1}(z) - k_{T:1}k_{R:2}(z)\right)}{\left(k_{T:2}k_{R:1}(z_0) - k_{T:1}k_{R:2}(z_0)\right)}.$$

Note that z_0 is initial position when $d_{T:R} = 20\,\text{cm}$. The range of vertical misalignment is $\pm 5\,\text{cm}$, resulting in $15\,\text{cm} \leq d_{T:R} \leq 25\,\text{cm}$. Fig. 3.6 shows the FC-TPM errors over the vertical Rx coil misalignment, where the worst-case error was 2.84%, showing that the sense coil geometry, which is a good choice for lateral misalignment, is not necessarily good for vertical misalignment. On the contrary, a particularly good set of two sense coils whose $\{r_1, r_2, d_{T:1}, d_{T:2}\}$ are $\{29.39, 21.94, 6.97, 2.07\}\,\text{cm}$ shows accurate results over the vertical misalignment but not over the lateral misalignment. This particular sense coil geometry results in a worst-case 0.07% error over the vertical misalignment, while the worst-case error over the lateral misalignment is 0.44%, as shown in Fig. 3.7.

A very particular sense coil geometry could exist, resulting in accurate FC-TPM over both

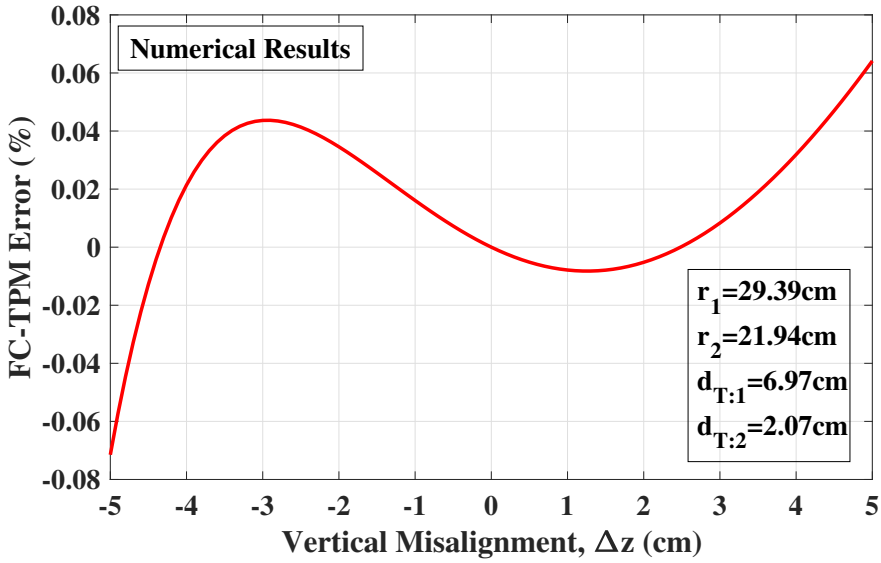

(a) FC-TPM error over the vertical Rx coil misalignment

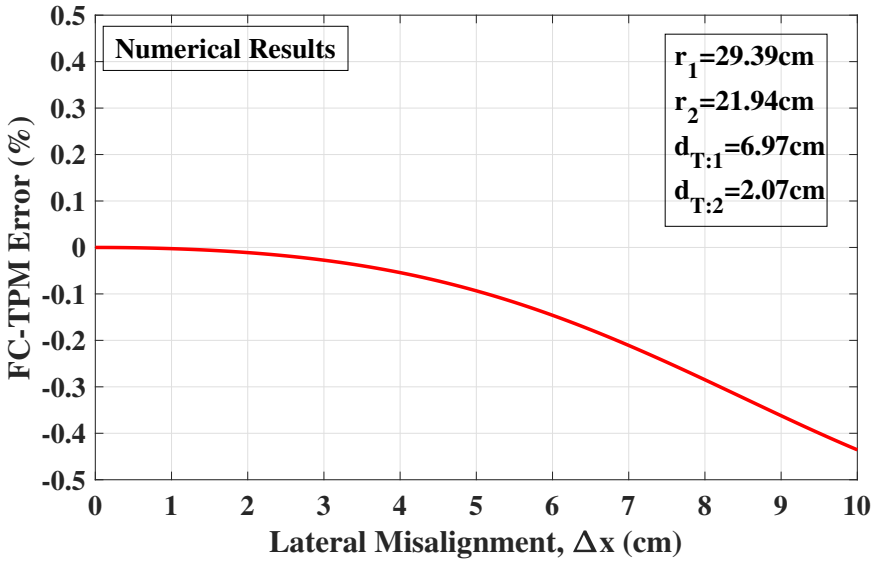

(b) FC-TPM error over the lateral Rx coil misalignment

Figure 3.7. A two sense coils geometry results in accurate transfer-power reconstruction over the vertical misalignment, but not over the lateral misalignment.

lateral and vertical misalignment. However, the sensitivity and complexity of finding geometries increase as the variations becomes multi-dimensional and simultaneous in practice. This is because the optimal geometries suitable for one axis variation are generally not favorable for other axis variations, as seen from the examples in Fig. 3.6 and 3.7. Furthermore, eddy current losses in the Tx and Rx coils can not be counted when two sense coils are used, resulting in inaccurate calculation of transfer-power in practice.[4] Chapter 3.3 presents ultimate solutions that do not count on the very particular sense coil geometries but use a unique combination of data obtained from multiple sense coils actually to cancel out the variations and results in accurate FC-TPM over Rx coil variations.

[4]Chapter 3.4.2.1 presents accurate FC-TPM, including eddy current losses in the Tx and Rx coils when multiple sense coils are used.

3.3 Accurate FC-TPM with Multiple Sense Coils Throughout Rx Coil Misalignment

To resolve the problem of parameter variation fundamentally, we employ multiple sense coils, as illustrated in Fig. 3.8, to collect more information, where non-varying geometric parameters, which are so calibrated initially, can be obtained over misalignment to determine the transfer-power. We found that a linear combination of pairwise-products of sense coil voltages determines the transfer-power accurately. The coefficients for the linear combination are geometric parameters that do not vary over misalignment. In fact, neither knowledge nor an explicit measurement of misalignment is needed to determine the transfer-power.

Despite the significant misalignment allowed for SAE J2954, the coupling coefficients from the Tx and sense coils to the Rx coil are well-approximated by quadratic functions (i.e., second-order polynomials) over the Rx coil misalignment. This quadratic approximation explains how a linear combination of pairwise-product of sense coil voltages can accurately determine transfer-power at any misalignment, with constant coefficients for the linear combination, hence allowing one time calibration. In fact, calibration requires neither knowledge nor explicit measurement of misalignment.

In this section, we show how the coupling coefficients can be approximated by quadratic functions of misalignment. We then present a formulation to determine transfer-power that is accurate over misalignment using multiple sense coil voltages.

3.3.1 Quadratic Approximation of Coupling Coefficient Variation over Misalignment

When the coupling coefficient from the Tx to Rx coil varies quadratically over the Rx coil's misalignment, it is advantageous to choose sense coil positions and radii so that the coupling coefficients from the sense coils to the Rx coil are also quadratic dominant. It is important to note that the coupling coefficient functions are positive definite; the quotient of positive definite quadratic

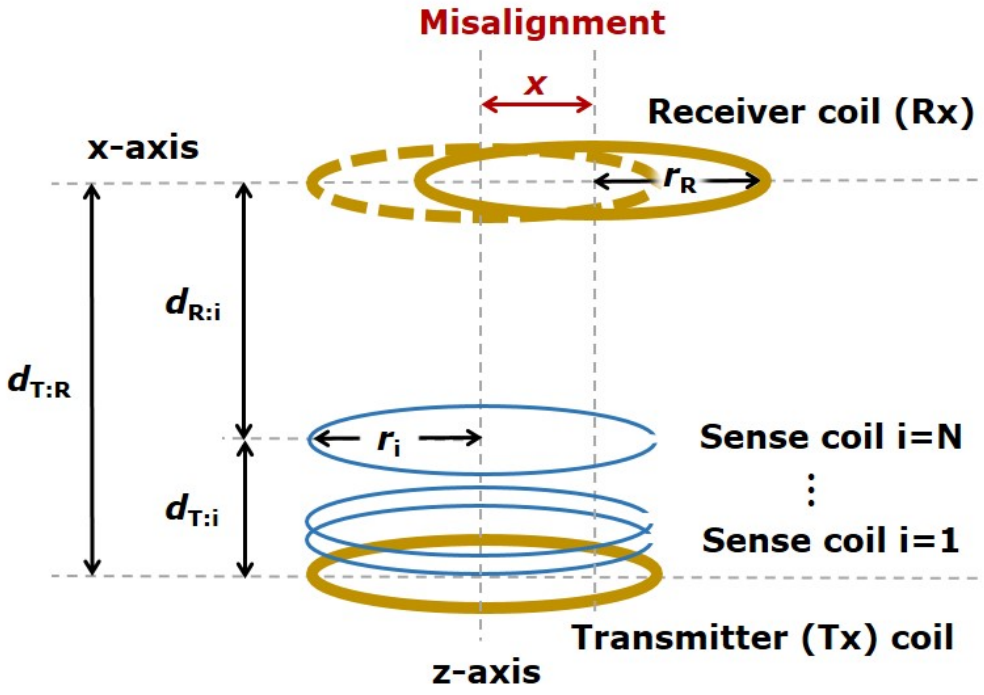

(a) The sense coils are placed coaxially with the Tx coil, which can be vertically stacked.

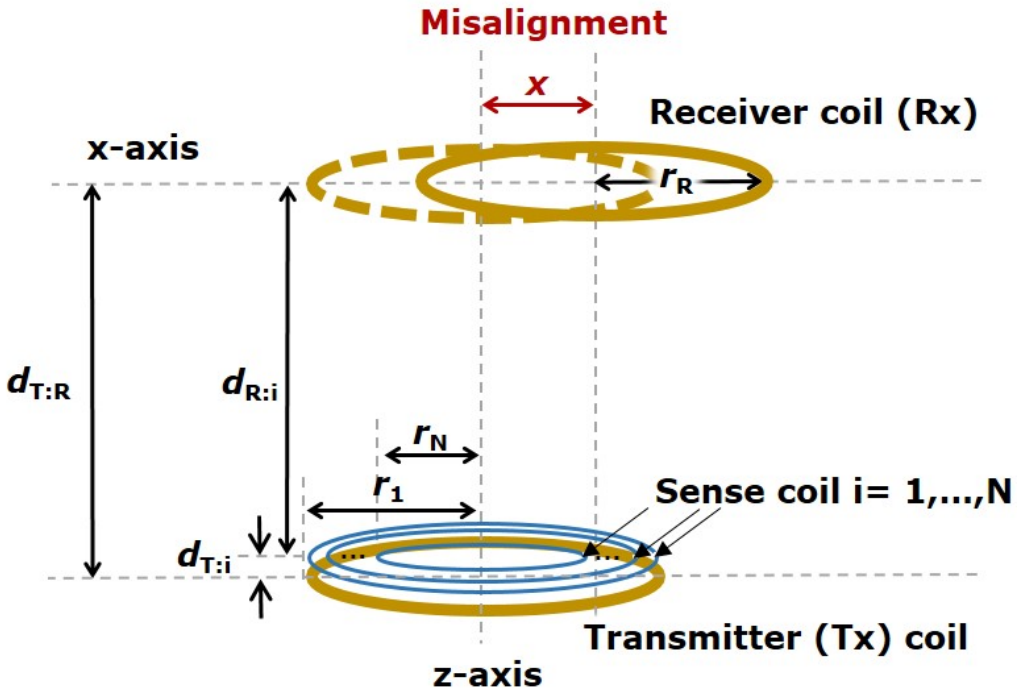

(b) Coplanar sense coils are on the same plane to have a low profile above the Tx coil. The radii of the sense coils are differentiated so that independent information regarding misalignment can be implicitly obtained.

Figure 3.8. Configurations of the Tx, Rx, and sense coils with Rx coil misalignment.

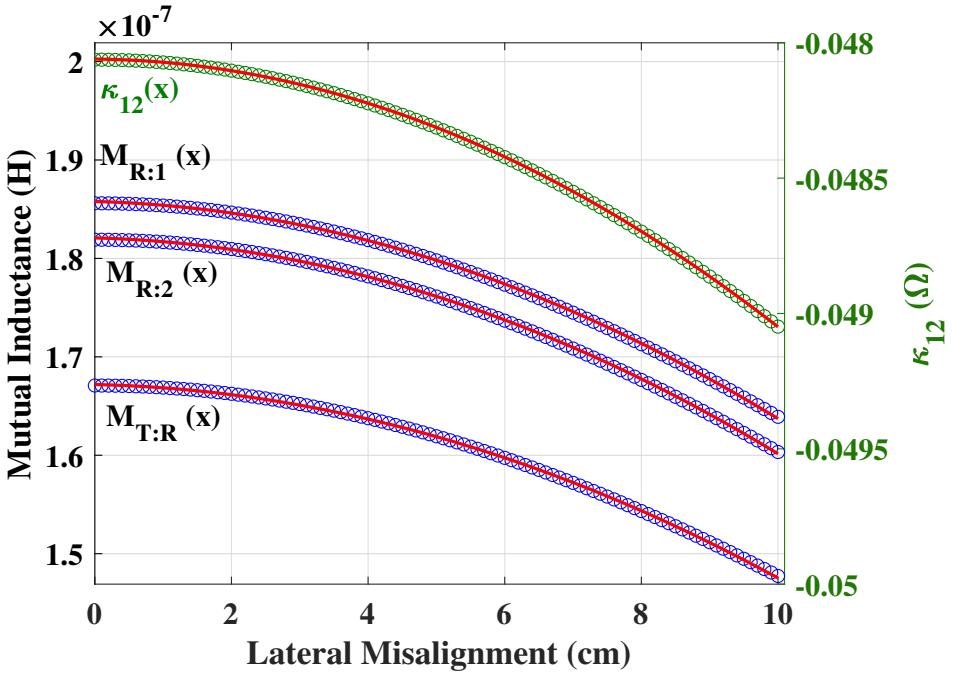

Figure 3.9. Numerical results of the relevant mutual inductances (blue-dots): (i) Tx-to-Rx; and (ii) Rx-to-sense-coils. The geometric parameter $\kappa_{12}(x)$ (green-dots) in (3.26) for two coplanar sense coils (sense coil 1 and 2, specified in Table 3.1) are plotted over Rx coil misalignment. Red lines are the corresponding second-order polynomial fits.

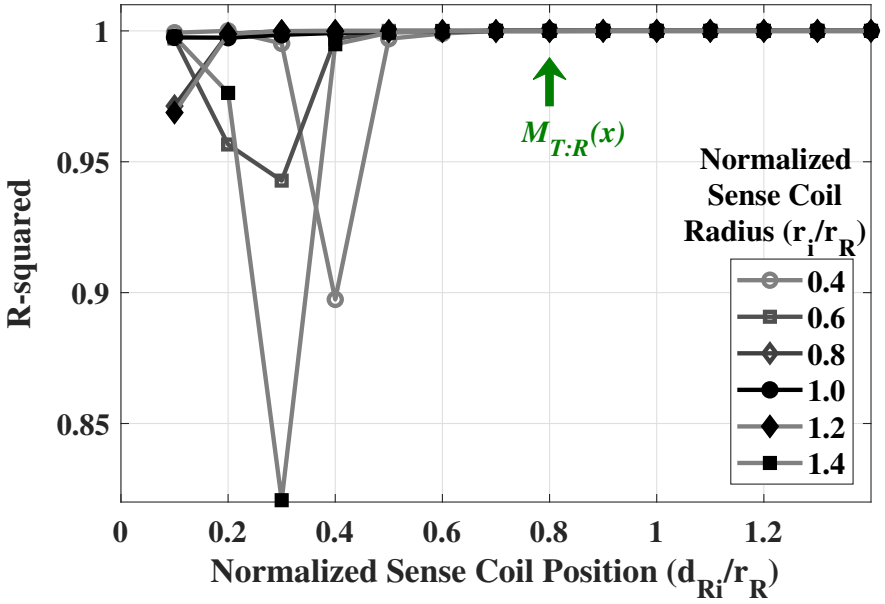

Figure 3.10. Numerical results of R-squared values of the second-order of polynomial fit of mutual inductance from the Rx coil over misalignment were plotted for different geometries. The R-squared values were obtained by the Curve Fitting Toolbox (MATLAB R2018b).

functions is also quadratic dominant, albeit over a narrower interval. Sense coils that are coaxially positioned with the Tx coil are especially good candidates for quadratic dominant coupling coefficients. In the following Section 3.3.2, we show how least-squares optimization of a parameterization of coupling coefficients based on quotients that form a quadratic dominant function is particularly good at determining transfer-power.

We derive a quadratic approximation for the mutual inductance and hence the coupling coefficient from Grover [56] for two circular filaments with lateral misalignment. The quadratic approximation is a Taylor expansion with respect to lateral misalignment. In bounding the Lagrange remainder, we show that this second-order Taylor approximation is accurate over the misalignment range of interest, which we detail in Appendix D. In Fig. 3.9, we show the calculated results for the (i) the mutual inductance, and hence the coupling coefficient, and (ii) the geometric parameter κ_{ij} for the Tx and Rx coils[5] using the numerical model for circular filaments in [55].

The mutual inductances and κ are very nearly quadratic with a *coefficient of determination* $R^2 > 0.999$.[6] We further investigated the quadratic dependence for different sense coil positions and radii using R^2. Fig. 3.10 shows that sense coil positions closer to the Tx coil are better.

3.3.2 FC-TPM Formulation Over Rx Coil Misalignment

Sense coil voltages implicitly contain information about the Rx coil misalignment. When combined with functions that implicitly contain information about the sense coil positions and sizes, transfer-power can be determined with minimal error from misalignment.

The transfer-power represented by (2.50) and (2.51) is a function of the lateral misalignment x of the Rx coil

$$P_{\text{Transfer}}(x) = \frac{1}{\kappa_{ij}(x)} \left\langle V_i(x), V_j(x) \right\rangle, \tag{3.5}$$

[5] Using 26 cm and 25.5 cm radii sense coils are placed on the same plane (coplanar) as shown in Fig. 3.8b and Table 3.1.

[6] R-squared (R^2) indicates the goodness of fit, ranging from 0 to 1. $R^2 = 1$ means that there is no error in the fitting [57].

where

$$\kappa_{ij}(x)=\omega\sqrt{L_iL_j}\frac{k_{T:i}k_{R:j}(x)-k_{T:j}k_{R:i}(x)}{k_{R:T}(x)}, \tag{3.6}$$

$$\left\langle V_i, V_j \right\rangle \triangleq \operatorname{Im}\left\{V_iV_j^*\right\}. \tag{3.7}$$

Note that $V_{i,j}(x)$ are sense coil voltages at a particular Rx coil misalignment x. We define $\left\langle V_i, V_j \right\rangle$ as the pairwise-product of sense coil voltages, where V_i and V_j are complex scalars. For power metering, the Tx and sense coils have fixed positions, whereas the electric vehicles (Rx coils) drive in to charge; therefore, the coupling coefficients between Tx and sense coils ($k_{T:i}$ and $k_{T:j}$) do not change.

If we use (3.5) to determine transfer power, the misalignment x and every coupling coefficient as a function of x must be explicitly and accurately known. However, in using multiple sense coils, we can transform the overdetermined set of sense coil voltages to a function that determines transfer-power from these sense coil voltages alone. We will show that this function can be simply calibrated over the span of misalignment, but without needing a measurement of misalignment at all.

In using multiple sense coils, the pairwise-product of voltages from each unique pair $\left\langle V_i, V_j \right\rangle$ can be linearly combined and scaled by corresponding coefficients α_{ij}

$$\begin{aligned}\sum_{i,j\in Q}\alpha_{ij}\left\langle V_i(x), V_j(x)\right\rangle &= P_{\text{Transfer}}(x)\left\{\sum_{i,j\in Q}\alpha_{ij}\kappa_{ij}(x)\right\},\\ Q &= \left\{(i,j)\in\mathbb{N}^2 \;\middle|\; i\le N, j\le N, \text{ and } i<j\right\},\end{aligned} \tag{3.8}$$

where N is the number of sense coils.

As discussed earlier, the function $\kappa_{ij}(x)$ is well-approximated by a quadratic polynomial

$$\begin{aligned}&\kappa_{ij}(x)\approx p_{ij}+q_{ij}x+r_{ij}x^2,\\ &\text{where } p,q,r\in\mathbb{R}.\end{aligned} \tag{3.9}$$

If we choose α_{ij} so that

$$\begin{aligned}\sum_{i,j\in Q}\alpha_{ij}\kappa_{ij} &\approx \sum_{i,j\in Q}\alpha_{ij}p_{ij}+\sum_{i,j\in Q}\alpha_{ij}q_{ij}x+\sum_{i,j\in Q}\alpha_{ij}r_{ij}x^2 \\ &\approx 1,\end{aligned} \tag{3.10}$$

where

$$\begin{aligned}&\sum_{i,j\in Q}\alpha_{ij}p_{ij}\approx 1,\sum_{i,j\in Q}\alpha_{ij}q_{ij}\approx 0,\sum_{i,j\in Q}\alpha_{ij}r_{ij}\approx 0, \\ &\alpha_{ij}\in\mathbb{R},\end{aligned} \tag{3.11}$$

and perform a least-squares optimization to obtain α_{ij}

$$\begin{aligned}&\underset{\alpha_{ij}}{\text{minimize}} \quad \left\| P_{\text{Transfer}}(x)-\sum_{i,j\in Q}\alpha_{ij}\left\langle V_i(x),V_j(x)\right\rangle \right\|_2 \\ &\text{subject to } \alpha_{ij}\in\mathbb{R},\end{aligned} \tag{3.12}$$

then the transfer-power can be determined despite misalignment from the linear combination of unique pairwise-products of sense coil voltages

$$\begin{aligned}&P_{\text{Transfer}}=\sum_{i,j\in Q}\alpha_{ij}\left\langle V_i,V_j\right\rangle, \\ &Q=\left\{(i,j)\in\mathbb{N}^2\,\middle|\, i\le N, j\le N, \text{ and } i<j\right\},\end{aligned} \tag{3.13}$$

where $V_i=V_i(x)$ and $V_j=V_j(x)$ are only voltage measurements and implicit functions of x; N is the number of sense coils. Note that the geometric parameters α_{ij}, which are calibrated initially, are constant (independent of x). Fig. 3.11 shows an example that a linear combination of quadratic functions κ_{ij} can be a constant with properly chosen geometric parameters α_{ij}.

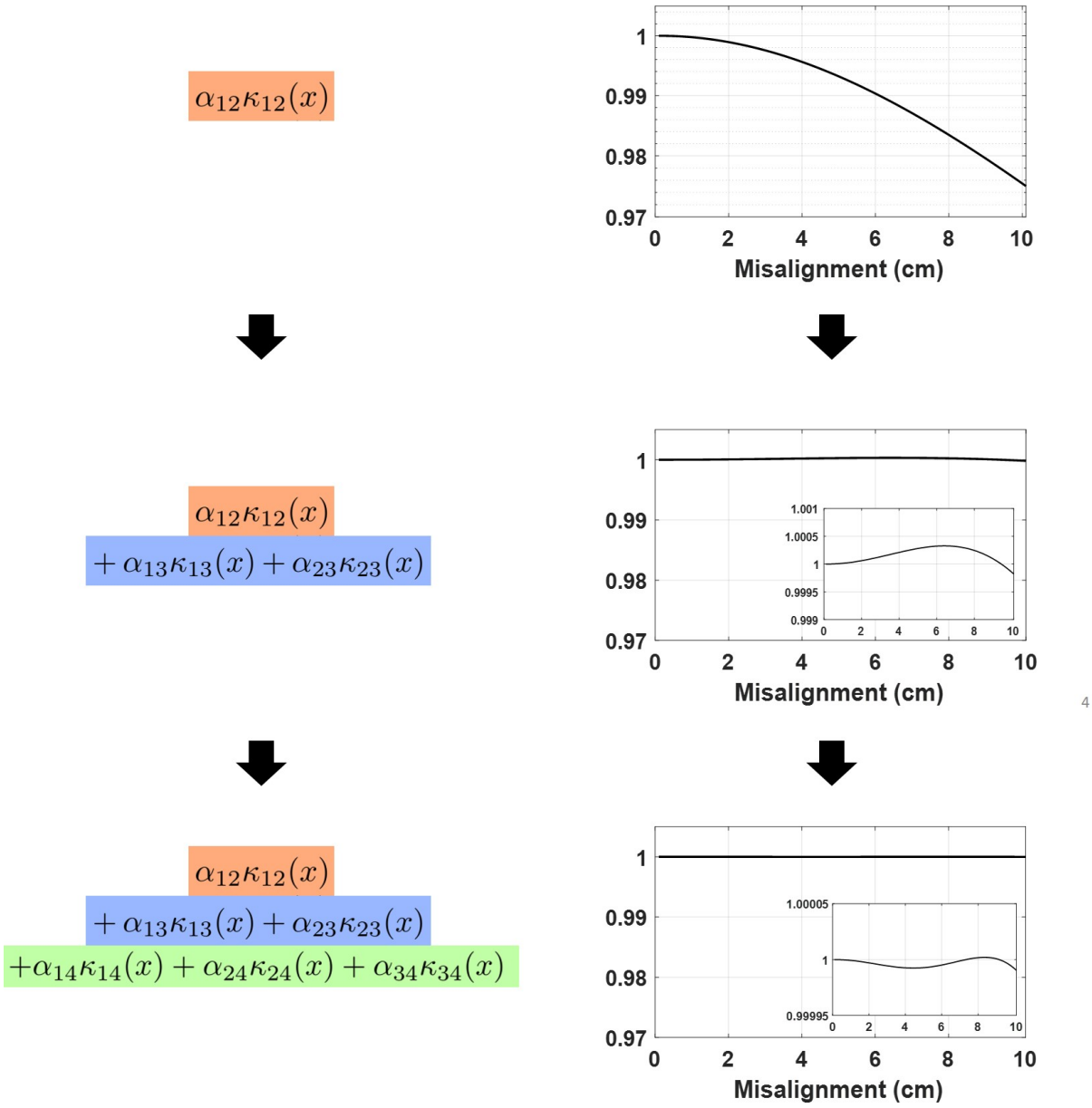

Figure 3.11. An example of a linear combination of quadratic κ functions, which results in a constant value.

3.3.3 Calibration of Constant Geometric Parameters Over Misalignment and FC-TPM Numerical Results

In this section, we explain how the geometric constants in the previous Section 3.3.2 can be calibrated. We then numerically evaluate FC-TPM over misalignment using well-known models from literature.

3.3.3.1 Formulating the Calibration Matrix and Vector

The calibration of the geometric parameters α_{ij} requires sense coil voltage measurements and transfer-power data from a reference standard. The sense coil voltage measurements are combined as uniquely-paired products in a data matrix

$$\mathbf{W} = \begin{pmatrix} \langle V_1(x_1,Z_1),V_2(x_1,Z_1)\rangle & \dots & \langle V_i(x_1,Z_1),V_j(x_1,Z_1)\rangle \\ \vdots & \ddots & \vdots \\ \langle V_1(x_m,Z_1),V_2(x_m,Z_1)\rangle & \dots & \langle V_i(x_m,Z_1),V_j(x_m,Z_1)\rangle \\ \langle V_1(x_1,Z_2),V_2(x_1,Z_2)\rangle & \dots & \langle V_i(x_1,Z_2),V_j(x_1,Z_2)\rangle \\ \vdots & \ddots & \vdots \\ \langle V_1(x_m,Z_2),V_2(x_m,Z_2)\rangle & \dots & \langle V_i(x_m,Z_2),V_j(x_m,Z_2)\rangle \\ \vdots & \ddots & \vdots \\ \vdots & \ddots & \vdots \\ \langle V_1(x_m,Z_n),V_2(x_m,Z_n)\rangle & \dots & \langle V_i(x_m,Z_n),V_j(x_m,Z_n)\rangle \end{pmatrix}. \tag{3.14}$$

The transfer-power corresponding to each row of $\mathbf{W}$ is contained in the elements of column vector $\mathbf{p}$

$$\mathbf{p} = \left[P_{\text{Transfer}}(x_1, Z_1)\ P_{\text{Transfer}}(x_2, Z_1) \cdots P_{\text{Transfer}}(x_m, Z_n) \right]^{\intercal}. \tag{3.15}$$

Each row of $\mathbf{W}$ corresponds to a particular measurement condition (e.g., misalignment, power, load, etc.). The number of unique pairings for the the pairwise-product of sense coil voltages from N sense coils is $N_w = {}_N C_2$. For l data points of variation that consists of m data points of

misalignment ($x_{1,\ldots,m}$) and n data points of Rx coil loading ($Z_{1,\ldots,n}$): $l = mn$, $\mathbf{W} \in \mathbb{R}^{l \times N_w}$, and $\mathbf{p} \in \mathbb{R}^{l \times 1}$.

The data for calibration needs to span the space of variation, which includes geometric variation (e.g., misalignment) and load. The variation in load needs to span the real impedances corresponding to the required measurement range for transfer-power.

It is worth noting that the variation encapsulated in $\mathbf{W}$ and $\mathbf{p}$ does not have to be uniform, nor does the explicit domain of variation (e.g., actual misalignment displacement x) need to be measured.

The vector of geometric parameters $\alpha_{ij} \in \mathbb{R}^{N_w \times 1}$ for N sense coils is

$$\boldsymbol{\alpha} = \begin{bmatrix} \alpha_{12} & \alpha_{13} & \ldots & \alpha_{ij} \end{bmatrix}^{\intercal}. \tag{3.16}$$

From (3.13),

$$\mathbf{W}\,\boldsymbol{\alpha} = \mathbf{p}, \tag{3.17}$$

which is overdetermined, allowing the calculation and hence calibration of $\boldsymbol{\alpha}$ using the least-squares method

$$\boldsymbol{\alpha} = (\mathbf{W}^{\intercal}\mathbf{W})^{-1}\,\mathbf{W}^{\intercal}\mathbf{p}\,. \tag{3.18}$$

3.3.3.2 Coil Configurations

Two different placements of sense coils were considered for the numerical analysis, as shown in Fig. 3.8 (a) and (b):

(a) Vertically Stacked Sense Coils: The N sense coils are vertically stacked above the Tx coil at 1 cm intervals. The radii of the Tx, Rx, and sense coils are identically 25 cm.

(b) Coplanar Sense Coils (Low-Profile): All N sense coils are concentric and placed on the same plane, which is 1 cm above the Tx coil. The sense coil radii varied from 26 cm to 23.5 cm, decreasing at 0.5 cm intervals.

For each case, the Tx, Rx, and sense coils have the same center axis (coaxial). Table 3.1 shows the specifications for each coil configuration.

TABLE 3.1
Configurations of the Tx, Rx, and Sense Coils

Parameters	Value	Parameters	Value
r_T,r_R	25 cm	$d_{T:R}$	20 cm
r_i (Stacked)	25 cm	$d_{T:i}$ (Stacked)	$i \cdot 1$ cm
r_i (Coplanar)	26 cm - $(i-1)\cdot 0.5$ cm	$d_{T:i}$ (Coplanar)	1 cm

3.3.3.3 Numerical Results

Mutual inductances were obtained from a well-known circular filament model [55] over the Rx coil misalignment x. The model assumptions include: (i) concentrated windings as shown in Fig. 3.8; (ii) fundamental frequency only; and (iii) no measurement noise. The Tx and Rx coils are driven by current sources.[7] The transfer-power and sense coil voltages were calculated with (2.12) and (2.46), respectively, at each misalignment. The equivalent circuit for the numerical model is shown in Fig. 2.10b. The geometric parameters α_{ij} were calibrated using sense coil voltages and transfer-power; the accuracy of FC-TPM was then evaluated using leave-one-out cross-validation (LOOCV) [58].[8] FC-TPM accuracy was evaluated for different numbers of sense coils (from two to six). For these numerical results, $m=11$ misalignment data points (0 to 10 cm at 1 cm intervals) and $n=6$ load data points were used to calibrate α_{ij}.

The FC-TPM errors over misalignment were calculated for each data point using LOOCV. The percentage errors are calculated between the standardized value $P_{\text{Transfer}}(x_m, Z_n)$, and the recon-

[7]The phases of the Tx and Rx currents were properly chosen to ensure the direction of power transfer to be from the Tx coil to the Rx coil, as shown in Section 2.2.1.

[8]In cross-validation, the data is split into two disjoint subsets: a calibration set and a validation set. The calibration is performed with the calibration set, which excludes the validation set. The accuracy of FC-TPM was evaluated with the validation set using the calibrated parameters. In LOOCV, the validation consists of one data point, and the calibration set consists of the other $l-1$ data points.

structed value $\hat{P}_{\text{Transfer}}(x_m, Z_n)$,

$$\varepsilon(x_m, Z_n) = \frac{\hat{P}_{\text{Transfer}}(x_m, Z_n) - P_{\text{Transfer}}(x_m, Z_n)}{P_{\text{Transfer}}(x_m, Z_n)} \times 100\,(\%) \tag{3.19}$$

where

$$\begin{aligned} P_{\text{Transfer}}(x_m, Z_n)&\text{: Reference standard transfer-power} \\ &= \text{Re}\left\{ j\omega M_{R:T}(x_m) I_R(Z_n) I_T(Z_n)^* \right\}, \end{aligned} \tag{3.20}$$

$$\begin{aligned} \hat{P}_{\text{Transfer}}(x_m, Z_n)&\text{: Transfer-power reconstructed with FC-TPM} \\ &= \sum_{i,j \in Q} \alpha_{ij} \left\langle V_i(x_m, Z_n), V_j(x_m, Z_n) \right\rangle. \end{aligned} \tag{3.21}$$

Fig. 3.12a and 3.12b show the FC-TPM errors over misalignment for two different sense coil placements, as defined in Fig. 3.8. We plotted the worst-case absolute error percentages of FC-TPM

$$\left| \varepsilon\left(\mathbf{u}\right) \right|_{\text{max}} \triangleq \max_k \left| \varepsilon\left(\mathbf{u}_k\right) \right|, \tag{3.22}$$

where $\mathbf{u}_k$ is the vector of parameter variations over which the error is calculated. The worst-case absolute errors at each lateral misalignment x were calculated and plotted in Fig. 3.12, where $\mathbf{u}_k = \begin{bmatrix} x & Z_k \end{bmatrix}$.

For both sense coil configurations, the errors were nearly constant over the misalignment with an increasing number of sense coils resulting in lower error. The lowest percentage errors were approximately $10^{-6}\%$ for six sense coils (green-circles). Coplanar sense coils have a lower profile and hence are more practical for deployment in charging stations; these results show that coplanar sense coils have comparable performance to coaxial sense coils that are not coplanar. Sensor placement and sizing are analyzed over trade-offs in Section 4.2 to corroborate the performance of coplanar configurations relative to other configurations.

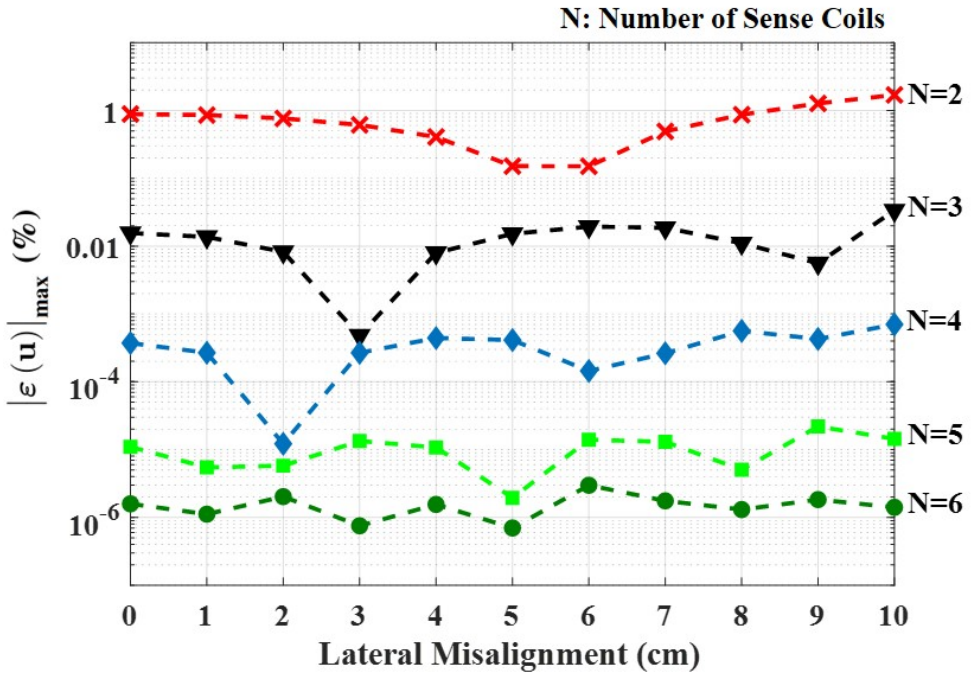

(a) Sense coils were vertically stacked coaxially at 1 cm intervals above the Tx coil, as shown in Fig. 3.8a.

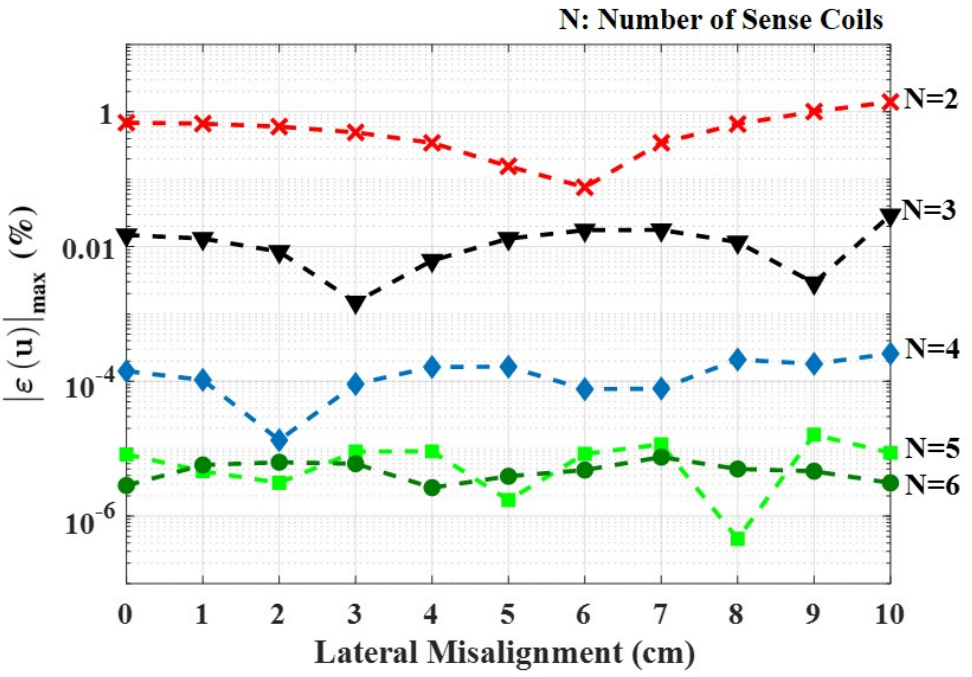

(b) Coplanar sense coils were placed coaxially, 1 cm above the Tx coil, as shown in Fig. 3.8b. The radii of the sense coils decrease from 26 cm at 0.5 cm intervals.

Figure 3.12. Results from the numerical model, verifying the accuracy of FC-TPM over misalignment.

3.3.4 FC-TPM Across Angular and Vertical Misalignment

Figure 3.13. Angular misalignment (left) and vertical misalignment (right) between the Tx and Rx coils.

In this section, the performance of coplanar multiple sense coils for FC-TPM is examined over Rx coil angular and vertical misalignment, as shown in Fig. 3.13. Using (3.5), transfer-power can be reconstructed by a pairwise-product of two sense coil voltages over angular misalignment θ and vertical misalignment z

$$P_{\text{Transfer}}(\theta) = \frac{1}{\kappa_{ij}(\theta)} \left\langle V_i(\theta), V_j(\theta) \right\rangle, \tag{3.23}$$

$$P_{\text{Transfer}}(z) = \frac{1}{\kappa_{ij}(z)} \left\langle V_i(z), V_j(z) \right\rangle, \tag{3.24}$$

where

$$\kappa_{ij}(\theta) = \omega \sqrt{L_i L_j} \frac{k_{T:i}k_{R:j}(\theta) - k_{T:j}k_{R:i}(\theta)}{k_{R:T}(\theta)}, \tag{3.25}$$

$$\kappa_{ij}(z) = \omega \sqrt{L_i L_j} \frac{k_{T:i}k_{R:j}(z) - k_{T:j}k_{R:i}(z)}{k_{R:T}(z)}, \tag{3.26}$$

$$\left\langle V_i, V_j \right\rangle \triangleq \text{Im}\left\{ V_i V_j^* \right\}. \tag{3.27}$$

Note that each misalignment is considered separately to elucidate that the same working principle of accurate FC-TPM with multiple sense coils can be applied to various misalignment types.

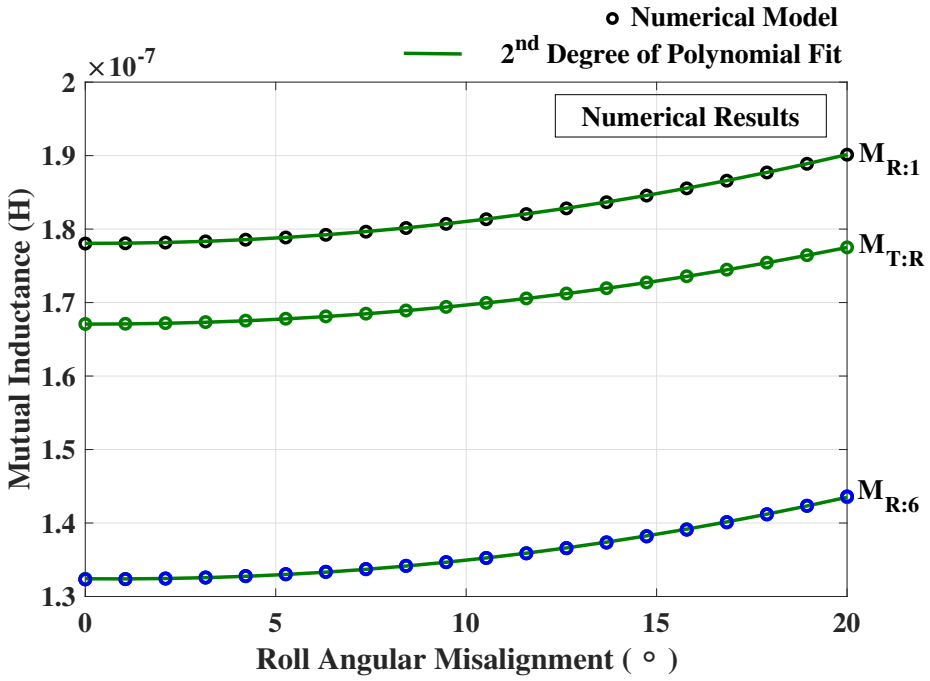

Figure 3.14. Second-order polynomial fits of the mutual inductance over angular misalignment.

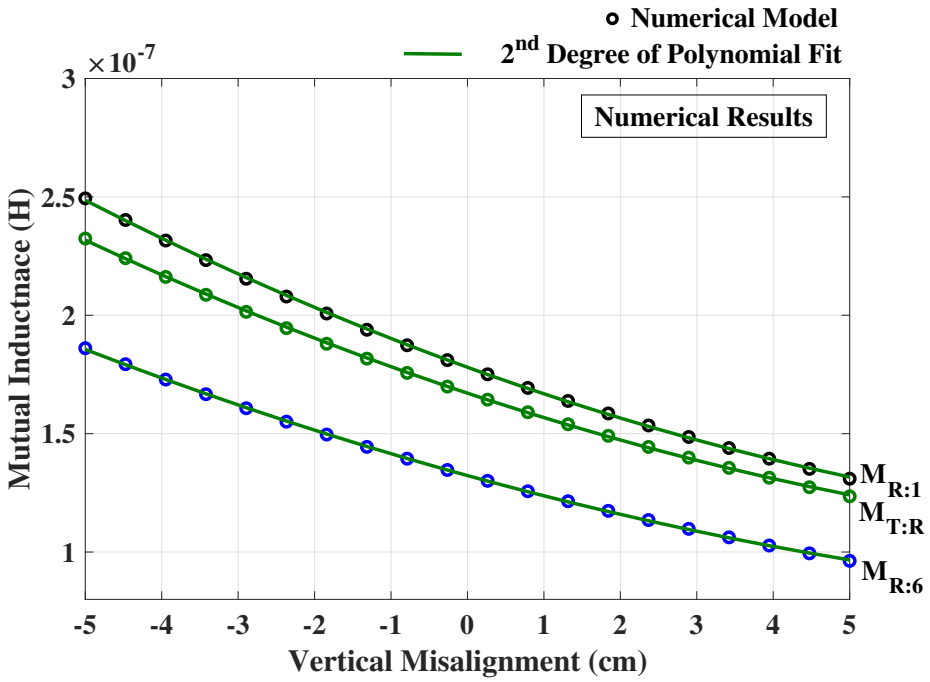

Figure 3.15. Second-order polynomial fits of the mutual inductance over vertical misalignment.

Section 3.4 presents accurate FC-TPM when there are multi-dimensional misalignment or variations (e.g., operating frequencies and wire types) at the same time.

Mutual inductance variation over each misalignment is calculated and approximated by quadratic polynomial functions. For the angular misalignment, roll (rotation around the x-axis) is considered, but due to the 360° circular symmetry of the Tx, Rx, and sense coils, the roll and pitch of are identical while yaw (rotation around the z-axis) can be ignored. In this analysis, 0° to 20° roll[9] ($\Delta\theta$) and -5 cm to 5 cm vertical misalignment (Δz) were varied. The Tx and Rx coil radii were 25 cm, where the Tx coil-to-Rx coil air gap was 20 cm. FC-TPM sense coils were single-turn, open-circuited, and placed on a flat-plane, 1 cm above the Tx coil. The radii of the sense coils 1 to 6 (labeling the outermost sense coil as one) were 25 cm to 20 cm, respectively, decreasing at 1 cm intervals, as shown in Fig. 3.13.

Fig. 3.14 and Fig. 3.15 show the polynomial approximation of the mutual inductance over angular and vertical misalignment. Circle-dots are the mutual inductance values at each misalignment point by the numerical model [55]. Green-lines are the second-order polynomial fits (provided by MATLAB Curve Fitting). Mutual inductance variations over both angular and vertical misalignment can be approximated by quadratic functions very well; all fits demonstrated a strong correlation with the data. For angular misalignment, the linear coefficient β_{ij} can, therefore, be found to satisfy

$$\sum_{i,j\in Q} \beta_{ij} \operatorname{Im}\left\langle V_i(\theta) V_j(\theta)\right\rangle = P_{\text{Transfer}}(\theta) \left\{ \sum_{i,j\in Q} \beta_{ij}\kappa_{ij}(\theta) \right\} \tag{3.28}$$

$$\approx P_{\text{Transfer}}(\theta), \tag{3.29}$$

when,

$$\sum_{i,j\in Q} \beta_{ij}\kappa_{ij}(\theta) \approx \sum_{i,j\in Q} \beta_{ij} a_{ij} + \sum_{i,j\in Q} \beta_{ij} b_{ij}\theta + \sum_{i,j\in Q} \beta_{ij} c_{ij}\theta^2 \approx 1, \tag{3.30}$$

[9]SAE J2954 requires wireless charging under a roll and pitch up to $\pm 2^\circ$, and a yaw up to $\pm 3^\circ$

where,

$$\kappa_{ij}(\theta) \approx a_{ij} + b_{ij}\theta + c_{ij}\theta^2,\ a, b, c \in \mathbb{R}. \tag{3.31}$$

Similarly, for the vertical misalignment z, the linear coefficient γ_{ij} can, therefore, be found to satisfy

$$\sum_{i,j\in Q} \gamma_{ij} \operatorname{Im}\left\langle V_i(z) V_j(z)\right\rangle = P_{\text{Transfer}}(z) \left\{ \sum_{i,j\in Q} \gamma_{ij}\kappa_{ij}(z) \right\} \tag{3.32}$$

$$\approx P_{\text{Transfer}}(z). \tag{3.33}$$

FC-TPM accuracy was tested for the angular and vertical misalignment. The different number of sense coils (two to six) were used for each test to verify the effectiveness of using multiple sense coils for accuracy. β_{ij} and γ_{ij} are the constant geometric parameters needed to be calibrated initially over each variation space. It is worth noting that; (i) there is no need to measure the misalignment quantity explicitly during the calibration; (ii) β_{ij} and γ_{ij} are fixed values that are not just for specific misaligned positions, but for all over the misalignment, meaning that only sense coil voltages are needed to be measured when we calculate the transfer-power at any misalignment.

Numerical data were obtained over: (i) 20 data points within a given range of each misalignment (a roll and vertical misalignment); (ii) where, at each data point in (i), 9 data points of different Rx coil current phases that are corresponding to different output load resistances. The FC-TPM errors were determined for each data points using leave-one-out cross-validation; (i) β_{ij} and γ_{ij} were calibrated using the training set which excluded a single validation set; (ii) the FC-TPM error ϵ for the validation set was calculated by comparing the true transfer-power (P_{Transfer}) and the one calculated by the FC-TPM ($\hat{P}_{\text{Transfer}}$), which are represented in (3.19).

Fig. 3.16 and Fig. 3.17 show the numerical results that the transfer-power was accurately reconstructed over misalignments; the percentage errors were nearly consistent along with misalignment. Increasing the number of sense coils resulted in better accuracy, where the primary source of the

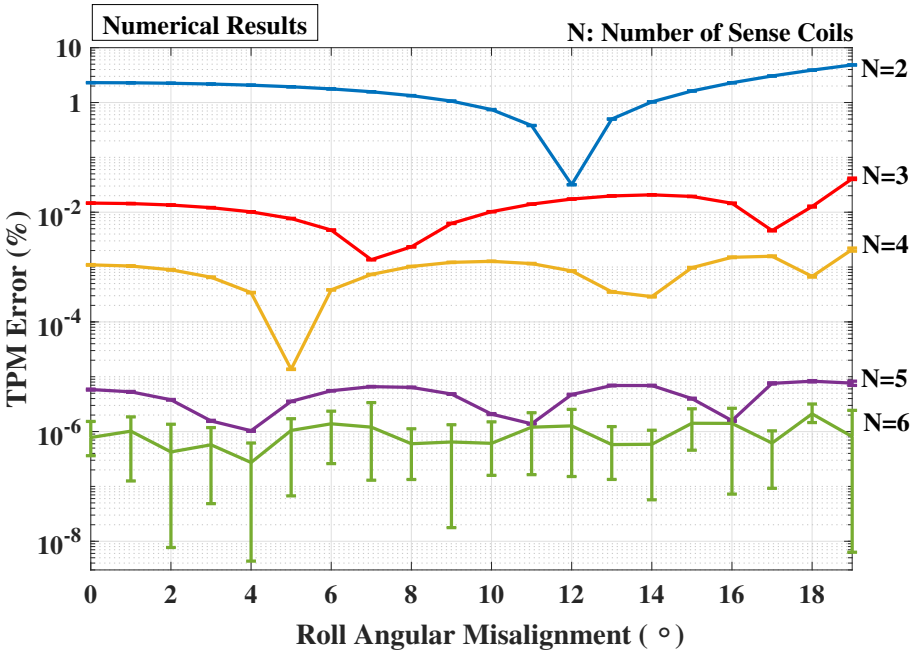

Figure 3.16. Numerical model results: TPM was accurate over angular misalignment (0 to 20°).

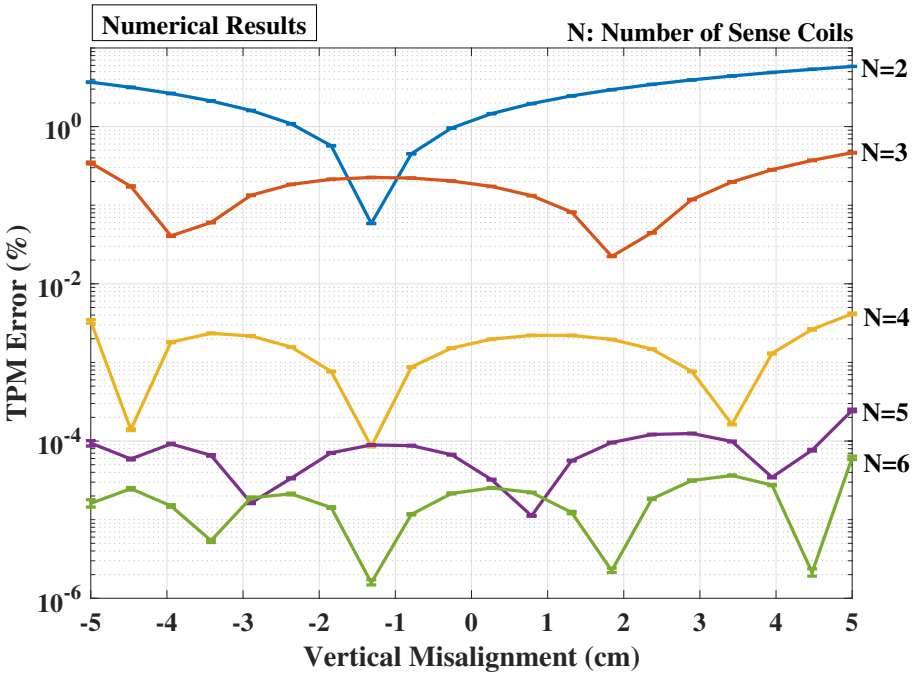

Figure 3.17. Numerical model results: TPM was accurate over vertical misalignment (-5 to 5 cm).

error is the higher-order deviation than that of the second-order polynomial approximation; the increasing number of sense coils can provide more information to cancel out the higher-order deviations. It is also worth noting that the transfer-power can be reconstructed under a wide range of the angular misalignment up to 20°, while the standard allows only a few degrees (±2 or 3°) of deviation.

3.3.5 FC-TPM Across Number of Turns Variation in Spiral Coils

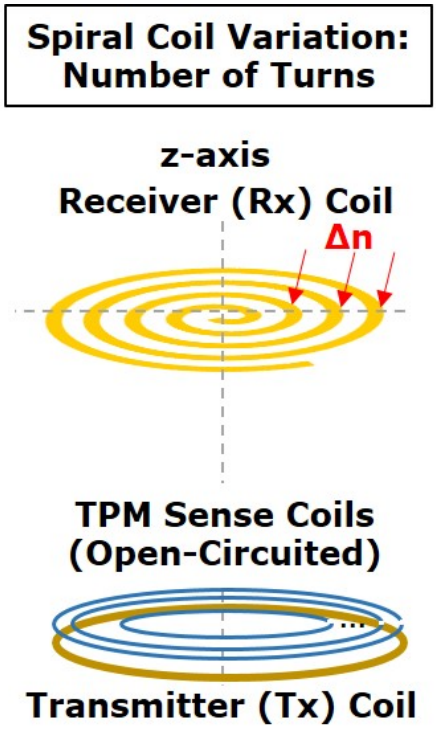

Figure 3.18. Changes in the number of turns of the spiral Rx coil.

Spiral coil is one of the popular and effective wireless power transfer coil winding types [59; 60; 61; 62; 63; 64]. In this section, one possible variation in the spiral Rx coil is considered for FC-TPM; the spiral Rx coils can have a different number of turns, as shown in Fig. 3.18. To calculate the mutual inductance between two spiral Tx and Rx coils effectively, the spiral coils are approximated by a combination of coplanar single-turn circular coils, as shown in Fig. 3.19. For the spiral coils, the mutual inductance can also be calculated using the numerical model[10]

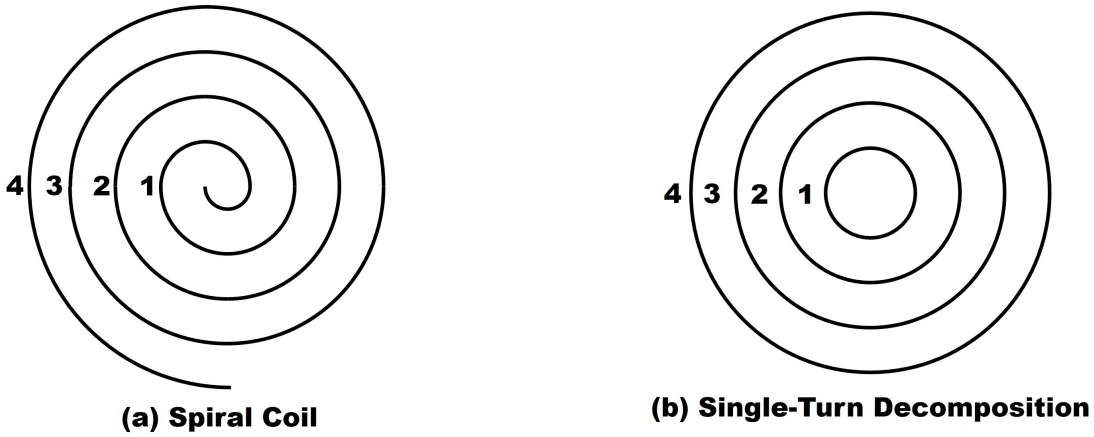

Figure 3.19. Single-turn decomposition of the spiral coils.

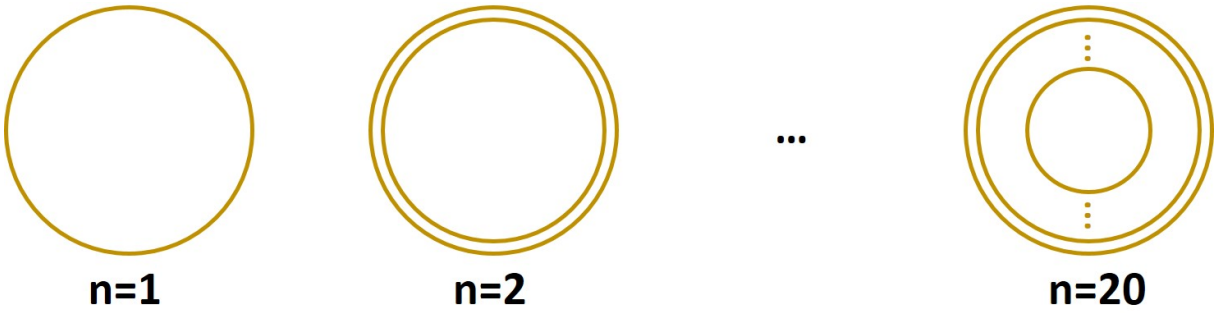

Figure 3.20. Changes in the number of the spiral coil-turn.

by decomposing spiral coils into a combination of concentric single-turn coils [65], as shown in Fig. 3.19; the mutual inductance ($M_{A:B}$) between two spiral coils (A and B) is calculated by accounting for every combination of the decomposed single-turn of both coils as,

$$M_{A:B} = \sum_{a=1}^{N_A} \sum_{b=1}^{N_B} M_{a:b}, \tag{3.34}$$

where N_A and N_B respectively represent the number of turns of the spiral coils. The numerical results were derived to confirm the effectiveness of the FC-TPM algorithm for spiral coil geometric variations. The Tx, Rx, and sense coil radii[11], and air-gap are the same as shown in Section 3.3.4. For the spiral Rx coils, the variation (Δn) started from single-turn ($n = 1$) coil having a 25 cm radius; increasing the number of turns by 20 while the radii of the coils decreased at 0.5 cm interval, as shown in Fig. 3.20.

The mutual inductances were calculated (dots) and fitted into the second-order polynomial functions (green-solid lines) for the variation, as shown in Fig. 3.21. The mutual inductance is well-approximated by the quadratic function. FC-TPM errors with multiple sense coils were examined over the variations of turn numbers of Rx spiral coils. The same FC-TPM algorithm, presented in Section 3.3.2 is used to calibrate the geometric parameter and reconstruct the transfer-power. Fig. 3.22 shows the numerical results that the transfer-power was accurately reconstructed over the coil turn number variations.

[10]Calculating the mutual inductance between spiral coils are difficult through 3-D finite element method (FEM) simulation due to the large amounts of time and processing power it requires.

[11]For the spiral configurations of the Tx and Rx coils, the radius refers to the most outer radius.

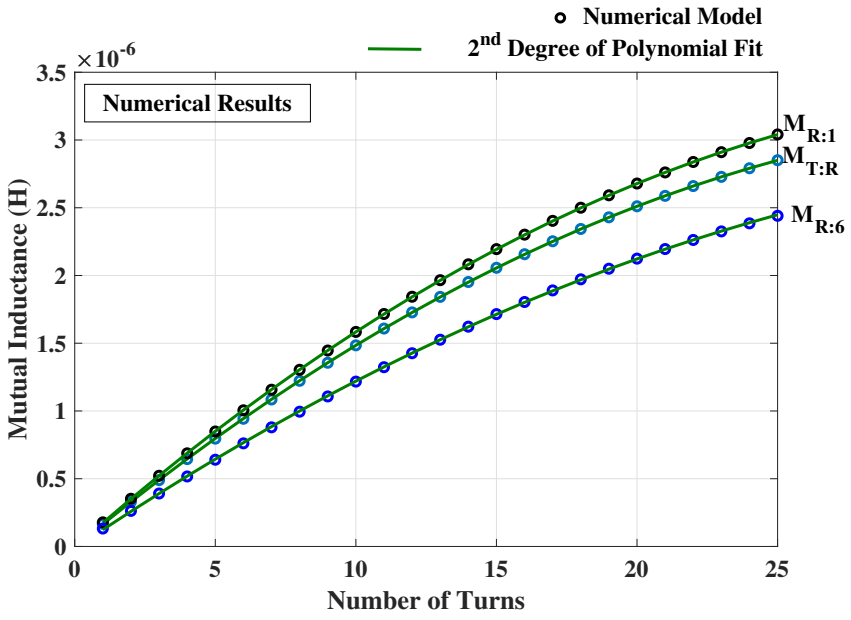

Figure 3.21. Mutual inductance variation and its second-order polynomial fit for the changes in the number of turns of the spiral Rx coil. Three representative mutual inductances are plotted.($M_{T:R}$: the Tx and Rx coil, $M_{R:1}$: Rx coil and sense coil 1 (the largest), $M_{R:6}$: the Rx coil and sense coil 6 (the smallest).

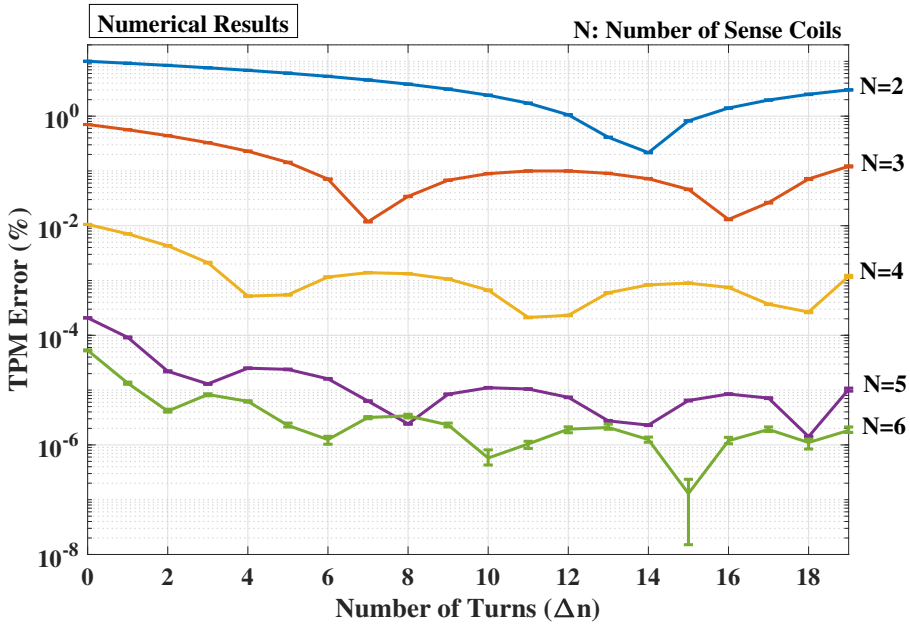

Figure 3.22. Numerical model results: TPM was accurate over the spiral coil-turn numbers variation.

3.4 Accurate FC-TPM over Multi-Dimensional Variations

In previous Section 3.3, the fundamental of the data combination of multiple sense coil voltages for accurate FC-TPM is shown over one-dimensional misalignment and variation.

In this section, FC-TPM is performed using numerical and FEM simulation analysis over multi-dimensional variations. Section 3.4.1 shows accurate FC-TPM over both vertical and lateral Rx coil misalignment. Section 3.4.2 presents FC-TPM with the external proximity eddy current loss, requiring a minimum of four sense coils. And then, lateral misalignment, litz wire type variations, and operating frequency variation are considered simultaneously for FC-TPM, where eleven sense coils are employed to reconstruct the transfer-power accurately, which also counts the eddy current losses.

3.4.1 Numerical Results for Lateral and Vertical Misalignment

When the Tx,Rx, and sense coils have the same configuration what is used in the Section 3.3, the geometric parameters α_{ij} are calibrated using the space, which is spanned over both Rx coil's lateral and vertical misalignment, as shown in Fig. 3.23. The sense coil voltage calibration matrix $\mathbf{W}$ is

$$\mathbf{W} = \begin{pmatrix} \langle V_1(x_1,z_1),V_2(x_1,z_1)\rangle & \dots & \langle V_i(x_1,z_1),V_j(x_1,z_1)\rangle \\ \vdots & \ddots & \vdots \\ \langle V_1(x_m,z_1),V_2(x_m,z_1)\rangle & \dots & \langle V_i(x_m,z_1),V_j(x_m,z_1)\rangle \\ \langle V_1(x_1,z_2),V_2(x_1,z_2)\rangle & \dots & \langle V_i(x_1,z_2),V_j(x_1,z_2)\rangle \\ \vdots & \ddots & \vdots \\ \langle V_1(x_m,z_2),V_2(x_m,z_2)\rangle & \dots & \langle V_i(x_m,z_2),V_j(x_m,z_2)\rangle \\ \vdots & \ddots & \vdots \\ \vdots & \ddots & \vdots \\ \langle V_1(x_m,z_n),V_2(x_m,z_n)\rangle & \dots & \langle V_i(x_m,z_n),V_j(x_m,z_n)\rangle \end{pmatrix}. \tag{3.35}$$

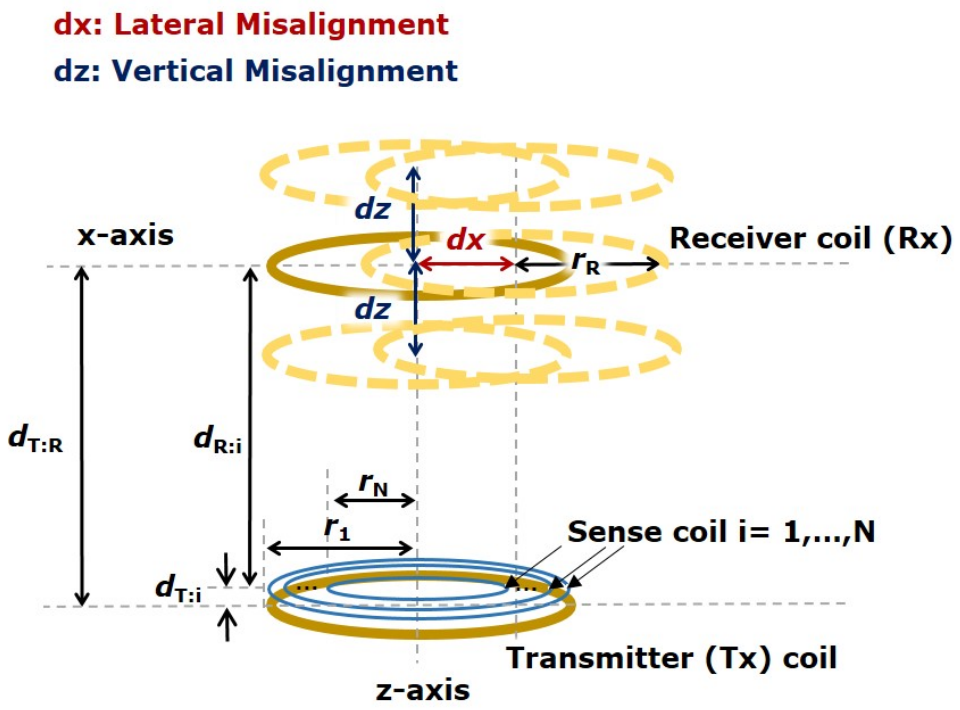

Figure 3.23. Configurations of the Tx, Rx, and sense coils with lateral and vertical Rx coil misalignment

The transfer-power calibration vector is

$$\mathbf{p} = \left[P_{\text{Transfer}}(x_1, z_1)\ P_{\text{Transfer}}(x_2, z_1) \cdots P_{\text{Transfer}}(x_m, z_n) \right]^{\mathsf{T}}, \tag{3.36}$$

where x_k and z_k are the lateral and vertical misalignment data points, respectively. The space of variation is shown in Fig. 3.24; the lateral misalignment ranged from 0 to 10 cm and the vertical misalignment ranged from -5 to 5 cm. A total of 121 data points were used (11 data points for each axis misalignment) and validated. Leave-one-out cross-validation (LOOCV) is used to validate the 121 data points. The calibration data matrix $\mathbf{W}$ and data vector $\mathbf{p}$ were created over 120 data points, which exclude a validation point, to calibrate the geometric parameters. The transfer-power was reconstructed for the validation point by using the sense coil voltages and geometric parameters. Every 121 data point was a validation point once.

Fig. 3.25 shows the numerical results of FC-TPM over lateral and vertical Rx coil misalignment simultaneously. FC-TPM errors were calculated for each validation point. Each error point at

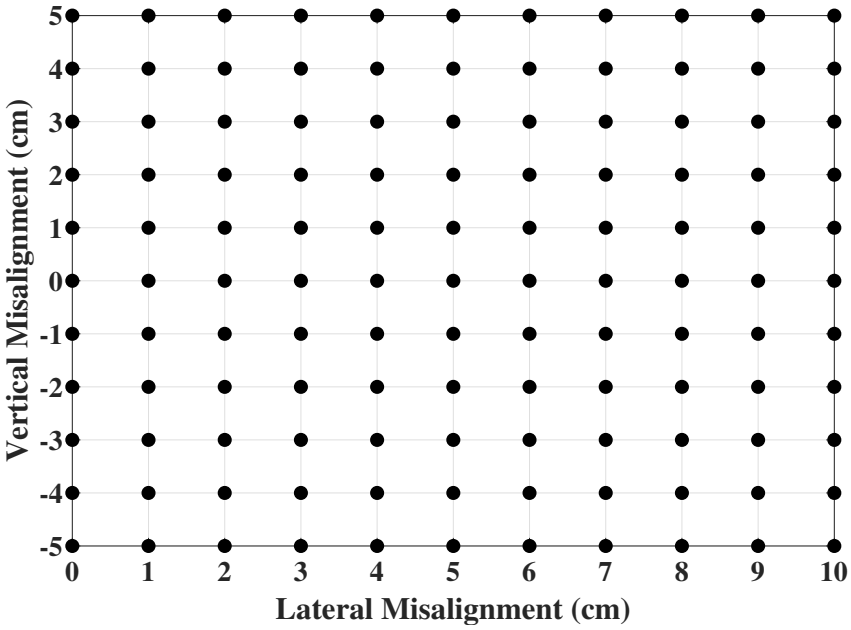

Figure 3.24. A space of variation was created over lateral and vertical Rx coil misalignment for calibration and validation. A total of 121 data-points were validated.

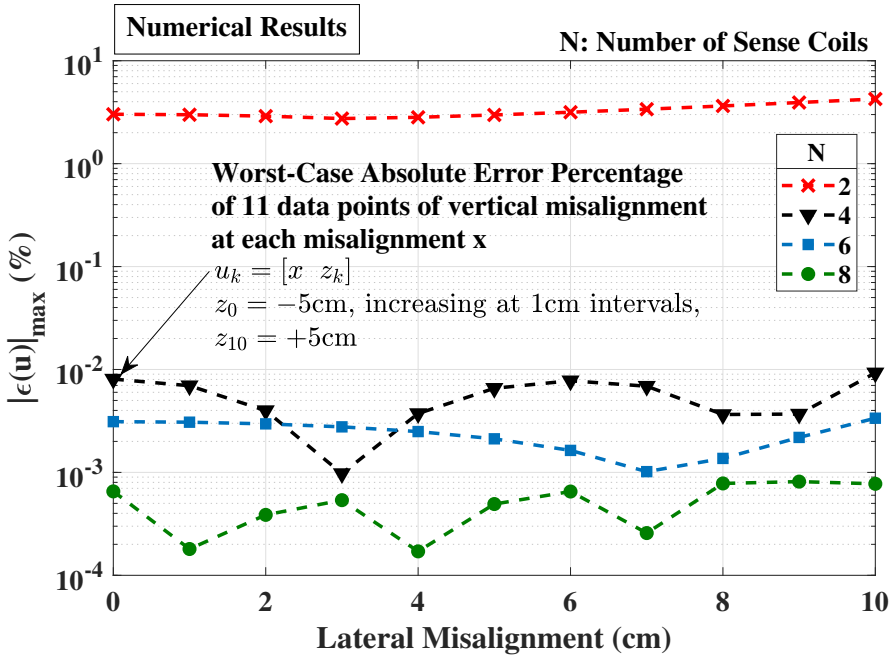

Figure 3.25. The worst-case absolute error percentage for each lateral misalignment as the number of sense coil is increased. Each point represents the worst-case error over 11 data points of vertical misalignment, ranged from -5 to 5 cm, at increasing 1 cm intervals.

each lateral misalignment in the figure represents the worst-case absolute error percentage, as defined in (3.22); the maximum error among 11 data points of vertical misalignment at a specific lateral misalignment was calculated and plotted. The transfer-power was reconstructed by different numbers of sense coils (e.g., $N = 2, 4, 6, 8$) to examine the effectiveness of using more coils to obtain more accurate results. Using eight sense coils reduced the error to below 0.001%.

3.4.2 FC-TPM With Eddy Currents, Rx Coil Misalignment, Different Litz Wire Types, and Different Operating Frequencies

Eddy currents in the Tx and Rx coils not only add to losses, as presented in Section 2.3, but also change the magnetic field geometry by changing the current distribution in the coils non-uniformly. The eddy currents can create a magnetic field with non-negligible coupling to the opposing coil. In other words, eddy currents induced on the Tx coil create fields that couple to the Rx coil and vice versa.

The induced eddy currents can be represented by additional windings in the transformer and the magnetic field geometry and hence coupling to different coils by the corresponding coupling coefficients. The variation in magnetic field geometry can be caused by a combination of (i) coil misalignment; (ii) different wire types (e.g., litz wire types); and (iii) a range of operating frequencies.

In this section, we extend the formulation in Section 2.4.2 and 3.3 to include eddy currents and to show how a greater number of sense coils can maintain the accuracy of FC-TPM when there are variations in Rx coil misalignment. A physical intuition of using multiple sense coils to reconstruct the transfer-power, including eddy current losses, is as follows. There are four windings of the Tx coil, Rx coil, Tx eddy current, and Rx eddy current that induce the sense coil voltages. Four sense coils are, therefore, the minimum number to reconstruct each winding current. This is simply expanding the two by two mutual inductance matrix dimension in (2.47) for the eddy current lossless system to that of four by four, which includes the Tx and Rx eddy currents. Transfer-power consists of the three power flows shown in Fig. 2.6, each of which is represented

by two winding currents relating to power transfer between the two windings. As the four sense coil voltages can calculate each winding current, the transfer-power can also be determined. More than four sense coils can provide information regarding Rx coil variations similar to what is shown in Section 3.3.2. Through electromagnetic finite element simulation, we also show that a greater number of sense coils maintain FC-TPM accuracy despite the effects of different types of wire and operating frequencies.

3.4.2.1 FC-TPM with Eddy Currents and Misalignment

When there are eddy currents in the Tx and Rx coils, the sense coil voltages V_i in (2.46) become

$$V_i = j\omega M_{T:i} I_T + j\omega M_{R:i} I_R + j\omega M_{t:i} I_t + j\omega M_{r:i} I_r. \tag{3.37}$$

Note that I_t, I_r are the eddy winding currents in the Tx and Rx coils, as discussed earlier in Section 2.3. $M_{t:i}, M_{r:i}$ are the mutual inductances from the eddy windings to the i^{th} sense coil.

For example, Tx, Rx, and eddy winding currents can be derived from four sense coil voltages $V_{1,..,4}$

$$\begin{pmatrix} I_T \\ I_R \\ I_t \\ I_r \end{pmatrix} = \frac{1}{j\omega} \begin{pmatrix} M_{T:1} & M_{R:1} & M_{t:1} & M_{r:1} \\ M_{T:2} & M_{R:2} & M_{t:2} & M_{r:2} \\ M_{T:3} & M_{R:3} & M_{t:3} & M_{r:3} \\ M_{T:4} & M_{R:4} & M_{t:4} & M_{r:4} \end{pmatrix}^{-1} \begin{pmatrix} V_1 \\ V_2 \\ V_3 \\ V_4 \end{pmatrix} \tag{3.38}$$

The transfer-power in (2.32) can be rewritten through (2.17)

$$P_{\text{Transfer}} = \text{Re}\left\{j\omega M_{R:T} I_R I_T^*\right\} + \text{Re}\left\{j\omega M_{T:r} I_r I_T^*\right\} - \text{Re}\left\{j\omega M_{R:t} I_t I_R^*\right\}, \tag{3.39}$$

where $M_{T:r}$ is the mutual inductance between (i) the Tx coil and (ii) the Rx coil's eddy current winding; $M_{R:t}$ is the mutual inductance between the Rx coil and the Tx coil's eddy current winding.

By combining (3.38) and (3.39), the transfer-power can still be determined from a linear com-

bination of the pairwise-product of sense coil voltages

$$P_{\text{Transfer}} = \sum_{i,j \in Q} \lambda_{ij} \left\langle V_i, V_j \right\rangle, \tag{3.40}$$

where

$$\begin{aligned} Q &= \left\{ (i,j) \in \mathbb{N}^2 \,\middle|\, i \leq N, j \leq N, \text{ and } i < j \right\}, \\ \left\langle V_i, V_j \right\rangle &\triangleq \text{Im} \left\{ V_i V_j^* \right\}. \end{aligned} \tag{3.41}$$

Detailed expressions for λ_{ij} using an inverse matrix of the mutual inductances in (3.38) is presented from (3.42) to (3.48). Note that a minimum of four sense coils $N=4$ are needed to determine four coil currents (I_T, I_R, I_t, I_r) and hence the transfer-power. If there are more than four sense coils, we can make use of the additional information by choosing four sense coil voltages at a time from the total of N sense coils, from which a total of ${}_NC_4$ different formulations of (3.40) are constructed to determine the transfer-power. Each formulation is a linear combination of the pairwise-products of two sense coil voltages chosen out of the four sense coils in the formulation. Using (3.40), all the formulations can be used to determine the transfer-power, which is detailed in (3.50).

The Tx, Rx, and eddy winding currents in (3.38) can be expressed as

$$\begin{pmatrix} I_T \\ I_R \\ I_t \\ I_r \end{pmatrix} = \frac{1}{\mathcal{D}} \frac{1}{j\omega} \begin{pmatrix} W_{T:1} & W_{R:1} & W_{t:1} & W_{r:1} \\ W_{T:2} & W_{R:2} & W_{t:2} & W_{r:2} \\ W_{T:3} & W_{R:3} & W_{t:3} & W_{r:3} \\ W_{T:4} & W_{R:4} & W_{t:4} & W_{r:4} \end{pmatrix} \begin{pmatrix} V_1 \\ V_2 \\ V_3 \\ V_4 \end{pmatrix}, \tag{3.42}$$

where $\mathcal{D}$ is the determinant and $W_{x:i}$ are the elements of the adjugate matrix of the mutual inductance matrix in (3.38).

For four sense coils, the transfer-power, decomposed into three power flows in (3.39), can be

represented by three independent linear combinations of pairwise-products of sense coil voltages

$$\begin{aligned} P_{\text{Transfer}} &= P_{\text{Tx:Rx}} + P_{\text{Loss,eddy(Rx)}} - P_{\text{Loss,eddy(Tx)}} \\ &= \operatorname{Re}\left\{j\omega M_{R:T} I_R I_T^*\right\} + \operatorname{Re}\left\{j\omega M_{T:r} I_r I_T^*\right\} - \operatorname{Re}\left\{j\omega M_{R:t} I_t I_R^*\right\} \\ &= \sum_{i,j\in Q} \mathcal{A}_{ij} \left\langle V_i, V_j \right\rangle + \sum_{i,j\in Q} \mathcal{B}_{ij} \left\langle V_i, V_j \right\rangle + \sum_{i,j\in Q} \mathcal{C}_{ij} \left\langle V_i, V_j \right\rangle, \end{aligned} \tag{3.43}$$

where

$$\begin{bmatrix} \mathcal{A}_{12} \\ \mathcal{A}_{13} \\ \mathcal{A}_{14} \\ \mathcal{A}_{23} \\ \mathcal{A}_{24} \\ \mathcal{A}_{34} \end{bmatrix} = \frac{M_{R:T}}{\omega \mathcal{D}^2} \begin{bmatrix} W_{T:1}W_{R:2} - W_{T:2}W_{R:1} \\ W_{T:1}W_{t:2} - W_{T:2}W_{t:1} \\ W_{T:1}W_{r:2} - W_{T:2}W_{r:1} \\ W_{R:1}W_{t:2} - W_{R:2}W_{t:1} \\ W_{R:1}W_{r:2} - W_{R:2}W_{r:1} \\ W_{t:1}W_{r:2} - W_{t:2}W_{r:1} \end{bmatrix}, \tag{3.44}$$

$$\begin{bmatrix} \mathcal{B}_{12} \\ \mathcal{B}_{13} \\ \mathcal{B}_{14} \\ \mathcal{B}_{23} \\ \mathcal{B}_{24} \\ \mathcal{B}_{34} \end{bmatrix} = \frac{M_{T:r}}{\omega \mathcal{D}^2} \begin{bmatrix} W_{T:1}W_{R:4} - W_{T:4}W_{R:1} \\ W_{T:1}W_{t:4} - W_{T:4}W_{t:1} \\ W_{T:1}W_{r:4} - W_{T:4}W_{r:1} \\ W_{R:1}W_{t:4} - W_{R:4}W_{t:1} \\ W_{R:1}W_{r:4} - W_{R:4}W_{r:1} \\ W_{t:1}W_{r:4} - W_{t:4}W_{r:1} \end{bmatrix}, \tag{3.45}$$

$$\begin{bmatrix} \mathcal{C}_{12} \\ \mathcal{C}_{13} \\ \mathcal{C}_{14} \\ \mathcal{C}_{23} \\ \mathcal{C}_{24} \\ \mathcal{C}_{34} \end{bmatrix} = -\frac{M_{R:t}}{\omega \mathcal{D}^2} \begin{bmatrix} W_{T:2}W_{R:3} - W_{T:3}W_{R:2} \\ W_{T:2}W_{t:3} - W_{T:3}W_{t:2} \\ W_{T:2}W_{r:3} - W_{T:3}W_{r:2} \\ W_{R:2}W_{t:3} - W_{R:3}W_{t:2} \\ W_{R:2}W_{r:3} - W_{R:3}W_{r:2} \\ W_{t:2}W_{r:3} - W_{t:3}W_{r:2} \end{bmatrix}. \tag{3.46}$$

The transfer-power can thus be represented as a linear combination of pairwise-products of sense

coil voltages in (3.40)

$$P_{\text{Transfer}} = \sum_{i,j \in Q} \lambda_{ij} \left\langle V_i, V_j \right\rangle, \tag{3.47}$$

where

$$\lambda_{ij} = \mathcal{A}_{ij} + \mathcal{B}_{ij} + \mathcal{C}_{ij}. \tag{3.48}$$

If there are more than four sense coils, we can choose four sense coil voltages at a time from the total of N sense coils, from which a total of ${}_NC_4$ different formulations of (3.47) are constructed to determine the transfer-power. The transfer-power, therefore, can be determined by (3.40) for $N > 4$ sense coils, when all the formulations are summed and divided by $N_w = {}_NC_4$, resulting in a linear combination of the all pairwise-product of two sense coil voltages out of N sense coils

$$P_{\text{Transfer}} = \frac{1}{N_w} \sum_{k=1}^{N_w} \sum_{\substack{i<j \\ i,j \in s_k}} \lambda_{ij}^{(k)} \left\langle V_i, V_j \right\rangle \tag{3.49}$$

$$= \sum_{i,j \in Q} \zeta_{ij} \left\langle V_i, V_j \right\rangle, \tag{3.50}$$

where

$$Q = \left\{ (i,j) \in \mathbb{N}^2 \,\middle|\, i \leq N, j \leq N, \text{ and } i < j \right\}, \tag{3.51}$$

$$\zeta_{ij} = \frac{1}{N_w} \sum_{k \in \mathcal{G}_{ij}} {\lambda_{ij}}^{(k)}, \tag{3.52}$$

$$\mathcal{G}_{ij} = \left\{ \mathcal{K} \subset \{1, ..., N_w\} \,\middle|\, k \in \mathcal{K} \text{ and } i, j \in s_k \right\}, \tag{3.53}$$

$$\mathcal{S} = \{ s_k |\, s_k \subset \mathcal{T},\, \text{n}(s_k) = 4 \}. \tag{3.54}$$

Note that when $\mathcal{T}$ is a set of N sense coils, $\mathcal{T} = \{1, 2, \ldots, N\}$, $\mathcal{S}$ is a collection with lexical ordering of all subsets of $\mathcal{T}$ that consists of combinations of four sense coils, where $\text{n}(\mathcal{S}) = N_w$.

One can observe in Fig. 3.26 the effect of differing numbers of sense coils on FC-TPM when there are eddy current losses in the WPT coils. A 2d axisymmetric FEM simulation in COMSOL

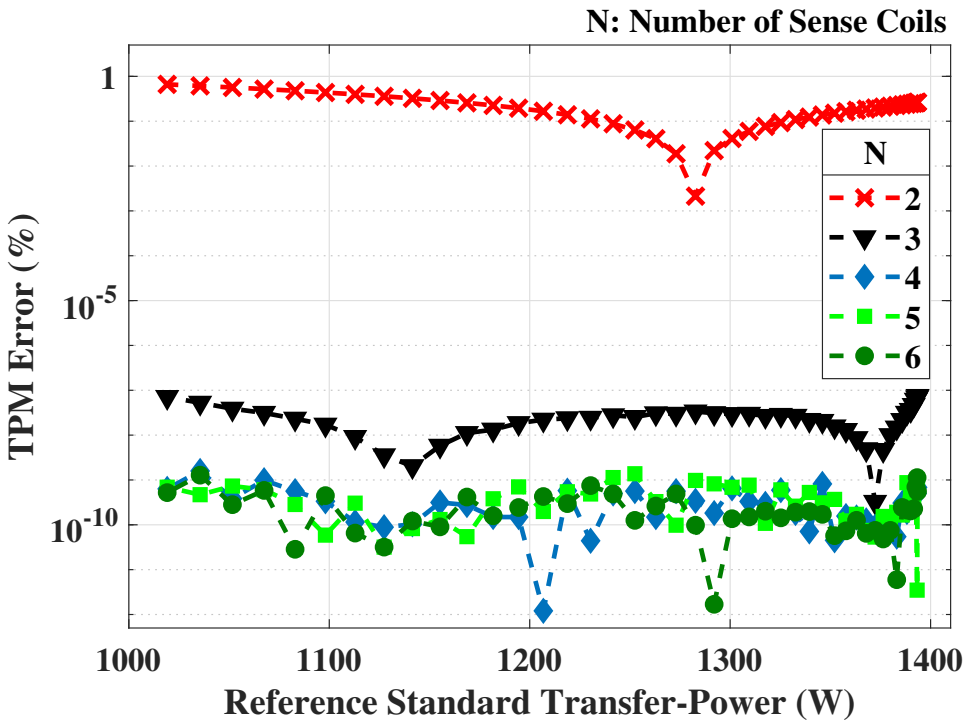

Figure 3.26. FEM simulation was performed to show FC-TPM errors when eddy currents in the Tx and Rx coils are included.

was performed for two solid-wire WPT coils with the same dimensions as the hardware in Chapter 5. From (3.38) and (3.39), when eddy currents are significant, four sense coils are needed. Fig. 3.26 shows that with two-sense coils the errors are a considerable 0.66%. As the number of sense coils increases to four, the error reduces to a much smaller $1.6\times10^{-9}\%$. Additional sense coils beyond four do not significantly improve the error for this case where the WPT coils are aligned.

In particular, this collection of four sense coils from the $N>4$ sense coils results in ${}_NC_4$ independent transfer-power formulations, where we can extend the principle of FC-TPM over misalignment in Section 3.3 to that which includes eddy current. By increasing the number of sense coils, the formulation in (3.40) can embed (3.13), ultimately resulting in a single set of geometric parameters that also include Rx coil misalignment together with the effects of eddy current.

The transfer-power at each misalignment x can be determined by

$$P_{\text{Transfer}}(x) = \sum_{i,j \in Q} \lambda_{ij}(x) \left\langle V_i(x), V_j(x) \right\rangle, \tag{3.55}$$

where $\lambda_{ij}(x)$ can be approximated by an n^{th}-order polynomial

$$\lambda_{ij}(x) = a_n^{ij} x^n + a_{n-1}^{ij} x^{n-1} + \ldots + a_0^{ij}. \tag{3.56}$$

If N (>4) sense coils are employed, there are $N_{\text{w}}(=_N C_4)$ independent transfer-power formulations for (3.55). Let $\mathcal{T}$ be a set of N sense coils, $\mathcal{T} = \{1, 2, \ldots, N\}$. $\mathcal{S}$ is a collection with lexical ordering of all subsets of $\mathcal{T}$ that consists of combinations of four sense coils; $\mathcal{S} = \{s_k |\, s_k \subset \mathcal{T},\, \text{n}(s_k) = 4\}$, where $\text{n}(\mathcal{S}) = N_w$. Each independent formulation, a linear combination of pairwise-products of sense coil voltages from $s_k \in \mathcal{S}$, has a distinct set[12] $\lambda_{ij}^{(k)}$ of geometric parameters, where $k \in \{1, ..., N_w\}$.

The linear combination of the N_w transfer-power formulations with constant coefficients δ_k is then

$$\sum_{k=1}^{N_w} \delta_k P_{\text{Transfer}}(x) = \sum_{k=1}^{N_w} \sum_{\substack{i<j \\ i,j \in s_k}} \delta_k \lambda_{ij}^{(k)}(x) \left\langle V_i(x), V_j(x) \right\rangle, \tag{3.57}$$

which approximates to a form like (3.13)

$$\begin{aligned} P_{\text{Transfer}} &= \sum_{i,j \in Q} \alpha_{ij} \left\langle V_i, V_j \right\rangle, \\ Q &= \left\{ (i,j) \in \mathbb{N}^2 \,\middle|\, i \le N, j \le N, \text{ and } i < j \right\}, \end{aligned} \tag{3.58}$$

when δ_k is optimized by choosing the appropriate sizes and positions of the sense coils so that

$$\sum_{k=1}^{N_{\text{w}}} \delta_k \approx 1 \text{ and } \sum_{k \in \mathcal{G}_{ij}} \delta_k \lambda_{ij}^{(k)}(x) \approx \alpha_{ij}, \tag{3.59}$$

[12]Note that the geometric parameters $\lambda_{ij}^{(k)}$ of the same pair of sense coils (i, j) for each subset s_k are distinct (e.g., $\lambda_{12}^{(1)} \neq \lambda_{12}^{(2)}$).

where

$$\mathcal{G}_{ij} = \left\{ \mathcal{K} \subset \{1, ..., N_w\} \,\middle|\, k \in \mathcal{K} \text{ and } i, j \in s_k \right\}, \tag{3.60}$$

which has ${}_{(N-2)}C_2$ elements; in other words, $\mathcal{G}_{ij}$ is a set of indices of s_k, which includes a specific sense coil pair i and j, noting that s_k is a set of combinations of four sense coils.[13]

The coefficients α_{ij} can be obtained from a least-squares optimization like (3.12)

$$\begin{aligned} &\underset{\alpha_{ij}}{\text{minimize}} \quad \left\| P_{\text{Transfer}}(x) - \sum_{i,j \in Q} \alpha_{ij} \left\langle V_i(x), V_j(x) \right\rangle \right\|_2 \\ &\text{subject to } \alpha_{ij} \in \mathbb{R}. \end{aligned} \tag{3.61}$$

The transfer-power can then be determined over the Rx coil misalignment by a single set of geometric parameters α_{ij}.

3.4.2.2 FEM Simulations of FC-TPM with Eddy Currents Over Multi-Dimensional Variations: Misalignment, Litz Wire Types, and Operating Frequencies

The principle that enables accurate FC-TPM over variations (e.g., misalignment) is the use of an overdetermined set of sense coils whose geometric parameters are such that the linear combination of the pairwise-products of their voltages are insensitive to errors from the variations. These had been presented in Sections 3.3.2 and 3.4.2.1.

The optimal linear coefficients are calibrated through the least-squares minimization of a calibration set, which is appropriately chosen over the range of variations of interest, as shown in (3.14)-(3.16). This formulation can be expanded to a multi-dimensional simultaneity of variations, such as having EVs (Rx coils) with different types of litz wires and operating frequencies. Calibration can be undertaken for both Tx and service station sense coils during manufacturing or when commissioned in the field for retrofits or repairs.[14]

[13] For example, when $N = 6$ and $N_w = 15$, then $\mathcal{T} = \{1, 2, 3, 4, 5, 6\}$ and $\mathcal{G}_{13} = \{1, 2, 3, 7, 8, 9\}$, where s_k includes the particular sense coil pair $(i, j) = (1, 3)$; $s_1 = \{1, 2, 3, 4\}, s_2 = \{1, 2, 3, 5\}, s_3 = \{1, 2, 3, 6\}, s_7 = \{1, 3, 4, 5\}, s_8 = \{1, 3, 4, 6\}, s_9 = \{1, 3, 5, 6\}$.

[14] From an arbitration perspective, with the inspection performed by an unbiased third party, the official trucks can

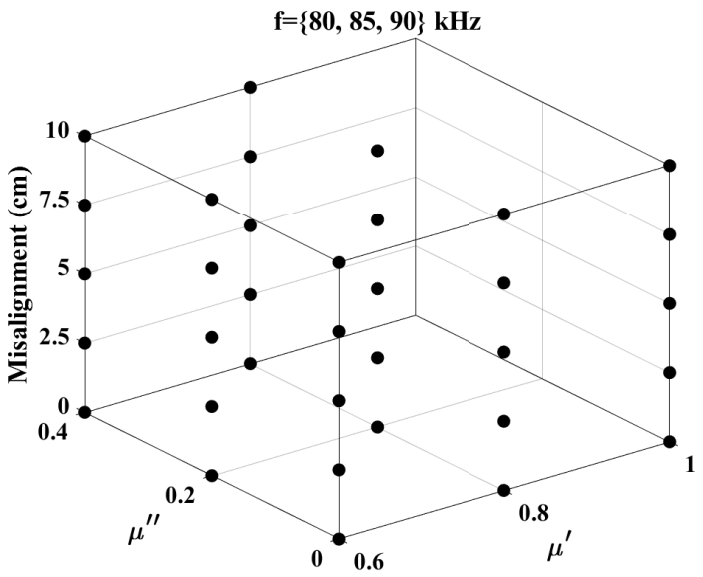

Figure 3.27. A space of variations was created over Rx coil misalignment, complex permeability, and operating frequency for calibration and validation. A total of 105 data-points were used, where each point in the plot above represents a variation over three frequencies.

Three-dimensional FEM simulations in COMSOL were performed to demonstrate accurate FC-TPM over multi-dimensional variations in the Rx coil, where the effects of eddy currents are included in the FEM simulation. The goal of the simulations is to confirm that transfer-power can be determined accurately using only a single set of geometric parameters regardless of those variations.

Notably, we show that using only a small number of wire types (including litz wire) for calibration, FC-TPM is accurate for a broad range of wire types that are not in the calibration set.

As illustrated in Fig. 3.27, FEM results consist of a total 105 data points, which are a combination of (i) Rx coil lateral misalignment: $\{0, 2.5, 5, 7.5, 10\,\text{cm}\}$; (ii) operating frequencies: $\{80, 85, 90\,\text{kHz}\}$, which are within the mandated range of SAE J2954 [45]; and (iii) seven complex permeabilities of different Rx windings: $\mu = 1$ (solid-wire) and $\mu' = \{0.8, 0.6\}$, $\mu'' = \{0, 0.2, 0.4\}$, where $\mu = \mu' - j\mu''$, which can model different bundles and strands of litz wire, using an equivalent

have their sense coils, attached to the Rx coils to inspect the charging stations' metering accuracy. This is possible because the official trucks and sense coils are calibrated over Tx coil variations in standard laboratories. This is analogous to the *Weights and Measures Program* today in that officials bring trucks with *provers* that are carefully calibrated in standard laboratories [66], [67] to check the accuracy of gas dispensers.

complex permeability model [68; 69]; it is worth noting that the range of μ' and μ'' in Fig. 3.27 covers a broad range of wire types [68; 69; 70].

Fig. 3.28 shows an example configuration for a particular simulation iteration. To alleviate the computational complexity of an already intensive 3-D simulation: (i) the Tx coil was modeled as a uniform surface current on a circular plane; (ii) the Rx coil was a single-turn circular coil; (iii) sense coil voltages were obtained post-simulation from the magnetic flux intersecting the coil area. The Rx coil radius was 12.5 cm, with a 5 mm diameter wire, specified in [45]. The Tx surface current's inner and outer radii were 5.5, and 12.5 cm, respectively. The air-gap between the Rx coil and the Tx surface current was 10 cm. The sense coils were located on a plane 1.25 cm above the Tx surface current. The sense coil radii ranged from 18.25 cm to 3.25 cm decreasing at 1.5 cm intervals.

The accuracy of FC-TPM was verified using leave-one-out cross-validation (LOOCV). We used entire data subsets for a particular litz wire type for validation. Specifically, in this particular variant of LOOCV, we iteratively left a particular litz wire type out of each calibration set and reserved it for validation to show that the calibration set can span the parameter variation space, hence maintaining FC-TPM accuracy over the broad range of litz wire variations. In particular, the validation set consisted of 15 data points of a single wire type (i.e., a specific complex permeability), which were obtained from five misalignment values $\{0, 2.5, 5, 7.5, 10\,\text{cm}\}$, and three frequency variations $\{80, 85, 90\,\text{kHz}\}$. The remaining 90 data points consisting of 6 wire types, each with 15 variations, were the calibration set. The geometric parameters α_{ij} were calculated at each LOOCV iteration for the calibration set using (3.14)-(3.18).

FC-TPM errors were calculated for each validation point. Using α_{ij} with 11 sense coil voltages, the transfer-power was determined for each point using (3.58) and the error was calculated with (3.19), where the reference standard transfer-power was calculated from (2.34). Fig. 3.29a shows the worst-case absolute error percentage, as defined in (3.22), for each type of wire (represented by the complex permeability) as the number of sense coils is increased, where $\mathbf{u}_k = \begin{bmatrix} \mu & x_k & f_k \end{bmatrix}$. Eleven sense coils reduced the error to below 0.1%. Fig. 3.29b shows the spread in error using

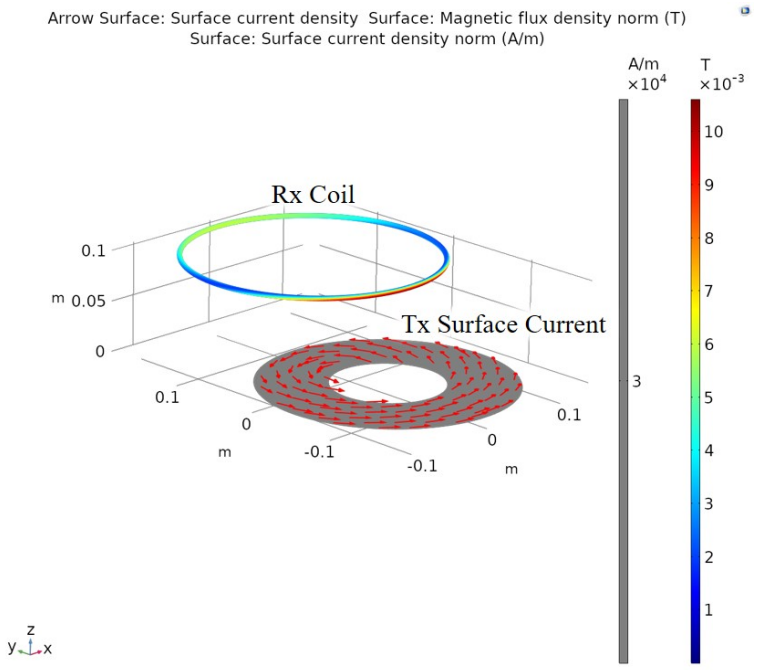

(a) The Tx coil current was modeled as a uniform surface current. The Rx coil is a single-turn circular coil.

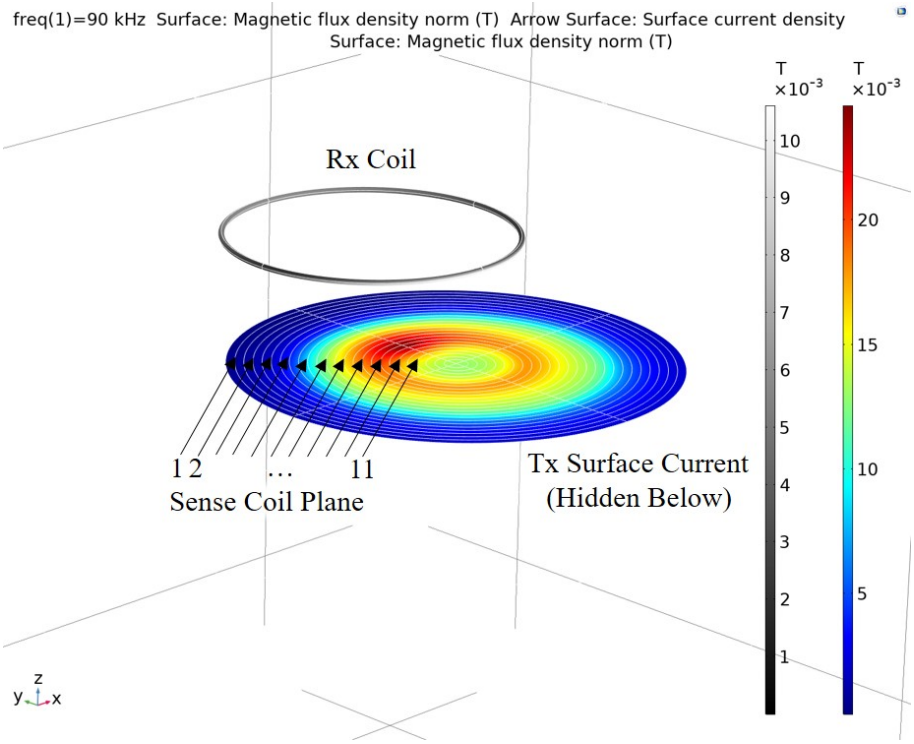

(b) 11-different induced voltages on the sense coil plane were calculated from the magnetic field.

Figure 3.28. 3-D FEM simulations were performed in COMSOL over a four-dimensional Rx coil variation $\{\mu', \mu'', x, f\}$.

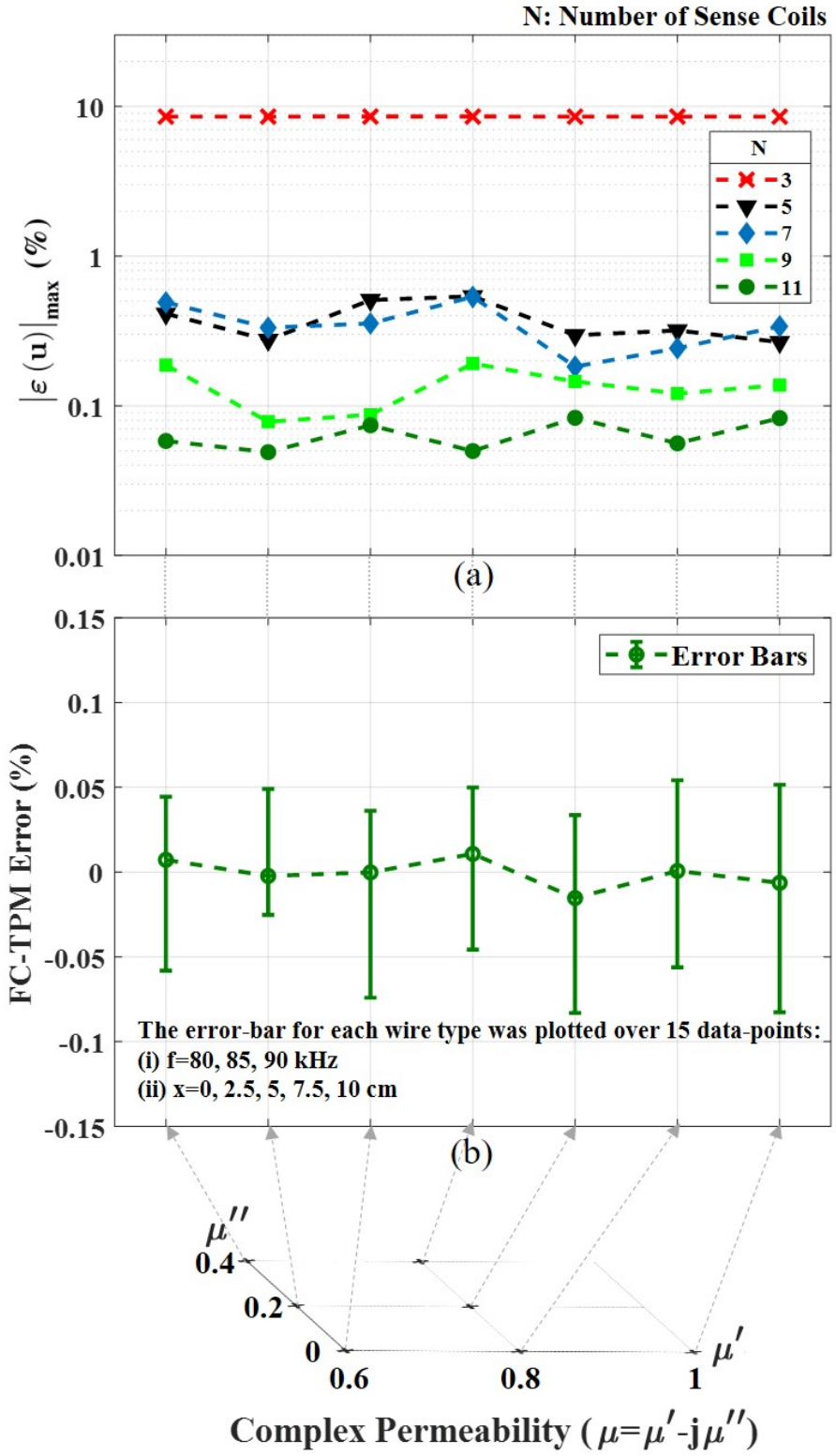

Figure 3.29. (a) The worst-case absolute error percentage for each type of wire (represented by the complex permeability) as the number of sense coils is increased. (b) The spread in error using 11 sense coils for each type of wire over both frequency and misalignment variation.

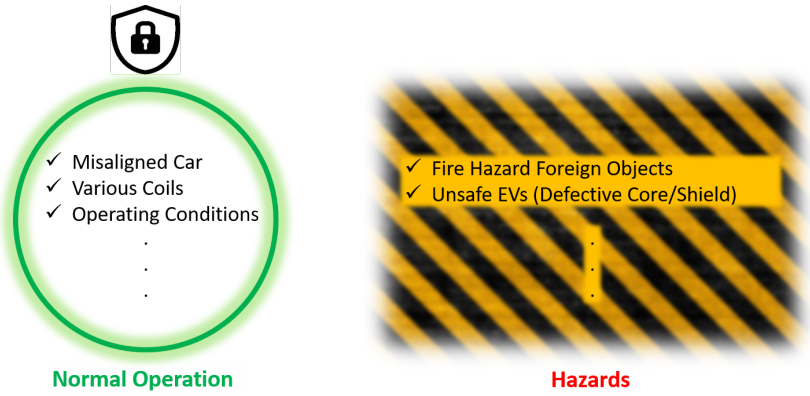

Figure 3.30. Hazard events can be diagnosed by distinguishing them from normal operation calibration space.

11 sense coils for each type of wire over frequency and misalignment variation; the errors were ranged from -0.083% to $+0.054\%$.

3.5 Electromagnetic Model-Based Safety Diagnostics for Wireless Power Transfer

This section introduces how the electromagnetic physics model used for FC-TPM can be extended to a diagnostic application for wireless power transfer. Accurate FC-TPM over geometric variations is presented in previous Section 3.4. The working principle is that coupling coefficients over a variation can be approximated by polynomials, where a linear combination of pairwise-product of sense coil voltages can eliminate the polynomial variations in transfer-power reconstruction. The linear combination coefficients are new geometric parameters, which are non-varying over the variation space, where calibration is performed.

The calibration space can then be defined within a normal operating space, where unaccounted electromagnetic geometries cause sequent errors in information reconstruction. Since each object in the electromagnetic physics model can be decomposed into a single winding, the sequent error is derived from the additional electromagnetic coupling brought from an object which is not counted in the normal operating space. Fig. 3.30 shows the conceptual diagram, which illustrates

hazard situations can be distinguished from the situations defined as normal operation. Chapter 6 presents *Electromagnetic Model-Based Foreign Object Detection* (EM-FOD), which uses the detection metric of the deviation due to a foreign object's electromagnetic coupling to the normal electromagnetic model, which consists of the Tx, Rx, and sense coils but not a foreign object.

CHAPTER 4

Electromagnetically Thin and Physically Flat Sense Coils

This section discusses how FC-TPM sense coils can be designed to be both physically and electromagnetically unobtrusive. Effective sensors should not affect that which it is measuring, nor should it negatively impact charging vehicles' primary mission. This section shows how the sense coils for FC-TPM can be constructed, so they are a minimal electromagnetic perturbation and be designed to be below the pavement. Using high fidelity FEM using COMSOL, we show that the eddy current losses dissipated in the sense coils are insignificant and hence electromagnetically "thin". We then show through a multi-objective optimization that a low-profile coplanar sense coil geometry, in other words "flat", has comparable performances to other optimized configurations.

4.1 Eddy Current Losses Dissipated in Open-Circuited Sense Coils

The sense coils are supplemental to a WPT charging system and should neither impact the efficiency nor perturb the electromagnetic fields. The sense coils are open-circuited, and hence do not carry terminal current, so there is no ohmic loss. A potential loss mechanism may be the eddy currents induced by the time-varying magnetic fields generated by the Tx and Rx coil currents; however, these losses are negligible when the sense coils are very thin; 50 AWG (0.025 mm

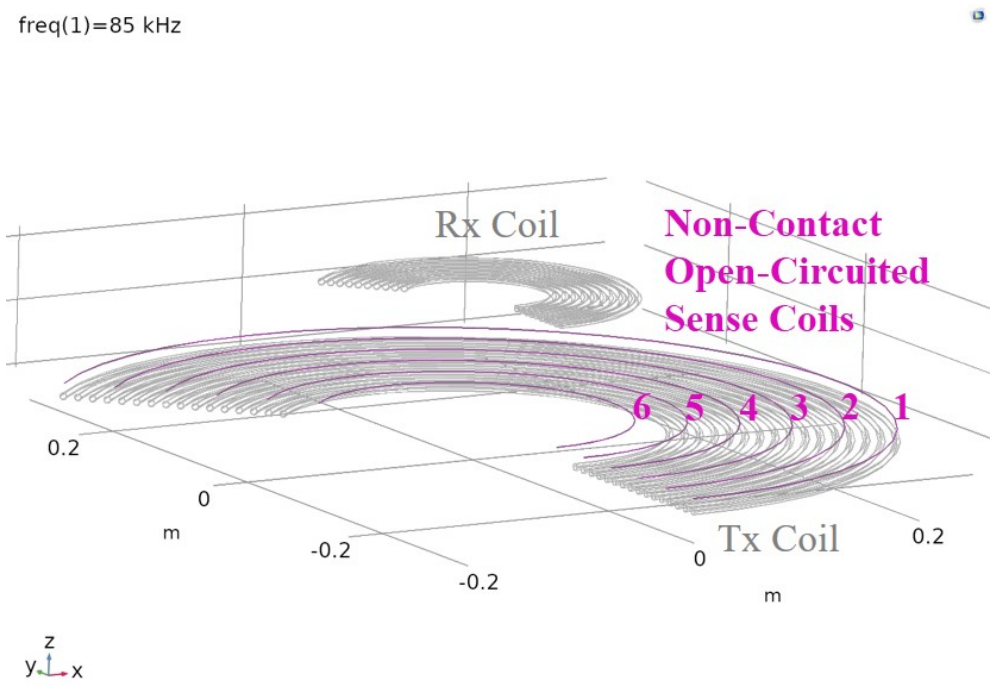

Figure 4.1. 2-D axisymmetric FEM simulation for analyzing eddy current losses in the sense coils. The coplanar sense coils were open-circuited and single-turn.

diameter) coaxial cable[1] is available commercially.

Eddy current losses in the sense coils were analyzed through 2-D axisymmetric FEM simulations with an extremely fine mesh in COMSOL. Open-circuited single-turn sense coils were placed 1 cm above the Tx coil, as shown in Fig. 4.1, where the Tx and Rx coils were multi-turn concentric circular coils, used in Section 2.3.3 for the WPT2/Z1 class. Eddy current losses were calculated for different numbers (one to six) and diameters (32 to 50 AWG, at 6 AWG intervals) of sense coils.

Figure 4.2 shows the efficiency loss from eddy currents in the sense coils. The diameter of the sense coils, which scales the loss as approximately cubic, is the dominant factor; whereas, the number of sense coils scale the loss linearly. Using commercially available 50 AWG coaxial cable, the eddy current loss only contributes less than $10^{-6}\%$ efficiency loss according to the results from these high fidelity electromagnetic FEM simulations.[2]

[1] The outer conductor is used as a Faraday shield, which is discussed in Section 5.

[2] A mesh-study was performed to ensure a convergent result as mesh size was decreased.

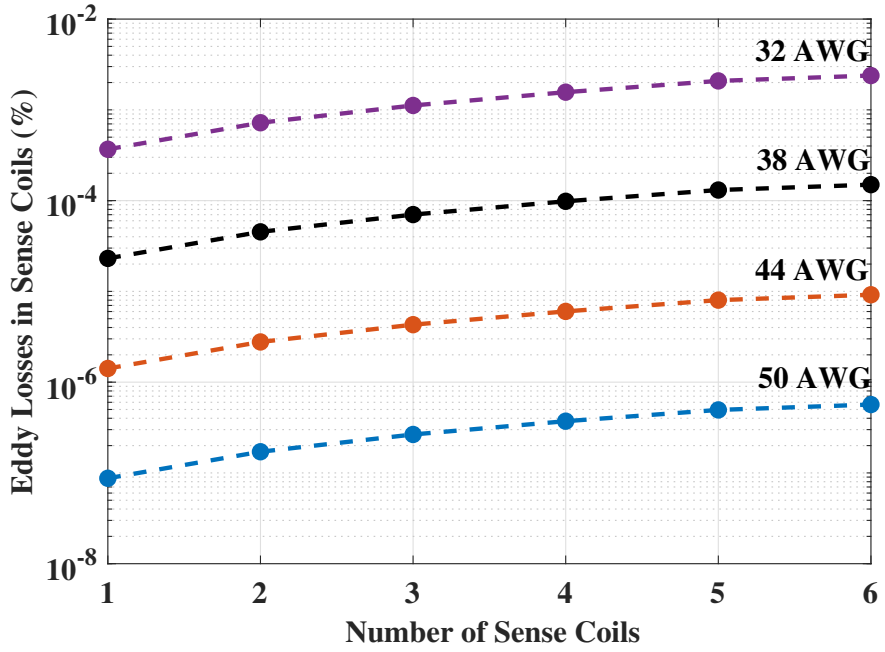

Figure 4.2. The efficiency loss from eddy currents in the sense coils: wire diameter and number of sense coils were varied.

4.2 Physically Flat Sense Coils: Performance Comparisons with Other Configurations

Physically flat sense coils are unobtrusive and can be installed above the transmitter coil and below the pavement if needed. In this section[3], we show that coplanar sense coils have comparable performance with other configurations. We use Monte Carlo methods to evaluate three performance metrics: (i) model matching; (ii) information diversity; and (iii) detectability. Pareto frontiers from a multi-objective optimization [71] of each configuration is used for comparison. The Pareto frontier is the best performance set for a particular configuration. In other words, by comparing Pareto frontiers, one compares the best cases of each configuration. Specifically, we compare coaxial sense coils that are restricted to the same plane, i.e., flat/coplanar, with those that are only restricted coaxially, but otherwise unrestricted.

A multi-objective optimization problem was formulated from the weighted sum of three penalty

[3]This section is worked by Xiaofan Cui and Sung Yul Chu at the University of Michigan.

functions [72]

$$
\begin{aligned}
\underset{\mathbf{r},\mathbf{d}}{\text{minimize}} \quad & \lambda_1 p_1 + \lambda_2 p_2 + \lambda_3 p_3 \\
\text{subject to} \quad & \mathbf{r} = [r_1 \; r_2 \; \cdots \; r_N] \,, \\
& \mathbf{d} = [d_{T:1} \; d_{T:2} \; \cdots \; d_{T:N}] \,, \\
& \hat{R}_{\text{min}} \leq \tfrac{r_i}{r_T} \leq \hat{R}_{\text{max}}, \\
& \hat{d}_{\text{min}} \leq \tfrac{d_{T:i}}{d_{T:R}} \leq \hat{d}_{\text{max}}, \\
& 0 \leq \lambda_1, \lambda_2, \lambda_3 \leq 1, \\
& \lambda_1 + \lambda_2 + \lambda_3 = 1.
\end{aligned}
\tag{4.1}
$$

Each penalty function (p_1, p_2, and p_3) ranges from zero to one, normalized over the Monte Carlo data from all the comparison configurations.

Together, these penalty functions represent a trade-off between (i) errors from mismatch between the sense coils and the models used for TPM reconstruction; (ii) sensitivity to measurement errors and noise in calibration; and (iii) signal-to-noise ratio in the sense coil measurement. The sense coil parameters that determine the penalty functions include the sense coil radii r_i and the vertical distance from the Tx coil to the sense coils $d_{T:i}$ for N sense coils, where $i \in \{1, ..., N\}$. $\hat{R}_{\text{min}}$ and $\hat{R}_{\text{max}}$ represent range of sense coil radii normalized to the Tx coil radius r_T. $\hat{d}_{\text{min}}$ and $\hat{d}_{\text{max}}$ are the sense coil positions above the Tx coil normalized to the distance between the Tx and Rx coils $d_{T:R}$. λ_i are the weights for the penalty functions.

The analysis and computation are tractable when eddy currents are neglected and only the principal transfer-power is used. The following subsections detail each penalty function and show the results of the comparison.

4.2.1 Model Matching

The errors in FC-TPM can be made small and insensitive to variation when the sizes and positions of the sense coils are chosen so that the deviation from the models used in reconstruction is small. p_1 penalizes model mismatch.

For example, when the mutual inductance from the Tx coil to the Rx coil varies so it is predominantly quadratic over Rx coil misalignment, placing the sense coils close to the Tx coil makes the corresponding geometric parameters also predominantly quadratic as discussed in Section 3.3. In this case, p_1 penalizes the non-quadratic deviations over Rx coil misalignment in the sense-to-Rx coil mutual inductance. The penalty function can be evaluated using Grover's expression for mutual inductance [56] with the quadratic model presented in Section 3.3.1.

$$p_1 = \frac{q_1(\mathbf{r},\mathbf{d}) - \min\limits_{\mathbf{r},\mathbf{d}} q_1(\mathbf{r},\mathbf{d})}{\max\limits_{\mathbf{r},\mathbf{d}} q_1(\mathbf{r},\mathbf{d}) - \min\limits_{\mathbf{r},\mathbf{d}} q_1(\mathbf{r},\mathbf{d})}, \tag{4.2}$$

where

$$\begin{aligned} &q_1(\mathbf{r},\mathbf{d}) \\ &= \log\left(\sum_{i\in\{1,\cdots,N\}} \frac{\left\| M_{R:i}(r_i, d_{T:i}, x) - \widehat{M}_{R:i}(r_i, d_{T:i}, x)\right\|_2^2}{\left\| M_{R:i}(r_i, d_{T:i}, x)\right\|_2^2}\right). \end{aligned} \tag{4.3}$$

$M_{R:i}(r_i, d_{T:i}, x)$ is the mutual inductance between the sense coil and Rx coil which is calculated from the Grover; $\widehat{M}_{R:i}(r_i, d_{T:i}, x)$ is the mutual inductance from the quadratic model; r_i is the radius of the i^{th} sense coil; $d_{T:i}$ is the distance between the i^{th} sense coil and the Tx coil; x is the Rx coil misalignment; and $\|\cdot\|_2$ is the $l_2[0, x_{\max}]$ norm over a closed interval and a sampling of the continuous functional $\widehat{M}_{R:i}(\cdot,\cdot,x)$ and its corresponding discrete data sequence $\widehat{M}_{R:i}(\cdot,\cdot,x[n])$.

4.2.2 Information Diversity

Overlapping information in the least-squares minimization of the data matrix of sense coil voltages $\mathbf{W}$, defined in (3.14), results in poor matrix conditioning and consequently sensitivity to noise and measurement error.

In the calibration of FC-TPM, least-squares minimization is performed, where $\mathbf{W}^{\mathrm{T}}\mathbf{W}$ is inverted in (3.18). When the sense coil voltages are independent, the calibration is robust to measurement noise. Hence, sense coils are chosen and arranged to minimize overlapping information in the voltages.

Mutual inductance can be used as a proxy for information overlap among sense coil voltages because mutual inductance is a measure of the shared magnetic flux between two sense coils and hence information. Large mutual inductance between two sense coils may physically mean that they are similar in size and/or proximal.

p_2 penalizes information similarity. It is formulated by normalizing and taking the logarithm of the sum of squares of the mutual inductances between sense coil pairs. p_2 ranges from from 0 to 1: '0' indicates that all pairs of sense coils have maximum independence given the optimization constraints; '1' indicates the worst-case among all sense coil configurations in all the comparison cases.

$$p_2 = \frac{q_2\left(\mathbf{r},\mathbf{d}\right) - \min\limits_{\mathbf{r},\mathbf{d}} q_2\left(\mathbf{r},\mathbf{d}\right)}{\max\limits_{\mathbf{r},\mathbf{d}} q_2\left(\mathbf{r},\mathbf{d}\right) - \min\limits_{\mathbf{r},\mathbf{d}} q_2\left(\mathbf{r},\mathbf{d}\right)}, \tag{4.4}$$

where

$$q_2\left(\mathbf{r},\mathbf{d}\right) = \log\left(\sum_{i,j\in Q} M_{i:j}^2\left(r_i, d_{T:i}, r_j, d_{T:j}\right)\right). \tag{4.5}$$

$M_{i:j}(r_i, d_{T:i}, r_j, d_{T:j})$ is the mutual inductance between the i^{th} and j^{th} sense coil. The mutual inductance increases as the two sense coils are closer to each other $d_{T:i} \to d_{T:j}$ and have similar radii $r_i \to r_j$, which penalizes the lack of information diversity.

4.2.3 Detectability

The detectability is the ability of a particular FC-TPM configuration to resolve a change in the transfer-power from a change in either the Tx or Rx coil current. This is equivalent to the signal-to-noise ratio (SNR) of the different sense coil voltages from the change in the Tx/Rx coil current to the instrumentation noise referred to the sense-coil voltage. The mutual inductances between the sense coils and the Tx coil $M_{T:i}$ or Rx coil $M_{R:i}$, determine the sense coil voltages from the Tx and Rx coil currents. p_3 penalizes poor SNR in the sense coil configuration; we assume that a change in Tx current is just as likely as a change in Rx current.

$$p_3 = \frac{q_3(\mathbf{r}, \mathbf{d}) - \min\limits_{\mathbf{r},\mathbf{d}} q_3(\mathbf{r}, \mathbf{d})}{\max\limits_{\mathbf{r},\mathbf{d}} q_3(\mathbf{r}, \mathbf{d}) - \min\limits_{\mathbf{r},\mathbf{d}} q_3(\mathbf{r}, \mathbf{d})}, \tag{4.6}$$

where

$$\begin{aligned} q_3(\mathbf{r}, \mathbf{d}) = & \sum_{i \in \{1, \cdots, N\}} \frac{1}{M_{T:i}^2(r_i, d_{T:i})} \\ & + \sum_{i \in \{1, \cdots, N\}} \frac{1}{M_{R:i}^2(r_i, d_{T:i})}. \end{aligned} \tag{4.7}$$

Note that $M_{T:i}(r_i, d_{T:i})$ is the mutual inductance between the Tx coil and the i^{th} sense coil and $M_{R:i}(r_i, d_{T:i})$ is the mutual inductance between the Rx coil and the i^{th} sense coil. We choose the Tx, Rx, and sense coils to be aligned for tractability. The total SNR is the harmonic mean of the SNR of each sense coil. p_3 penalizes overly large- or small-sized sense coils, or positions which are far from both the Tx and Rx coils.

4.2.4 Comparison Results

Good sense coils have: (i) small quadratic approximation error for the mutual inductance over Rx coil misalignment; (ii) diverse information, which minimizes the least-squares errors during calibration; and (iii) good signal-to-noise ratio in the sense coil voltages for accurate transfer-

power reconstruction. It is worth noting that the three penalty functions are counteractive vis-à-vis the sense coil positions and sizes. Based on observations, (i) p_1 is smaller when the sense coils are all near the Tx coil; (ii) p_2 is smaller when the sense coils are far apart and have different sizes; and (iii) p_3 is smaller when the sense coils are of similar size to and in joint proximity to the Tx and Rx coils.

The performance metrics of coplanar sense coil configurations are compared to other sense coil geometries with fewer restrictions for $N=6$ sense coils. Design classes such as sense coil configurations should be compared by their optimal designs on Pareto frontiers. The class of coplanar sense coil configurations (i) is topologically defined by the constraints that the sense coils share the same axis (coaxial) and lie on the same plane

$$d_{T:1} = d_{T:2} = \cdots = d_{T:6}. \tag{4.8}$$

Sense coil configuration class (ii) is topologically constrained only to be coaxial.

A numerical comparison was performed using identical Tx and Rx coil radii ($r_{_T} = r_{_R} = 22.5\,\text{cm}$) separated by $d_{T:R} = 20\,\text{cm}$, which corresponds to the hardware in Section 5. The addition geometric constraints are $\hat{R}_{\text{min}} = 0.44$, $\hat{R}_{\text{max}} = 1.78$, $\hat{d}_{\text{min}} = 0.05$, and $\hat{d}_{\text{max}} = 0.95$.

The Pareto frontier is found by an exhaustive search following the non-uniformly distributed search points; there are dense search points of radii and distances based on the prior knowledge on the optimal geometry; sense coils that are closer to the Tx coil and that are similar in size to the Tx or Rx coil, show a good performance. Each Pareto frontier is obtained for configuration class (i): coaxial sense coils that are restricted to the same plane (i.e., coplanar configurations) and configuration class (ii): coaxial sense coils which can be coaxial, stacked, or a mixed combination (i.e., mixed configurations). For the coplanar configuration, class (i), there are over 20 million (20,990,002) search points[4] from six sense coil combinations, as shown in Fig. 4.3a. For the mixed configurations,class (ii), there are 206 search points for each sense coil, resulting in more than 98

[4]For example, given each height of coplanar plane, there are ${}_nC_6$ search points from n different radii for six sense coils. Total sum of all combinations for all 19 heights results in 20,990,002 search points.

billion ($_{206}C_6$) entire search points from six sense coil combinations, as shown in Fig. 4.3b. Each search space is large enough to cover the sense-coil geometries, which are physically realizable.

Pareto frontier was found by iteratively examining all search points' penalty functions. The penalty function vector $\mathbf{p}_i$ is created for each search point

$$\mathbf{p}_i = \begin{bmatrix} p_1(i) \\ p_2(i) \\ p_3(i) \end{bmatrix}. \tag{4.9}$$

The Pareto frontier matrix $\mathbf{P}$ can be constructed by selectively including the penalty function vectors corresponding to specific search points i as a column vector; $\mathbf{P}$ is updated by augmenting i^{th} column vector $\mathbf{p}_i$ if $\mathbf{p}_i$ is not greater than any column vector in current Pareto frontier matrix $\mathbf{P}$. In other words, if all of elements in the i^{th} penalty function vector $\mathbf{p}_i$ are greater than that in each column vector in current Pareto frontier matrix, then the i^{th} search point is excluded for the Pareto frontier matrix, resulting in minimization of weighted sum of three penalty functions by Pareto-efficiency [73; 74]. Algorithm 1 contains a pseudo-code implementation for finding Pareto frontier.

After finding the Pareto frontier for each constraint, sense coil geometries outside of the search space were sampled in Monte Carlo simulations to verify the Pareto frontier; Monte Carlo is used to examine the penalty functions of non-optimal points and confirm that the Pareto frontier forms the boundary and is close to non-optimal points. In other words, there is no non-optimal point outside of the frontier. Manhattan sampling [75] is used for the grid of Monte Carlo, as shown in Fig. 4.4; the search space $\left(\frac{r_i}{r_T}, \frac{d_{T:i}}{d_{T:R}}\right)$ is uniformly partitioned into 3×3 rectangular regions. These 9 rectangular regions are exhaustively travelled. For each coordinate, 10 search points were randomly generated resulting in 90 points for each sense coil. There are total $_{90}C_6$ search points for Monte Carlo simulations, and 1 million points are used to plot in Fig. 4.5.

The optimal points for the coplanar and mixed configurations, shown in Fig. 4.5, form surfaces which are the Pareto frontiers for each of the multi-objective optimizations. The hollow yellow

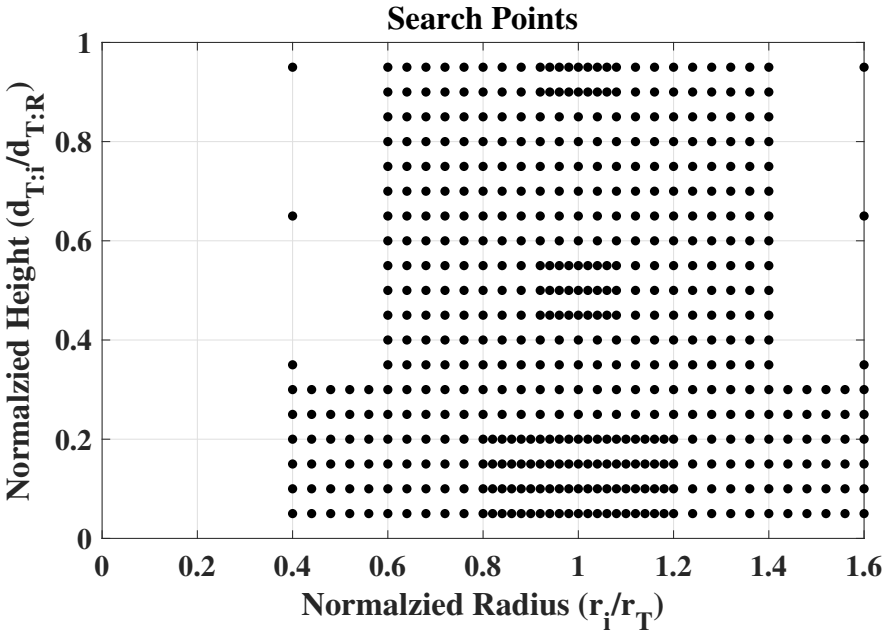

(a) Search points for coplanar configurations.

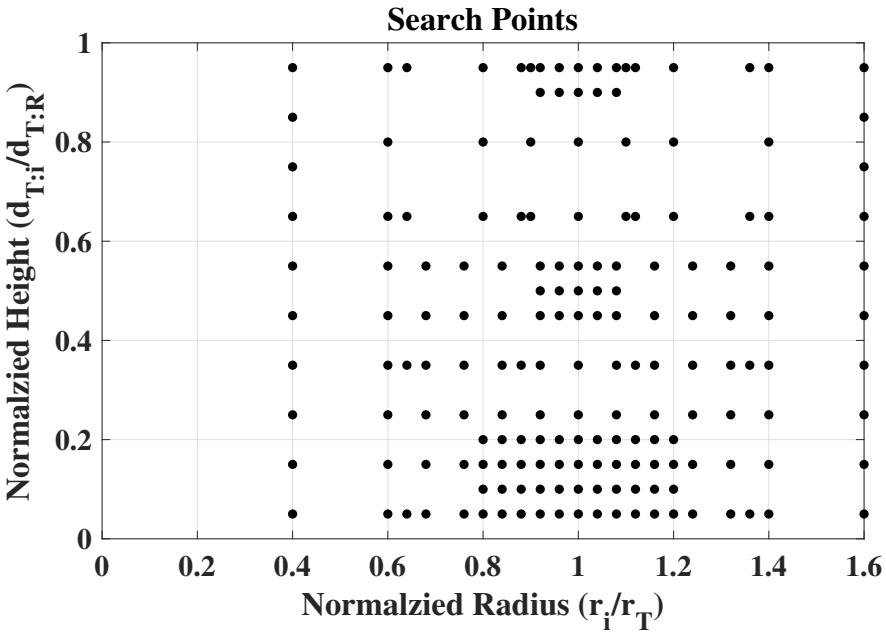

(b) Search points for mixed configurations.

Figure 4.3. The exhaustive search points for finding Pareto frontier for each sense coil.

Algorithm 1 Exhaustive Pareto Frontier Search

flag $\leftarrow 0$
Frontier$_{\text{temp}} \leftarrow [\,]$
$\mathbf{P} \leftarrow \mathbf{p_1}$
while $i \geq 2$ is in search space **do**
  while j is in Pareto frontier space **do**
    if $\mathbf{p}_j > \mathbf{p}_i$ **then**
      flag$\leftarrow 0$
    else if $\mathbf{p}_j < \mathbf{p}_i$ **then**
      flag$\leftarrow 1$
      Break
    else
      flag$\leftarrow 0$
      Frontier$_{\text{temp}} \leftarrow$ merge(Frontier$_{\text{temp}}, \mathbf{p}_j$)
    end if
  end while
  if flag==0 **then**
    Frontier$_{\text{temp}} \leftarrow$merge(Frontier$_{\text{temp}}, \mathbf{p}_i$)
    $\mathbf{P} \leftarrow$ Frontier$_{\text{temp}}$
  end if
  flag$\leftarrow 0$
  Frontier$_{\text{temp}} \leftarrow [\,]$
end while
return $\mathbf{P}$

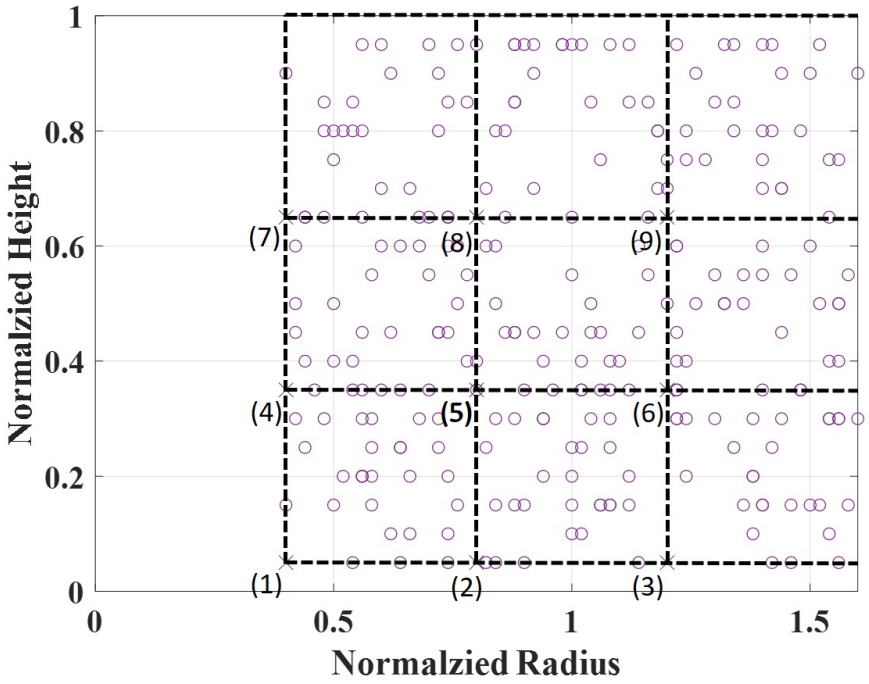

Figure 4.4. Search points for finding non-optimal sense coil geometries.

circles correspond to the Pareto frontier for coplanar sense coil configurations (i); the solid blue circles correspond to less restrictive sense coil configurations (ii); and the solid grey circles correspond to non-optimal points. The Pareto frontiers largely overlap, which indicates that coplanar sense coils have comparable performance to less restrictive sense coil geometries.

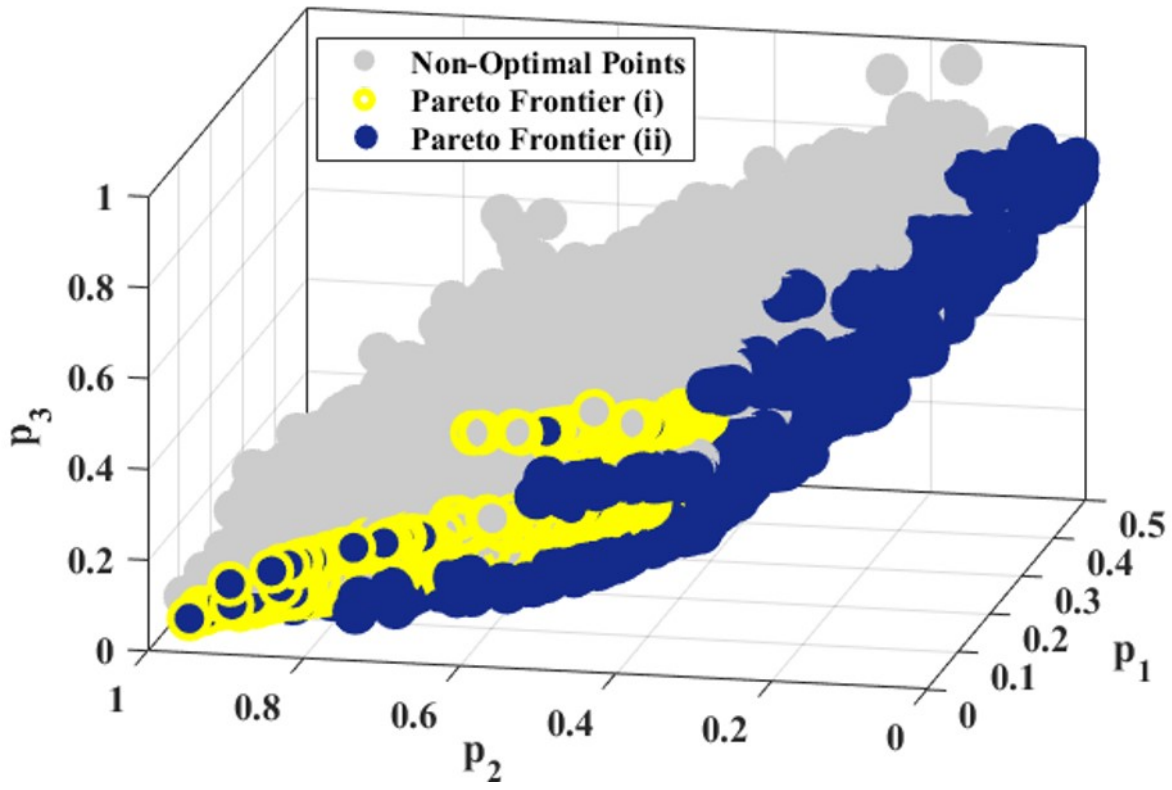

Figure 4.5. Comparison results between coaxial-coplanar and coaxial-unrestricted sense coils. The yellow shows the Pareto frontier (optimal points) when sense coils are restricted to coplanar configurations. The blue shows the Pareto frontier (optimal points) when there is no restriction on the coaxial sense coil placement. The grey shows some non-optimal sense coil geometries.

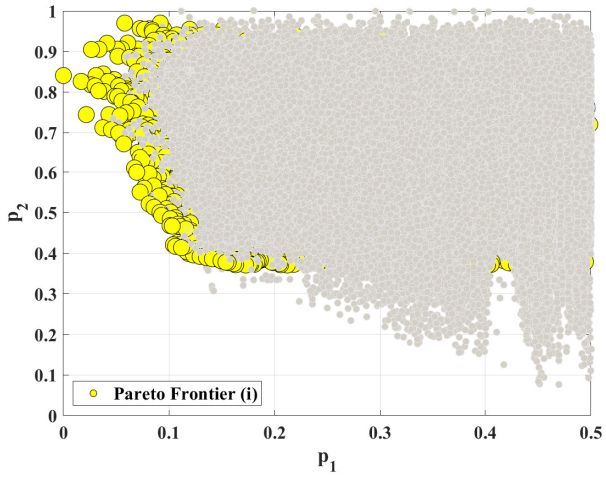

(a) p_1 and p_2

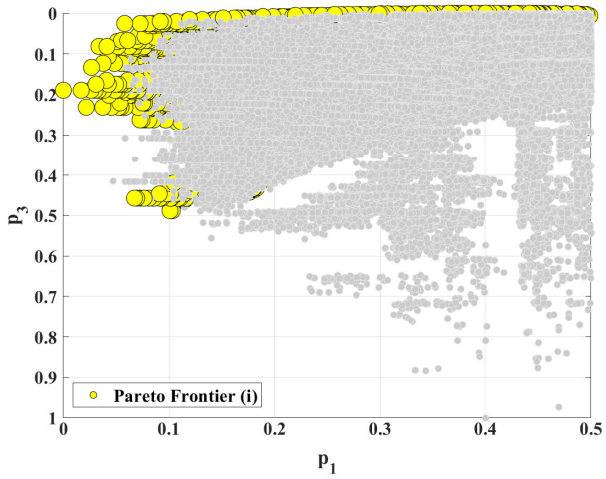

(b) p_1 and p_3

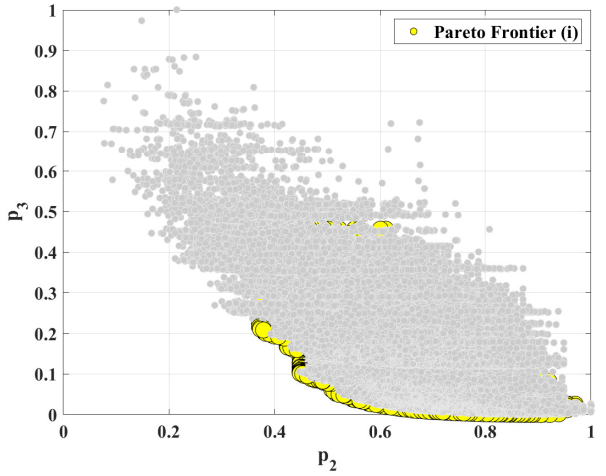

(c) p_2 and p_3

Figure 4.6. 2D projection of the comparison results in Fig. 4.5 for coplanar sense coils. Grey dots are non-optimal points.

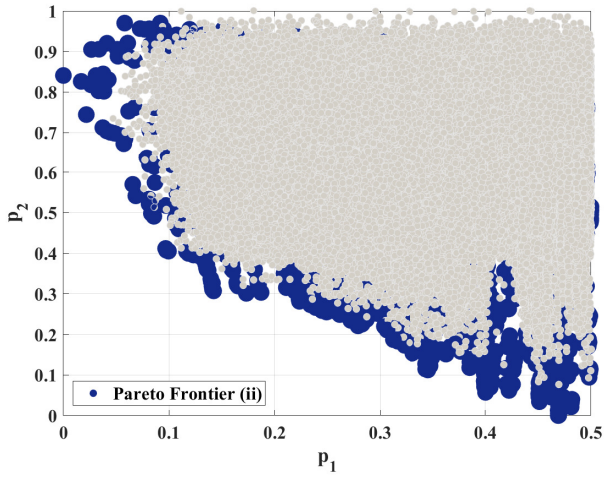

(a) p_1 and p_2

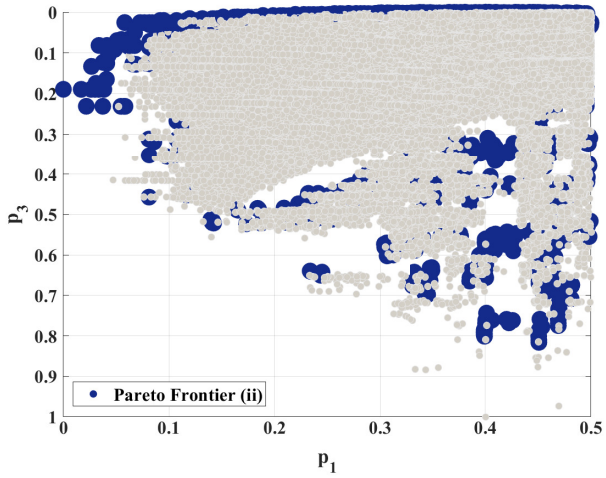

(b) p_1 and p_3

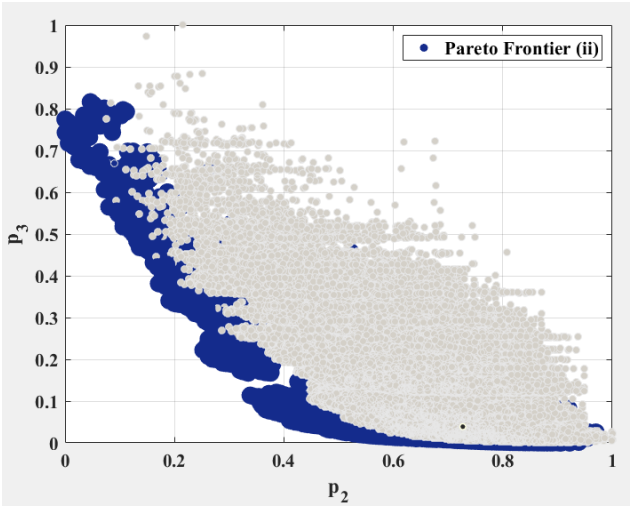

(c) p_2 and p_3

Figure 4.7. 2D projection of the comparison results in Fig. 4.5 for non restricted sense coils on the coaixal sense coil placement. Grey dots are non-optimal points.

CHAPTER 5

Hardware for Faraday Coil Transfer-Power Measurement

This chapter presents the demonstration of accurate FC-TPM in hardware over a standardized Rx coil misalignment of up to 10 cm with a 1 kW wireless power transfer system. For this demonstration, 1 kW WPT testbed was built, where total loss was designed to be approximately 10% to highlight FC-TPM's loss disaggregation by measuring transfer-power, which differs from the front-end or output dc power. In the hardware, the transmitter and receiver coils are designed to be solenoidal (co-axial) without using magnetic cores to demonstrate and focus on the essence of research concept.

Section 5.1 discusses how current-mode class D converters can be designed to drive 1 kW level wireless power transfer coils. Section 5.2 discusses the design methodology for wireless power transfer coils and sense coils, where loss budget of the WPT system is shown in Section 5.3. Section 5.4 presents reference standard transfer-power which is used for calibration. Section 5.5 shows the hardware results.

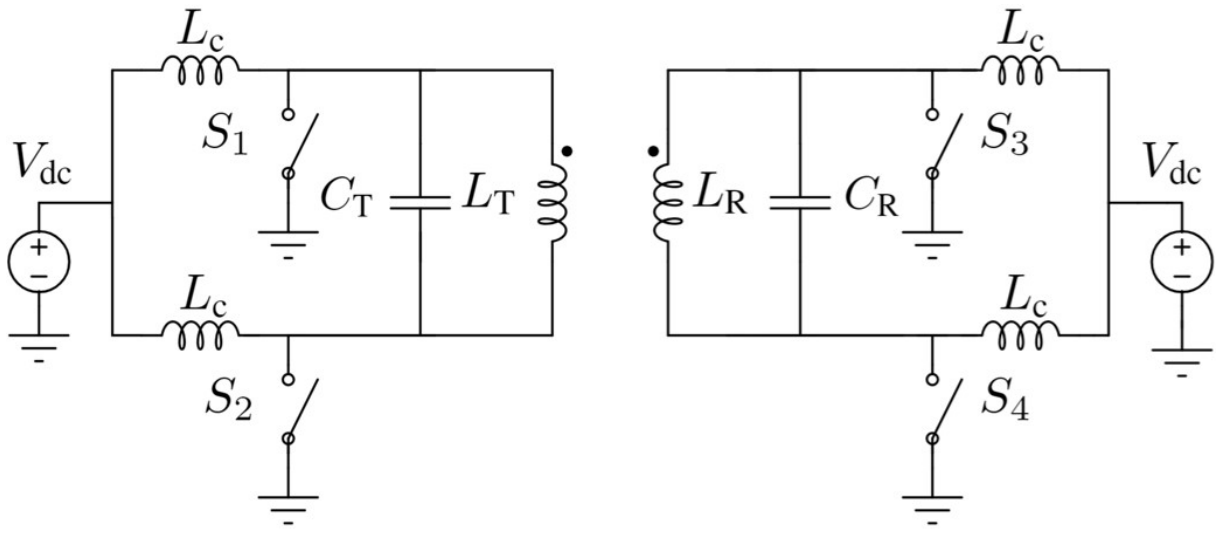

Figure 5.1. Current-mode class D (CMCD) converter topology: the Tx and Rx coils are driven by each CMCD converter.

5.1 Power Converters for Driving 1 kW Wireless Power Transfer Coils

A current-mode class D (CMCD) topology is used for driving both the Tx and Rx coils in this hardware demonstration, as shown in Fig. 5.1. The CMCD topology is a good candidate for peer-to-peer bi-directional wireless power transfer [76; 77; 78]. Therefore, for the FC-TPM hardware demonstration, driving both the Tx and Rx coils by each CMCD converter is beneficial to have calibration data points by controlling the phase difference between the two coil currents resulting in phase shift power modulation, which is corresponding to different output load conditions. This section presents the design procedures and loss calculation for the CMCD converters[1] to drive 1 kW wireless power transfer.

5.1.1 Coupling Coefficient Between the Tx and Rx Coils

The coupling coefficient between the Tx and Rx coils determines the transfer-power, as derived in (2.12). Knowing the coupling coefficient through FEM simulation could be the first step to

[1]The CMCD converters used for the hardware demonstration were designed and manufactured by Xin Zan and Sung Yul Chu at the University of Michigan.

designing a power converter to achieve a target power level. 10 turn, 45 cm diameter solenoid Tx and Rx coils whose air-gap was 20 cm were modeled in 2-D axisymmetric FEM simulation in COMSOL, as shown in Fig. 5.2. The Tx coil was driven by a current of 15 A, and the Rx coil was open-circuited to calculate the coupling coefficient. The coupling coefficient can be calculated from the open-circuit Rx coil voltage using (2.25) when the Rx coil current $I_R = 0$. Table 5.1 shows the variables from the simulations.[2]

TABLE 5.1
COMSOL Simulation Results for the Coupling Coefficient Calculation between the Tx and Rx Coils

Parameters	Value	Parameters	Value
r_T,r_R	22.5 cm	$d_{T:R}$	20 cm
f	85 kHz	N	10 turns
I_T	15 A	I_R	0 A
L_T,L_R	99.5 μH	V_R	(-0.013+103.68i) V
$M_{T:R}$	12.94 μH	$k_{T:R}$	0.13

$r_{T,R}$ are the radii of the Tx and Rx coils.
$d_{T:R}$ is the air-gap between the Tx and Rx coils.
f is the operating frequency.
N is the number of turns for the Tx and Rx coils.
V_R is the open-circuited Rx coil voltage (Cartesian representation).
$k_{T:R}$ is the coupling coefficient between the Tx and Rx coils.

5.1.2 1 kW CMCD Converter Design

The design parameters for CMCD converters to drive a 1 kW WPT system can be theoretically determined [76], when the fixed parameters are: (i) 85kHz switching frequency f; (ii) coupling coefficient $k_{T:R}$; (iii) self-inductance of the Tx and Rx coils L_T, L_R; (iv) choke inductance L_c; and (v) transfer-power P_{Transfer}. From [76] for a lossless case, the rms coil voltage $V_{\text{coil}}(= V_T = V_R)$ is

$$V_{\text{coil}} = \sqrt{P_{\text{Transfer}} \frac{\omega(1 - k_{T:R}^2) L_T}{k_{T:R}}}. \tag{5.1}$$

[2]The self inductance L_T and L_R were calculated using (2.25) when there is only one coil where another coil was removed.

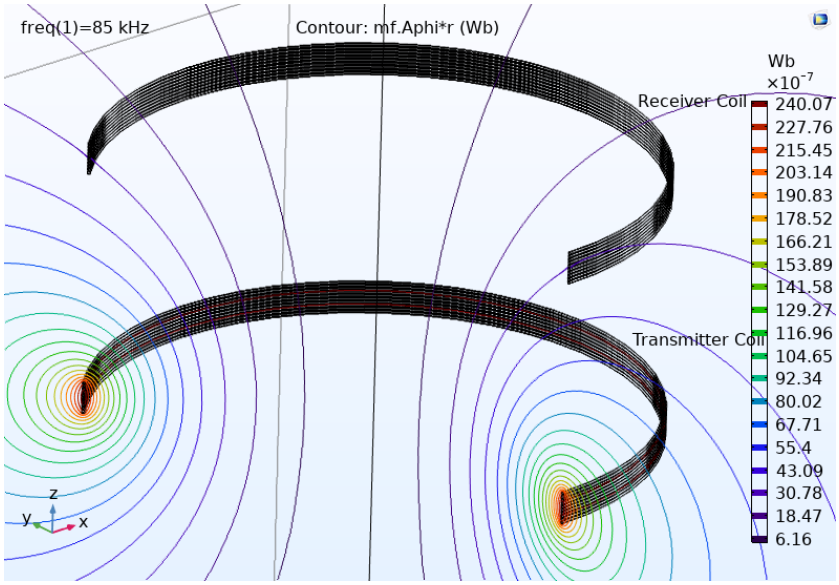

Figure 5.2. Coupling coefficient between the solenoid Tx and Rx coils are obtained through FEM simulation in COMSOL.

Note that the phase difference between the Tx and Rx coil voltage is 90°. The self-inductance of the Tx and Rx coils is the same. The switch voltage is then a half-sine wave (50% duty cycle), as illustrated in Fig. 5.6, resulting in the dc input voltage V_{dc}

$$V_{\text{dc}} = \frac{V_{\text{coil,peak}}}{\pi} \tag{5.2}$$

as the average voltage of the choke inductor is zero. The coil current can be calculated from the coil voltage, inductance, and angular frequency. The dc input and choke current is determined from the dc power and transfer-power. The design parameters are presented in Table 5.2.

5.1.3 Choke Inductor Design

5.1.3.1 Current Ripple

The choke inductance L_c should be large enough to convert the dc voltage source to the dc current source, shown in Fig. 5.1. The choke inductance L_c is chosen and designed to be 10 mH, which is approximately 100 times larger than the Tx and Rx coil inductance L_T, L_R. The ripple of the

TABLE 5.2
Design Parameters for 1 kW CMCD Power Converters

Parameters	Value	Parameters	Value
$k_{T:R}$	0.13	P_{Transfer}	1,000 W
L_c	10 mH	L_T,L_R	99.5 μH
f	85 kHz	$\theta_{V_T} - \theta_{V_R}$	90°
$V_{\text{coil,peak}}$	896 V	$I_{\text{coil,peak}}$	16.9 A
V_{dc}	285 V	I_{dc}	3.5A
I_s	2.48 A	I_c	1.75 A

P_{Transfer} is defined in the lossless systems.
L_c is the choke inductance.
L_T and L_R are the self inductance of the Tx and Rx coils.
$\theta_{V_T} - \theta_{V_R}$ is the Tx and Rx coil voltage phase difference.
$V_{\text{coil,peak}}$ is the peak coil voltage.
$I_{\text{coil,peak}}$ is the peak coil current.
V_{dc} is the dc supply voltage.
I_s is switch rms current.
I_c is choke dc current.

choke current ΔI_c is limited to be approximately 10% of the average dc choke current to reduce the harmonic injection from the ripples [77].

5.1.3.2 Core Design and Loss Analysis

The Iron powder core was chosen for the choke inductor to achieve the target inductance of 10 mH. Table 5.3 presents the number of turns calculation corresponding to three different core models from Micrometals, Inc. Corresponding core and winding losses are also calculated to achieve the target efficiency of the wireless power transfer system.[3] 18 AWG copper wire is used to calculate winding losses. From the loss analysis, T650-66 is a good candidate. Total four choke inductors are needed for Tx and Rx CMCD converters. Theoretically, 10.8 W is dissipated in the choke inductors.

[3] The core loss is calculated using the equation provided by the datasheets: https://datasheets.micrometals.com/T650-66-DataSheet.pdf

5.1.4 Components

Silicon Carbide (SiC) MOSFETs are chosen for high voltage CMCD converter switches; C3M0075-120K is used whose on resistance $R_{\text{DS(on)}}$ is 75 mΩ, where the conducting loss is calculated to be 0.46 W per each switch. A gate driver is used to drive the semiconductor switches[4] TI's UCC21530 isolated dual channel gate driver, which is good enough to drive 85 kHz switching converters, is used. The gate driver loss [79] is 0.13 W, where the gate charge of SiC MOSFET is 51 nC and gate drive supply voltage is 30 V. The switch voltages of CMCD converters are plotted using Spice simulation, as shown in Fig. 5.6.

The peak resonant capacitor voltage is approximately 900 V and current is 17 A, as shown in Fig. 5.4 and Fig. 5.5, where the capacitance for the resonance with 99.5 μH wireless charging coil at 85 kHz is approximately 36 nF, calculated from [77]

$$C_T = \frac{1}{\omega^2(1-k^2)L_T}. \tag{5.3}$$

A polypropylene film/foil capacitor (Type 715P) from Cornell Dubilier Electronics, Inc is a good selection to satisfy both the voltage rating and capacitance values. Two capacitors can be connected in parallel to achieve a certain capacitor value from the limited product capacitance values. In this theoretical analysis, it is assumed that two same capacitors whose equivalent series resistance are 0.079 Ω are connected in parallel and share the coil current. The estimated capacitor loss is 5.63 W for each Tx and Rx converter when the coil current is 11.9 A_{rms}.[5]

A circuit analysis is also performed in LTspice for the configuration, as shown in Fig. 5.3. The coil voltages, coil currents, switch voltages, and choke current simulation results are shown in Fig. 5.4, Fig. 5.5, Fig. 5.6, and Fig. 5.7 respectively.

[4]Function generators were used to provide the pulse signals for the gate drivers.

[5]For the hardware demonstration, 22 nF and 10 nF capacitors are connected in parallel, whose equivalent series resistance are 0.079 Ω and 0.11 Ω when the coil current is 12 A_{rms}. The expected losses are 6.86 W per each converter in hardware.

TABLE 5.3
Core Design and Loss Analysis

Parameters	T650-52	T650-26	T650-66
A_L (nH/N^2)	405	434	380
Target Inductance (mH)	10	10	10
N	157	152	162
I_{dc} (A)	1.75	1.75	1.75
ΔI (A)	0.168	0.168	0.168
L_e (cm)	39.9	39.9	39.9
$H_{\text{ac,max}}$ (AT/m)	722	698	746
$H_{\text{ac,min}}$ (AT/m)	623	602	643
μ_i (max)	73.5	73.5	64.7
μ_i (min)	74.3	74.3	65.3
$B_{\text{ac,max}}$ (T)	0.067	0.064	0.06
$B_{\text{ac,min}}$ (T)	0.058	0.056	0.053
B_{pk} (T)	0.0043	0.0041	0.0039
B_{pk} (Gauss)	42.9	41.4	39
Core Loss Constant, a	1.00E+09	1.00E+09	1.72E+10
Core Loss Constant, b	1.10E+08	1.10E+08	4.96E+07
Core Loss Constant, c	2.10E+07	1.90E+06	1.23E+06
Core Loss Constant, d	6.90E-14	1.90E-13	1.73E-14
Effective Core Volume (cm^3)	734	734	734
Core Loss (W)	1.51	3.33	0.34
Mean Length Per Turn (cm)	22.7	22.7	22.7
R (Ω)	0.75	0.72	0.77
Winding Loss (W)	2.29	2.21	2.36
Total Loss (W)	3.8	5.54	2.71

L_e is thee effective magnetic path length.
N is required number of turns for the target inductance.
R is calculated when 18 AWG copper wire is used whose resistance per meter is 20.95 $m\Omega$/m.

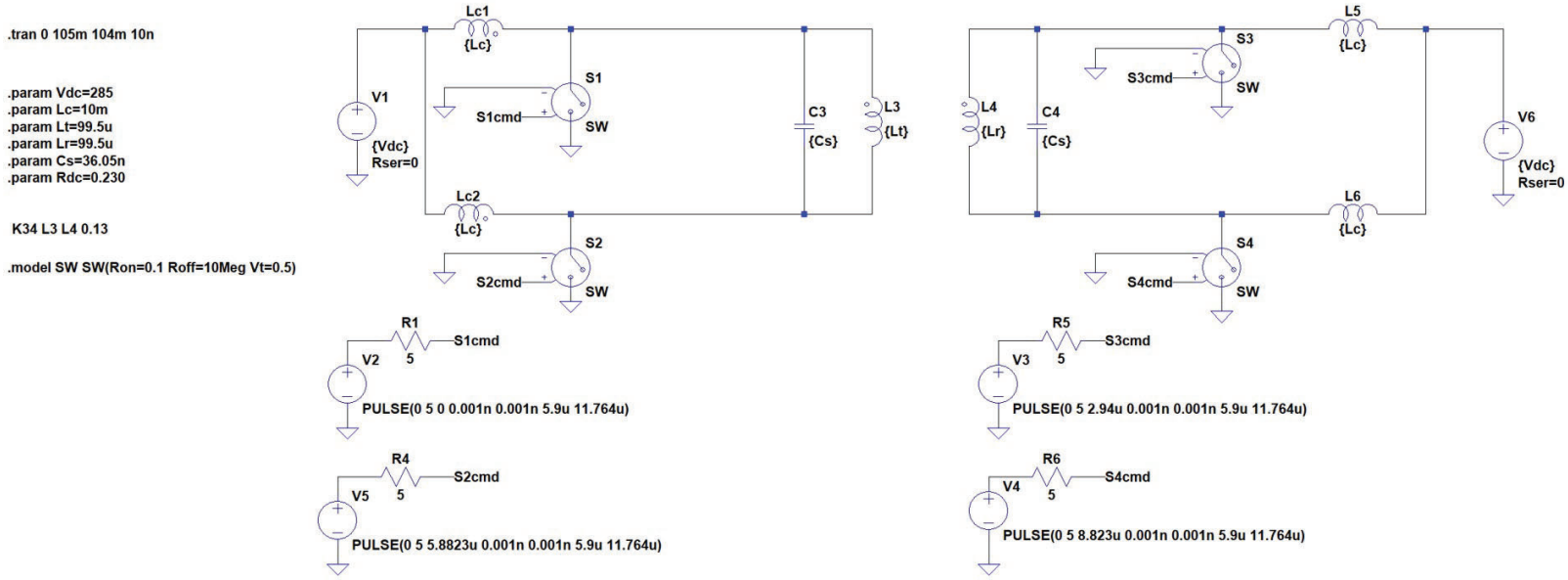

Figure 5.3. LTspice analysis model for CMCD converters to drive the Tx and Rx coils.

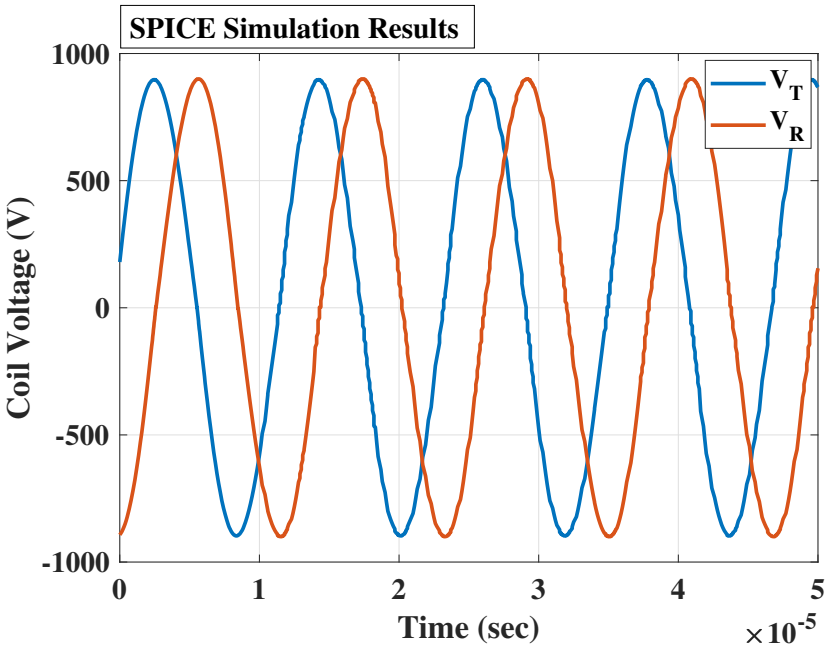

Figure 5.4. Simulated Tx and Rx coil voltages in CMCD converters. The voltages are the differential measurements between the coil terminals.

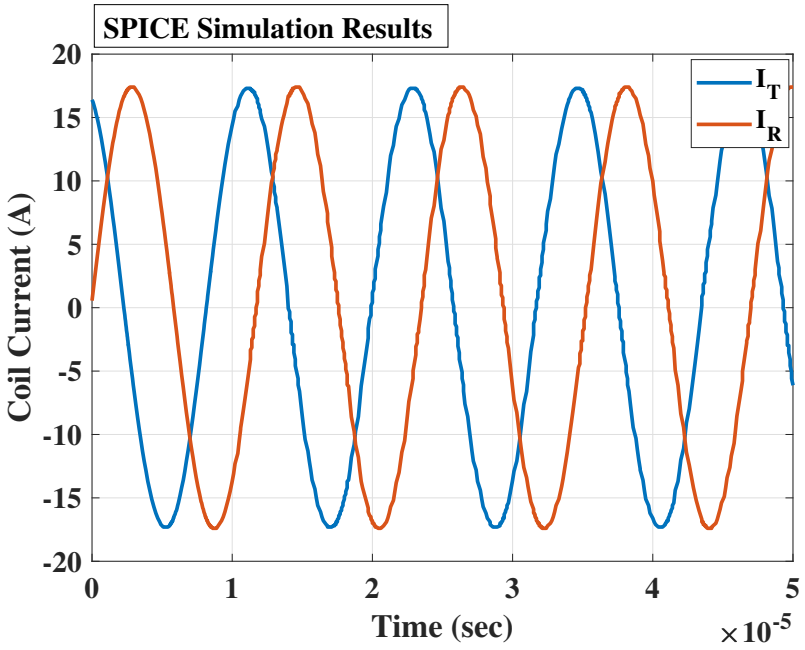

Figure 5.5. Simulated Tx and Rx coil currents in CMCD converters.

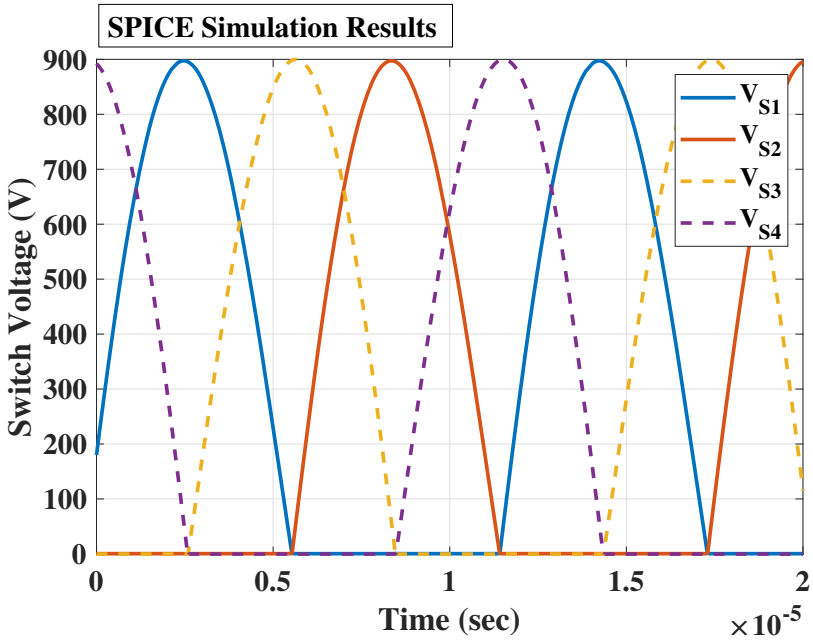

Figure 5.6. Simulated switch voltages of CMCD converters: the phase shift between S_1 and S_2, and S_3 and S_4 are 180° because of complementary switching. The Tx and Rx CMCD's switches are out of phase to maximize transfer-power.

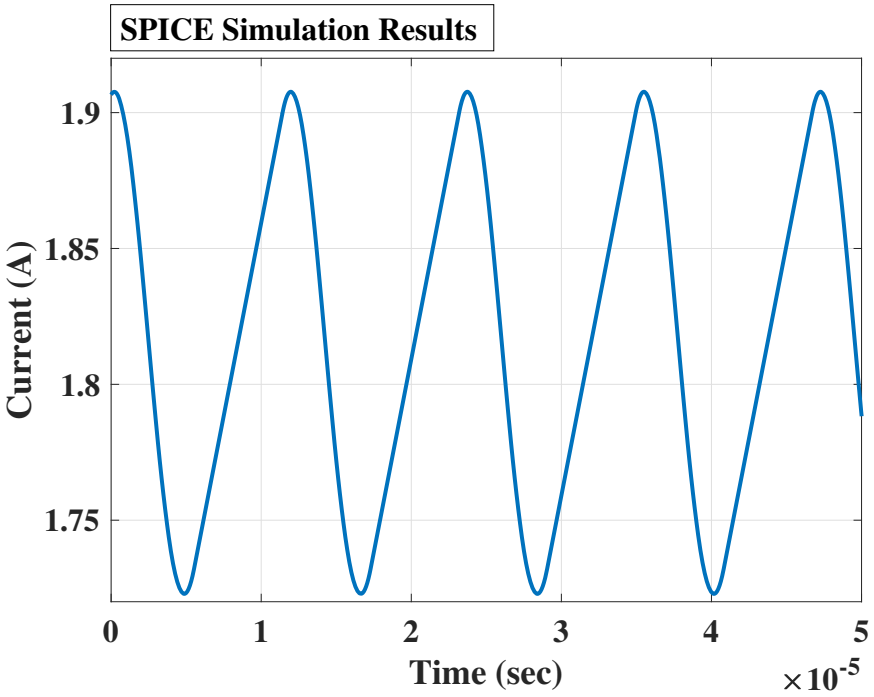

Figure 5.7. Simulated choke dc current of CMCD converters for 1kW wireless power transfer.

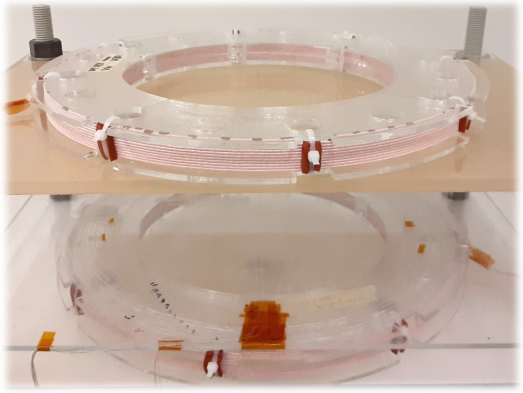

Figure 5.8. Circular Tx and Rx coils, wound by litz wires.

5.2 Wireless Power Transfer Coil

Design high power and current wireless power transfer coils can be divided into several steps. Litz wire is widely used for wireless power transfer applications because of low ac resistance, and thus low winding loss from electrically insulated multistrand wires, and hence have a better performance against skin effect, where each thin strand is smaller than the skin depth [7; 80; 81; 82; 83; 84; 85].

The main designing factors are (i) coil current; (ii) coil inductance which determines mutual inductance between the Tx and Rx coils, and hence, transfer-power; (iii) winding loss; and (iv) operating frequency, which determines the skin depth. From those considerations, (i) litz wire strands and bundles, and thus the wire diameter; and (ii) the number of turns can be determined. In this dissertation, coil shape is selected as a circular solenoid, as shown in Fig. 5.8. Besides, the Tx and Rx coils' winding losses are not minimized[6] to demonstrate FC-TPM's loss disaggregation effectively.

[6]The total loss, however, is designed to be less than 15% of the input power, i.e., 85% of efficiency, which is specified by SAE J2954 [45].

5.2.1 Litz Wire

The wire gauge can be determined by the operating frequency, which determines the skin effect. The calculation of the skin depth δ is shown in [86]

$$\delta = \sqrt{\frac{\rho}{\pi \mu f}}, \tag{5.4}$$

where ρ is the resistivity and μ is the permeability. The skin depth of the copper[7] is 0.224 mm when the operating frequency of the ac current is 85 kHz. The diameter of 38 AWG wire is 0.101 mm, and thus can be a good candidate as a single strand size for a litz wire.

For the hardware demonstration, Elektrisola's 270 strands of 38 AWG litz wire[8] served with nylon (outer insulator) is used. The Tx and Rx coils are each ten-turn solenoids, whose diameter is 45 cm, where the coil winding resistance is measured to be 230.6 mΩ for the Tx and Rx coils and loss is estimated to be 32.8 W when the rms coil current is $11.9 A_{\text{rms}}$.[9] The quality factor of the Tx and Rx coils whose self-inductance is measured to be 108 μH are approximately 230 at 85 kHz.

5.2.2 Coil Form

A coil form is needed to wind the Tx and Rx coils. Acrylic is a good material for coil form, which is robust, heat-resistive, non-magnetic, and easily cut by a laser cutter. Fig. 5.9 shows the coil schematic for laser cutting, using the Universal Laser Cutter (PLS 6.75). The outer part has holes designed to be used as (i) finger grip during winding; (ii) fastening by cable ties after winding.[10] The outer part is 1.5 cm wider than the inner part so that it can be used as a support fixture for the first turn of the winding. Quarter-inch thickness acrylic plates are used for each part, where two outer parts and four inner parts, which are calculated from ten-turn solenoid coil height, are attached by an epoxy adhesive. Fig. 5.10 shows the solenoid coil on the circular coil form.

[7] The resistivity, $\rho = 1.68 \times 10^{-8}\,\Omega\, m$.
[8] The outer diameter of the litz wire is 2.5 mm.
[9] The winding resistance of the Tx and Rx coils are measured by an Agilent E4980 LCR meter.
[10] Silicon gasket tapes are placed between the litz wires and cable ties.

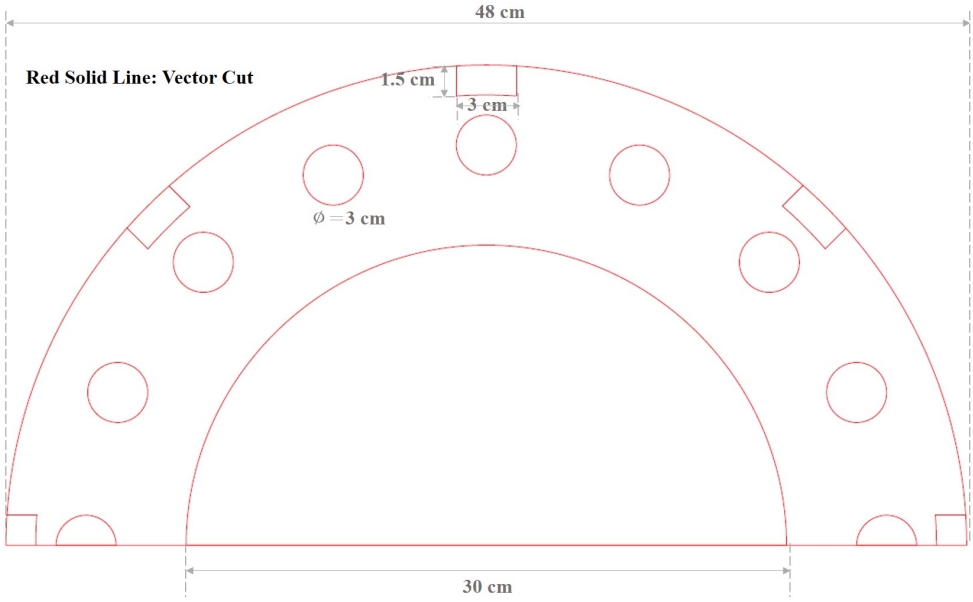

(a) The outer part of the Tx and Rx coil form.

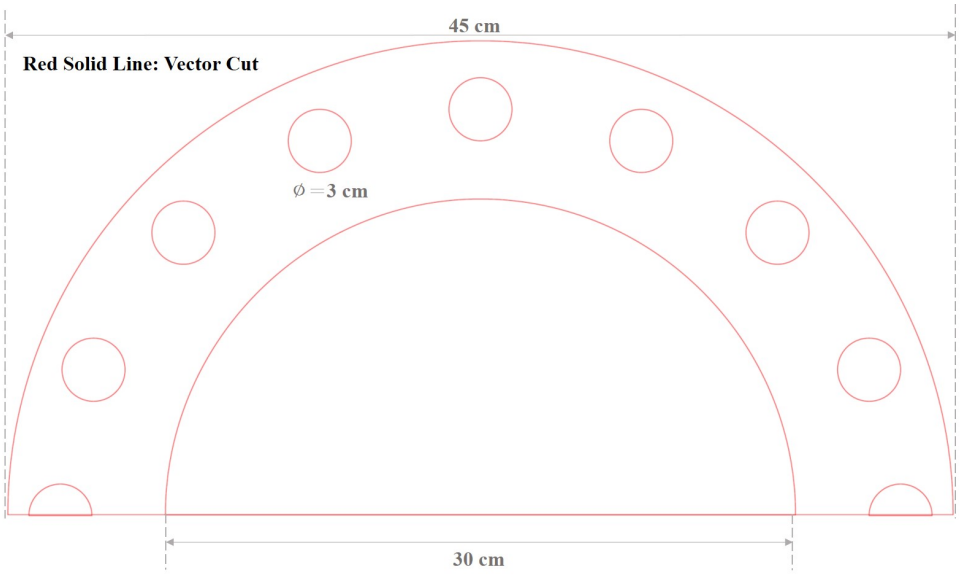

(b) The inner part of the Tx and Rx coil form.

Figure 5.9. The acrylic form is used to wind the Tx and Rx solenoid coils.

Figure 5.10. A solenoid coil is wound on the cicular coil form.

5.2.3 Litz Wire Termination: Soldering

After winding the Tx and Rx coils on the form, each terminal of the litz wire should be soldered for connection to the CMCD converters. A solder pot (American Beauty's 1lb solder pot) can be used, as shown in Fig. 5.11a, where 1-2/3 lb bar solder (Kester 04-6337-0030) is melted in the solder pot.[11] The terminal of the litz wire with nylon served is dipped in the flux (Kester 959) first and then is dipped in the solder pot. The cross-area of the soldered end should be well-covered with the solder. A ring terminal connector can be used for the soldered end. 10-12 AWG crimp type ring connector (2-34854-1, CONN RING CIRC 10-12AWG) is used for the Tx and Rx coil termination, as shown in Fig. 5.11b.

5.2.4 Sense Coils

Very thin coaxial cable, 42 AWG (0.06335 mm outer diameter, Alpha Wire A9442W), was used for each single-turn sense coil winding. The coaxial cable was configured so the outer braid acted as an electrostatic shield from the high voltage Tx and Rx windings[12][87]. The largest sense coil

[11] A solder pot should be used in a vented fume hood.
[12] Only one terminal of the shield was grounded to preclude a shorted turn.

(a) (b)

Figure 5.11. Litz wire termination: (a) a solder pot is used for soldering each end of litz wires (b) a soldered wire is terminated by a crimp ring connector.

radius is 45 cm, which has a 486 pF parastic capacitance[13] and 4.25 μH[14], resulting in 3.5 MHz self-resonance frequency, which is approximately 40 times higher than the operating frequency 85 kHz. The coaxial cable is embedded into the traces, which are engraved by a laser cutter, on the acrylic plate, as shown in Fig. 5.12. Fig. 5.13 shows the sense coil configuration on the flat plane.

5.3 Loss Budget for Wireless Power Transfer System

From the theoretical analysis for the Tx and Rx CMCD converters in Section 5.1, and coil loss estimation in Section 5.2.1, the input dc power-to-output dc power efficiency of wireless power transfer system $\eta = P_{\text{out}}/P_{\text{in}} \times 100\,(\%)$, which is shown in Fig. 5.19, is calculated to be 91.4 %. The input dc power is the transfer-power plus losses in the Tx CMCD converter and the output dc power is the transfer-power minus the Rx CMCD converter losses. The loss budget pie chart is illustrated in Fig. 5.14.

[13]The parastic capacitance is calcuated by 33.6pF/ft specification.
[14]The self inductance of the sense coil is measured by LCR meter.

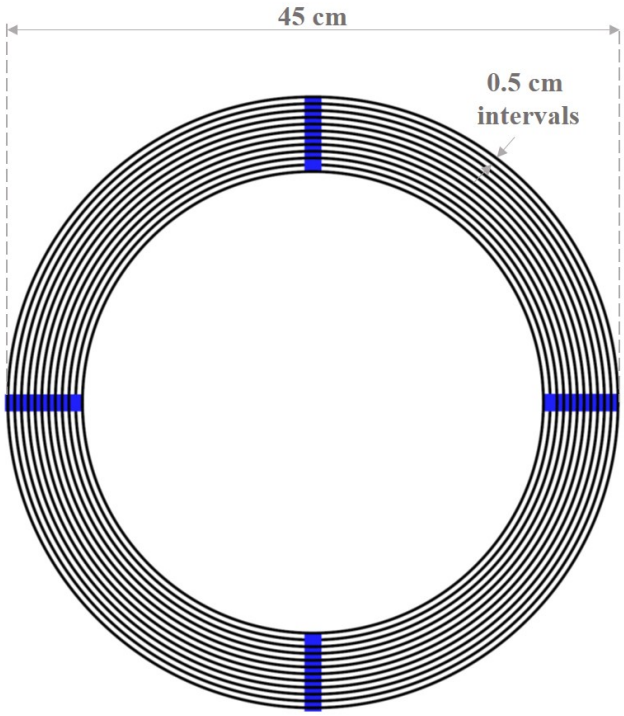

Figure 5.12. The form for winding single turn sense coils. 42 AWG coaxial wires can be embedded into the engraved trace.

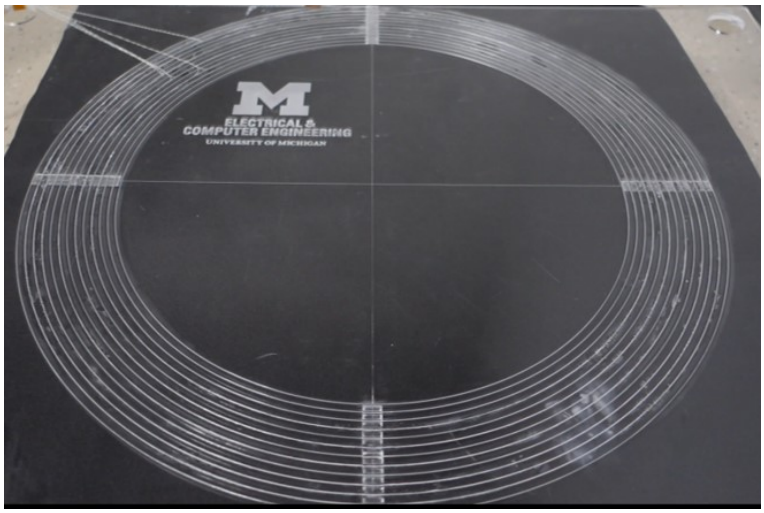

Figure 5.13. Single-turn open-circuited sense coils are embedded into the engraved acrylic form.

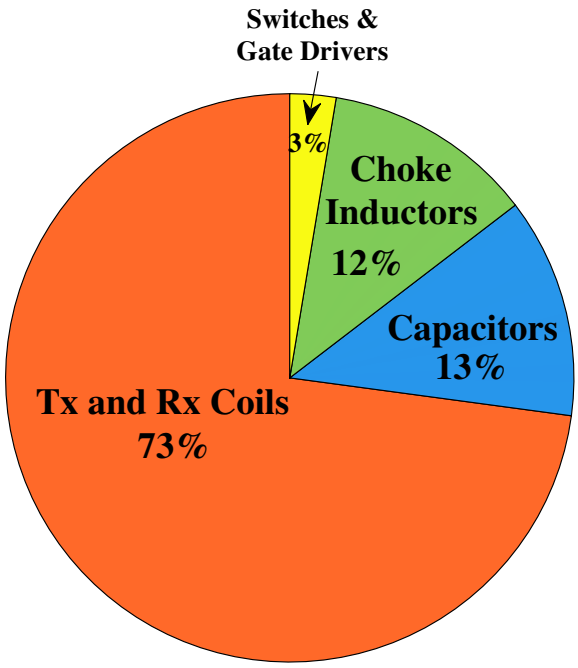

Figure 5.14. The loss contribution from the Tx and Rx coils, choke inductors, capacitors, switches, and gate drivers.

5.4 Reference Standard Transfer-Power for the Calibration of FC-TPM

Geometric constants that relate the sense coils' voltages to transfer-power need to be calibrated accurately. A standard protocol is two-level calibration, where field standards are calibrated through reference standards in laboratories.[15] The calibration strategy for FC-TPM is presented in [88] and Chapter 7; the reference standard Tx coil is designed in the standard laboratories to calibrate field-standard sense coils in calibration vehicles over misalignment. The field standards are then deployed to energy service stations and calibrate FC-TPM sense coils in the charging station. Note that we can access the Tx and Rx terminals in laboratories, and the standard Tx coil is designed to be air-core to make the calibration straightforward and accurate.[16]

This section discusses how we can obtain an accurate reference standard transfer-power for FC-TPM in laboratories. We present a reliable method against phase error in the coil voltage measurement; the strategy is using only magnitude of the open-circuited Rx coil voltage and Tx coil current to approximate the mutual reactance between the Tx and Rx coils. We fully utilize availability in laboratories that; (i) the Tx and Rx coil terminals are accessible; and (ii) reference standard mutual reactances can be obtained over misalignment, from which the reference standard transfer-powers can be independently determined for the calibration of field standard sense coils over misalignment. In other words, this method is accurate for the calibration in standard laboratories, but is not suitable for metering during charging because; (i) *trusted third party* metering does not allow the access on neither Tx (providers) nor Rx (customers) coil terminals; (ii) this method passes on the cost to vehicle owners to equip accurate calibrated sensor; (iii) misalignment cannot be accounted from calibration due to varying mutual reactance over misalignment, that are not the

[15] *Weights and Measures* provers are calibrated in standard laboratories, and being used to test the accuracy of dispensers in fields [66], [67]

[16] There is no saturation and nonlinearity in air-core inductors. This strategy is conceptually analogous to using air-core inductors in standards measurement, such as a LISN (line impedance stabilization network) Wireless power transfer with magnetic cores can potential be metered in the field using multiple sense coils by treating the magnetic cores as a geometric variation similar to how misalignment is handled in Section 3.4; FC-TPM of WPT with magnetic cores is the subject of active research.

case of using FC-TPM.

FC-TPM requires its geometric parameters α_{ij} from (3.13) to be calibrated for metering. As shown from (3.14) to (3.18), transfer-power should be known for the calibration of α_{ij}; an independent measurement of transfer-power is needed for the reference standard transfer-power.

Equation (2.12) shows that principal transfer-power is determined by the mutual reactance $\omega M_{T:R}$ from the Tx coil to the Rx coil, and the Tx and Rx coil currents I_T, I_R. We decompose the mutual reactance $\omega M_{R:T}$ to (i) the standard mutual reactance $\omega \check{M}_{R:T}$ that can be measured by only using magnitude of the open-circuited Rx coil voltage V_R and Tx coil current I_T, and (ii) $\gamma_{_T} R_R$, which accounts for the electromagnetic coupling from the Tx coil current to the Rx coil, as presented in Section 2.3.1.2. The transfer-power is then

$$P_{\text{Transfer}} = \text{Re}\left\{ j\omega M_{R:T} I_R I_T^* \right\} \tag{5.5}$$

$$= \text{Re}\left\{ j\sqrt{(\omega \check{M}_{R:T})^2 - (\gamma_{_T} R_R)^2}\ I_R I_T^* \right\}, \tag{5.6}$$

where $\omega M_{R:T}$ is derived from the open-circuited Rx coil voltage V_R, which can be derived from (2.25) with zero Rx coil current

$$\omega M_{R:T} = \frac{V_R}{jI_T} + j\gamma_{_T} R_R, \tag{5.7}$$

and the reference standard mutual reactance $\omega \check{M}_{R:T}$ is defined as the magnitude of ratio of the V_R to the I_T

$$\omega \check{M}_{R:T} \triangleq \left| \frac{V_R}{jI_T} \right|. \tag{5.8}$$

The reference standard transfer-power $\check{P}_{\text{Transfer}}$ is then defined by $\omega \check{M}_{R:T}$

$$\check{P}_{\text{Transfer}} \triangleq \text{Re}\left\{ j\omega \check{M}_{R:T} I_R I_T^* \right\}. \tag{5.9}$$

Note that when $\gamma_{_T} R_R$ is negligible ($\gamma_{_T} R_R \ll \omega M_{R:T}$), the true transfer-power P_{Transfer} in (5.5) is accurately approximated by $\check{P}_{\text{Transfer}}$, where the percentage error ϵ_M is

$$\begin{aligned} \epsilon_M &= \left| \frac{\check{P}_{\text{Transfer}} - P_{\text{Transfer}}}{P_{\text{Transfer}}} \right| \times 100\,(\%) \\ &= \left| \sqrt{(1 + \left(\frac{\gamma_{_T} R_R}{\omega M_{R:T}} \right)^2} - 1 \right| \times 100\,(\%). \end{aligned} \tag{5.10}$$

The error ϵ_M is particularly small especially for the typically loosely-coupled air-core wireless power transfer coils that have negligible $\gamma_{_T} R_R$.

2-D axisymmetric FEM simulations were performed to verify the negligible error ϵ_M of reference standard transfer-power for WPT coils, which was used in the hardware demonstration. Fig. 5.15 illustrates the flow chart for calibration and subsequent transfer-power measurement. As a worst-case simulation, 2.5 mm diameter solid copper wires were used to make 45 cm diameter single-turn circular coils; 10 of these circular coils were stacked to emulate the solenoidal Tx and Rx coils, where the solenoids' center-to-center air-gap was 20 cm. The error ϵ_M is only $6.7{\times}10^{-7}\%$ when $\omega M_{R:T}$ is 6.967 Ω. In this thesis hardware demonstration, therefore, the reference standard transfer-power is obtained from the mutual reactance measurement method.

5.4.1 Sensitive AC Power Measurement

There is an alternative method that derives transfer-power from terminal-power measurement, as presented in Section 2.3.2 through winding loss analysis of input and output power. This method, however, uses ac power measurement at the WPT coil terminal that is sensitive to the phase angle error between the voltage and current measurement. The Tx and Rx coil terminal-powers are

$$P_{\text{Tx}} = |V_T||I_T| \cos\theta_T, \tag{5.11}$$

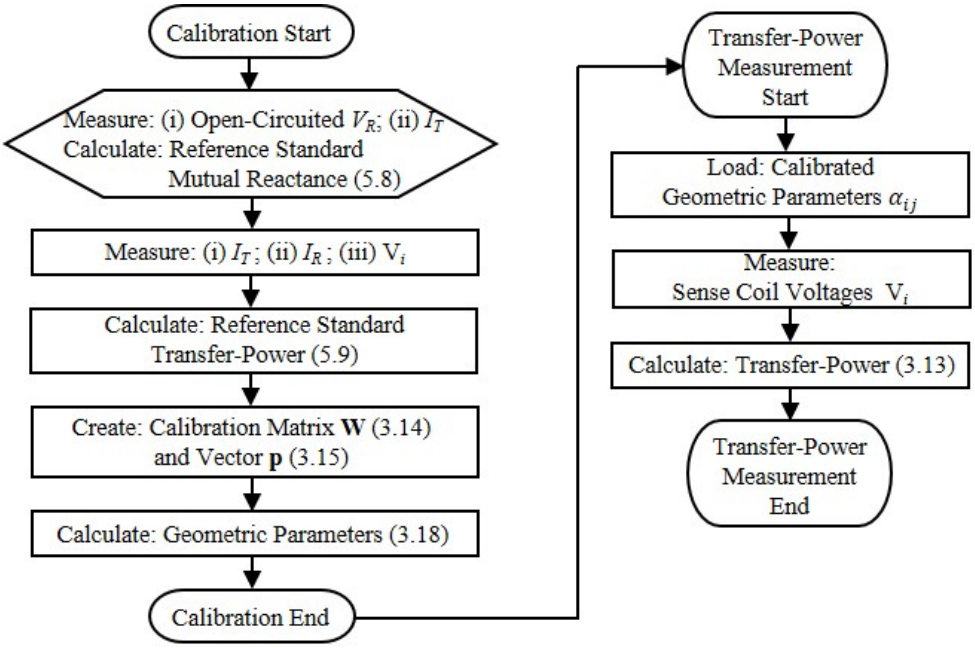

Figure 5.15. A flow chart for calibration and subsequent transfer-power measurement with corresponding equation references.

$$P_{\text{Rx}} = |V_R||I_R| \cos\theta_R, \tag{5.12}$$

where θ_T, θ_R are the phase angle difference between the coil voltages and currents. The error sensitivity over the phase angle for the power measurement at the electrical terminals of Tx and Rx coils becomes

$$\frac{dP_{\text{Tx}}}{d\theta_T} = -|V_T||I_T| \sin\theta_T, \tag{5.13}$$

$$\frac{dP_{\text{Rx}}}{d\theta_R} = -|V_R||I_R| \sin\theta_R. \tag{5.14}$$

From (5.13) and (5.14), one observes that coil terminal-power measurement for loosely coupled wireless power transfer coils is phase error sensitive because the phase angle of the coil terminal-voltage and current is close to 90 °, which results in maximum error sensitivity. This can be verified that pure inductive coil's power factor is zero (i.e., 90 ° between the coil voltage and current phases), where loosely coupled wireless power transfer coils result in a small deviation from zero power factor. For example of lossless coils, the transmitter and receiver coil voltage V_T and V_R,

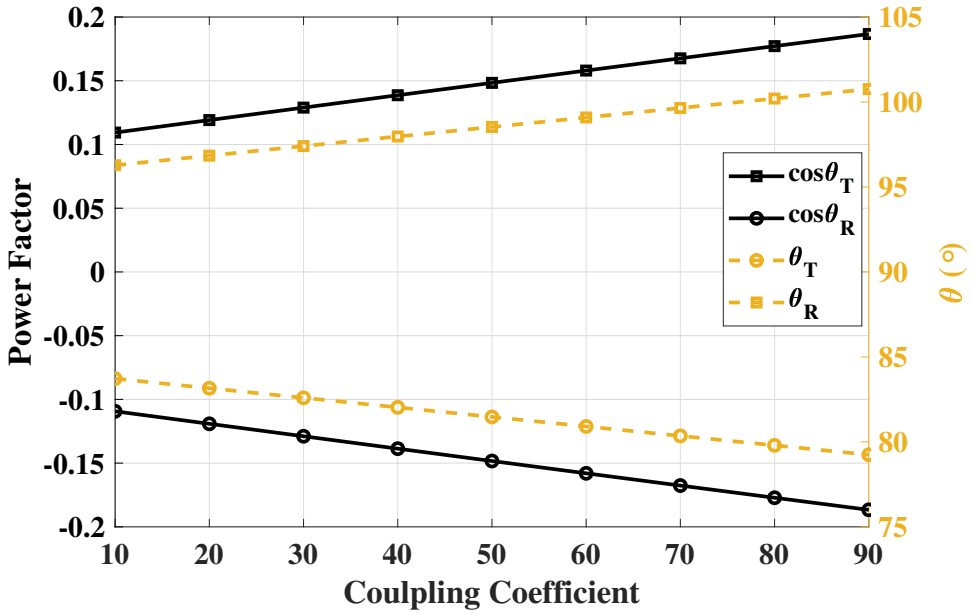

Figure 5.16. The Tx and Rx coil's power factors are plotted, respectively, when the coupling coefficients are varied.

represented in (2.8) and (2.9), is

$$V_T = j\omega L_T I_T + j\omega M_{R:T} I_R \tag{5.15}$$

$$V_R = j\omega L_R I_R + j\omega M_{R:T} I_T, \tag{5.16}$$

and if the Tx and Rx coil currents are out of phase (e.g., $I_R = -jI_T$), then the power factors are

$$\cos\theta_T = \frac{\mathrm{Re}\{V_T I_T^*\}}{|V_T I_T^*|} = \frac{M_{T:R}}{\sqrt{M_{T:R}^2 + L_T^2}} \tag{5.17}$$

$$\cos\theta_R = \frac{\mathrm{Re}\{V_R I_R^*\}}{|V_R I_R^*|} = \frac{-M_{T:R}}{\sqrt{M_{T:R}^2 + L_R^2}}. \tag{5.18}$$

Fig. 5.16 shows that the power factor approaches to zero as the coupling decreases.[17]

The power factors are also numerically analyzed with a given coupling coefficient of 0.13, derived from Section 5.1.1, when the phase difference between the Tx and Rx coil current is varied,

[17] SAE J2954 specifies the coupling coefficient ranges from 0.084 to 0.249 [45].

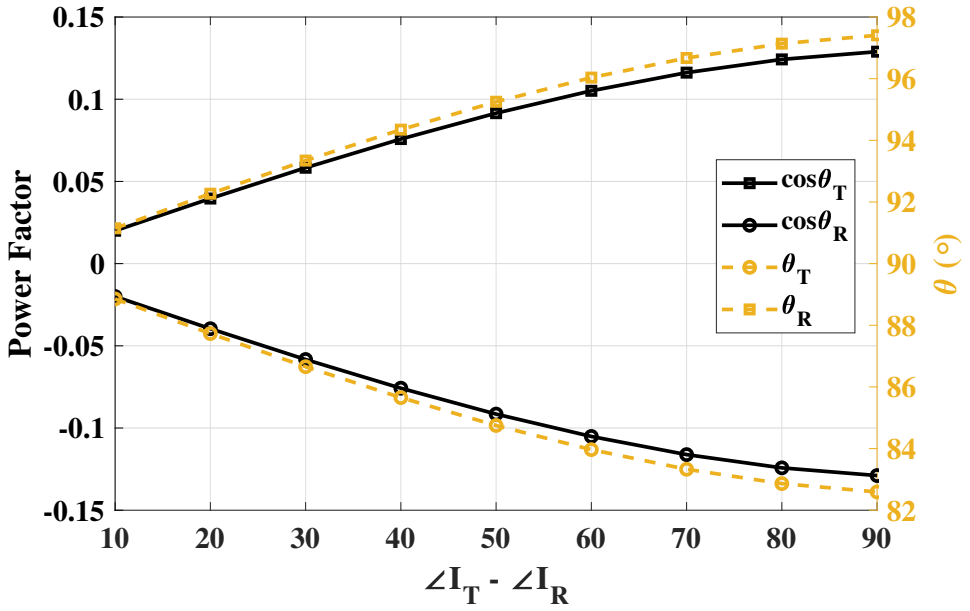

Figure 5.17. The Tx and Rx coil's power factors are plotted for a fixed Tx and Rx coil current, respectively, when the Tx and Rx coil current phase differences are varied.

which is more general cases. The self-inductance of Tx and Rx coils are fixed as 100μH. Fig. 5.17 shows that the power factor ranges from 0.02 to 0.13, resulting in sensitive power measurement. Using a reference standard transfer-power presented in (5.8) and (5.9), which is not sensitive to phase errors between the coil voltage and current measurements, is, therefore, a robust method for calibration of FC-TPM, and used for the hardware demonstration.

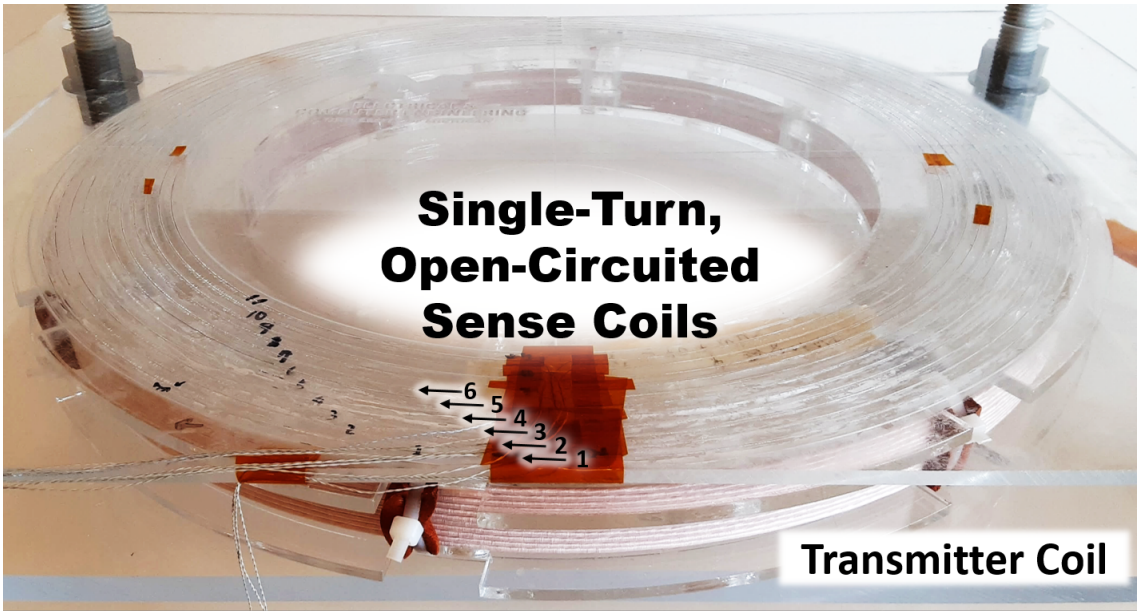

Figure 5.18. Sense coils are in the flat plane above the Tx coil.

5.5 Hardware Results

We demonstrated Faraday coil transfer-power measurement (FC-TPM) in hardware with a 1 kW wireless charging system that operates at 85 kHz using 270 strands of 38 AWG (0.101 mm diameter) litz wire for the Tx and Rx coils. The Tx and Rx coils are each ten-turn solenoids, whose diameter is 45 cm with an air gap ($d_{T:R}$) of 20 cm between the coils. Each of the FC-TPM sense coils are single-turn, open-circuited, and placed on the same plane 2.5 cm above the Tx coil ($d_{T:i}$), as shown in Fig. 5.18. Table 5.4 shows the specifications of the Tx, Rx, and sense coils.[18]

The Tx and Rx coil were driven by identical current-mode class D (CMCD) converters [76; 77; 89]; the power level from the Tx to the Rx coil was adjusted by changing the phase angle of the gate signals, hence changing the corresponding WPT coil voltages and currents [76]. The dc output of the receiver was recirculated to the input of the transmitter, with a single dc power supply V_{dc} holding the voltage of the shared dc node fixed while supplying the power loss. The CMCD WPT circuit configuration is shown in Fig. 5.19; one of the CMCD printed circuit boards is shown in Fig. 5.20. Appendix E shows the schematic and pcb layout for the CMCD converter.

[18]The self-inductances of the Tx and Rx coil were measured by an Agilent E4980 LCR meter.

TABLE 5.4
WPT Coil Specifications

Parameters	Value	Parameters	Value
r_T,r_R	22.5 cm	r_i	22.5 - $0.5 \cdot (i-1)$ cm
L_T	108.8 μH	$d_{T:R}$	20 cm
L_R	108.4 μH	$d_{T:i}$	2.5 cm

r_T, r_R, r_i: the radii of the Tx, Rx, and sense coils
L_T, L_R: the self-inductance of the Tx (Rx) coil
$d_{T:R}$: the distance between the Tx and Rx coil (center to center)
$d_{T:i}$: the distance between the Tx (center) and sense coils
i: the index of the sense coils

TABLE 5.5
Current-Mode Class D Converters Components

Parameters	Value	Parameters	Value
SiC MOSFET	C3M0075120K	Resonant Capacitors	32 nF
Gate Driver	UCC21530	Switching Frequency	85 kHz

1.2 kV SiC MOSFETs were used to block the 1 kV drain voltages. Table 5.5 lists the components specifications. The resonant capacitors were chosen to carry the nearly 12 A_{rms} current. Fig. 5.21 shows the Tx and Rx coil voltages and currents that demonstrate kW-level WPT, driven by two CMCD converters. Note that V_{TX} and $-I_{RX}$ (current into the receiver) are nearly in phase to deliver real power from the transmitter to the receiver.

The FC-TPM system was built as shown in Fig. 5.22. Current transformers (Pearson Model 110) were used to measure the Tx and Rx coil currents. The Tx and Rx coil current, and sense coil voltage data were each 16 megasample recordings on an Elsys TraNET 204E with a TCPE-8016-4S data acquisition system at 20 Msamples/s, 16-bit resolution; Fig. 5.23 shows the recorded coil currents and sense coil voltages.

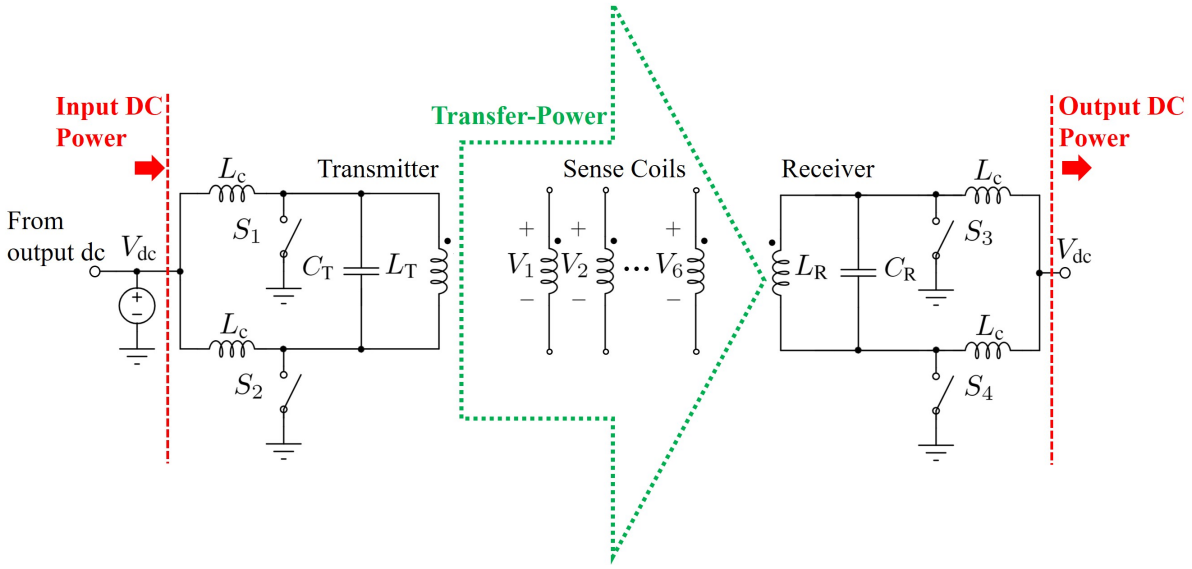

Figure 5.19. Current-mode class D wireless power transfer system with open-circuited FC-TPM sense coils. DC current was recirculated with the input and output voltage held fixed.

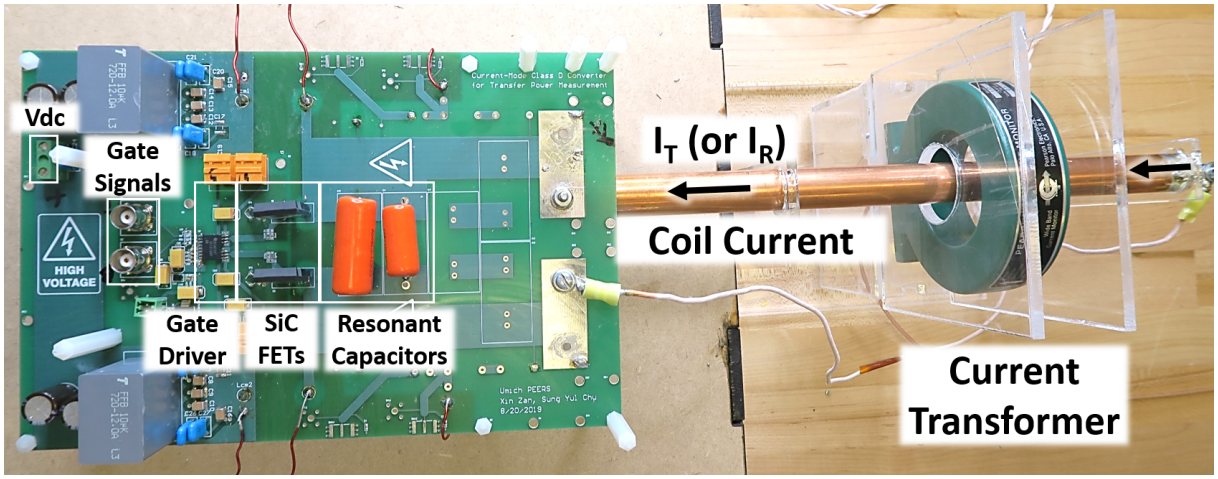

Figure 5.20. 1 kW current-mode class D converters were designed to drive the WPT coils. A Pearson current transformer (CT) was used to measure the Tx and Rx coil current using a rigid copper tube at the center of the CT to maintain accuracy.

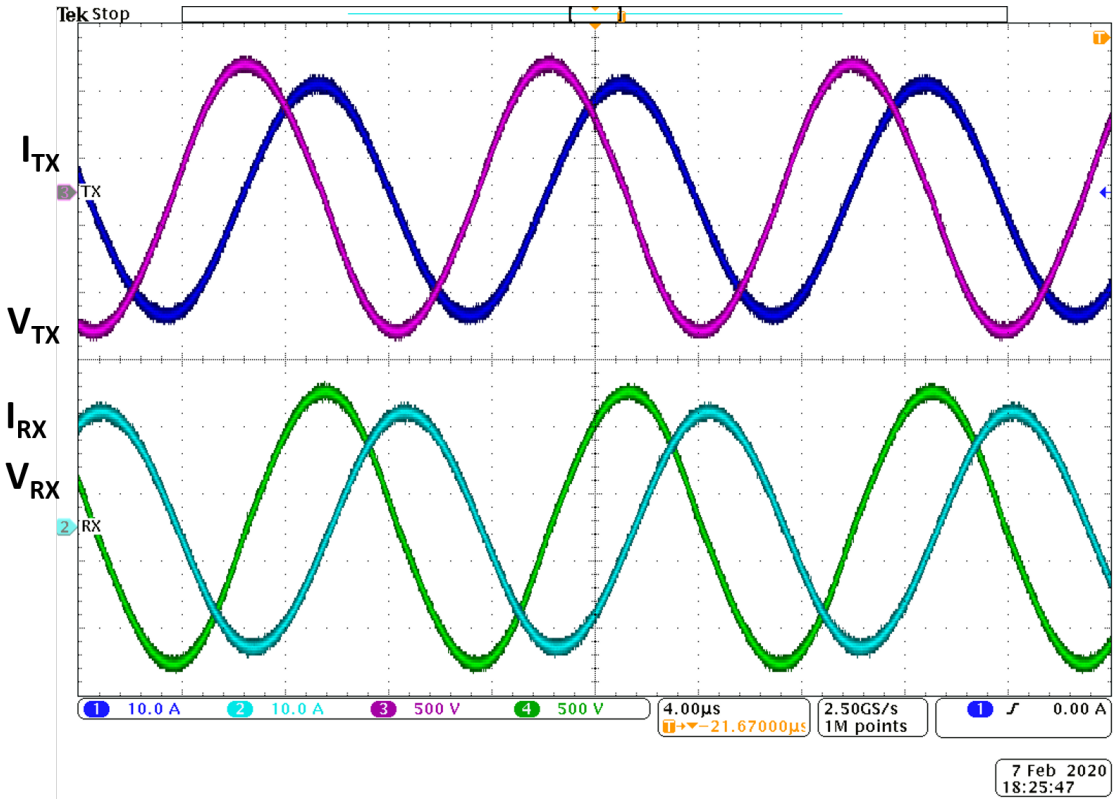

Figure 5.21. Tx and Rx coil voltages and currents driven by CMCD converters.

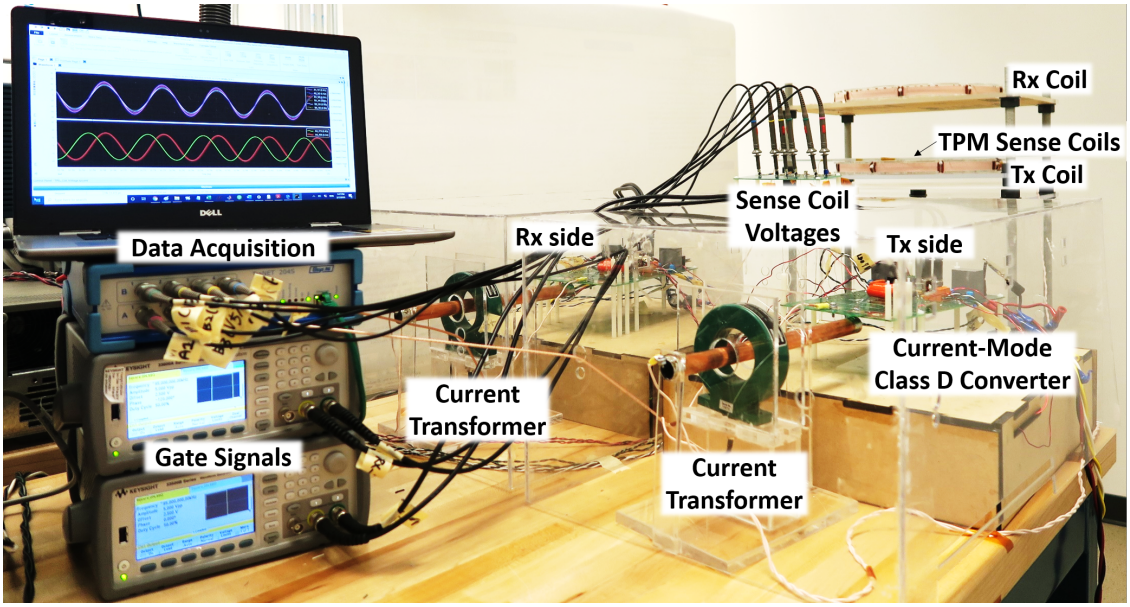

Figure 5.22. Faraday coil transfer-power measurement (FC-TPM) test system.

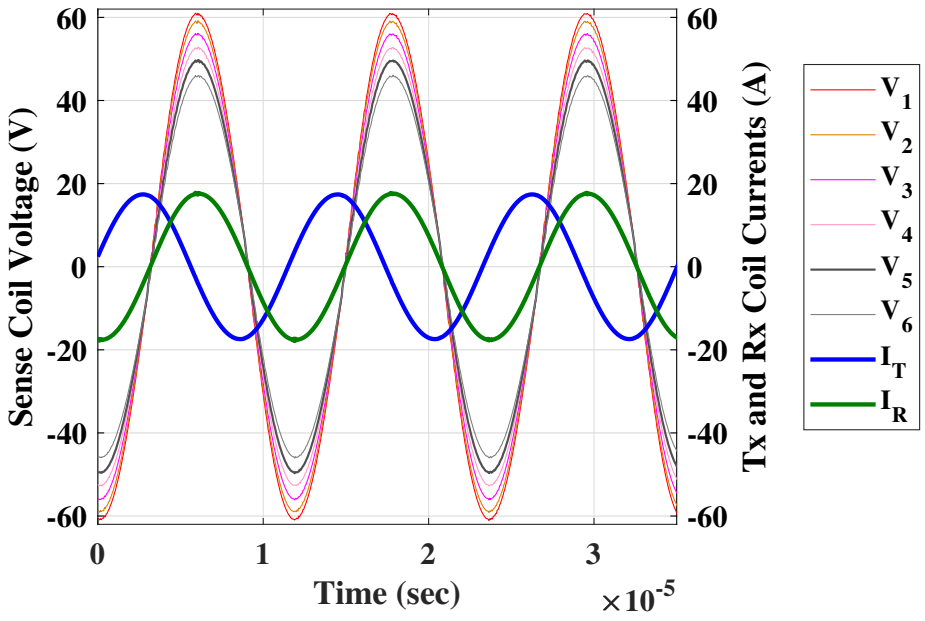

Figure 5.23. Sense coil voltages and Tx, Rx coil currents were measured and recorded by a 20 Msamples/s, 16-bit data acquisition system for FC-TPM.

5.5.1 FC-TPM with Two Sense Coils

We show FC-TPM can be demonstrated in hardware by confirming that the transfer-power can be accurately determined by using sense coil voltages together with calibrated geometric parameters. Using aligned and stationary Tx and Rx coils, we examined the accuracy from using only two sense coils (22.5 and 17.5 cm radii).

Only one single geometric parameter (2.51) needed to be calibrated using the least-squares minimization in Section 3.3.3 performed over load. The data space spanned a variation in transfer-power by sweeping the phase difference between Tx and Rx coil currents at constant amplitude.[19] The reference standard transfer-power was measured simultaneously as described in Section 5.4.

LOOCV (leave-one-out cross-validation) was used to validate the accuracy of FC-TPM; the geometric parameter was determined by the calibration set (9 data points), the transfer-power of the validation set (1 data point) was determined from (2.50), and the reconstruction errors in (3.19)

[19]We varied the phase of the Rx coil drain voltages over 10 data points, resulting in changes in the coil currents, which corresponds to different equivalent output load resistances in Rx.

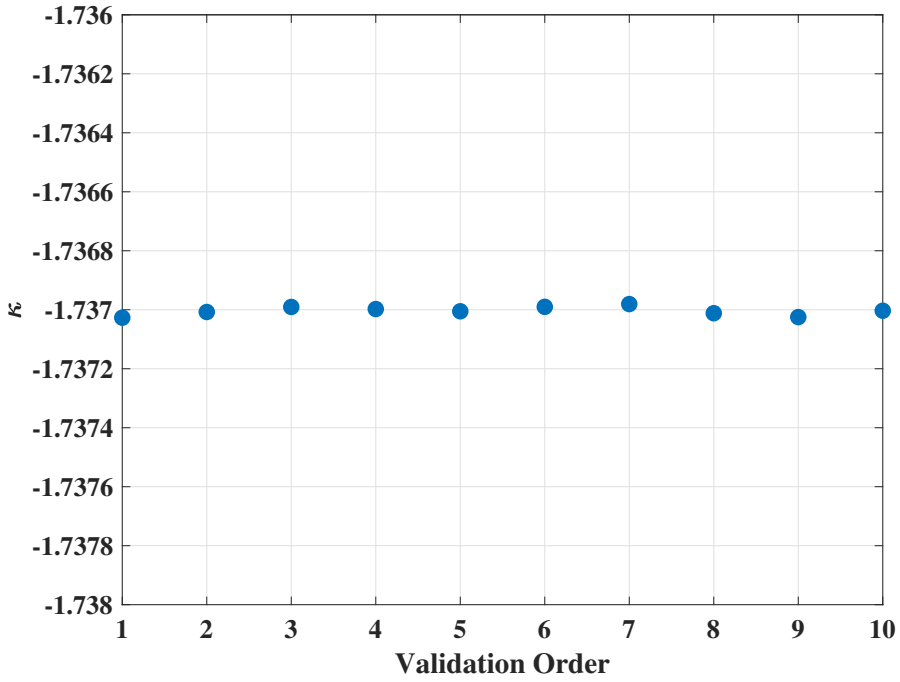

Figure 5.24. The geometric parameter is calibrated using the calibration set (9 data points) for each validation set. In this hardware demonstration, the calibration is repeated 10 times for each validation data point using corresponding different calibration set.

were calculated based on the test procedures, which are shown in Fig. 5.15. For example, suppose each data point is numbered consecutively from one to ten. In that case, the geometric parameter is calibrated to validate data 1 using the calibration set, which consists of data 2 to 10. Similarly, the calibration is performed using data 1 and data 3 to 10 for the validation of data 2. Fig. 5.24 shows that the geometric parameter calibrated for each validation cycle is nearly consistent.

The FC-TPM errors are shown in Fig. 5.25b. The hardware errors ranged from -0.009% to 0.015%. By using the appropriate litz wire in our WPT coils, eddy currents can be made negligible. In Fig. 5.25, two sense coils (22.5 and 17.5 cm radii) were used for the FC-TPM of aligned WPT coils described above. Calibrated principal transfer-power using (2.49) is shown for solid wire in COMSOL FEM simulation in Fig. 5.25a and litz wire in hardware in Fig. 5.25b. From Section 3.4.2, using two sense coils for FC-TPM when there are eddy current losses in the WPT coils result in non-negligible errors. This is manifested in the solid wire in Fig. 5.25a as a systematic error with increasing transfer-power; this systematic error can be interpreted as the error

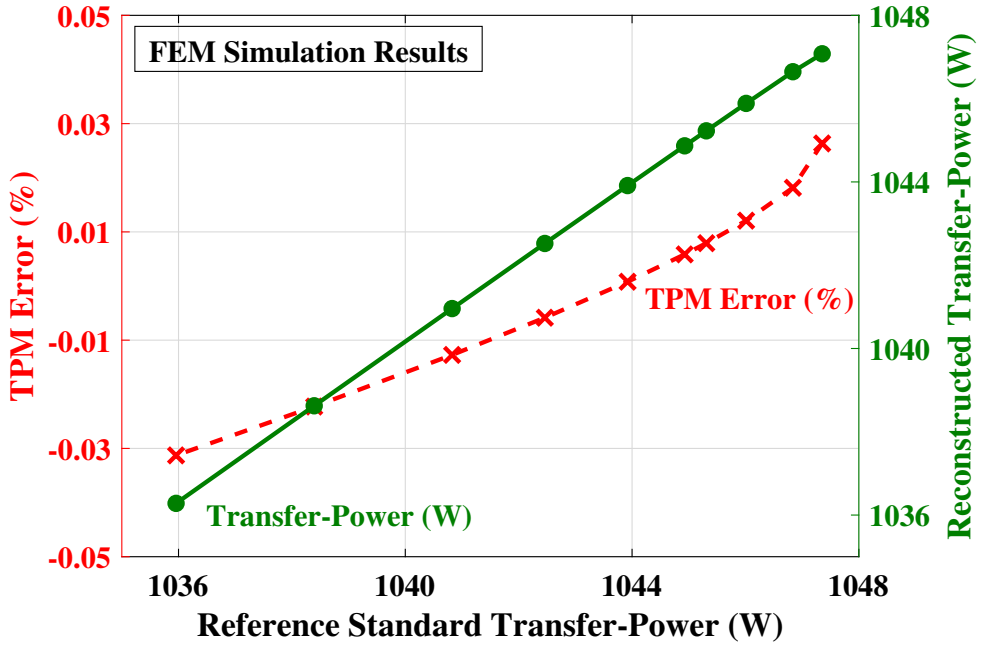

(a) COMSOL FEM results for solid-wire Tx and Rx coils.

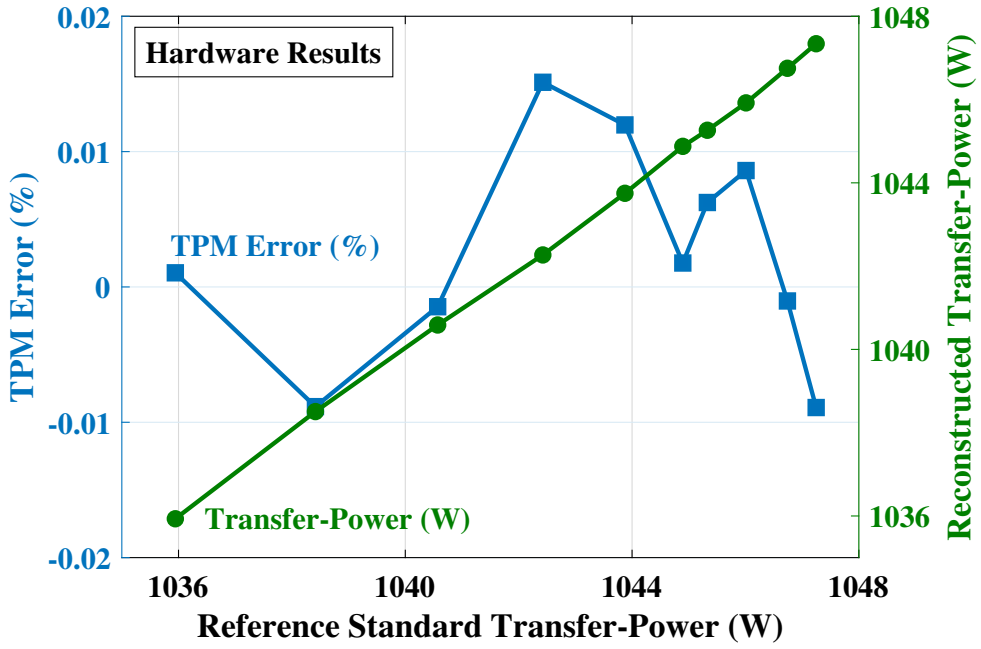

(b) Hardware results of FC-TPM for an aligned Rx coil. Reconstructed transfer-power through FC-TPM is compared with the reference standard transfer-power at each validation point.

Figure 5.25. Solid wire and litz wire are compared for Tx and Rx coils using FEM and hardware for principal FC-TPM.

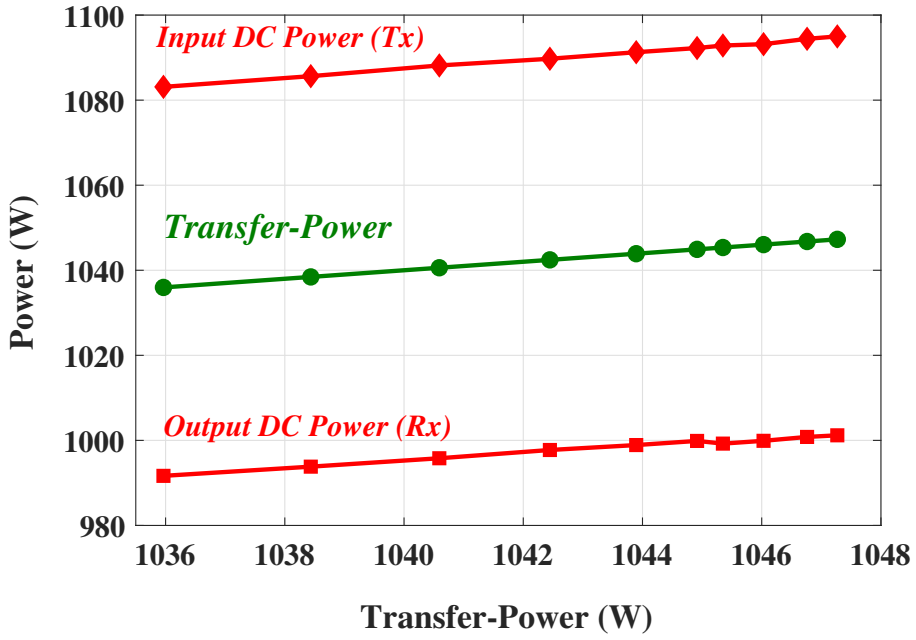

Figure 5.26. Transfer-power is compared to dc input and output power measured at the electrical terminals. Terminal power is fundamentally not the same as transfer-power.

from the excess loss imposed by the additional eddy current winding in the transformer model in Section 3.4.2.1. Fig. 5.25b shows errors that can be attributed in part to measurement and reference standard calibration that includes sensor error, noise, and digital quantization.

The transfer-power is also compared in Fig. 5.26 to the input and output dc power to highlight and demonstrate the principle that measuring transfer-power disaggregates the Tx and Rx losses to enable fair metering.

FC-TPM was also demonstrated over a wide range of power levels as illustrated in Fig. 5.27, where the error is less than 0.1% (-0.011% to 0.096%) from 60 W to 1 kW.

5.5.2 FC-TPM Over Misalignment

We demonstrated FC-TPM over Rx coil misalignment using six sense coils (radii from 20 to 22.5 cm at 0.5 cm intervals). The Rx coil was misaligned[20] by up to 10 cm (6 data points: 0 to 10 cm at 2 cm intervals), as shown in Fig. 5.28. The data matrix $\mathbf{W}$ and vector $\mathbf{p}$ spans six mis-

[20]Specified in SAE J2954 [45].

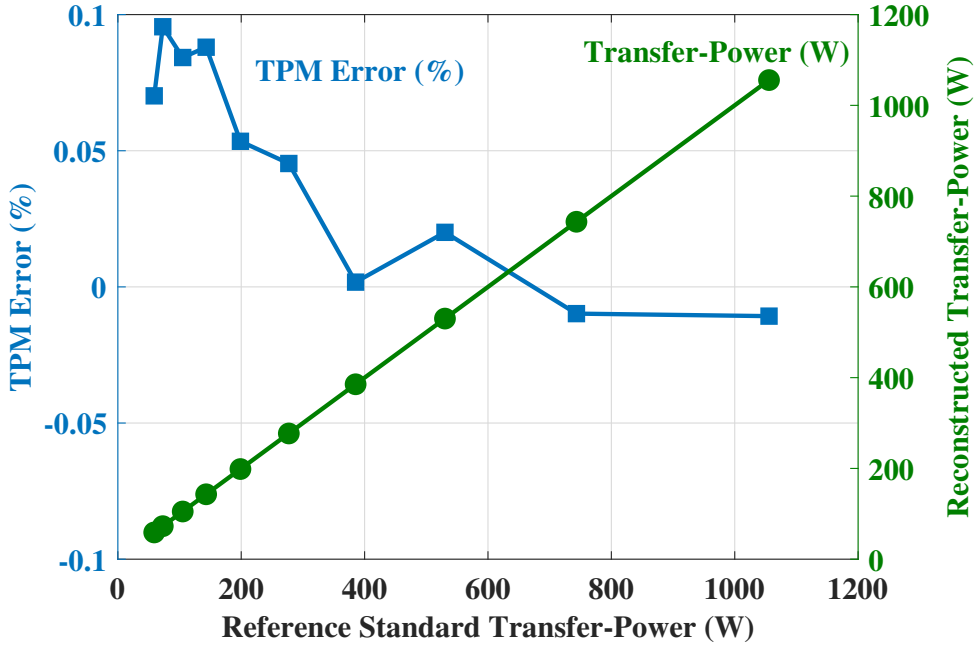

Figure 5.27. FC-TPM was demonstrated in hardware over a wide range of power levels.

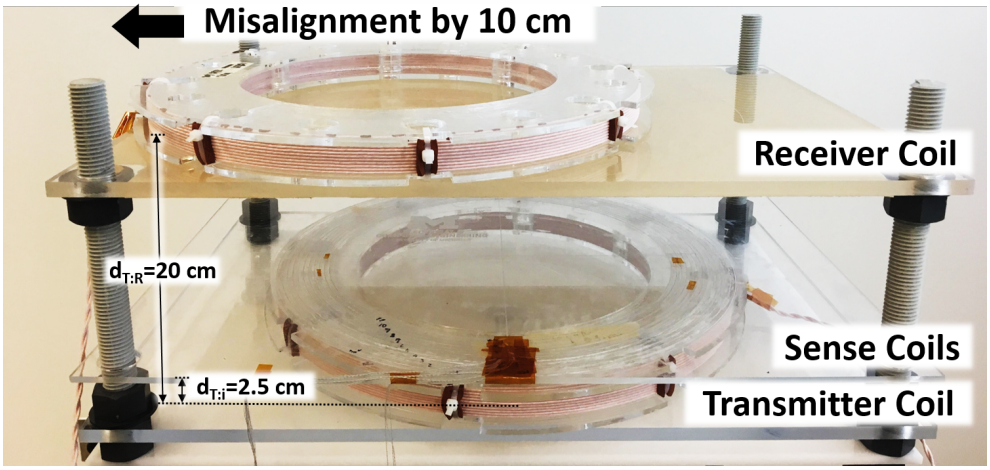

Figure 5.28. Faraday coil transfer-power measurement was demonstrated over SAE J2954 Rx coil misalignment.

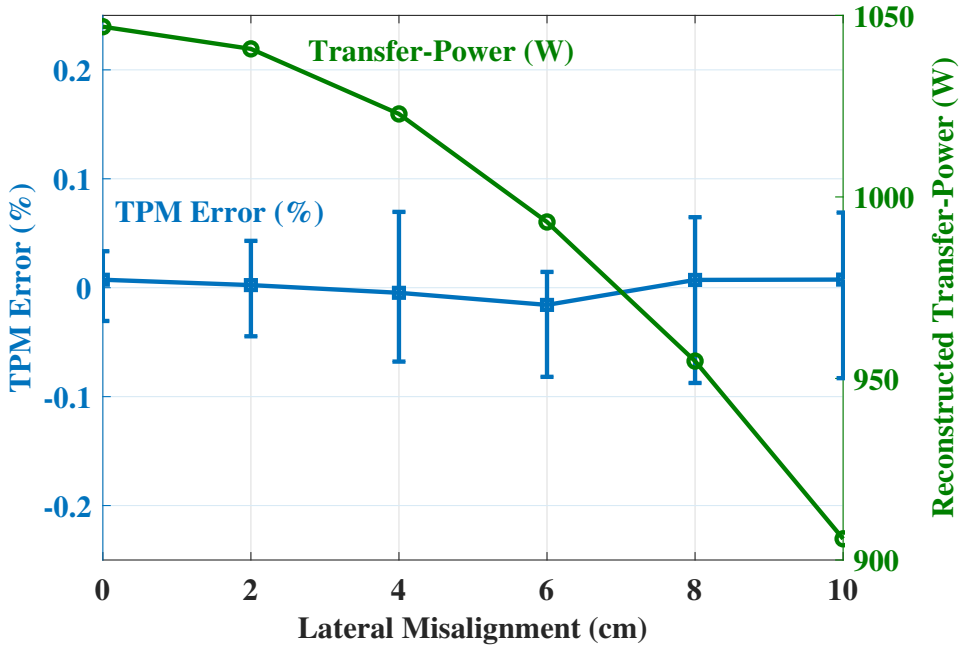

Figure 5.29. Hardware results for FC-TPM errors over Rx coil misalignment. The transfer-power can be determined accurately despite misalignment.

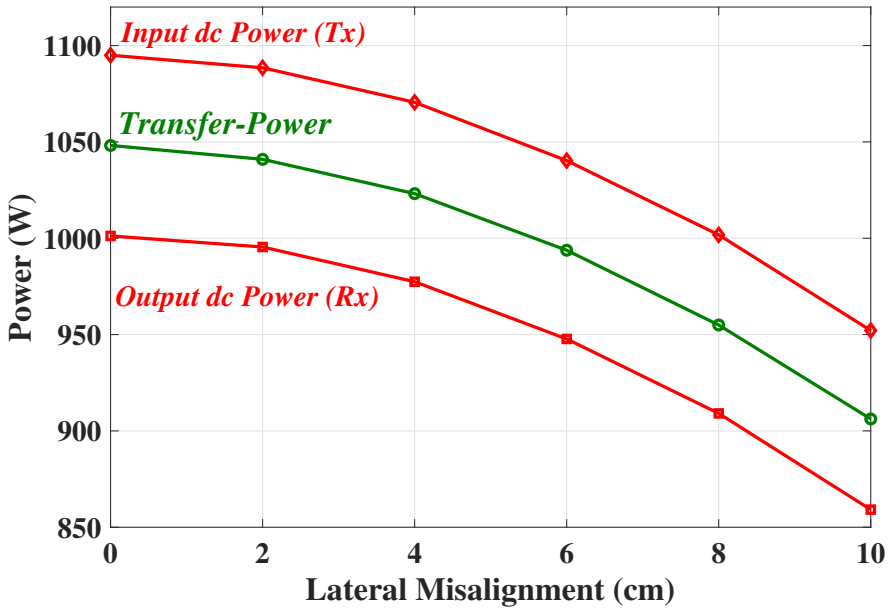

Figure 5.30. Hardware Results: FC-TPM disaggregates the Tx and Rx losses over misalignment.

alignment values and ten Tx-Rx coil current phase differences to calibrate the geometric parameters α_{ij} according to (3.18). The percentage FC-TPM errors ϵ at each validation data point were calculated with (3.19) and plotted in Fig. 5.29. The error bars represent the range of errors at each misalignment point. The errors ranged from -0.087% to 0.07% and were very nearly consistent, demonstrating accurate FC-TPM over misalignment. It is worth noting that the explicit measurement of misalignment was not needed either for calibration or transfer-power estimation because the sense coil voltages and the constant geometric parameters encapsulate all the necessary information. The transfer-power is compared to the input and output dc power over misalignment in

TABLE 5.6
Input,Transfer, and Output Power Over Misalignment

Misalignment (cm)	Input DC Power (W)	Transfer-Power (W)	Output DC Power (W)
0	1,095	1,047	1,001
2	1,088	1,041	995.5
4	1,070	1,022	977.4
6	1,040	993.1	947.7
8	1,001	954.8	909.1
10	952.1	906.0	859.2

Table 5.6 and Fig. 5.30.

The dependence of FC-TPM errors to different numbers (from two to six) of sense coils were investigated. Fig. 5.31 shows the worst-case absolute error percentage of FC-TPM at 1 kW, as defined in (3.22), of 10 data point variations in Tx-Rx coil current phase difference at each misalignment point. The greater the number of sense coils, the smaller the FC-TPM errors, which is expected because more information is available to determine the transfer-power over misalignment.

The geometric parameters which correspond to each validation data point are plotted in Fig. 5.32. For example, suppose each data point is numbered consecutively from 1 to 60. In that case, the geometric parameters are calibrated to validate data 1 using the calibration set, which consists of data 2 to 60. The geometric parameters α_{ij} are generally consistent but having some variations over the validation data points. As having seen from (3.14), (3.15), and (3.18), the system is overdetermined

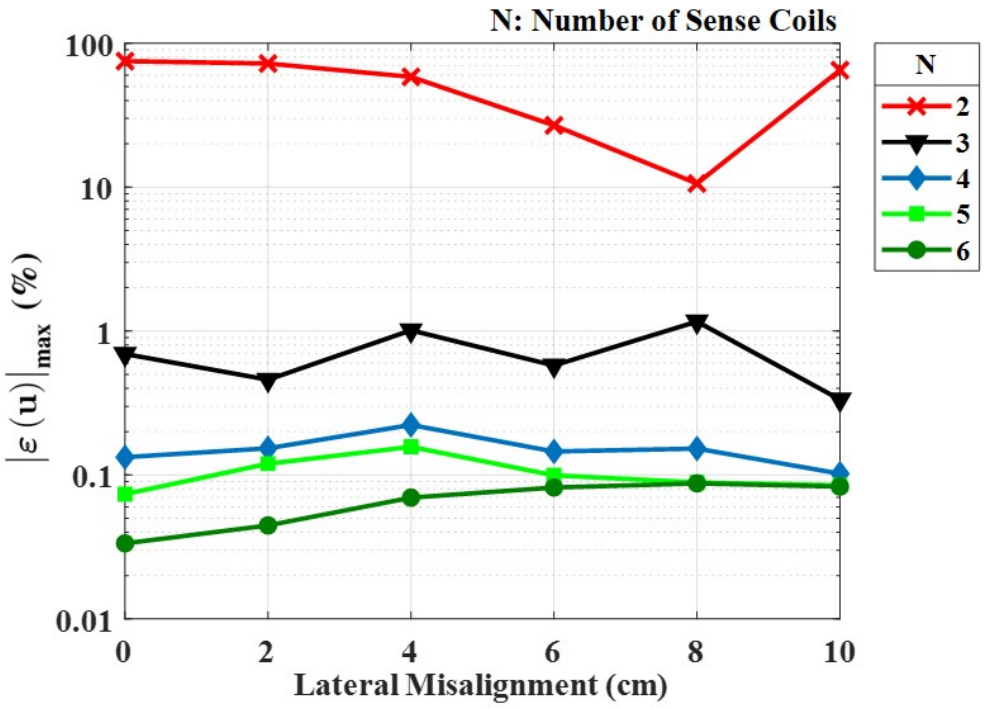

Figure 5.31. Hardware Results: FC-TPM accuracy was verified for different numbers of sense coils. An increasing number of sense coils results in more information and therefore better accuracy.

resulting in existence of multiple α_{ij} for different validation data points. In other words, over some errors ϵ, the solutions can be multiples that satisfy the least-squares simultaneously. The geometric parameters can be potentially further consistent when the information diversity, presented in Section 4.2, is secured through an optimal sense coil placement. In addition, the geometric parameters were calibrated using 60 data points all at once, as a comparison to the results using LOOCV. Each α_{ij}, which are fixed over 60 data points, solid-lines in Fig. 5.33a, is used to reconstruct the transfer-power for each validation point, and the FC-TPM errors are plotted in Fig. 5.33b; a single set of geometric parameters (solid lines) over 60 data points also results in accurate FC-TPM over misalignment.

5.5.3 Numerical Error Analysis of FC-TPM for Noise in Measurements

Noise in the measurement causes error in the transfer-power measurement. This is because the calibration of FC-TPM uses the least-squares in (3.18) from the measured sense coil voltages

Figure 5.32. The geometric parameters for six sense coils over misalignment were calibrated using the calibration set (59 data points) for each validation data point. In this hardware demonstration, the calibration was repeated 60 times for each validation data point using a corresponding different calibration set. The TPM Error for each validation point was calculated in Fig. 5.29.

as well as the Tx and Rx coil currents to calculate the reference standard transfer-power in (5.9). FC-TPM errors were numerically analyzed to explain the hardware results when each measurement of the signal has a certain noise. The additive white Gaussian noise (AWGN) was added to each sense coil voltage, Tx and Rx coil currents equally, which were obtained by the numerical model used in Section 3.3.3.3, where the coplanar sense coils, shown in Table 5.4 were used. FC-TPM errors were evaluated for different signal-to-noise ratio (SNR) and different numbers of sense coils using LOOCV, as shown in Section 3.3.3. Fig. 5.34 shows the FC-TPM errors that were the worst-case absolute error percentage, defined in (3.22), where $\mathbf{u}_k = \begin{bmatrix} \text{SNR} & x_k & Z_k \end{bmatrix}$; in other words, the worst-case percentage error over misalignment and load variations at each SNR was calculated. As SNR increases, the errors are saturated to the noise-free model error, shown in Fig. 3.12 . As SNR decreases, FC-TPM error increases, indicating that the error can be lower bounded based on the measurements' noise.

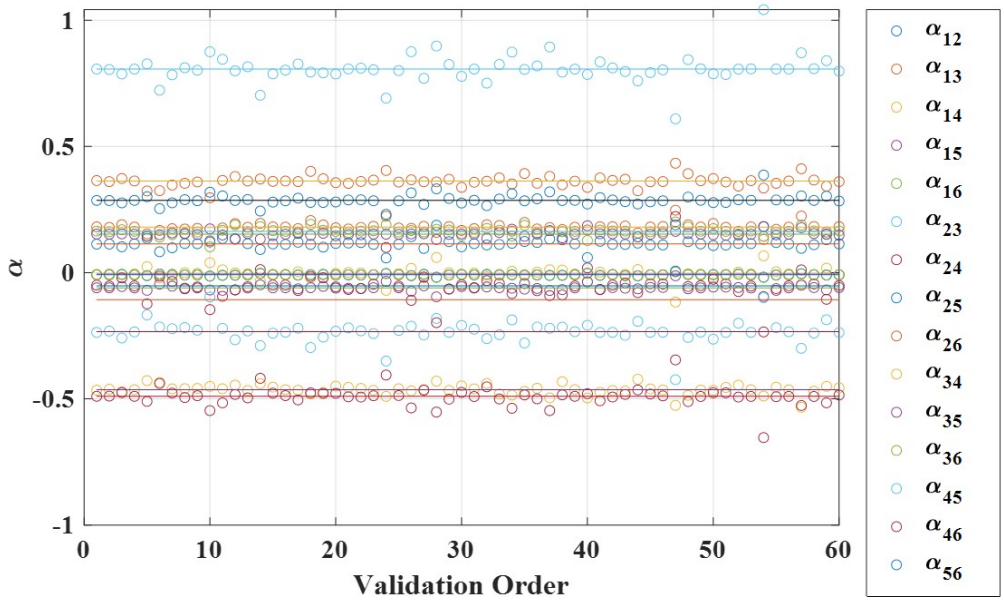

(a) Solid lines represent the fixed geometric parameters calibrated using all 60 data points together. The solid lines were compared to the circle-dots in Fig. 5.32, geometric parameters obtained using LOOCV.

(b) Using the fixed geometric parameters, which were the same for 60 data points, FC-TPM errors were calculated. Fixed geometric parameters over 60 data points also result in accurate FC-TPM over misalignment.

Figure 5.33. The geometric parameters α_{ij} were calibrated using all 60 data points together as a comparison to the results from LOOCV. And then, the FC-TPM errors were calculated using the geometric parameters for the 60 data points.

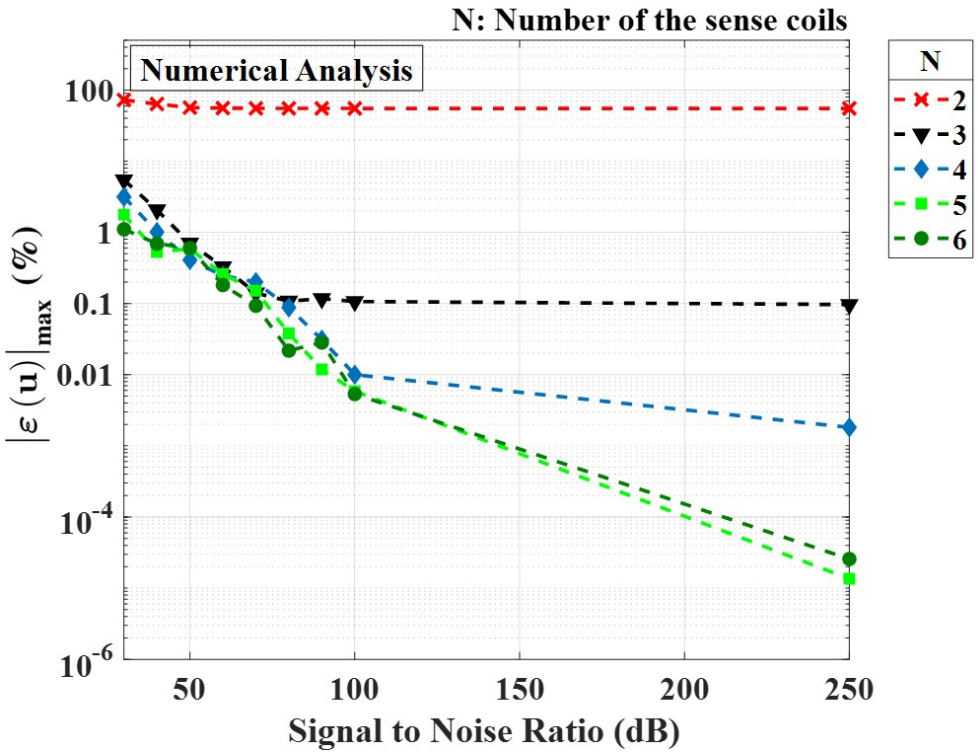

Figure 5.34. FC-TPM errors were numerically analyzed to the signal to noise ratio of the measurement of the Tx, Rx coil currents and sense coil voltages.

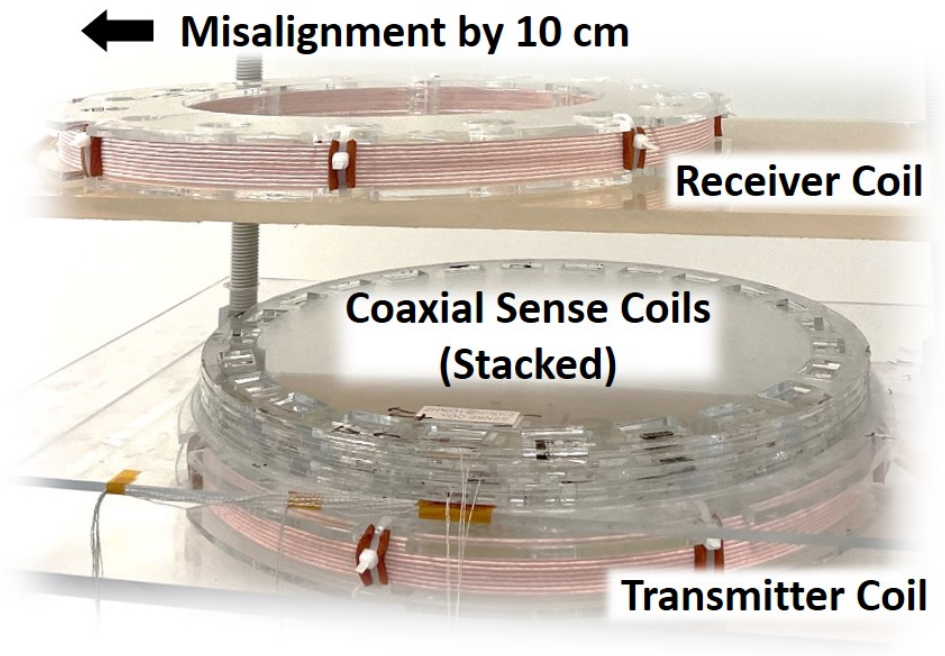

Figure 5.35. FC-TPM was demonstrated over Rx coil misalignment when coaxially stacked sense coils were used.

5.5.4 Performance Comparison to Coaxially Stacked Sense Coils

We replaced the coplanar sense coils with coaxially stacked sense coils, as illustrated in Fig. 5.35, to show the comparable performance of FC-TPM using the two different sense coil configurations. First, we examined the accuracy of using two 22.5 cm radii sense coils, which are coaxially stacked 3.5 cm and 7.5 cm above the Tx coil, respectively. A total of 10 data points using different equivalent output load resistances were validated, and Fig. 5.36 shows the hardware results; the FC-TPM errors ranged from -0.011% to 0.009%, which are comparable to the errors from using coplanar sense coils in Fig. 5.25b.

We also demonstrated FC-TPM over Rx coil misalignment using six coaxially stacked sense coils (vertical distances above the Tx coil from 3 cm to 5.5 cm at 0.5 cm intervals), as shown in Fig. 5.35. Fig. 5.37 shows the percentage error, where the error bars represent the range of error at each misalignment point. The errors ranged from -0.082% to 0.071%, which are comparable to the errors from using coplanar sense coils in Fig. 5.29.

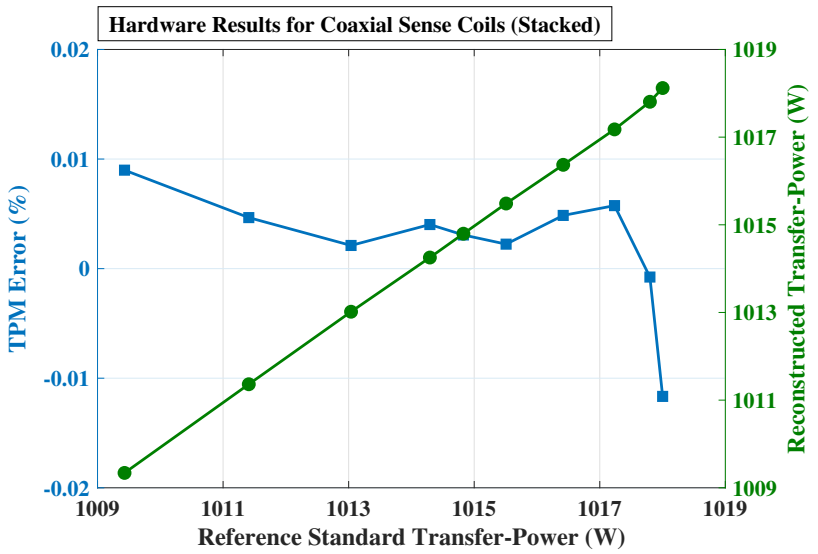

Figure 5.36. Hardware results for FC-TPM errors for an aligned Rx coil when the coaxial sense coils are vertically stacked. The performance is comparable to that of the coplanar sense coils.

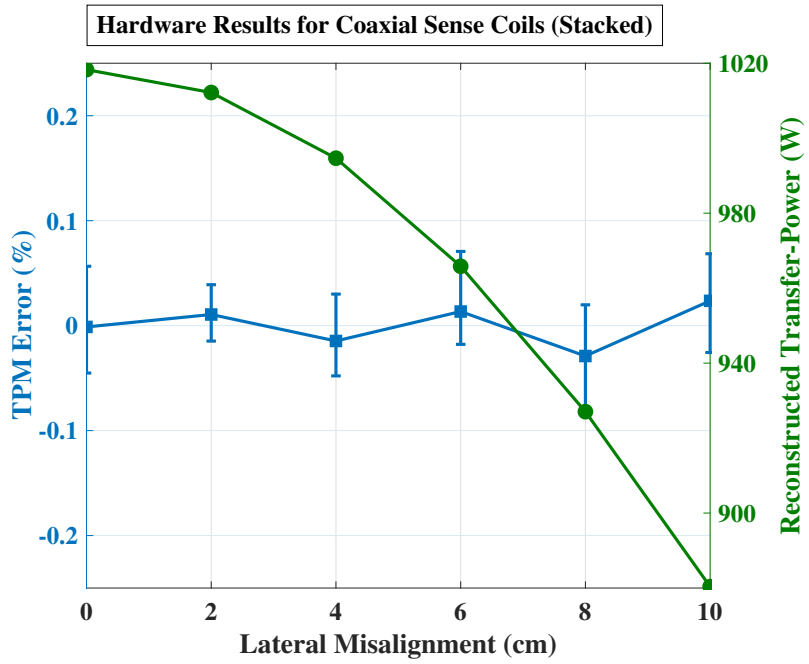

Figure 5.37. Hardware results for FC-TPM errors over Rx coil misalignment when the coaxial sense coils are vertically stacked. The performance is comparable to that of the coplanar sense coils.

5.5.5 Future Implementation

Sense coils are the primary sensors, single-turn and open-circuited; conductors can be direct-printed on an insulator like FR4 and thus inherently inexpensive and straightforward to manufacture. Commercial off-the-shelf (COTS) analog-to-digital converters (ADCs) can be used to measure the sense coil voltages, and a field-programmable gate array (FPGA) can process the data. A digital signal processing (DSP) microcontroller (MCU) can control the measurements and communicate with other devices. The hardware cost is expected to be similar to typical measurement systems [38; 90; 91; 92] including those planned for metering in the NIST-sponsored U.S. National Work Group (USNWG) on Measuring Systems for Electric Vehicle Fueling and Submetering (EVF&S) [93]. Furthermore, the non-contact method of FC-TPM has an additional cost savings in that the high voltage safety and insulation that is required for typical terminal voltage and power measurements is not needed.

CHAPTER 6

Electromagnetic Model-Based Foreign Object Detection for Wireless Power Transfer

Foreign objects near wireless power transfer (WPT) systems are fire hazards that must be detected. In this chapter, an accurate method is presented for foreign object detection based on an electromagnetic model for WPT. Foreign objects are detected by quantifying the deviation from a normal model. This deviation is caused by the foreign object's additional electromagnetic coupling. Advantages of this method include invariance to receiver coil misalignment, and power level, allowing low-power detection prior to startup. Electromagnetic model-based foreign object detection (EM-FOD) was demonstrated in hardware to detect a 2 cm diameter U.S. nickel coin in a kilowatt-level wireless power transfer system, using a pre-startup power of only 9 W. Furthermore, foreign objects can be detected regardless of an Rx coil misalignment of up to 10 cm.

6.1 Chapter Introduction

Safety is vital in transportation. Wireless charging for electric vehicles has unique safety concerns in that a strong time-varying electromagnetic field for power transfer can threaten passenger safety. Foreign objects near magnetic wireless power transfer systems are one fire hazard because they can heat from eddy currents and cause a fire. In this Chapter, an accurate and low-power low-risk foreign object detection is presented for safe wireless power transfer.

When foreign objects encroach (Fig. 1.3), they perturb the electromagnetic field from that gen-

erated by the transmitter (Tx) and receiver (Rx) coil currents alone. This disturbance is used to derive a metric for FOD. An accurate electromagnetic model of magnetic WPT had been presented in Chapter 2, 3, 4, and 5 for Faraday coil transfer-power measurement (FC-TPM), which consists of the Tx, Rx, and sense coils. A transformer model for the WPT coil voltages and currents is derived from the electromagnetic field, which can be reconstructed from a linear combination of sense coil voltages. We use this model as the *normal model*, which we extend to the *adverse model* by the inclusion of electromagnetic coupling from foreign objects. The deviation of the adverse model from the normal model, then indicates the measure of disturbance. This *normal model* is generally applicable to magnetic WPT [94], which has been shown to be invariant to power and Rx coil misalignment [95], thus making this electromagnetic model-based FOD (EM-FOD) appealing. Model-based fault detection, which is effective, reliable, and easily integrated with the existing systems, can be found in other applications such as switching power converters [96].

Several methods for FOD have been previously presented including using differences in the induced voltages of sets of sense coils [43; 44; 97; 98; 99; 100], the impedance of the sensing patterns [101], the quality factor of the Rx coil [102], power or eddy current loss estimation [103; 104; 105], and variation in the Tx and Rx coil voltages and currents [106; 107; 108]. Lidar devices [109], radar sensors [110], thermal cameras [111], video sensors [112], cameras and image processing [113], and machine learning for reflection coefficient variation [114] are also used for foreign object detection in wireless power transfer.

There are challenges to these methods including: (i) risks in needing to resolve potentially small unsafe foreign objects by operating charging coils at high power for methods that directly use the voltage and current output of an electromagnetic sensor (e.g., sense coils); (ii) large, expensive, or layered sensor arrays or grids to cover the area of interest if specific positions or coordinates are needed to identify the variations; (iii) detection metrics that vary over Rx coil misalignment, which changes electromagnetic coupling hence affecting sensor impedance, mutual inductance, and power (or loss); (iv) blind zones from sensor array symmetries such as with magnetically induced voltage differences between symmetric coil configurations; and (v) expensive auxiliary

systems with potential vulnerabilities to fouling, including cameras or image sensors to identify foreign objects through image detection.

EM-FOD employs two open-circuited single-turn sense coils to reconstruct the Tx coil current. For the reconstruction, sense coil voltages and geometric parameters, which encapsulate the electromagnetic couplings between the Tx, Rx, and sense coils, are required. When there is a foreign object, the Tx coil current reconstruction is no longer accurate because the geometric parameters do not represent the additional coupling from the eddy winding in the foreign object; this results in a *sequent error*. The true Tx coil current is separately measured and compared to the reconstructed Tx coil current; the additional reconstruction error or *sequent error* results from a foreign object because of additional electromagnetic coupling, hence becoming useful as the detection metric. Furthermore, by employing a few more sense coils (e.g., five sense coils), foreign objects can be detected accurately over Rx coil misalignment, where only sense coil voltages and Tx coil current are required to be measured.

EM-FOD has advantages which overcome the challenges of existing methods, including: (i) invariance to output loads, hence also power level, allowing low-power tests prior to startup; (ii) invariance to coil misalignment; (iii) wide dynamic range; (iv) small number and small-sized sense coils whose electromagnetic contribution is negligible; (v) cost-effectiveness—using the same sense coils for metering (FC-TPM); (vi) no sensitivity dead-zones; all foreign objects within the electromagnetic space of WPT can be detected; (vii) access is unneeded to the Rx coil current and voltage (on a mobile EV); only the Tx coil current is required, which is stationary.

This chapter is organized as follows. Section 6.2 introduces the strategy of the electromagnetic foreign object detection (EM-FOD). Section 6.3 presents the theory of EM-FOD, specifically the theory of Tx coil current reconstruction and using the *sequent error* as a detection metric for a foreign object are mathematically presented. Section 6.4 demonstrates EM-FOD using finite element method (FEM) simulations by showing the sequent errors in the Tx coil current reconstruction due to various foreign objects. Section 6.5 presents the theory of accurate Tx coil current reconstruction over Rx coil misalignment when multiple sense coils are employed. Section 6.6 demonstrates an

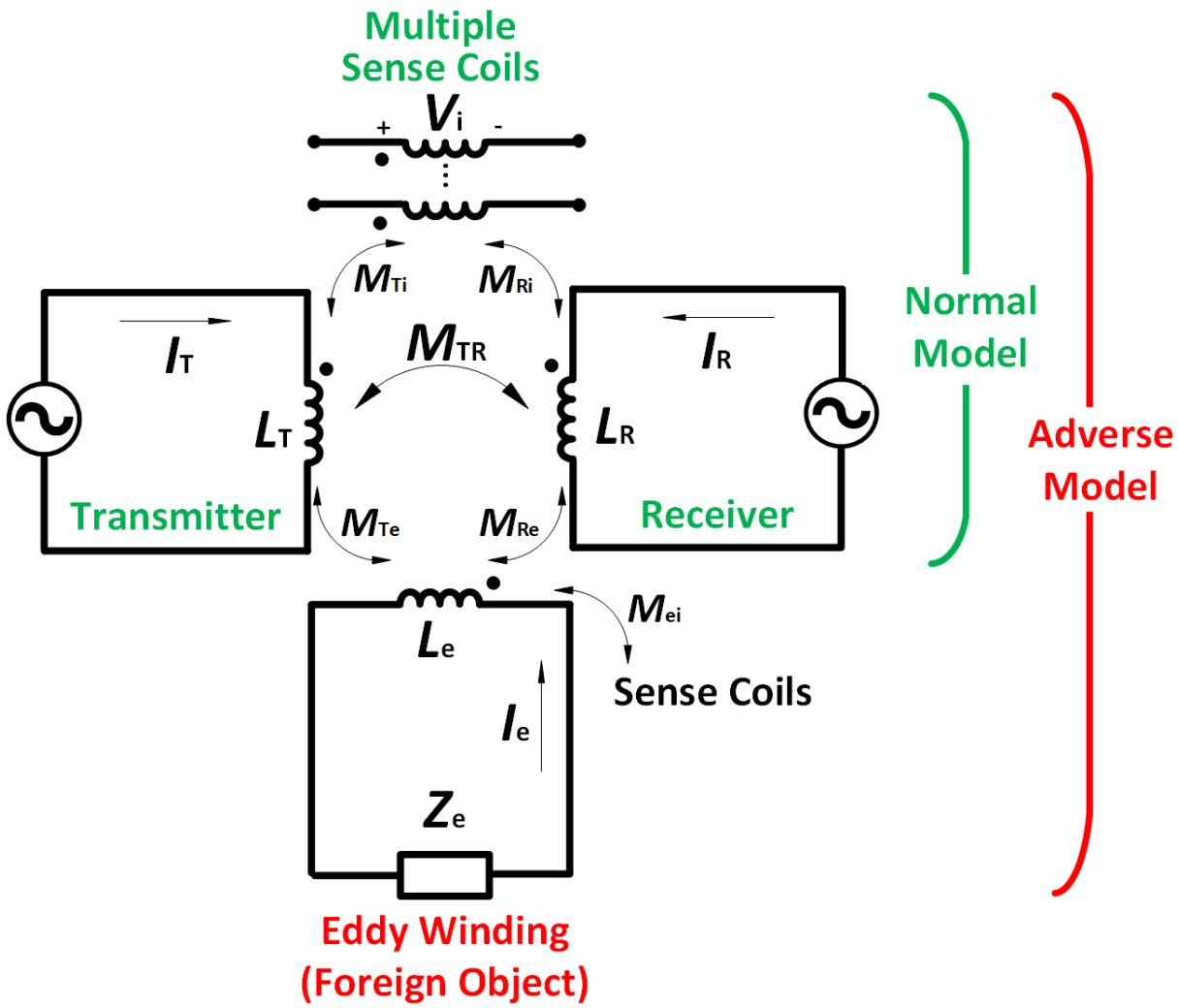

Figure 6.1. The normal transformer model consists of the Tx, Rx, and sense coils. A foreign object causes an adverse model. The eddy currents in the Tx and Rx coil currents are omitted in this diagram for simplicity.

accurate EM-FOD at low operating power, which is low-risk. Section 6.7 demonstrates EM-FOD in hardware over a standardized Rx coil misalignment of up to 10 cm.

6.2 Foreign Object Detection Strategy

Foreign objects can be detected by quantifying the deviation from the normal electromagnetic model for WPT. Fig. 6.1 shows the *normal model* presented in [94] along with the extension to the *adverse model* that includes the electromagnetic coupling of a foreign object.

The *normal model* includes the Tx, Rx, and sense coils. The variables in the model are the Tx and Rx coil voltages and currents, which are derived from the electromagnetic field; a linear combination of sense coil voltages can reconstruct these voltages and currents, as derived in (2.47) and [94].

The coupling between a foreign object and other coils can be analyzed by an eddy current winding model; the eddy current in the foreign object can be modeled as a transformer winding [50; 51], as shown in Fig. 6.1. The deviation of the *adverse model* from the *normal model* can then be quantified (discussed further in Section 6.3). The geometric parameters are the coefficients used to reconstruct the Tx coil current from the linear combination of sense coil voltages, which contain a *sequent error* in the *adverse model*. The Tx coil current is chosen as the variable for comparison because: (i) the Tx coil is stationary, inaccessible to users, and thus secure; (ii) the alternative of using the voltage measured at the electrical terminal of the coil results in an inaccurate reconstruction of the model because it contains not only the coil voltage but also the voltage drops from winding and eddy losses [41; 115]; (iii) the Tx coil current can be reconstructed by non-varying geometric parameters regardless of Rx coil misalignment. EM-FOD is practical for charging stations in that only sense coil voltages are required to be measured with a straightforward calibration of the geometric parameters in advance.

Calibration of the geometric parameters is initially performed in the *normal model* (no foreign objects); the parameters implicitly contain the magnetic and geometric information among the Tx, Rx, and sense coils. After calibration, EM-FOD uses measurements of the Tx coil current and sense coil voltages. Tx coil current is reconstructed from a linear combination of the sense coil voltages using the pre-calibrated (no foreign objects) geometric parameters. Foreign objects are detected from the sequent error between the measured and reconstructed Tx coil current; a foreign object in the electromagnetic space causes a sequent error from the additional coupling between the foreign object and other coils. Fig. 6.2 shows the EM-FOD strategy with the *sequent error* in the Tx coil current reconstruction as the detection metric.

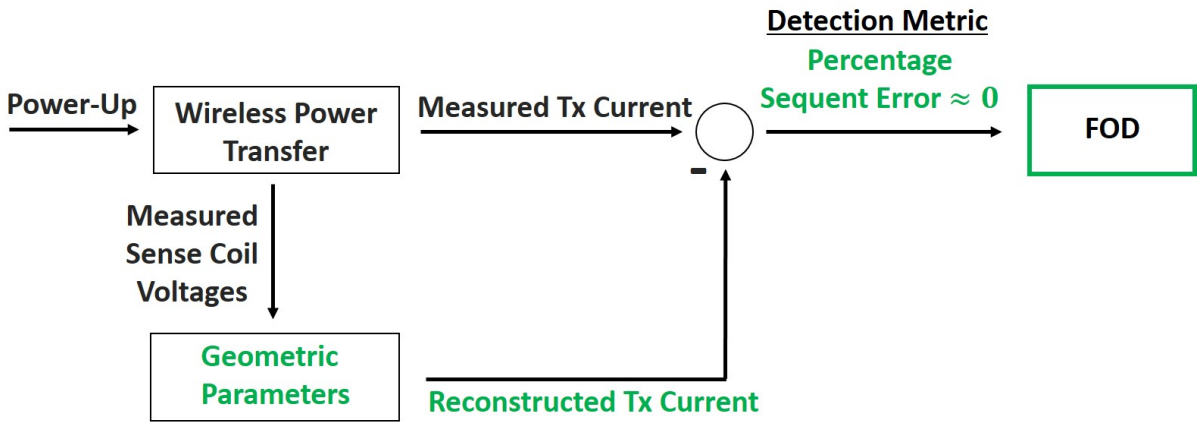

(a) The Tx coil current is reconstructed accurately with no sequent error when there is no foreign object.

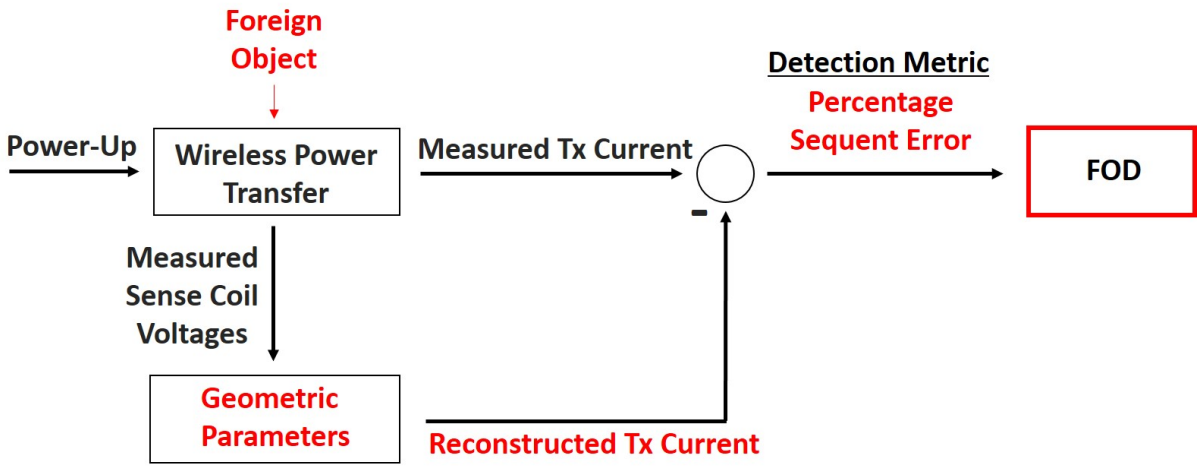

(b) When there is a foreign object, the Tx coil current reconstruction contains a sequent error.

Figure 6.2. Working principle of model-based foreign object detection; detection metric is the sequent error in the Tx coil current reconstruction.

6.3 Theory: Deviation from the Normal Electromagnetic Model

6.3.1 Transmitter Current Reconstruction Using Sense Coil Voltages in the Normal Model

6.3.1.1 Eddy Current Lossless Tx and Rx Coils

When the Tx and Rx coils are wound by a fine litz wire, the external proximity eddy currents, derived in Section 2.3.1.2, can be neglected, resulting in simplified sense coil voltage representation. The two sense coil voltages[1] (V_1, V_2) in the *normal model* are superpositions of the induced voltages from the Tx and Rx coil currents (I_T, I_R)

$$\begin{aligned} V_1 &= j\omega M_{T:1} I_{\mathrm{T}} + j\omega M_{R:1} I_R \\ V_2 &= j\omega M_{T:2} I_{\mathrm{T}} + j\omega M_{R:2} I_R. \end{aligned} \tag{6.1}$$

The Tx and Rx coil currents can then be represented as a linear combination of the sense coil voltages

$$\begin{pmatrix} I_T \\ I_R \end{pmatrix} = \frac{1}{\mathcal{D}} \begin{pmatrix} M_{R:2} & -M_{R:1} \\ -M_{T:2} & M_{T:1} \end{pmatrix} \begin{pmatrix} \dfrac{V_1}{j\omega} \\ \dfrac{V_2}{j\omega} \end{pmatrix}, \tag{6.2}$$

where each subscript T and R refer to the Tx and Rx coils, respectively; 1 and 2 refer to the sense coils; $M_{i:j}$ is the mutual inductance between coils i and j; $\mathcal{D}$ is the determinant of the mutual inductance matrix, which can be found in (6.4); and ω is the angular frequency.

The Tx coil current can be re-written using the geometric parameters α_i,

$$I_T = \alpha_1 V_1 + \alpha_2 V_2 \tag{6.3}$$

[1] There is no self-induced voltage in the sense coils; the open-circuited sense coils currents are zero.

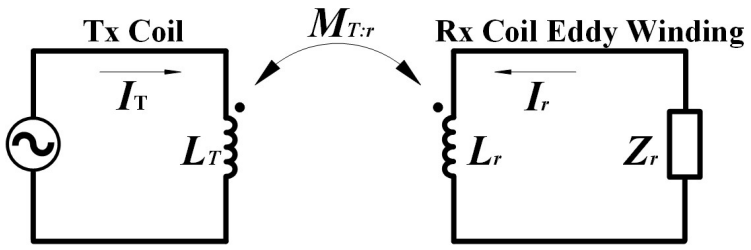

(a) The Tx coil current induces the eddy currents in the Rx coil.

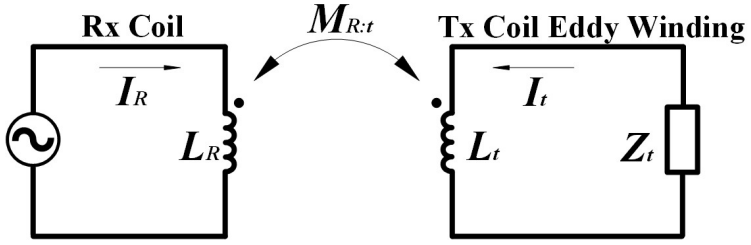

(b) The Rx coil current induces the eddy currents in the Tx coil.

Figure 6.3. The equivalent circuit for the winding model of the eddy currents.

where,

$$\alpha_1 = \frac{M_{R:2}}{j\omega\mathcal{D}}, \quad \alpha_2 = -\frac{M_{R:1}}{j\omega\mathcal{D}}, \tag{6.4}$$
$$\mathcal{D} = M_{T:1}M_{R:2} - M_{R:1}M_{T:2}.$$

6.3.1.2 Lossy Tx and Rx Coils: General Analysis

The Tx coil current I_T can be reconstructed by two open-circuited sense coil voltages V_1, V_2 despite the external proximity eddy currents in the Tx and Rx coils. In the normal model, there are four windings which are electromagnetically coupled to the sense coils and hence induce the sense coil voltages: (i) the Tx coil; (ii) the Rx coil; (iii) the eddy current in the Tx coil, which is induced by the Rx coil current; and (iv) the eddy current in the Rx coil, which is induced by the Tx coil current. It is worth noting that the time-varying Tx coil current forms the eddy current I_r in the Rx coil as an external proximity effect. The Rx coil current also forms the eddy current I_t in the Tx coil, as shown in Fig. 6.3. These eddy currents are also modeled as single windings [50; 51] which contribute to inducing the sense coil voltages. The two sense coil voltages[2] (V_1, V_2) in the *normal*

[2]There is no self-induced voltage in the sense coils; the open-circuited sense coils currents are zero.

model are superpositions of the induced voltages from the Tx, Rx, and eddy windings currents (I_T, I_R, I_t, I_r)

$$V_1 = j\omega M_{T:1} I_T + j\omega M_{R:1} I_R + j\omega M_{t:1} I_t + j\omega M_{r:1} I_r, \tag{6.5}$$

$$V_2 = j\omega M_{T:2} I_T + j\omega M_{R:2} I_R + j\omega M_{t:2} I_t + j\omega M_{r:2} I_r, \tag{6.6}$$

where each subscript T and R refer to the Tx and Rx coils, respectively; t and r refer to the eddy winding in the Tx and Rx coils, respectively; 1 and 2 refer to the sense coils; $M_{X:Y}$ is the mutual inductance between coils X and Y. The eddy current I_t and I_r can be represented by the source coil current I_R and I_T

$$I_t = \frac{j\omega M_{R:t}}{-(Z_t + j\omega L_t)} I_R, \tag{6.7}$$

$$I_r = \frac{j\omega M_{T:r}}{-(Z_r + j\omega L_r)} I_T. \tag{6.8}$$

where $M_{T:r}$ is the mutual inductance between the Tx coil and the eddy winding in the Rx coil; $M_{R:t}$ is the mutual inductance between the Rx coil and eddy winding in the Tx coil; Z_t and Z_r are the equivalent impedance in the Tx and Rx coil eddy winding. Using (6.7) and (6.8), the sense coil voltages in (6.5) and (6.6) can be represented by the Tx and Rx coil current

$$V_1 = j\omega \left(M_{T:1} + m_{r:1}\right) I_T + j\omega \left(M_{R:1} + m_{t:1}\right) I_R, \tag{6.9}$$

$$V_2 = j\omega \left(M_{T:2} + m_{r:2}\right) I_T + j\omega \left(M_{R:2} + m_{t:2}\right) I_R, \tag{6.10}$$

where

$$m_{t:i} = \frac{j\omega M_{t:i} M_{R:t}}{-(R_t + jX_t + j\omega L_t)}, \tag{6.11}$$

$$m_{r:i} = \frac{j\omega M_{r:i} M_{T:r}}{-(R_r + jX_r + j\omega L_r)}. \tag{6.12}$$

The Tx coil current can then be reconstructed as a linear combination of two sense coil voltages V_1 and V_2

$$\begin{pmatrix} I_T \\ I_R \end{pmatrix} = \frac{1}{\mathcal{D}} \begin{pmatrix} M_{R:2} + m_{t:2} & -M_{R:1} - m_{t:1} \\ -M_{T:2} - m_{r:2} & M_{T:1} + m_{r:1} \end{pmatrix} \begin{pmatrix} \dfrac{V_1}{j\omega} \\ \dfrac{V_2}{j\omega} \end{pmatrix}, \tag{6.13}$$

where

$$\mathcal{D} = (M_{T:1} + m_{r:1})(M_{R:2} + m_{t:2}) - (M_{R:1} + m_{t:1})(M_{T:2} + m_{r:2}). \tag{6.14}$$

The Tx coil current I_T can be re-written using the *normal geometric parameters* α_i

$$I_T = \alpha_1 V_1 + \alpha_2 V_2, \tag{6.15}$$

where

$$\alpha_1 = \frac{M_{R:2} + m_{t:2}}{j\omega\mathcal{D}}, \tag{6.16}$$

$$\alpha_2 = \frac{-M_{R:1} - m_{t:1}}{j\omega\mathcal{D}}. \tag{6.17}$$

It is worth noting that the eddy winding currents I_t and I_r, the corresponding induced voltages in sense coil voltages, and hence $m_{t:i}$ and $m_{r:i}$ can be significantly reduced if a litz wire with fine strands is used for the Tx and Rx windings, resulting in the geometric parameters, derived in (6.4).

6.3.2 Sequent Error in the Transmitter Current Reconstruction in the Adverse Model

6.3.2.1 Eddy Current Lossless Tx and Rx Coils

The Tx, Rx, sense coils, and eddy winding of a foreign object (subscript: e) are included in the *adverse model* as shown in Fig. 6.1. The two sense coil voltages then have the additional induced

voltages (a) and (b), from the eddy winding current (I_e)

$$\begin{aligned} V_1 &= j\omega M_{T:1} I'_T + j\omega M_{\mathrm{R}:1} I'_R + \underbrace{j\omega M_{e:1} I_e}_{\text{(a)}} \\ V_2 &= j\omega M_{T:2} I'_T + j\omega M_{R:2} I'_R + \underbrace{j\omega M_{e:2} I_e}_{\text{(b)}}, \end{aligned} \tag{6.18}$$

where the Tx and Rx coil currents of the *adverse model* are I'_T and I'_R. Then, (6.18) can be re-written with respect to the deviation of the geometric parameter ($\Delta M_{i:j}$),

$$\begin{aligned} V_1 &= j\omega\big(M_{T:1} + \Delta M_{T:1}\big) I'_T + j\omega\big(M_{R:1} + \Delta M_{R:1}\big) I'_R \\ V_2 &= j\omega\big(M_{T:2} + \Delta M_{T:2}\big) I'_T + j\omega\big(M_{R:2} + \Delta M_{R:2}\big) I'_R, \end{aligned} \tag{6.19}$$

where,

$$\Delta M_{i:j} = M_{e:i} M_{e:j} \frac{-j\omega Z_e - \omega^2 L_e}{Z_e^2 + \omega^2 L_e^2}. \tag{6.20}$$

Note that I_e in (6.18) can be represented as the superposition of the Tx and Rx coil currents [51], which results in (6.20). The Tx coil current (I'_T) of the *adverse model* is therefore,

$$I'_T = \alpha'_1 V_1 + \alpha'_2 V_2, \tag{6.21}$$

where,

$$\begin{aligned} \alpha'_1 &= \frac{M_{R:2} + \Delta M_{R:2}}{j\omega \mathcal{D}'}, \\ \alpha'_2 &= \frac{-M_{R:1} - \Delta M_{R:1}}{j\omega \mathcal{D}'}, \\ \mathcal{D}' &= \mathcal{D} + \Delta\mathcal{D}, \\ \Delta\mathcal{D} &= (M_{T:1}\Delta M_{R:2} - M_{R:1}\Delta M_{R:2}) \\ &\quad + (M_{T:1}\Delta M_{T:1} - M_{T:2}\Delta M_{R:1}) \\ &\quad + (\Delta M_{T:1}\Delta M_{R:2} - \Delta M_{R:1}\Delta M_{T:2})\,. \end{aligned} \tag{6.22}$$

The detection metric Γ is the absolute percentage sequent error ϵ_d; the *sequent error* in Tx coil current reconstruction when *normal geometric parameters* are derived when there is no foreign object in (6.16) and (6.17); The reconstructed Tx coil current $\hat{I}_T$ is

$$\hat{I}_T = \alpha_1 V_1 + \alpha_2 V_2. \tag{6.23}$$

The detection metric becomes

$$\Gamma = \epsilon_d = \left| \frac{I'_T - \hat{I}_T}{I'_T} \right| \times 100\,(\%) \tag{6.24}$$

$$= \left| 1 - \left(\frac{\mathcal{D}'}{\mathcal{D}} - \zeta \right) \right| \times 100\,(\%), \tag{6.25}$$

where,

$$\begin{aligned} \zeta &= \frac{\Delta M_{R:2} - \Delta M_{R:1}\nu}{M_{R:2} + \Delta M_{R:2} - M_{R:1}\nu - \Delta M_{R:1}\nu}, \\ \nu &= \frac{M_{T:2} + \Delta M_{T:2} + \big(M_{R:2} + \Delta M_{R:2}\big)\gamma}{M_{T:1} + \Delta M_{T:1} + \big(M_{R:1} + \Delta M_{R:1}\big)\gamma}, \\ \gamma &= \frac{-\omega^2 L_R + j\omega M_{T:R} Z_R}{Z_R^2 + \omega^2 L_R^2}, \end{aligned} \tag{6.26}$$

Z_R is the equivalent output impedance of the Rx coil. Note that if there is no foreign object, then $\mathcal{D}'=\mathcal{D}$, and ζ is zero, and therefore the relative error goes to zero.

6.3.2.2 Lossy Tx and Rx Coils: General Analysis

The eddy winding of a foreign object (subscript: e) is included in the *adverse model* as shown in Fig. 6.1. The two sense coil voltages V_1 and V_2 then have the additional induced voltages (a) and

(b) from the eddy winding current I_e

$$V_1 = j\omega \left(M_{T:1} + m_{r:1}\right) I'_T + j\omega \left(M_{R:1} + m_{t:1}\right) I'_R + \underbrace{j\omega M_{e:1} I_e}_{\text{(a)}} \tag{6.27}$$

$$V_2 = j\omega \left(M_{T:2} + m_{r:2}\right) I'_T + j\omega \left(M_{R:2} + m_{t:2}\right) I'_R + \underbrace{j\omega M_{e:2} I_e}_{\text{(b)}}, \tag{6.28}$$

where the Tx and Rx coil currents of the *adverse model* are I'_T and I'_R. Then, (6.27) and (6.28) can be re-written with respect to the deviation of the geometric parameter ($\Delta M_{X:i}$),

$$V_1 = j\omega \left(M_{T:1} + m_{r:1} + \Delta M_{T:1}\right) I'_T + j\omega \left(M_{R:1} + m_{t:1} + \Delta M_{R:1}\right) I'_R, \tag{6.29}$$

$$V_2 = j\omega \left(M_{T:2} + m_{r:2} + \Delta M_{T:2}\right) I'_T + j\omega \left(M_{R:2} + m_{t:2} + \Delta M_{R:2}\right) I'_R, \tag{6.30}$$

where

$$\Delta M_{X:i} = M_{X:e} M_{e:i} \frac{-j\omega Z_e - \omega^2 L_e}{Z_e^2 + \omega^2 L_e^2}. \tag{6.31}$$

Note that I_e in (6.27) and (6.28) can be represented as the superposition of the Tx and Rx coil currents [51], which results in (6.31). The Tx coil current I'_T of the *adverse model* is therefore,

$$I'_T = \alpha'_1 V_1 + \alpha'_2 V_2, \tag{6.32}$$

where

$$\alpha'_1 = \frac{M_{R:2} + m_{t:2} + \Delta M_{R:2}}{j\omega \mathcal{D}'}, \tag{6.33}$$

$$\alpha'_2 = \frac{-M_{R:1} - m_{t:1} - \Delta M_{R:1}}{j\omega \mathcal{D}'}, \tag{6.34}$$

$$\mathcal{D}' = \mathcal{D} + \Delta\mathcal{D}, \tag{6.35}$$

$$\begin{aligned}\Delta\mathcal{D} = &\left(M_{T:1} + m_{r:1}\right)\Delta M_{R:2} - \left(M_{R:1} + m_{t:1}\right)\Delta M_{T:2} \\ &+ \left(M_{R:2} + m_{t:2}\right)\Delta M_{T:1} - \left(M_{T:2} + m_{r:2}\right)\Delta M_{R:1} \\ &+ \Delta M_{T:1}\Delta M_{R:2} - \Delta M_{R:1}\Delta M_{T:2}.\end{aligned} \tag{6.36}$$

An effective detection metric Γ for EM-FOD can be chosen to be the *sequent error* in Tx coil current reconstruction when *normal geometric parameters*[3] α_1 and α_2 are used for the reconstruction. The reconstructed Tx coil current $\hat{I}_T$ is

$$\hat{I}_T = \alpha_1 V_1 + \alpha_2 V_2. \tag{6.37}$$

The detection metric Γ is the absolute percentage sequent error ϵ_d:

$$\Gamma = \epsilon_d = \left| \frac{I'_T - \hat{I}_T}{I'_T} \right| \times 100\,(\%) \tag{6.38}$$

$$= \left| 1 - \left(\frac{\mathcal{D}'}{\mathcal{D}} - \zeta \right) \right| \times 100\,(\%), \tag{6.39}$$

where

$$\zeta = \frac{\Delta M_{R:2} - \Delta M_{R:1}\nu}{M_{R:2} + m_{t:2} + \Delta M_{R:2} - \left(M_{R:1} + m_{t:1}\right)\nu - \Delta M_{R:1}\nu}, \tag{6.40}$$

$$\nu = \frac{M_{T:2} + m_{r:2} + \Delta M_{T:2} + \left(M_{R:2} + m_{t:2} + \Delta M_{R:2}\right)\gamma}{M_{T:1} + m_{r:1} + \Delta M_{T:1} + \left(M_{R:1} + m_{t:1} + \Delta M_{R:1}\right)\gamma}, \tag{6.41}$$

$$\gamma = \frac{-\omega^2 M_{T:R} L_R - j\omega M_{T:R} Z_R}{Z_R^2 + \omega^2 L_R^2}. \tag{6.42}$$

Z_R is the equivalent output impedance of the Rx coil. Note that if there is no foreign object, then $\mathcal{D}'=\mathcal{D}$, and ζ is zero, and therefore the relative sequent error goes to zero.

[3]Normal geometric parameters are derived when there is no foreign object in (6.16) and (6.17).

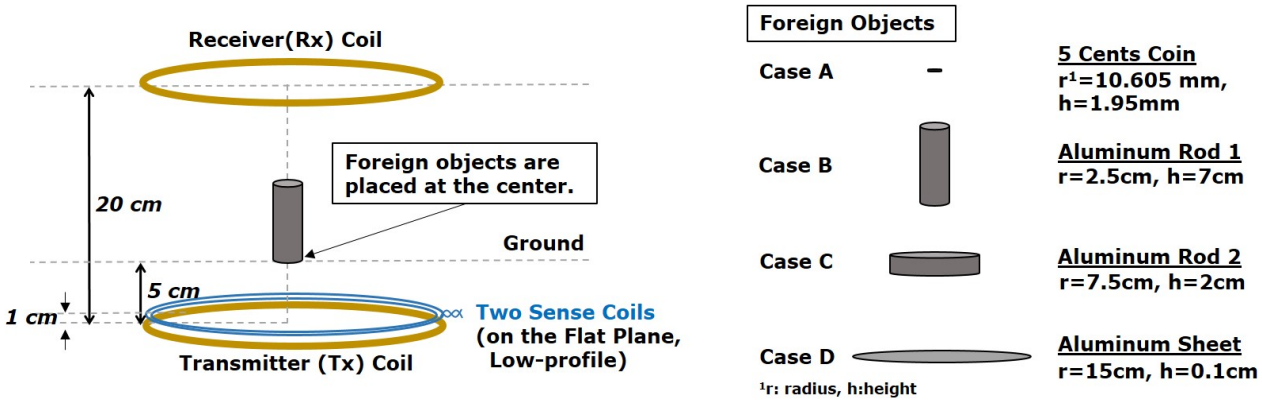

Figure 6.4. Configurations of the electromagnetic model-based foreign object detection for wireless power transfer for FEM simulations.

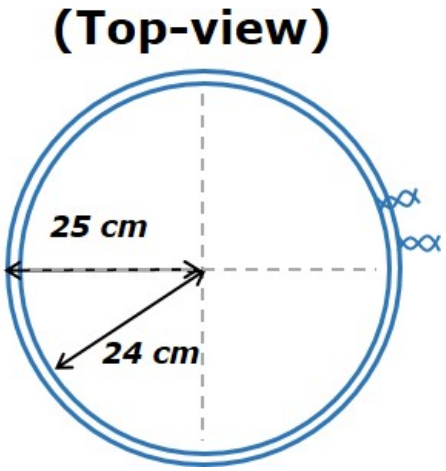

Figure 6.5. Two open-circuited single-turn sense coils are placed on the same flat plane (for low-profile).

6.4 Simulation Results

The electromagnetic model-based foreign object detection (EM-FOD) was verified through finite element method (FEM) simulation in COMSOL. Fig. 6.4 shows the configurations of the EM-FOD for the simulations. Two open-circuited sense coils (25 and 24 cm radii) were placed on the same flat plane, as shown in Fig. 6.5, which was 1 cm above the Tx coil. Four different foreign objects were placed on the ground, which was 5 cm above the Tx coil.

2-D axisymmetric FEM simulations were performed, as shown in Fig. 6.6; sense coil voltages were obtained when the Tx and Rx coils were driven by current sources.

Following the EM-FOD strategy in Section 6.2, the geometric parameters ($\alpha_{1,2}$) were calibrated initially in the *normal model* (no foreign objects). A sufficient number of data points were used to calibrate the geometric parameters accurately; in this simulation, the Rx coil currents were varied over n data points, corresponding to different output load resistances in the Rx.

From the n data points, the calibration data matrix of sense coil voltages $\mathbf{V}$, the Tx coil current data vector $\mathbf{I_T}$, and geometric parameters vector $\boldsymbol{\alpha}$, can be constructed

$$\begin{aligned}
\mathbf{V} &= \begin{pmatrix} V_1(z_1) & V_2(z_1) \\ V_1(z_2) & V_2(z_2) \\ \vdots & \vdots \\ V_1(z_n) & V_2(z_n) \end{pmatrix}, \\
\alpha &= \begin{bmatrix} \alpha_1 & \alpha_2 \end{bmatrix}^\intercal, \\
\mathbf{I_T} &= \begin{bmatrix} I_T(z_1) & I_T(z_2) & \dots & I_T(z_n) \end{bmatrix}^\intercal.
\end{aligned} \tag{6.43}$$

From (6.15),

$$\mathbf{I_T} = \mathbf{V}\,\boldsymbol{\alpha}. \tag{6.44}$$

The *normal geometric parameters* (α_1, α_2) can then be calibrated using least-squares

$$\boldsymbol{\alpha} = (\mathbf{V}^\intercal\mathbf{V})^{-1}\,\mathbf{V}^\intercal\mathbf{I_T}. \tag{6.45}$$

To evaluate EM-FOD after calibration, the Tx coil currents were reconstructed with and without foreign objects using the *normal geometric parameters*. Note that in the EM-FOD detection metric Γ, defined in (6.38), I_T' is the measured Tx coil current, which is the true value. In this simulation, the Rx coil currents were varied over 8 data points, which generated small Tx powers[4] (2.1 to 3.54 W), as shown in Fig. 6.7a; in the *normal model* (no foreign objects) (green-circles), the geometric parameters were calibrated, and then the Tx coil current was reconstructed; according

[4]The transmitter power is the real power, measured at the transmitter coil terminal.

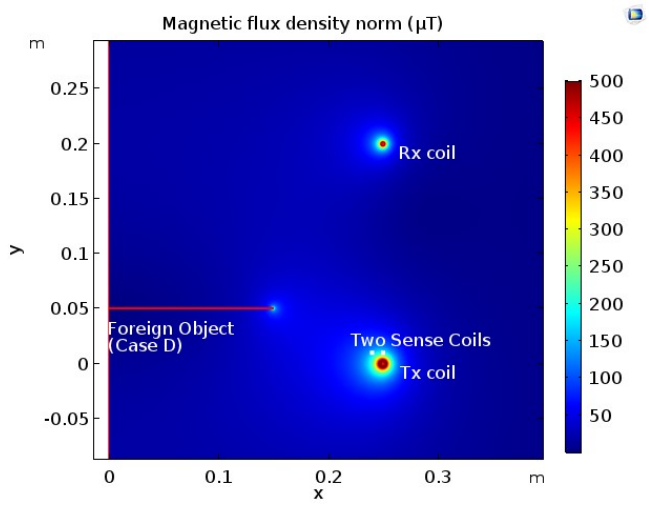

Figure 6.6. 2-D axisymmetric FEM simulation of EM-FOD. The foreign object is electromagnetically coupled to the Tx, Rx, and sense coils. (In the colormap, the magnetic flux density norm was bounded for the better visualization.)

to leave-one-out cross-validation (LOOCV) [58], this results in an accurate estimation.

Fig. 6.7a shows that the EM-FOD detection metric Γ increases significantly when a *normal model* has been calibrated and there are foreign objects. Note that the detection metric is plotted in logarithmic scale to highlight the wide dynamic range of the measurement.

Two additional data points, having higher Tx powers (P_{Tx}), were also tested to show the power-level invariance of EM-FOD; the Tx and Rx coil were driven by higher currents. The detection metric Γ was calculated through (6.38), using the *normal geometric parameters*, calibrated at low power. Fig. 6.7b shows the detection metric did not change from that at low power; a low-power test, which is safer and less hazardous can now be performed prior to startup. This is so because the sequent error from current reconstruction only depends on the additional electromagnetic coupling from the foreign objects, resulting in detection metric that is invariant to absolute power level. Fig. 6.8 shows that the current reconstruction error only depends on the ratio of eddy losses from foreign objects to the Tx power.

Foreign objects can also be detected when there is no Rx coil before EVs come to charge. The same geometric parameters, which were calibrated without a foreign object but with an Rx coil, were used for a Tx coil reconstruction. In this simulation, the Rx coil was removed to emulate charging stations' idle status, where there are only the Tx and sense coils, as shown in Fig. 6.9.

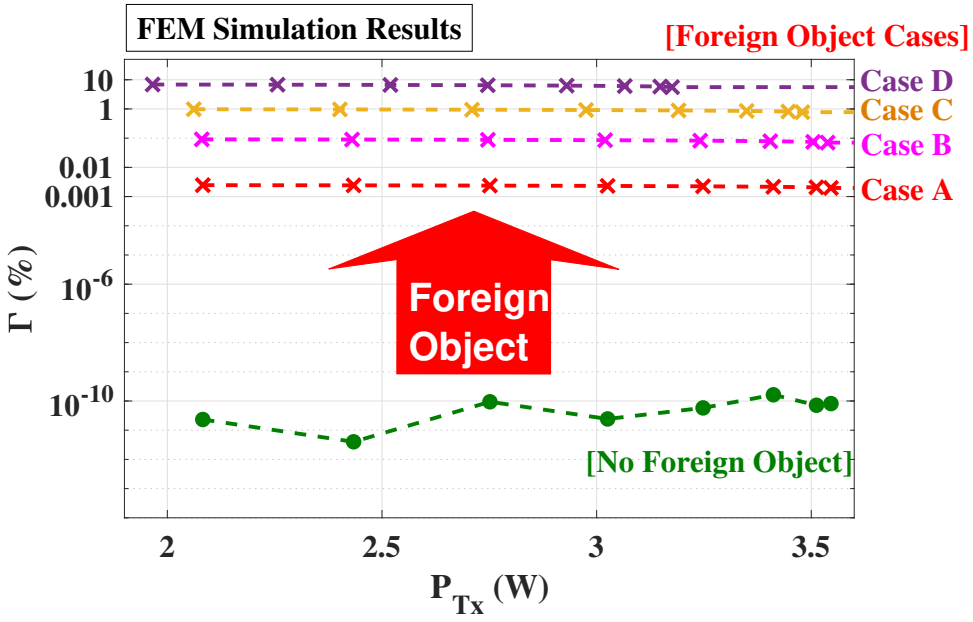

(a) The foreign objects caused the Tx current reconstruction deviation Γ.

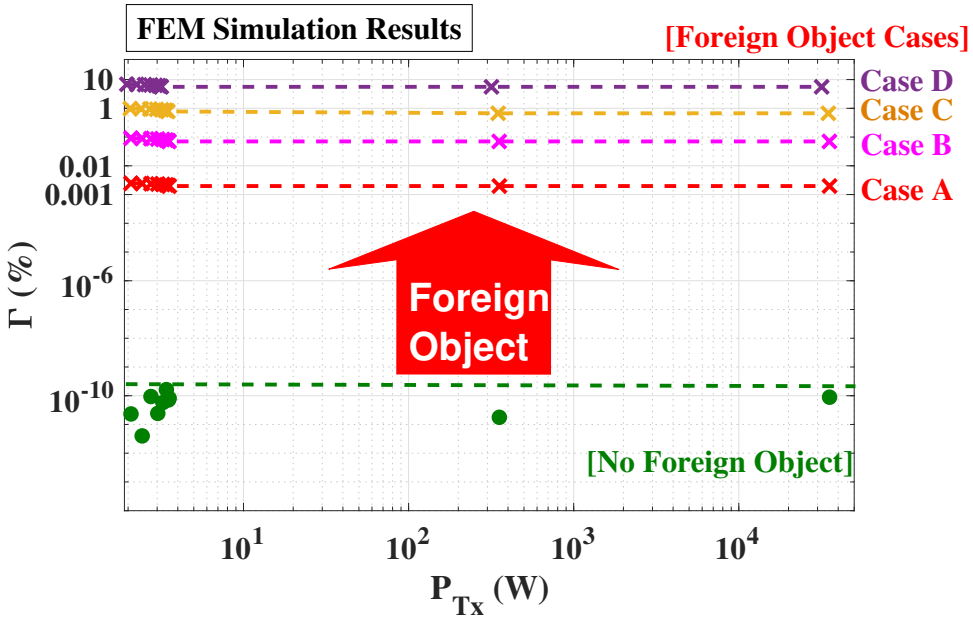

(b) The Tx current reconstruction deviation were invariant to power levels.

Figure 6.7. The Tx current reconstruction deviation with and without foreign objects.

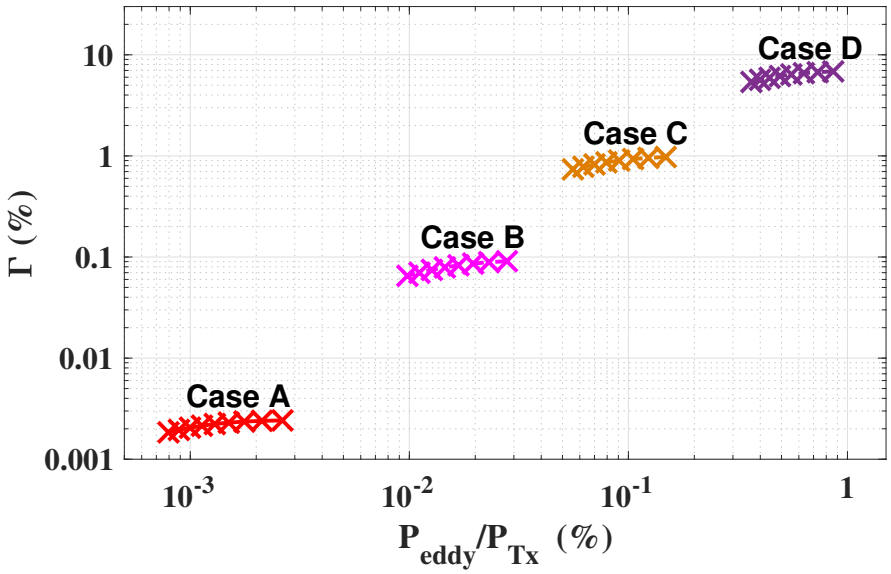

Figure 6.8. The Tx current reconstruction errors depended on the ratio of the eddy losses from foreign objects, to the Tx power.

Four different foreign objects were placed, and the Tx coil current was reconstructed. Fig. 6.10 shows that the detection metric increases despite no Rx coil.

The Rx coil current is another information that can be reconstructed from the sense coil voltages and geometric parameters, as derived in (6.13)

$$I_R = \delta_1 V_1 + \delta_2 V_2 \tag{6.46}$$

where,

$$\begin{aligned} \delta_1 &= \frac{-M_{T:2} - m_{r:2}}{j\omega\mathcal{D}}, \\ \delta_2 &= \frac{M_{T:1} + m_{r:1}}{j\omega\mathcal{D}}, \\ \mathcal{D} &= (M_{T:1} + m_{r:1})(M_{R:2} + m_{t:2}) - (M_{R:1} + m_{t:1})(M_{T:2} + m_{r:2}). \end{aligned} \tag{6.47}$$

Thus, the open-circuited Rx coil, thus zero Rx coil current, can provide information on the diagnostics of the wireless power transfer system. To verify the zero Rx coil current reconstruction,

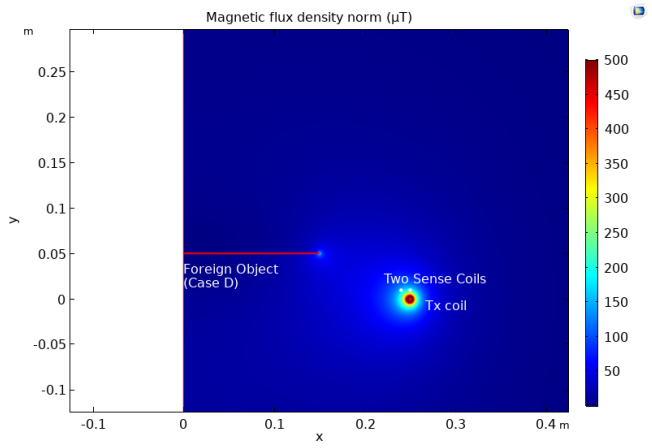

Figure 6.9. 2-D axisymmetric FEM simulation of EM-FOD. An Rx coil is removed. The foreign object is electromagnetically coupled to the Tx and sense coils. (In the colormap, the magnetic flux density norm was bounded for the better visualization.)

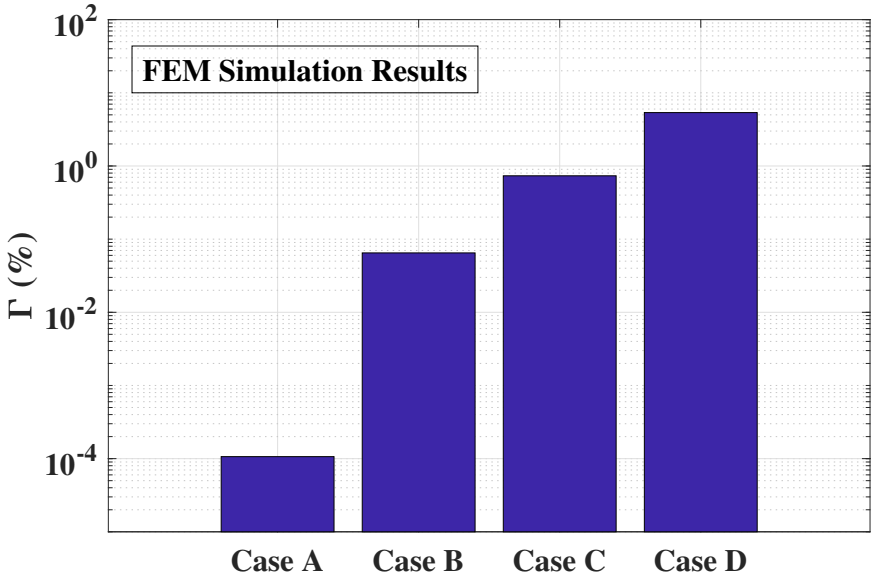

Figure 6.10. When there is no Rx coil, foreign objects can be detected from the detection metric.

TABLE 6.1
Different Coil Current for Test Points

Test Point	I_T (Source Current)	I_R (Reconstructed Current)
1	$(9.8 + j1.7)$ A	$(-0.25 + j0.5) \times 10^{-10}$ A
2	$(9.7 + j2.6)$ A	$(-0.22 + j0.5) \times 10^{-10}$ A
3	$(9.4 + j3.4)$ A	$(-0.3 + j0.5) \times 10^{-10}$ A
4	$(9.0 + j4.2)$ A	$(-0.4 + j0.4) \times 10^{-10}$ A
5	$(8.7 + j5.0)$ A	$(-0.1 + j0.6) \times 10^{-10}$ A
6	$(8.2 + j5.7)$ A	$(-0.2 + j0.5) \times 10^{-10}$ A
7	$(7.7 + j6.4)$ A	$(-0.4 + j0.3) \times 10^{-10}$ A
8	$(7.1 + j7.1)$ A	$(-0.5 + j0.2) \times 10^{-10}$ A

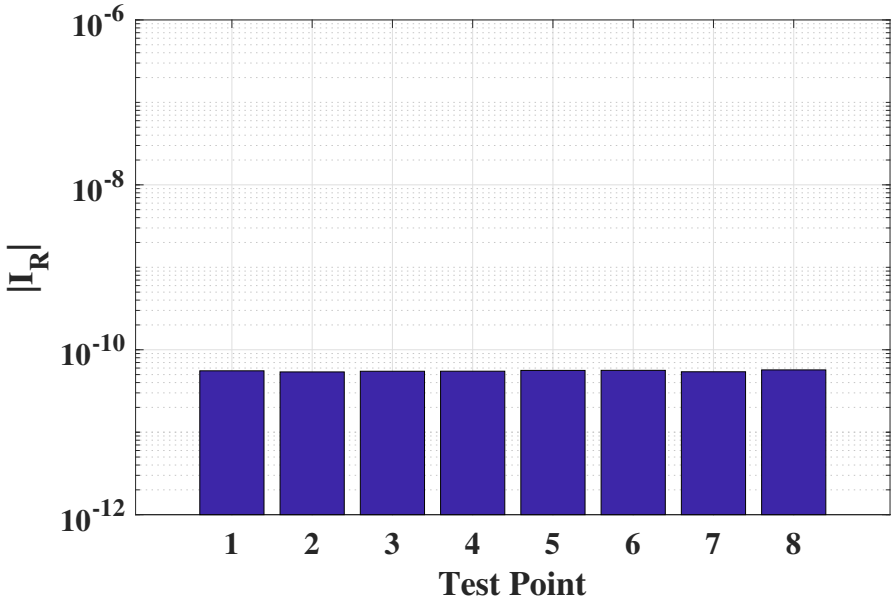

Figure 6.11. The open-circuited Rx coil currents are well reconstructed, as having zero magnitude.

the geometric parameters δ_1 and δ_2, derived in (6.47) for Rx coil reconstruction are calibrated. The Rx coils were reconstructed for 8 different test points (different Tx coil source currents). Table 6.1 shows the coil currents for different test points. Fig 6.11 shows that open-circuited Rx coil current, zero current, can also be reconstructed by showing insignificant magnitudes.

6.5 Misalignment Invariant EM-FOD

For a practical EM-FOD, *adverse models* need to be distinguished from what are considered 'normal' deviations from our original *normal model*. For example, Tx and Rx coil misalignment should be considered normal. In this section, we will show how a flat configuration of multiple sense coils on the same axis and plane can be used to eliminate a sequent error from misalignment. It is worth noting that in this method, explicit measurement of misalignment is not needed either for current reconstruction or calibration.

Misalignment between the Tx and Rx coil can cause a sequent error in the Tx coil current reconstruction despite the absence of a foreign object when using only two sense coils. This is so because the geometric parameters, which are a function of the mutual inductances in (6.4), (6.16) and (6.17) vary over misalignment; however the geometric parameters are calibrated initially for a fixed Tx and Rx coil configuration[5] and assumed constant in the *normal model*. Fig. 6.13 shows the numerical results of the sequent error in the Tx coil current reconstruction over Rx coil misalignment when only two sense coils are used with the corresponding geometric parameters[6] α_1 and α_2; the greater the misalignment, the larger the sequent error, despite there being no foreign object. The sequent error is no longer a good detection metric because of misalignment when only two sense coils are used.

By employing multiple sense coils, the Tx coil current can be reconstructed accurately with insignificant sequent error when the geometric parameters are non-varying values over misalign-

[5]Perfect alignment of the Tx and Rx coil (x=0, in Fig. 6.12) is assumed to be the configuration of the *normal model*.

[6]The geometric parameters are calibrated when the Tx and Rx coils are aligned, $x = 0$. The sizes and positions of two sense coils are shown in Table 6.2, where $i = 1, 2$.

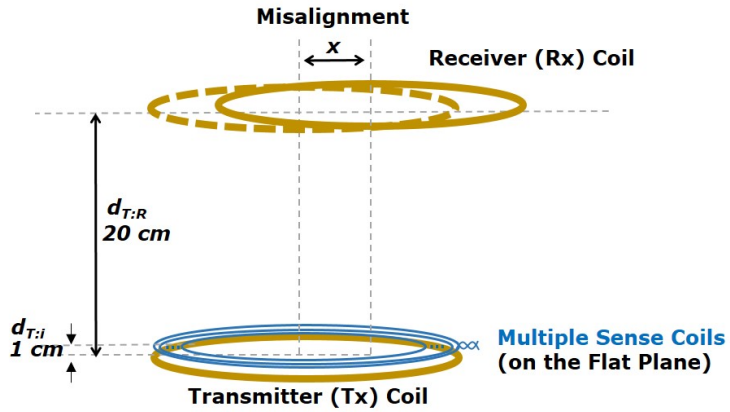

Figure 6.12. The Rx coil can be misaligned by x cm. Multiple sense coils, on the same flat plane, are employed to derive non-varying geometric parameters, and thus making sequent error a valid detection metric for EM-FOD over Rx coil misalignment.

ment, resulting in a new normal model that considers the misalignment 'normal'. Foreign objects can then be detected regardless of misalignment.

Errors caused by the misalignment in Transfer-Power Measurement (TPM) were similarly corrected by employing multiple sense coils with the corresponding algorithm in Chapter 3, which is based on quadratically varying coupling coefficients between the mobile Rx coil and coaxially placed coils over misalignment, as shown in Fig. 6.12. In this chapter, the same multiple sense coils, which are placed coaxially with the Tx and Rx coil (at $x = 0$), are used to take advantage of the quadratic coupling coefficients and mutual inductances. The winding loss, which includes the ohmic loss and external proximity eddy current loss in the Tx and Rx coils are neglected[7] to elucidate the principle of accurate Tx coil reconstruction over misalignment.

6.5.1 Theory: Misalignment Invariant Detection Metric Using Sequent Error

Sense coil voltages $V_i(x)$ at misalignment x, can be represented in terms of the Tx coil current I_T and voltage V_T

$$V_i(x) = j\omega M_{T:i} I_T(x) + j\omega M_{R:i}(x) I_R(x) \tag{6.48}$$

[7]The eddy currents in the Tx and Rx coils are neglected; $I_t, I_r = 0$.

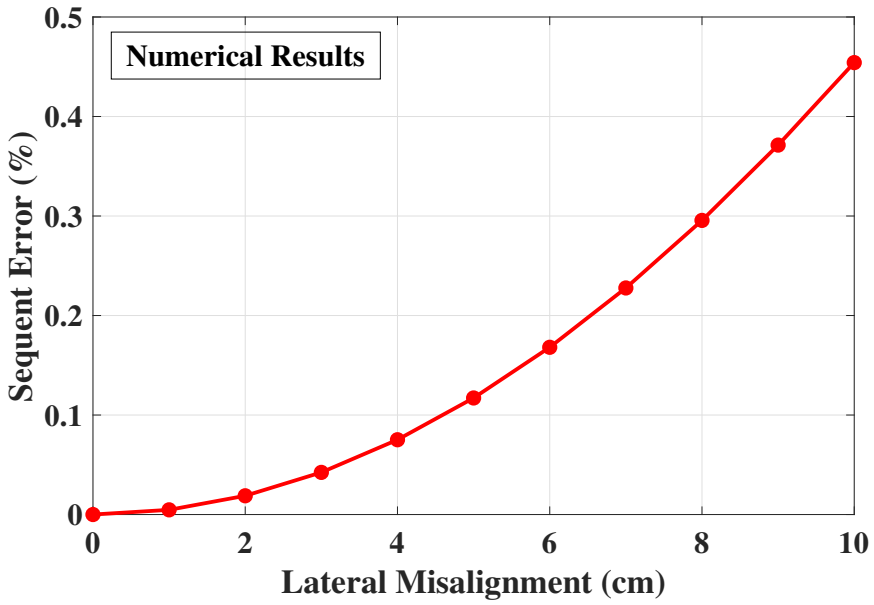

Figure 6.13. Numerical results: when only two sense coils and the corresponding geometric parameters (calibrated at zero misalignment with no foreign object) are used for Tx coil current reconstruction, the sequent error significantly increases with Tx and Rx coil misalignment.

$$= j\omega \left(M_{T:i} - \frac{M_{R:i}(x)}{M_{T:R}(x)} L_T \right) I_T(x) + \frac{M_{R:i}(x)}{M_{T:R}(x)} V_T(x), \tag{6.49}$$

where,

$$I_R(x) = \frac{V_T(x) - j\omega L_T I_T(x)}{j\omega M_{T:R}(x)}. \tag{6.50}$$

Note that the mutual inductance between the Tx coil and sense coil, $M_{T:i}$ is constant over misalignment. Equation (6.48) can be rewritten with the parameter $\mathbf{m}_i(x)$,

$$V_i(x) = j\omega \left(M_{T:i} - \mathbf{m}_i(x) L_T \right) I_T(x) + \mathbf{m}_i(x) V_T(x), \tag{6.51}$$

where,

$$\mathbf{m}_i(x) = \frac{M_{R:i}(x)}{M_{T:R}(x)}. \tag{6.52}$$

The parameter $\mathbf{m}_i(x)$ can be well-approximated by a quadratic [95]

$$\begin{aligned} &\mathbf{m}_i(x) \approx p_i + q_i x + r_i x^2, \\ &\text{where } p, q, r \in \mathbb{R}. \end{aligned} \tag{6.53}$$

N sense coil voltages in (6.51) can be linearly combined by real coefficients β_i,

$$\sum_{i=1}^{N} \beta_i \frac{V_i(x)}{j\omega} = I_T(x) \sum_{i=1}^{N} \left(\beta_i M_{T:i} - \beta_i \mathbf{m}_i(x) L_T\right) + \frac{V_T(x)}{j\omega} \sum_{i=1}^{N} \beta_i \mathbf{m}_i(x). \tag{6.54}$$

β_i for quadratically-varying mutual inductance are found to be

$$\sum_{i=1}^{N} \beta_i M_{T:i} \approx 1, \tag{6.55}$$

$$\sum_{i=1}^{N} \beta_i \mathbf{m}_i(x) \approx 0, \tag{6.56}$$

where

$$\sum_{i=1}^{N} \beta_i p_i \approx 0, \ \sum_{i=1}^{N} \beta_i q_i \approx 0, \ \text{and} \ \sum_{i=1}^{N} \beta_i r_i \approx 0, \tag{6.57}$$

resulting in the reconstruction of the Tx coil current over misalignment x by the sense coil voltages and the real coefficient β_i,

$$\sum_{i=1}^{N} \beta_i \frac{V_i(x)}{j\omega} \approx I_T(x). \tag{6.58}$$

Note that new geometric parameters $\lambda_i = \beta_i / j\omega$ are constant and can be initially calibrated, meaning that the Tx coil current can be reconstructed at any misalignment x; only the geometric parameters and sense coil voltages are needed without explicit measurements of the misalignment.

A least-squares optimization is used to obtain λ_i

TABLE 6.2
Specifications of Numerical Models

Parameters	Value	Parameters	Value
r_T,r_R	25 cm	r_i	26 - $(i \cdot 1)$ cm
$d_{T:R}$	20 cm	$\max(x)$	10 cm
$d_{T:i}$	1 cm	$\min(x)$	0 cm

$$\begin{aligned} &\underset{\lambda_i}{\text{minimize}} \quad \left\| I_T(x) - \sum_{i=1}^{N} \lambda_i V_i(x) \right\|_2 \\ &\text{subject to} \quad \lambda_i \in \mathbb{C}. \end{aligned} \tag{6.59}$$

6.5.2 Numerical Model Verification

Numerical models[8], which were derived from a mutual inductance model [55], verify accurate Tx coil current reconstruction, and thus non-varying detection metric over misalignment. Sense coil voltages were obtained by (6.48) at each misalignment x, when the Tx and Rx coils were driven by current sources. Fig. 6.12 shows the configuration of the coils. Table 6.2 shows each coil's size and position; the radii of the Tx (r_T) and Rx (r_R) coils were 25 cm, where the two coils were separated by 20 cm ($d_{T:R}$). Multiple sense coils were placed on a flat plane, which was 1 cm ($d_{T:i}$) above the Tx coil. The number of sense coils, used for the reconstruction, was varied from two to five to study the effectiveness of employing an increasing number of sense coils in reducing the sequent error from misalignment when there is no foreign object; the radii of sense coils r_1 to r_5 ranged from 25 to 20 cm, respectively, decreasing at 1 cm intervals. We will show that these additional sense coils eliminate the sequent error in lateral misalignments of up to 10 cm.

For the calibration of geometric parameters λ_i, numerical data was obtained over: (i) n data points of the Rx coil current (corresponding to different load resistance); (ii) m data points of misalignment (not necessarily uniform). The calibration matrix and vector can then be constructed

[8]Assumptions in the numerical models are: (i) filament coils; (ii) fundamental only; (iii) noiseless.

to solve the least-squares optimization in (6.59), when there are N sense coils. The sense coil voltage measurements are combined in a data matrix

$$\mathbf{V} = \begin{pmatrix} V_1(x_1,z_1) & V_2(x_1,z_1) & \dots & V_N(x_1,z_1) \\ V_1(x_1,z_2) & V_2(x_1,z_2) & \dots & V_N(x_1,z_2) \\ \vdots & \vdots & \ddots & \vdots \\ V_1(x_1,z_n) & V_2(x_1,z_n) & \dots & V_N(x_1,z_n) \\ \hdashline V_1(x_2,z_1) & V_2(x_2,z_1) & \dots & V_N(x_2,z_1) \\ V_1(x_2,z_2) & V_2(x_2,z_2) & \dots & V_N(x_2,z_2) \\ \vdots & \vdots & \ddots & \vdots \\ V_1(x_2,z_n) & V_2(x_2,z_n) & \dots & V_N(x_2,z_n) \\ \hdashline \vdots & \vdots & \ddots & \vdots \\ V_1(x_m,z_n) & V_2(x_m,z_n) & \dots & V_N(x_m,z_n) \end{pmatrix}. \tag{6.60}$$

The Tx coil current corresponding to each row of $\mathbf{V}$ is contained in the elements of column vector $\mathbf{I_T}$

$$\mathbf{I_T} = \begin{bmatrix} I_T(x_1,z_1) & I_T(x_1,z_2) & \dots & I_T(x_m,z_n) \end{bmatrix}^\intercal. \tag{6.61}$$

Each row of $\mathbf{V}$ corresponds to different measurement conditions such as misalignment and loads.

The vector of geometric parameters λ_i for N sense coils is

$$\boldsymbol{\lambda} = \begin{bmatrix} \lambda_1 & \lambda_2 & \dots & \lambda_N \end{bmatrix}^\intercal. \tag{6.62}$$

From (6.58),

$$\mathbf{I_T} = \mathbf{V}\,\boldsymbol{\lambda}. \tag{6.63}$$

The geometric parameters (λ_i) can then be calibrated using the least-squares

$$\boldsymbol{\lambda} = (\mathbf{V}^\intercal\mathbf{V})^{-1}\,\mathbf{V}^\intercal\mathbf{I_T}. \tag{6.64}$$

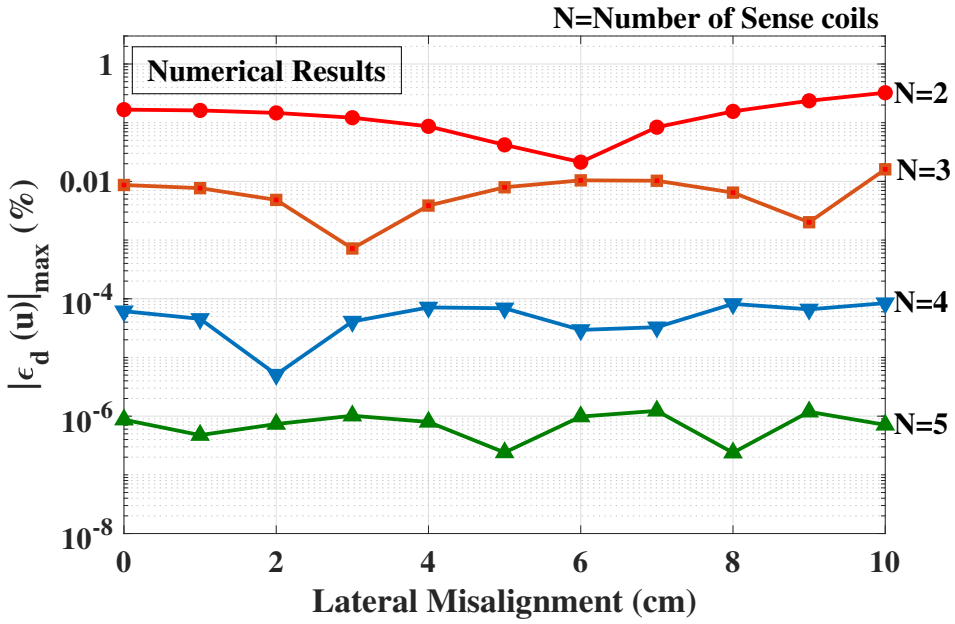

Figure 6.14. Numerical model results: the Tx coil current can be reconstructed accurately by sense coil voltages and non-varying geometric parameters regardless of Rx coil misalignment.

The sequent error was determined for each data point using LOOCV[9]; the absolute percentage sequent error of the Tx coil current reconstruction over Rx coil misalignment is

$$\epsilon_d(x_m, z_n) = \left| \frac{I_T(x_m, z_n) - \hat{I}_T(x_m, z_n)}{I_T(x_m, z_n)} \right| \times 100\,(\%) \tag{6.65}$$

where,

$$\begin{aligned} &\hat{I}_T(x_m, z_n) : \text{Reconstructed Tx coil current} \\ &= \sum_{i=1}^{N} \lambda_i V_i(x_m, z_n) \end{aligned} \tag{6.66}$$

In this numerical model verification, $n = 9$ data points of the Rx coil current and $m = 11$ data points of misalignment (0 to 10 cm, 1 cm interval) were used to calibrate λ_i.

The worst-case absolute sequent percentage error at each lateral misalignment x was calculated

[9]If there are total $m \times n$ data points, then the calibration of the geometric parameters is performed with $m \times n - 1$ data points. The sequent error for Tx coil current reconstruction is evaluated with one data point which is not used for the calibration.

TABLE 6.3
Specifications of Stacked Sense Coils

Parameters	Value	Parameters	Value
$r_{_T}$,$r_{_R}$	25 cm	r_i	25 cm
$d_{T:R}$	20 cm	$\max(x)$	10 cm
$d_{T:i}$	i cm	$\min(x)$	0 cm

TABLE 6.4
Specifications of Sense Coils Close To Rx Coil

Parameters	Value	Parameters	Value
$r_{_T}$,$r_{_R}$	25 cm	r_i	25 cm
$d_{T:R}$	20 cm	$\max(x)$	10 cm
$d_{T:i}$	(20-i) cm	$\min(x)$	0 cm

and plotted in Fig. 6.14, where

$$\left|\epsilon_d\left(\mathbf{u}\right)\right|_{\max} \triangleq \max_k \left|\epsilon_d\left(\mathbf{u}_k\right)\right|. \tag{6.67}$$

Note that $\mathbf{u}_k$ is the vector of variations over which the sequent error is calculated. In this plot, $\mathbf{u}_k = \begin{bmatrix} x & z_k \end{bmatrix}$. With multiple sense coils and calibration over misalignment, the sequent error from misalignment decreased significantly. Moreover, as more sense coils were employed, the sequent error became negligible, i.e. $10^{-6}\%$ error, when 5 sense coils were used (green-upright triangles). This sequent error from misalignment represents the baseline for the foreign object detection metric Γ.

The sequent error over misalignment when the sense coils are stacked, as shown in Fig. 6.15, is also numerically analyzed. Similar to what is presented in FC-TPM error correction over misalignment in Chapter 3, stacked sense coils show accurate Tx coil reconstruction over Rx coil misalignment, as shown in Fig. 6.16.

However, sense coils cannot place nearby the Rx coil, as shown in Fig. 6.17 and Table 6.4,

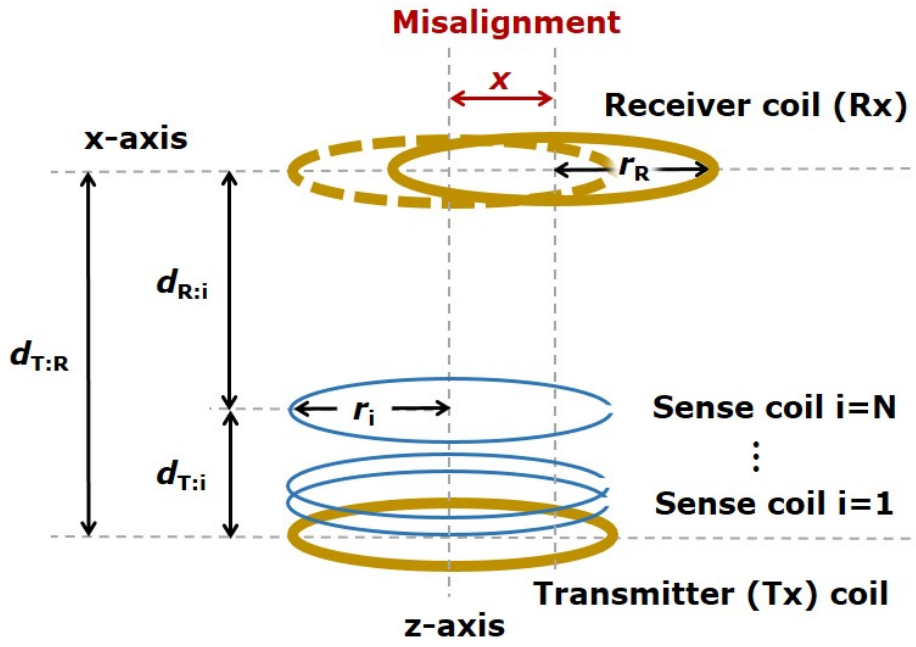

Figure 6.15. The sense coils are stacked for the Tx coil current reconstruction over Rx coil misalignment.

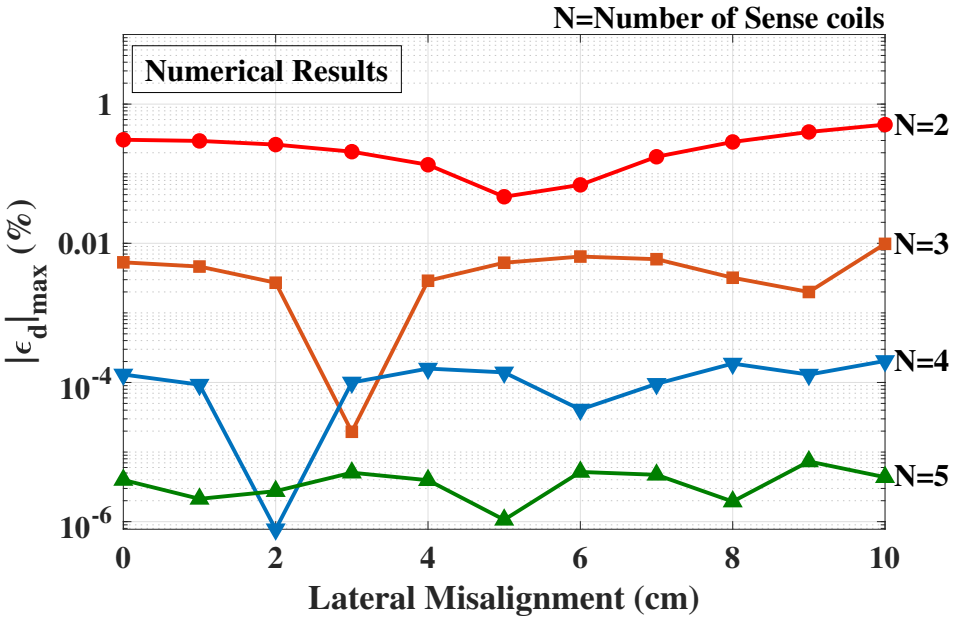

Figure 6.16. Numerical model results: the Tx coil current can be reconstructed accurately by stacked sense coil voltages and non-varying geometric parameters regardless of Rx coil misalignment.

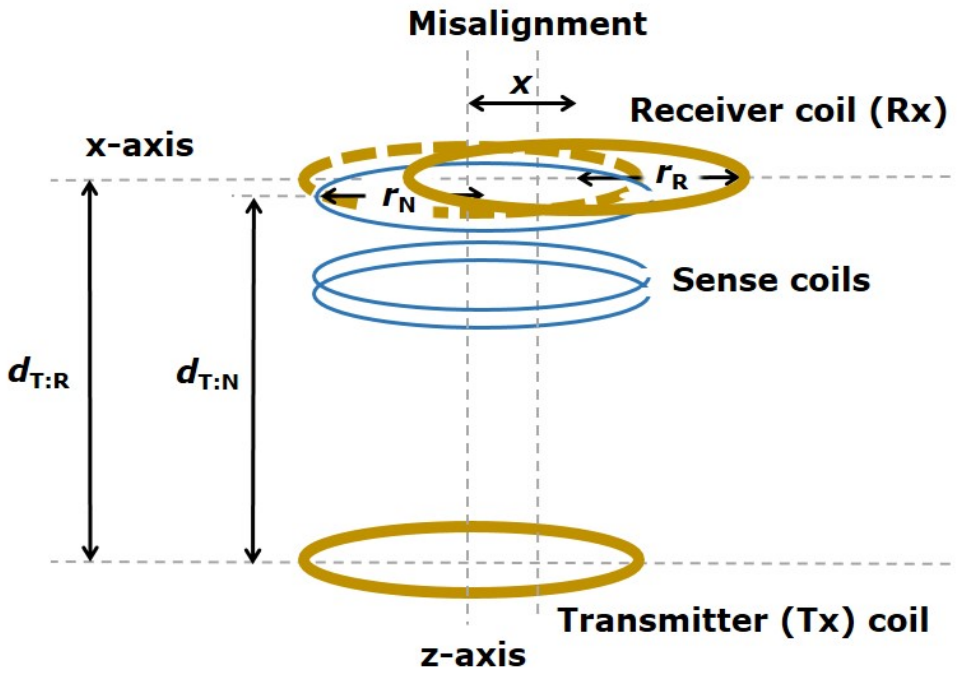

Figure 6.17. The sense coils are placed nearby Rx coil, resulting in inaccurate Tx coil reconstruction over misalignment.

because the coupling coefficients between the Rx and sense coils are significantly different from that between the Rx and Tx coils, which is quadratic over misalignment, as shown in Fig. 6.18. As expected, the Tx coil reconstruction is not accurate over Rx coil misalignment. Fig. 6.19.

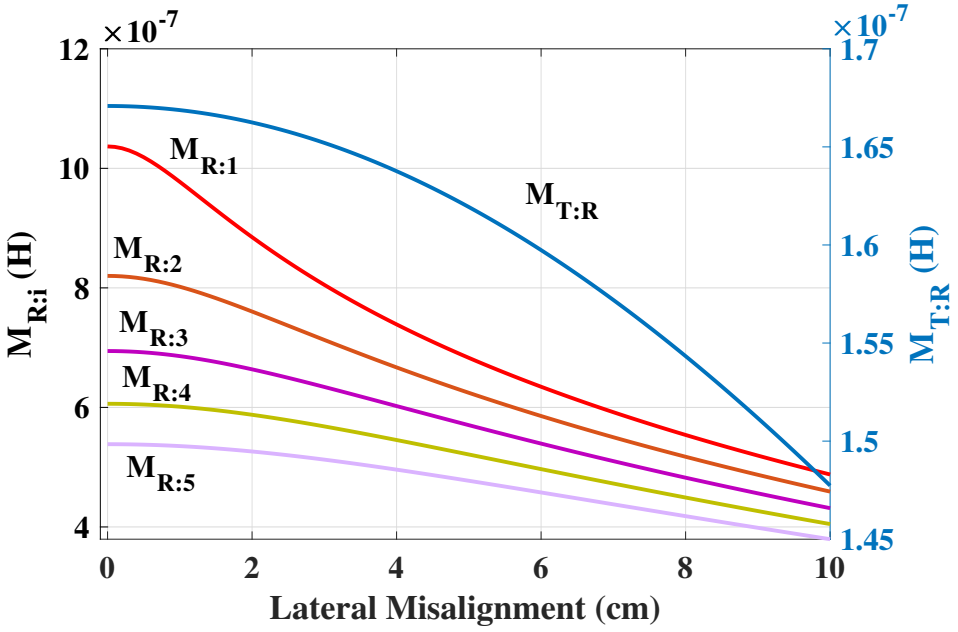

Figure 6.18. When the sense coils are close to the Rx coil, the mutual inductance between two coils is not quadratic, comparing to quadratic mutual inductance between the Tx and Rx coils.

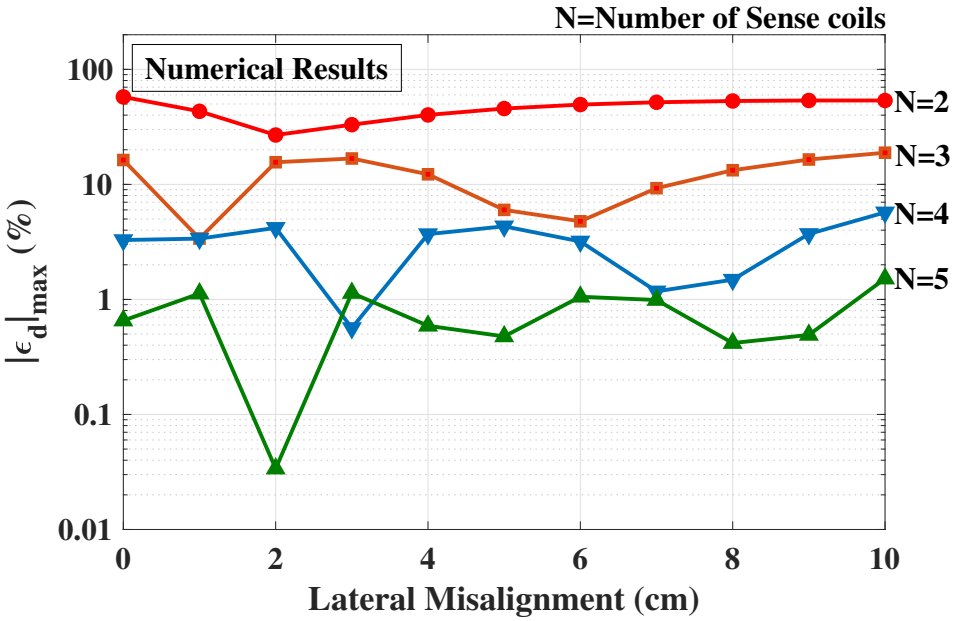

Figure 6.19. Numerical model results: the Tx coil current is not reconstructed accurately by sense coils which are closer to mobile Rx coil.

6.6 Hardware Results

Electromagnetic model-based foreign object detection (EM-FOD) was demonstrated in hardware. In this section, it is demonstrated that foreign objects at three representative locations can be detected at a low pre-startup power level (9 W) by only two single-turn sense coils. The same foreign object detection is performed at a kW-level high power to show that the EM-FOD metric is power level invariant.

Sense coils consist of 42 AWG (0.06335 mm outer diameter) coaxial wires;[10] they are single-turn, open-circuited, and placed on the same plane, which is 2.5 cm above the Tx coil, as shown in Fig. 6.20 and Fig. 6.21. Two sense coils (22.5 and 17.5 cm radii) were used to reconstruct the Tx coil current, where the radii of the Tx and Rx coils were 22.5 cm each.

The Tx and Rx coils were driven by identical current-mode class D (CMCD) converters [76; 77], whose circuit diagram is shown in Fig. 6.22. The phase angle between two gate signals in one converter[11] was maintained as 90° [76]. The phase angle of the gate signals between the Tx- and Rx-side CMCD converters S_1 and S_3 were adjusted to effect changes in the coil currents that correspond to different equivalent output load resistances to obtain the data for the calibration.

A single dc power supply held the shared voltage V_{dc} for the dc input and output, where the dc output of the receiver CMCD converter was fed into the dc input of the transmitter. The power supply only supplied the power loss where the power contributing to the wireless power transfer circulated inside the loop. The entire EM-FOD testbed is shown in Fig. 6.23. The Tx coil current was measured by a current transformer (Pearson Model 110).

When the positions of the Tx and Rx coils were fixed, the geometric parameters α_1 and α_2 in the *normal model* in (6.16) and (6.17), i.e. with no foreign objects, were calibrated. After calibration, three different foreign objects: (i) 16 oz aluminum can; (ii) aluminum foil; and (iii) U.S. nickel coin, were placed in three different locations: (i) center; (ii) middle; and (iii) edge

[10] The braid of the coaxial cable, grounded on only one end, is used as an electrostatic shield from the high voltage Tx and Rx windings [87].

[11] The phase angles are: (i) between S_1 and S_2 pair in the Tx side CMCD converter; and (ii) between S_3 and S_4 pair in the Rx side CMCD converter.

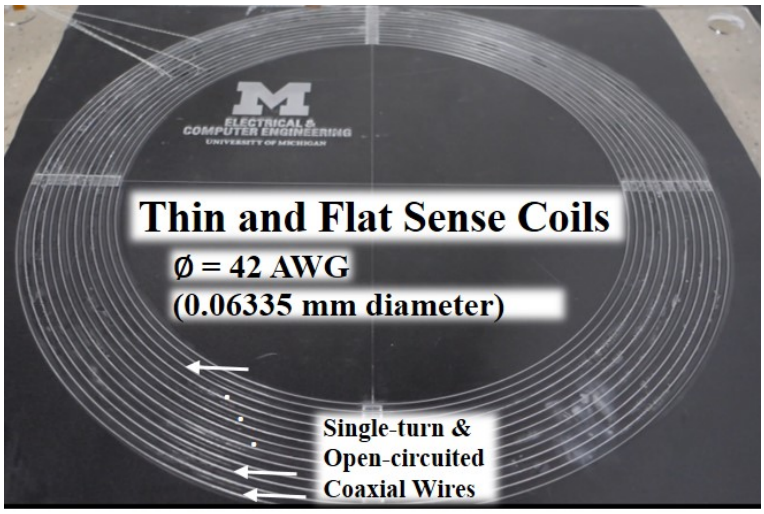

Figure 6.20. Single-turn sense coils are thin and flat. 42 AWG (0.06335 mm diameter) wires were used for the hardware testbed.

above the Tx coil, as shown in Fig. 6.24 and Fig 6.25. The EM-FOD detection metric Γ, defined in (6.38), was calculated with and without foreign objects. The input dc power supply voltage (V_{dc}) was 29 V, and the operating frequency for WPT was 85 kHz, as specified in SAE J2954. The sense coil voltages and Tx coil current were recorded on an Elsys TraNET 204E, which provided 20 MHz sampling frequency with 16-bit resolution, as shown in Fig. 6.26.

Fig. 6.27 shows the experimental results. The Tx coil current reconstruction was accurate (0.006% for the worst-case error) when there was no foreign object. After the foreign objects were placed in the WPT system, the detection metric increased according to the volume and position of the foreign objects, which demonstrated that the metric indicates the quantity of electromagnetic coupling to the foreign objects. Note that the metric was plotted in logarithmic scale. When the 21 mm diameter U.S. nickel coin was placed on the center, the detection metric was at least 5.7 times higher than the metric without a foreign object. When the 16 oz aluminum can was located in the edge, the detection metric was more than 1,000 times higher. It is worth noting that the pre-startup power level was low (9 W), meaning that a kW-level full-power test, which may be high-risk, is not necessarily needed. The power level was increased to a 1,018 W to verify that EM-FOD is power level invariant. The input dc voltage was 302.5 V and the Tx coil current was 11.9 A_{rms}, as shown in Fig. 6.28. The EM-FOD detection metric Γ at kW-level full-power was

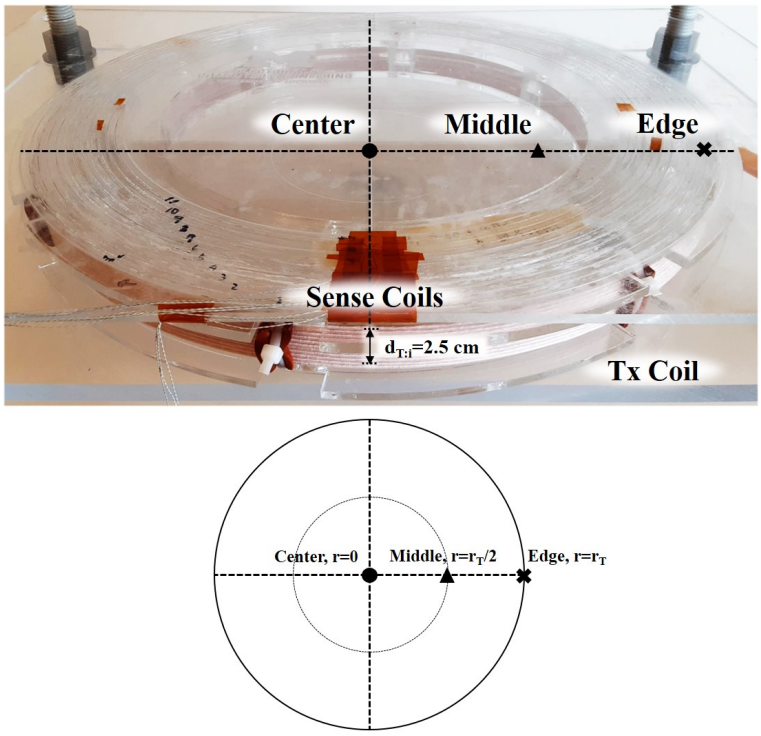

Figure 6.21. EM-FOD with three different foreign objects was examined at three different locations.

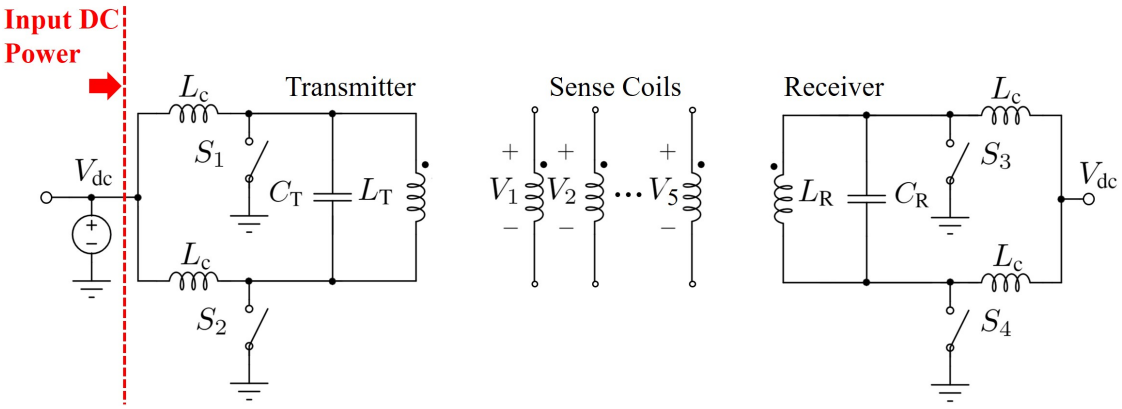

Figure 6.22. The Tx and Rx coils were driven by current-mode class D converters. Two sense coils were used for demonstrating EM-FOD with a stationary Rx coil. Five sense coils were used for misalignment-invariant EM-FOD demonstration, presented in Section 6.7.

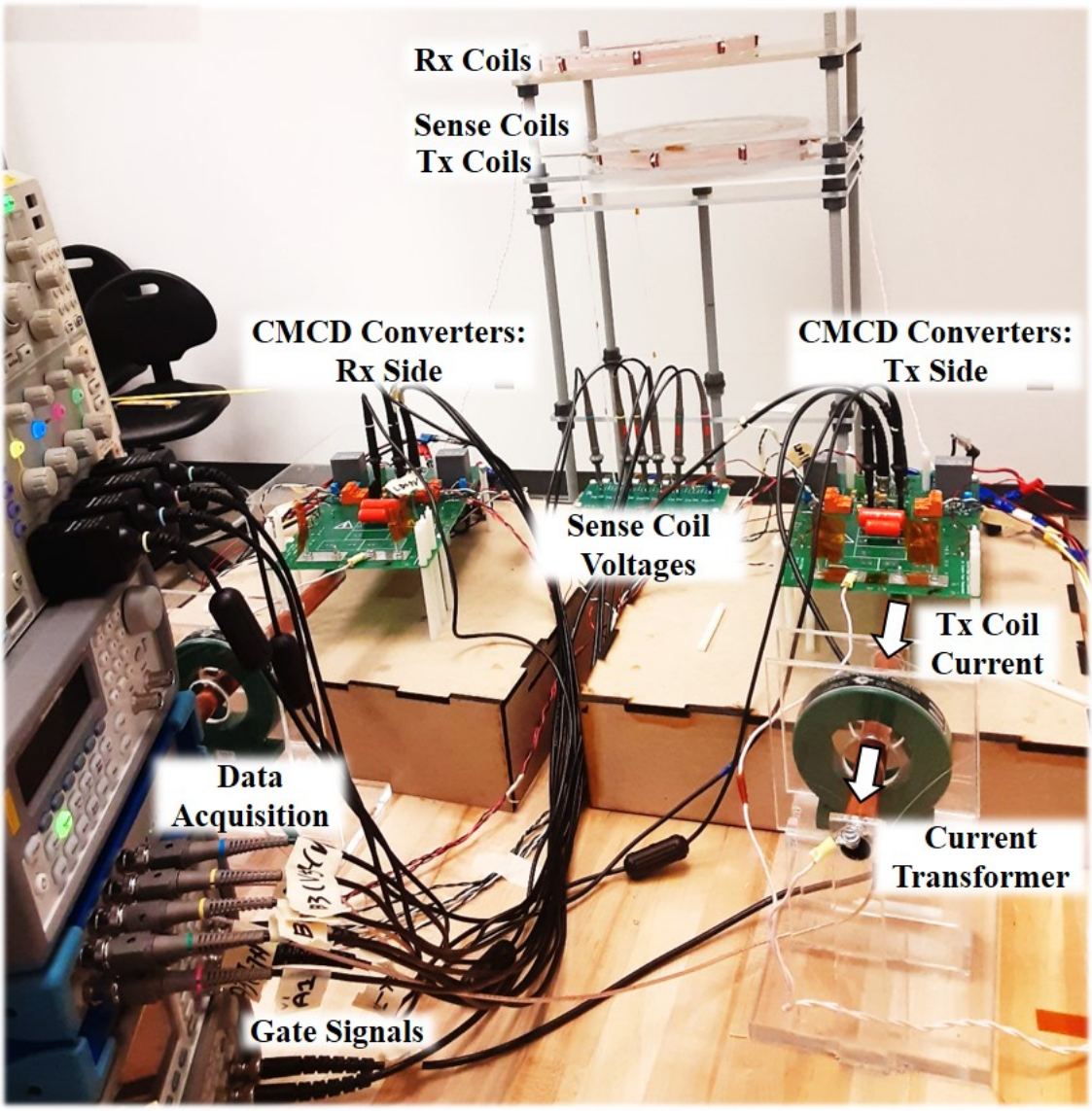

Figure 6.23. Electromagnetic model-based foreign object detection (EM-FOD) on a wireless power transfer testbed.

Figure 6.24. EM-FOD with three different foreign objects was examined.

nearly invariant from the metric at the pre-startup power level of 9 W, to within experimental precision, as shown in Fig. 6.29.

6.7 Hardware Results: Misalignment Invariant EM-FOD

Misalignment invariant EM-FOD was also demonstrated in hardware using five-sense coils (radii of 22.5, 21.5, 20.5, 19.5, and 18.5 cm), which were placed on the same flat plane, as shown in Fig. 6.20. A 16 oz aluminum can, aluminum foil, and a U.S. nickel coin at the edge were tested with up to 10 cm lateral misalignment (based on SAE J2954) of the Rx coil, as shown in Fig. 6.30. Sense coil voltages and the Tx coil currents are shown in Fig. 6.31. When there was no foreign object, the geometric parameters, λ_i were calibrated. After the calibration, the foreign objects were placed, and the Tx coil currents were reconstructed again at each misalignment.

Fig. 6.32 shows the hardware results. When there is no foreign object, the Tx coil currents are

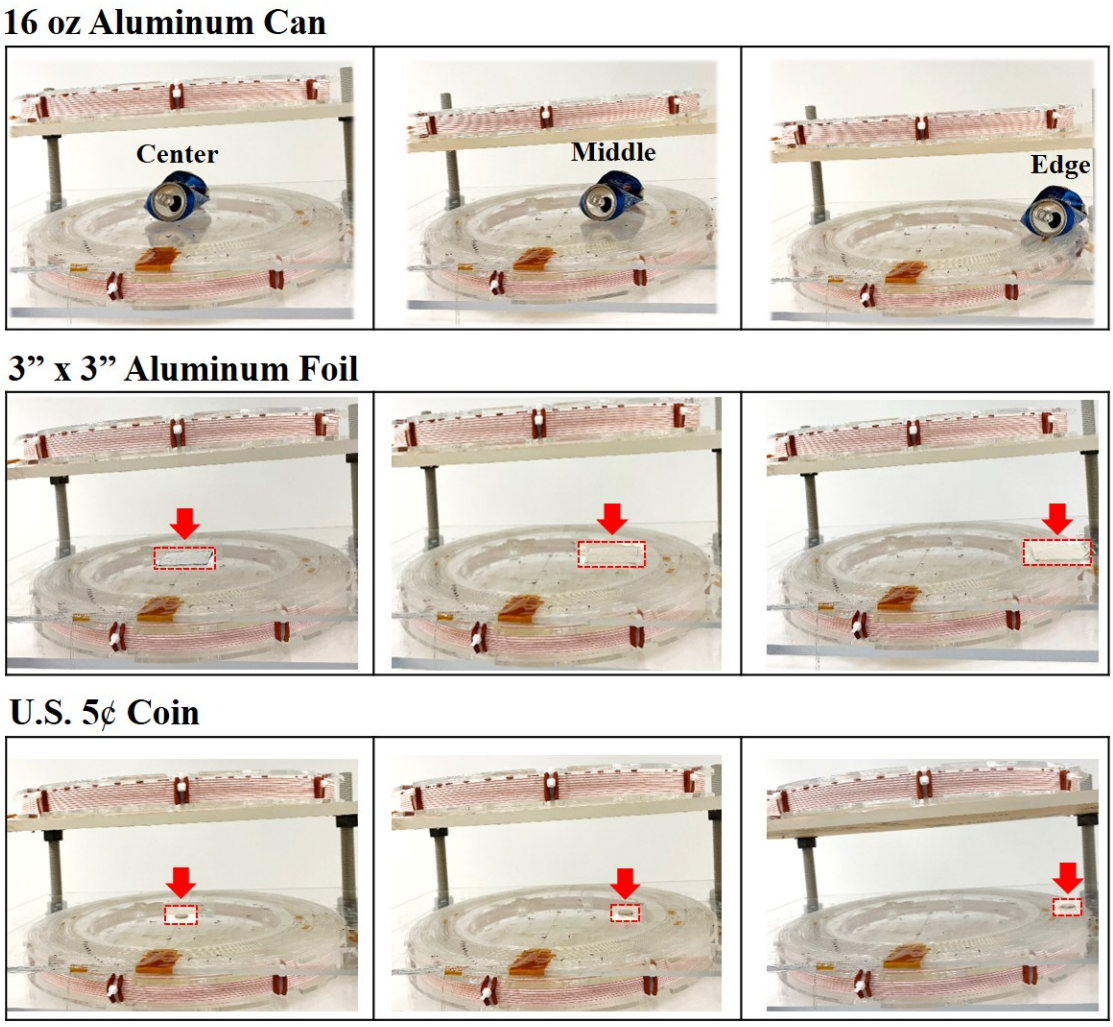

Figure 6.25. EM-FOD with three foreign objects in different positions was examined.

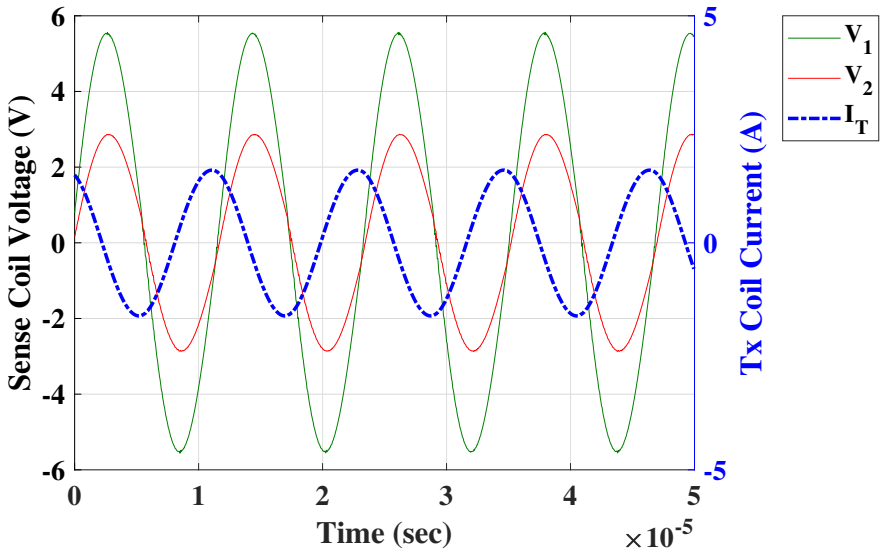

Figure 6.26. Sense coil voltages and the Tx coil current when the input Tx power was 9 W. The Tx coil current was 1.1 A_{rms}. The data was measured and recorded by a 20 Msamples/s, 16-bit data acquisition system.

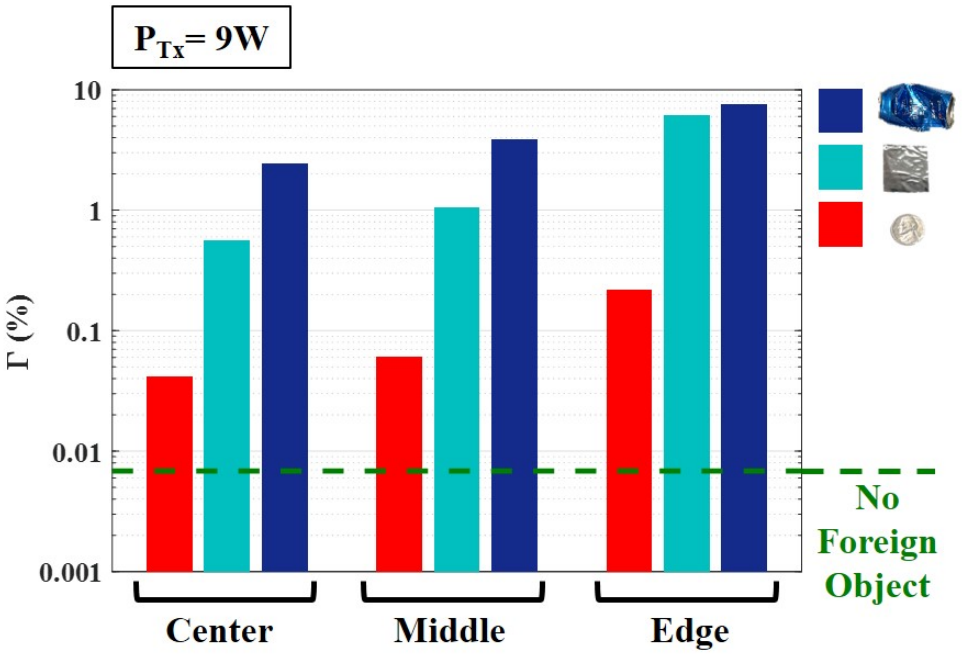

Figure 6.27. Hardware results for the EM-FOD with two sense coils, when the input power was only 9 W. With no foreign object, the detection metric Γ (y-axis, logarithmic scale) was within 0.01%. With a foreign object, the detection metric significantly increased.

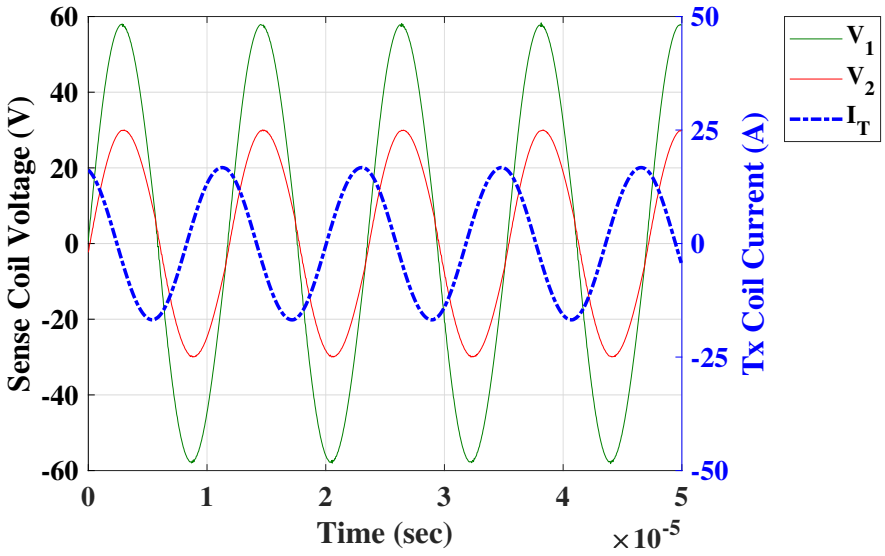

Figure 6.28. Sense coil voltages and the Tx coil current when the input Tx power was 1,018 W. The Tx coil current was 11.9 A_{rms}. The data was measured and recorded by a 20 Msamples/s, 16-bit data acquisition system.

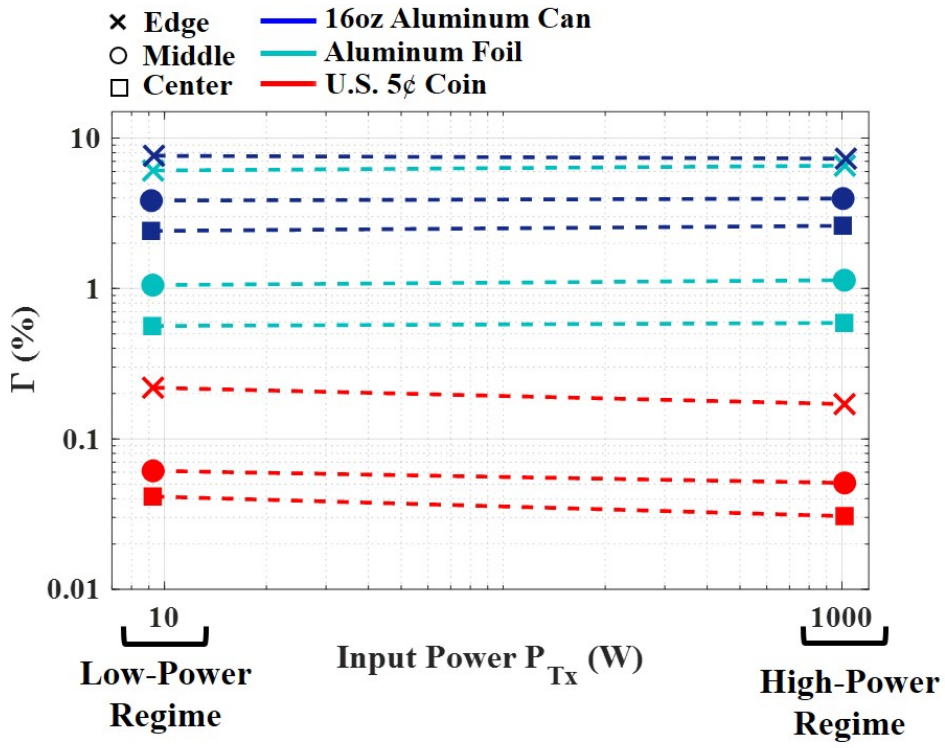

Figure 6.29. The detection metric was invariant from low- to high-power levels.

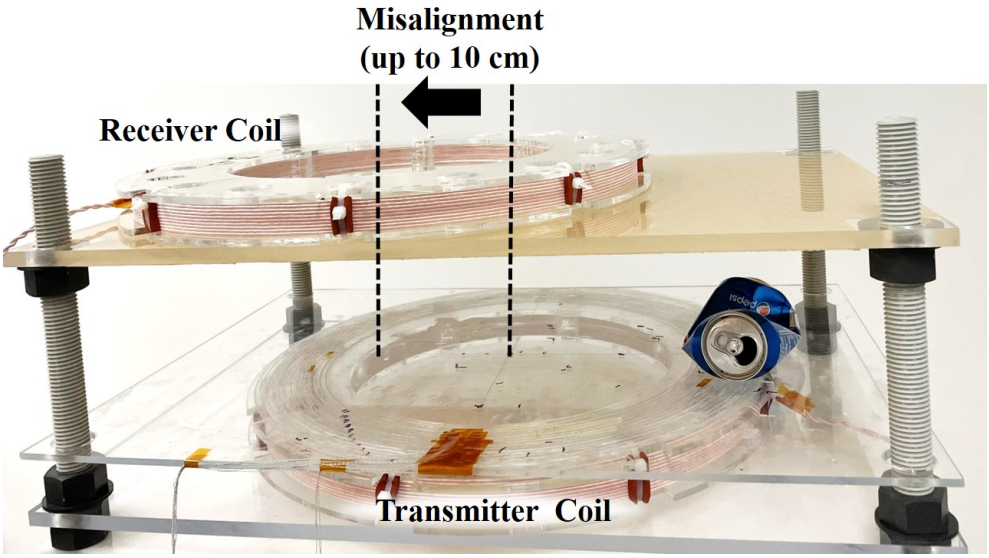

Figure 6.30. Hardware setup for EM-FOD over Rx coil misalignment.

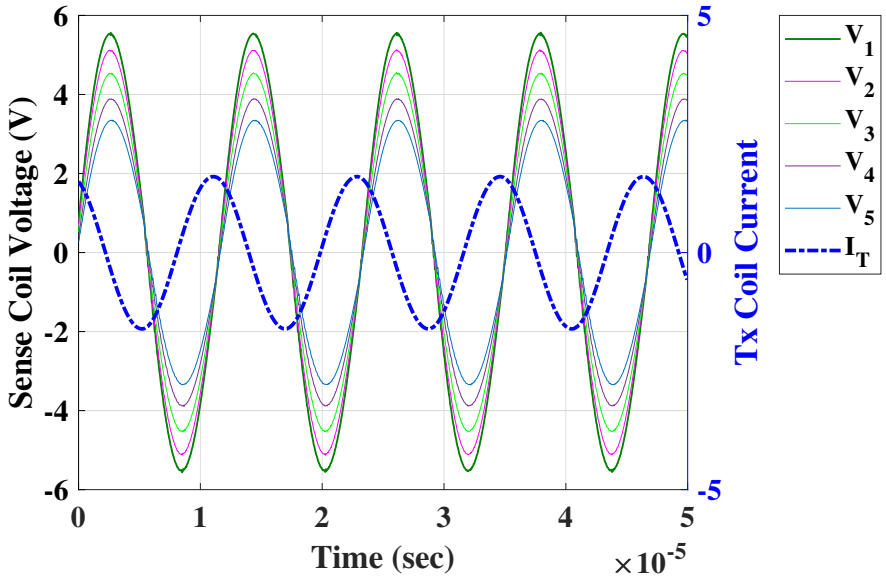

Figure 6.31. Five sense coil voltages and the Tx coil current: the Tx coil current was 1.1 A_{rms}, when the input Tx power was 9 W. This data was plotted when the misalignment was 0 cm, where input power was the maximum.

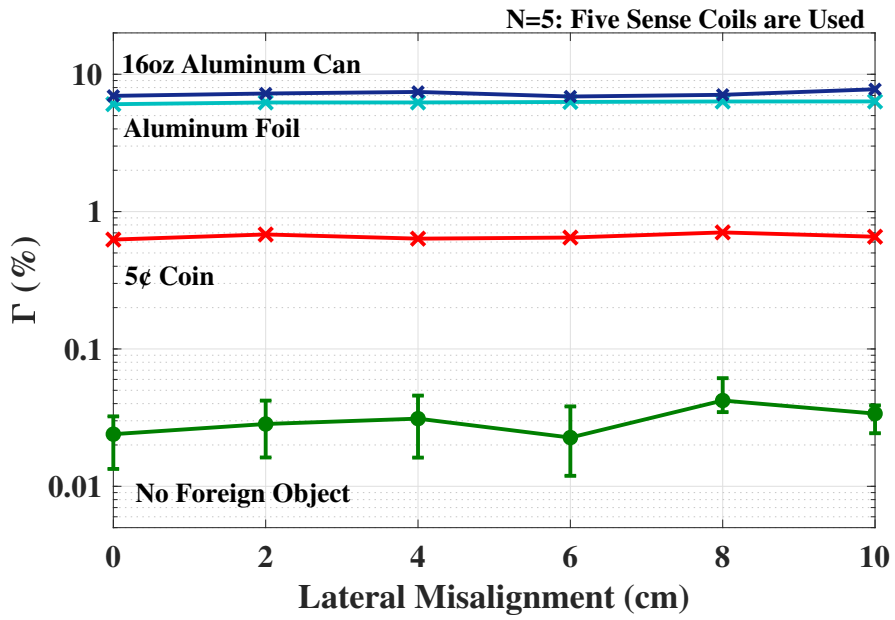

Figure 6.32. Hardware results for EM-FOD over Rx coil lateral misalignment; a foreign object at the edge can be resolved by the sequent errors from the transmitter coil current reconstruction as the detection metric regardless of misalignment.

reconstructed accurately (0.06% worst-case error) over misalignment. As expected, the detection metric Γ increases significantly when there is a foreign object. The metric is very nearly consistent over misalignment, which demonstrates misalignment invariant EM-FOD.

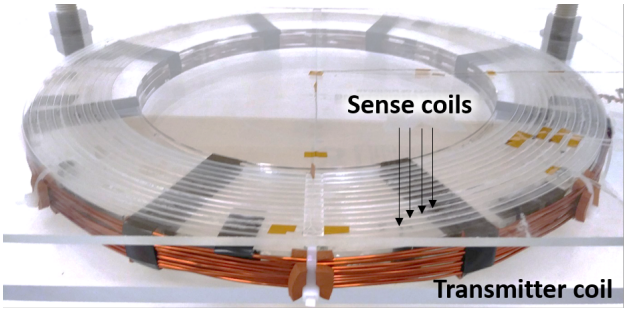

Figure 6.33. Single-turn sense coils are placed above the solid copper wire wound Tx coil.

6.8 Hardware Results II: Different Driving Circuits With Solid Tx and Rx Wires

In this hardware demonstration, the Tx and Rx coils are changed to the solid copper wires,[12] and the driving circuits of the Tx coil is series-series resonated [12] half-bridge inverter when the Rx coil is connected to the passive- resistive load, as shown in Fig 6.33 and Fig. 6.34. Accurate EM-FOD with two sense coils is shown when Tx and Rx coils are solid copper wires, driven by series-series resonant half-bridge circuit.

The same 42 AWG (0.06335 mm outer diameter) coaxial wires were used for sense coils; they were single-turn, open-circuited, and placed on the same plane, which was 2 cm above the Tx coil, as shown in Fig. 6.33. Two sense coils (21.5 and 19.5 cm radii) were used to reconstruct the Tx current, where the radii of the Tx and Rx coils were 23 cm each. The geometric parameters $\alpha_{1,2}$ in the *normal model* in (6.15), without foreign objects, were calibrated by four different resistive loads (R_L = 15, 20, 30, and 40 Ω) in the Rx output, as shown in Fig. 6.35. After calibration, two different aluminum cans (4 oz and 16 oz) were placed in three different locations above the Tx coil, as shown in Fig. 6.34. The detection metric was calculated for both cases with and without foreign objects. The input dc power supply voltage (V_{dc}) was 25 V, and operating frequency for WPT was 90 kHz.

Fig. 6.36 shows the experimental results. The Tx current reconstruction was accurate (0.01%

[12] In general, the copper wires have larger eddy current losses than litz wire.

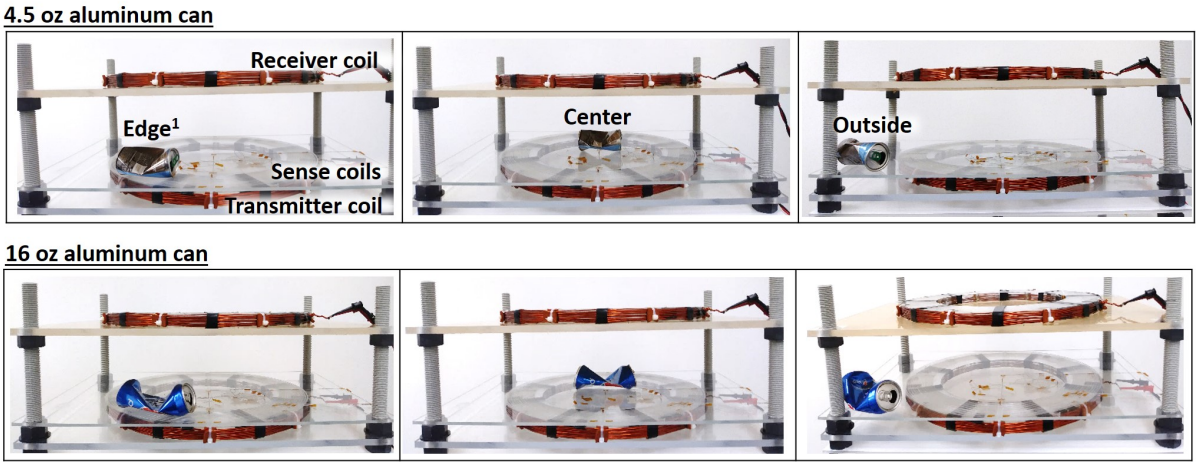

Figure 6.34. Hardware setup for the electromagnetic model-based foreign object detection (EM-FOD). Two different-sized aluminum cans were used as foreign objects and placed at three different location (edge, center, and outside) to the Tx coil.

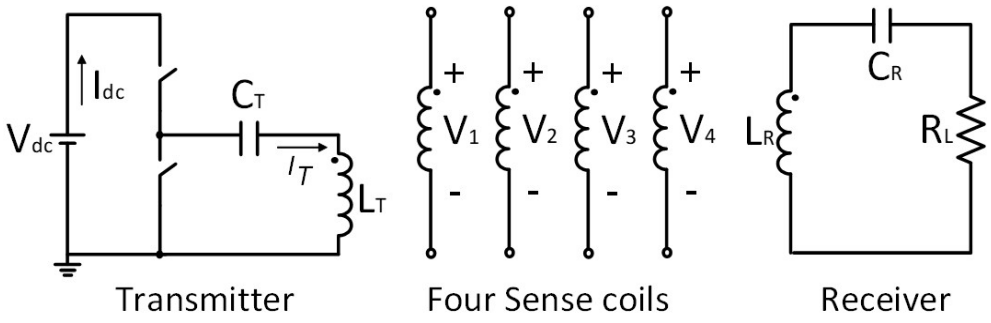

Figure 6.35. Series-series resonant WPT with sense coils was used in hardware. Two sense coils were used for demonstrating EM-FOD at fixed Rx coil. Four sense coils were used for demonstrating misalignment-invariant EM-FOD.

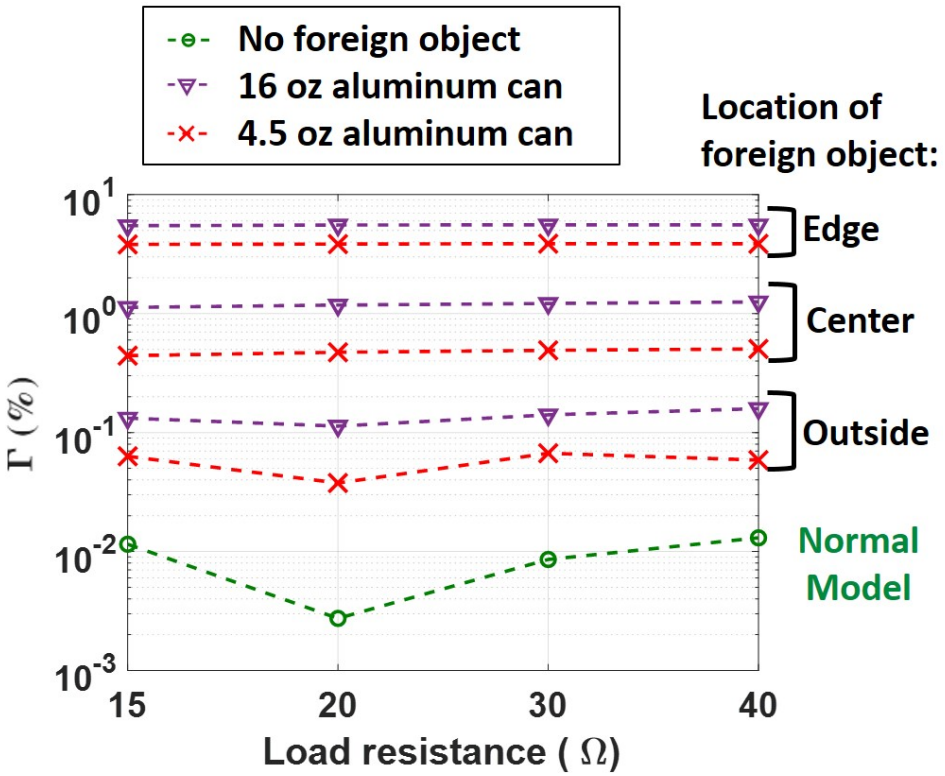

Figure 6.36. Hardware results for the EM-FOD with two sense coils. The detection metric when there is no foreign objects (y-axis, logarithmic scale) were within 0.01%. The detection metric increased with foreign objects.

of the worst case error) when there was no foreign object. After the aluminum cans were placed in the WPT system, the detection metric Γ increased according to the volume and position of the cans, which demonstrated that the metric indicates the quantity of electromagnetic coupling to the foreign objects. Note that the detection metric was plotted in logarithmic scale. The detection metric, caused by foreign objects, were at least 40 times higher than the metric without foreign objects, when they were within the boundaries of WPT, e.g. edge and center (Fig. 6.34), and approximately a factor of 5 when the foreign objects were outside the Tx coil. Furthermore, foreign objects were detected even when the input power levels were low (below 22 W).

Misalignment invariant EM-FOD was demonstrated with solid copper Tx and Rx coils and same power electronics driving circuit using four-sense coils (radii of 22.5, 21.5, 20.5, 19.5 cm), which were placed on the same flat plane, as shown in Fig. 6.33. A 16 oz aluminum can at the edge of the Tx coil was tested with up to 10 cm lateral misalignment of the Rx coil. Calibration of the geometric parameter, λ_i was performed when there was no foreign object by 24 data points; 4 data points from the resistive loads in the Rx output (15, 20, 30, and 40 Ω), were measured at each misalignment point (6 data points: 0 to 10 cm, 2 cm interval).

After the calibration, the aluminum can was placed, and the Tx currents were reconstructed again at each misalignment, using the same geometric parameters, λ_i.

Fig. 6.38 shows the hardware results. When there is no foreign object, the Tx currents are reconstructed accurately (0.06% worst-case error) over misalignment. Furthermore, the detection metric still increases significantly when there is a foreign object (purple-inverted triangles). The detection metric is very nearly consistent over misalignment, which demonstrates misalignment invariant EM-FOD with lossy solid wire Tx and Rx coils, driven by series-series resonant half-bridge power converter.

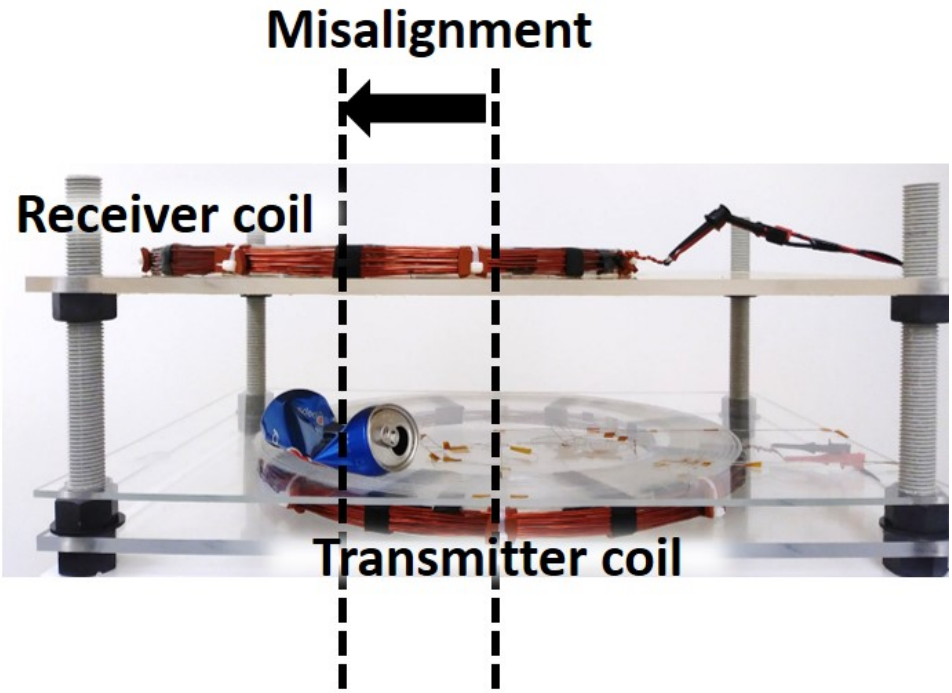

Figure 6.37. Hardware setup for EM-FOD under Rx coil's misalignment.

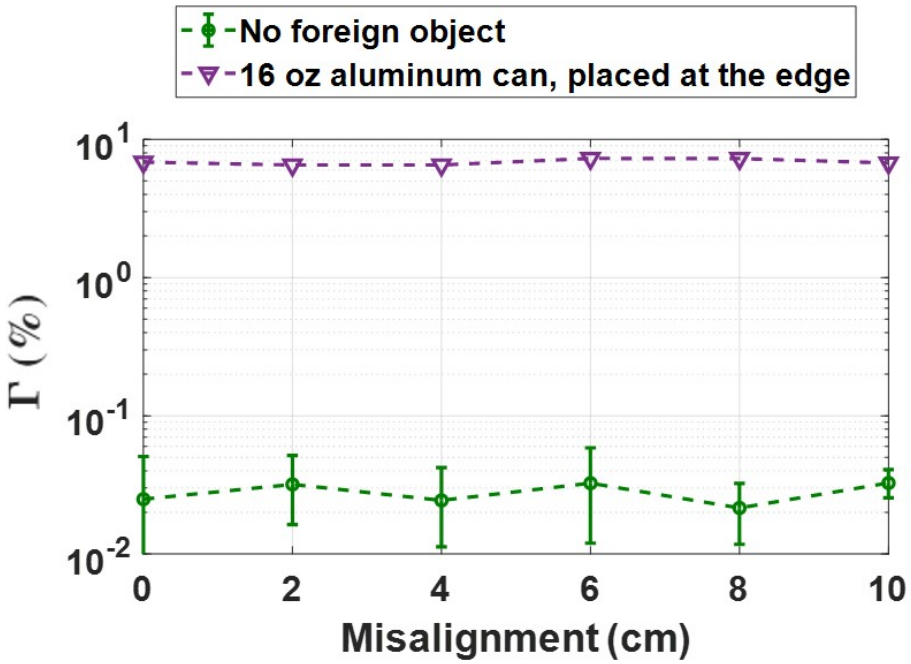

Figure 6.38. Hardware results for EM-FOD under misalignment; the foreign object can be detected by the detection metric regardless of the misalignment.

CHAPTER 7

Calibration-Transfer Strategy

A robust calibration method is needed for the fair and accurate measurement of the wireless power transferred to electric vehicles using FC-TPM. A prevalent obstacle to affordable, reliable, and accurate measurements in the field is lack of suitable *transfer standards*. In this chapter, both a transfer standard and a calibration path are presented towards the standardization of power metering in wireless power transfer.

7.1 Chapter Introduction

Calibration accuracy can be severely degraded through poor *transfer standards*. Primary calibration is performed in a controlled environment in a standard laboratory using a *certified standard*, which can be an involved and time-consuming process. However, calibrations in the field at energy service stations[1] require mobile measurement equipment and transfer standards that are robust, affordable, and fast despite mechanical and environmental stresses from constant transport and outdoor exposure.

In this chapter, a calibration-transfer strategy is presented as part of a practical FC-TPM system that is meant to be compatible with SAE J2954 [45] for wireless charging of EVs. The transfer calibration uses calibrated open-circuited sense coils (provers), which are inherently robust and agnostic to variations in the more sensitive mobile receiver. These provers are calibrated in standards

[1] Estimated to be at least 121,998 in the US when considering stores that also sold gasoline according to the National Association of Convenience Stores (NACS) in 2018.

Figure 7.1. A gas dispenser's metering accuracy is tested through various Weights and Measures Programs. A photo was taken from 'Taking Measure' blog of the National Institute of Standards and Technology (NIST) (Credit: T.Butcher, NIST [1]).

laboratories using terminal measurements from carefully constructed and maintained transmitter coils with meticulously modeled and measured losses.

This calibration strategy is analogous to the current standards for fuel metering of gasoline pumps [116] specified by the Weights and Measures Programs at the National Institute of Standards and Technology (NIST) as illustrated in Fig. 7.1; every meter in every fuel dispenser is inspected annually for accuracy. A prover (calibrated gasoline container) is used to test the accuracy of on-site fuel dispensers. The prover is calibrated and approved in authorized standards laboratories according to provisions in NIST Handbook 105-3 [66].

7.2 Overview of Calibration in Transfer-Power Measurement

Transfer-power is defined in Chapter 2 as the real power, purely dispensed from the Tx coil to the Rx coil through the air. Faraday Coil Transfer-power measurement (FC-TPM) employs open-circuit sense coils that are electromagnetically coupled to the Tx and Rx coils from which transfer-power is reconstructed from sense coil voltages and geometric parameters, derived in (3.13) in Chapter 3. Note that the geometric parameters are constant with respect to different lateral misalignment of the Rx coil, which means the geometric parameters can be calibrated initially without having to account for misalignment later. This calibration requires an independent measurement of transfer-power, presented in Section 5.4. Calibration can also depend on a gold standard transmitter coil with a known loss model and electromagnetic geometry under environmentally-controlled conditions if transfer-power is determined by terminal currents and voltages from this gold-standard transmitter coil, along with the loss models, which include winding and eddy current losses. It is worthwhile to note that the design objective of this transmitter is not efficiency nor high power, but rather a design that is straightforward to analyze, model, and measure; for example, it might consist of cylindrical copper wires rather than litz wire and have an air core rather than a magnetic core.[2]

Uncontrolled environments such as a mobile calibrator with a transfer standard are problematic if a calibrated Rx coil is used as the transfer standard; temperature fluctuations and mechanical stresses cause unpredictable losses and geometry variations. The following section will present a transfer standard that relies on calibrated open-circuited sense coils, whose outputs do not depend on their resistance. Their small physical size and encapsulation are robust to mechanical stresses.

[2]Inductors in standards measurements like a LISN (line-impedance stabilization network) follow conceptually similar strategies in inductor design.

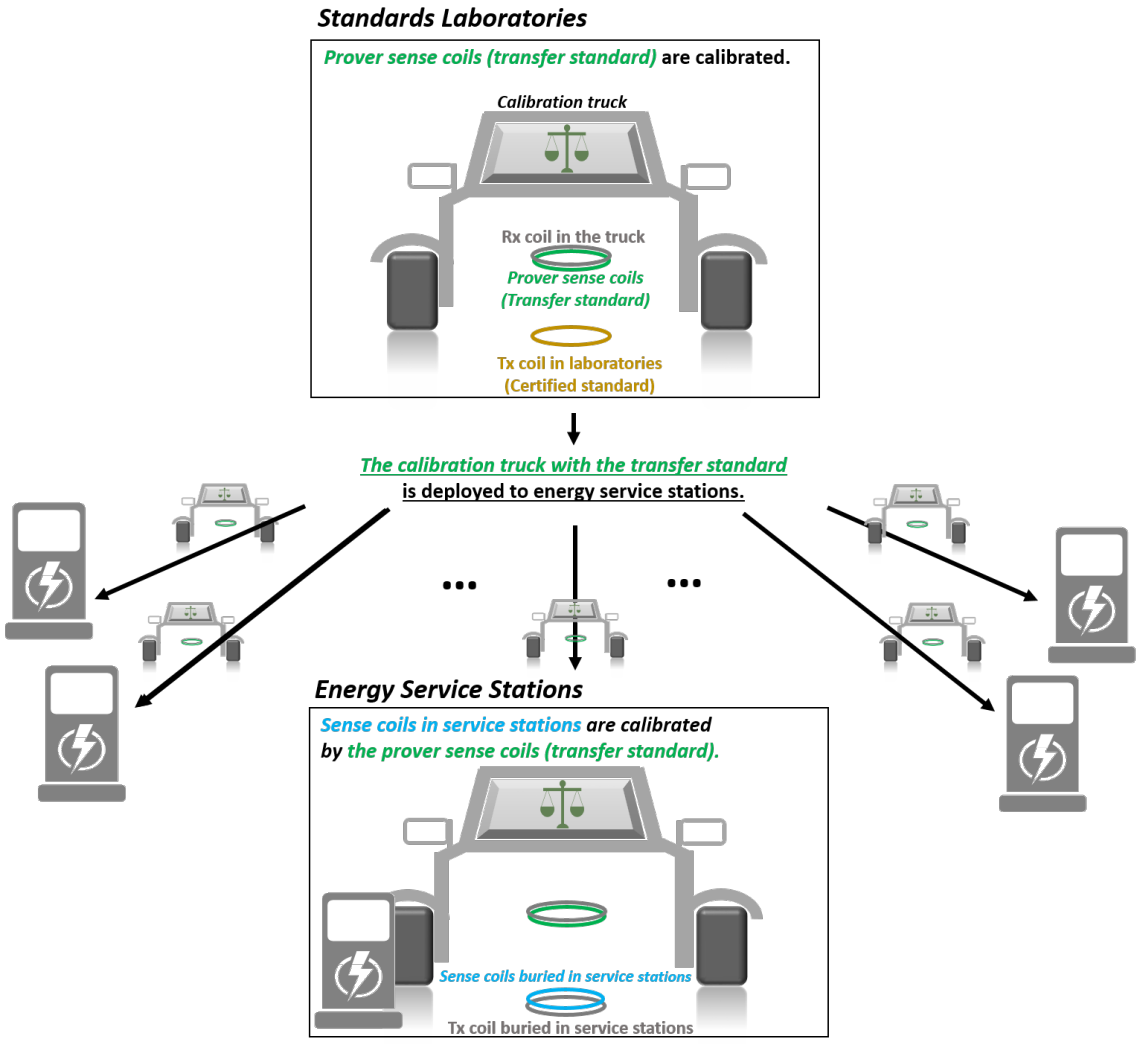

Figure 7.2. Calibration-Transfer Strategy. Prover sense coils (*transfer standard*)[green], calibrated in standards laboratories with a *certified standard* (Tx coil) are deployed to energy service stations to calibrate WPT charger sense coils [blue].

7.3 Calibration-Transfer Strategy

Using calibrated open-circuit sense coils (provers) as a transfer standard requires a calibration strategy; this is illustrated in figure 7.2 with the following steps.

7.3.1 Calibration of Prover Sense Coils in Standards Laboratories

The calibration of the prover sense coils in standards laboratories (figure 7.3) is the most accurate because the Tx coils used as certified standards are carefully characterized and are maintained in a controlled environment. The calibration of the prover coils can be performed slowly, which reduces the measurement errors due to white noise.

7.3.2 Calibration of Wireless Charger Sense Coils in Service Stations

Calibration trucks with prover sense coils are deployed to energy service stations as illustrated in figure 7.4. The prover coils provide the transfer-power measurements needed to calibrate each charger transmitter's FC-TPM sense coils. These prover coils are calibrated for the particular charger's transmitter, but represent an independent measurement that does not require electrical measurements from the transmitter.

7.3.3 Electric Fuel Metering by TPM for Wireless Charging

Calibrated FC-TPM ensures trusted independent measurements of power transferred to EVs (figure 7.5). Only sense coil voltages are needed, which results in robust and accurate metering.

7.4 Numerical Models and Results

Numerical models similar to that used in Section 3.3.3.3 were used to evaluate the accumulation of modeling errors in the transfer of calibrations. Well-known mutual inductance models for circular and filamentary coils were used. Results for the modeling and validation of multiple (six)

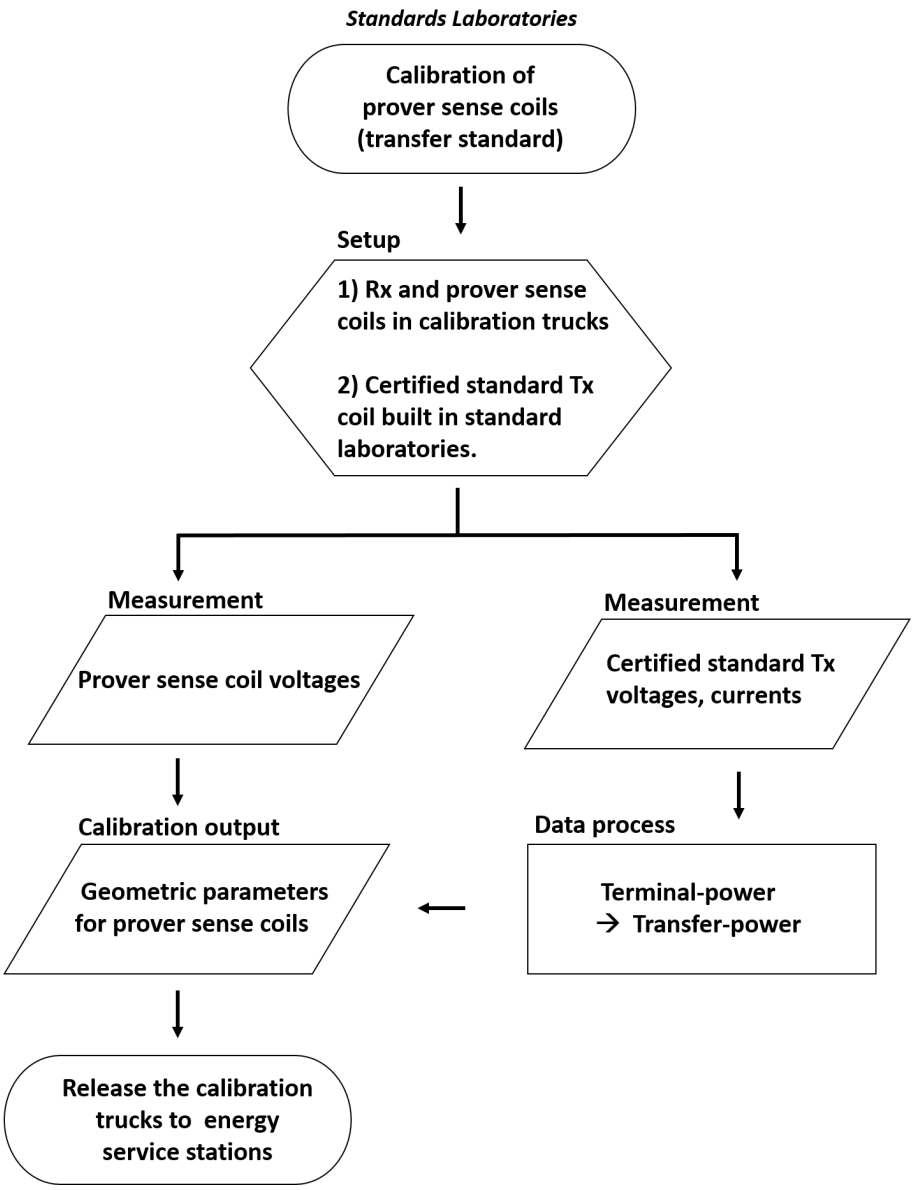

Figure 7.3. Calibration of prover sense coils (*transfer standard*) by a *certified standard* (Tx coil) in standards laboratories.

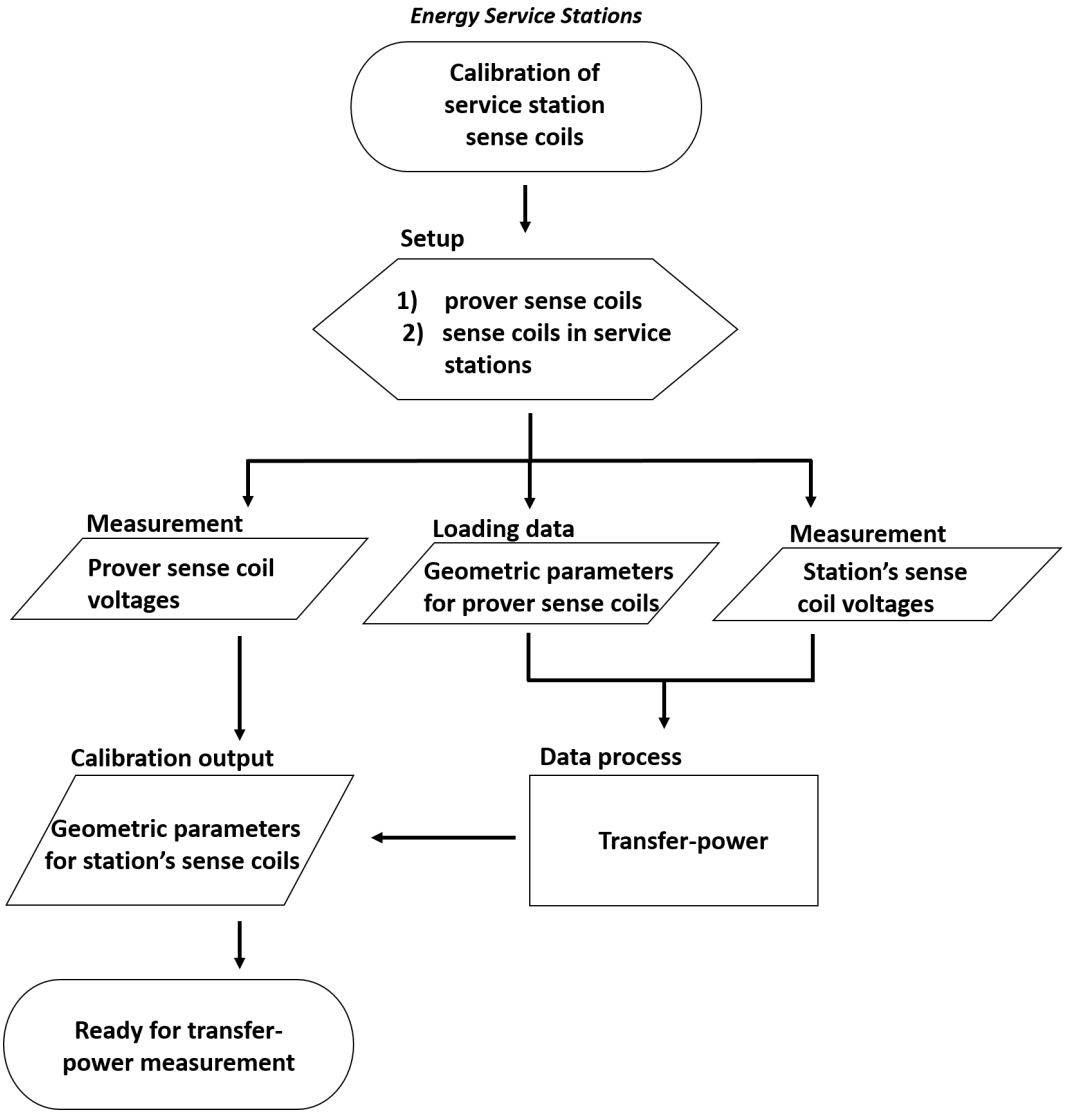

Figure 7.4. Calibration of charger sense coils in energy service stations using measurements from prover sense coils.

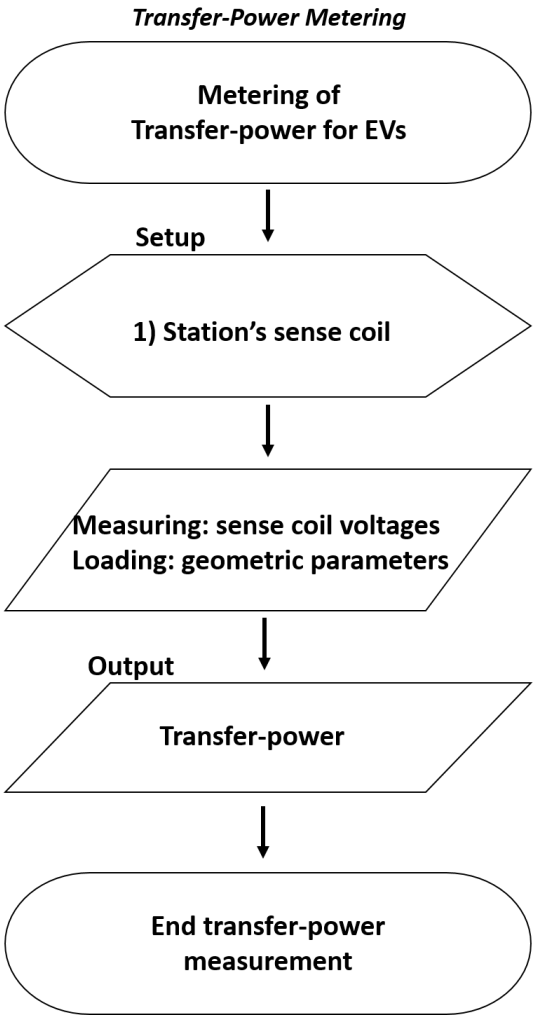

Figure 7.5. Transfer-power metering is used for transactions. Sense coil voltages with calibrated geometric parameters are used to determine the transfer-power.

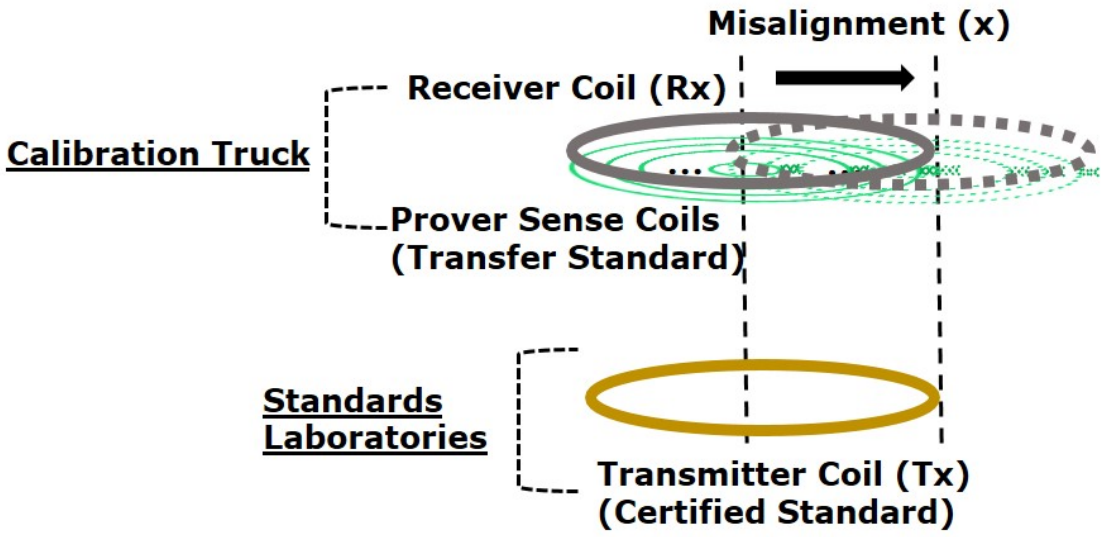

Figure 7.6. Configuration for calibration of coplanar prover sense coils [green] in standards laboratories.

coplanar sense coils that are used for the prover and energy service station sense coils are shown. Through this numerical model, coplanar sense coils, and prover sense coils on the Rx side were demonstrated. Coplanar coils are extremely low-profile and are more robust to geometry changes from mechanical stresses.

The sense coils were placed in the flat plane with different radii (25, 24, 23, 22, 21, and 20 cm). The Tx and Rx coil radii were 25 cm, as shown in figure 7.7. The distance between the Tx and Rx coil was 20 cm. Rx coil currents corresponding to different resistances were varied over 10 data points to calibrate geometric parameters, while using a fixed Tx current. The Tx, Rx, and sense coil voltages were derived from the Tx and Rx coil currents and model parameters; the mutual inductance calculations shown in [55].

Rx coil misalignments of up to 10 cm (SAE J2954) are validated. Numerical data was calculated over a range of equivalent Rx coil resistances (10 data points) and misalignments (11 data points: 0 to 10 cm, 1 cm interval). Calibration was performed with an augmented data set, and TPM errors were determined for each data point using leave-one-out cross-validation (LOOCV) [58]. The configuration of prover sense coils for calibration using in standards laboratories is shown in figure 7.6. Calibration trucks consist of an Rx coil and prover sense coils together with mea-

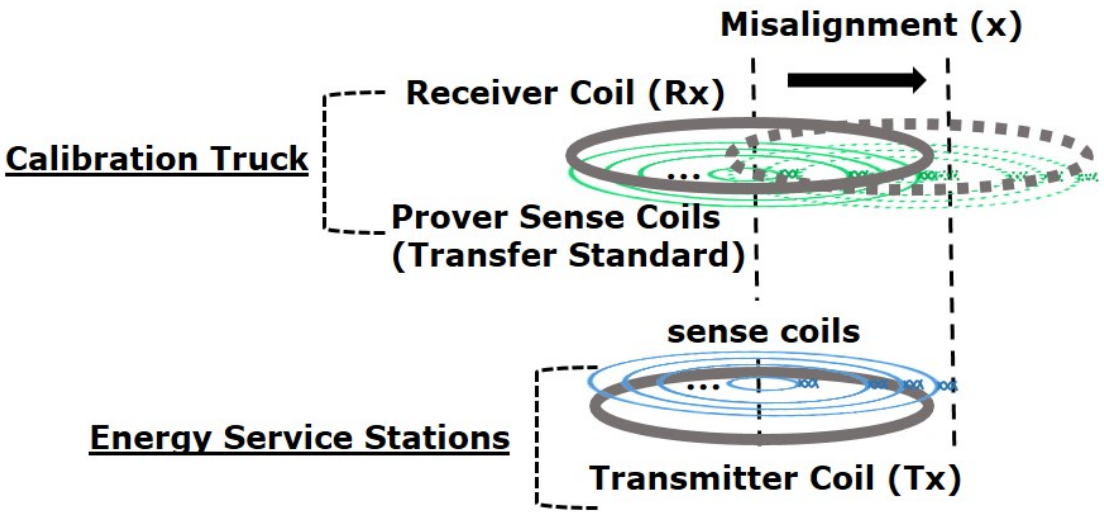

Figure 7.7. Configuration for calibration of TPM coils [blue] in energy service stations. The measurements from the prover sense coils [green] are used to transfer the calibration.

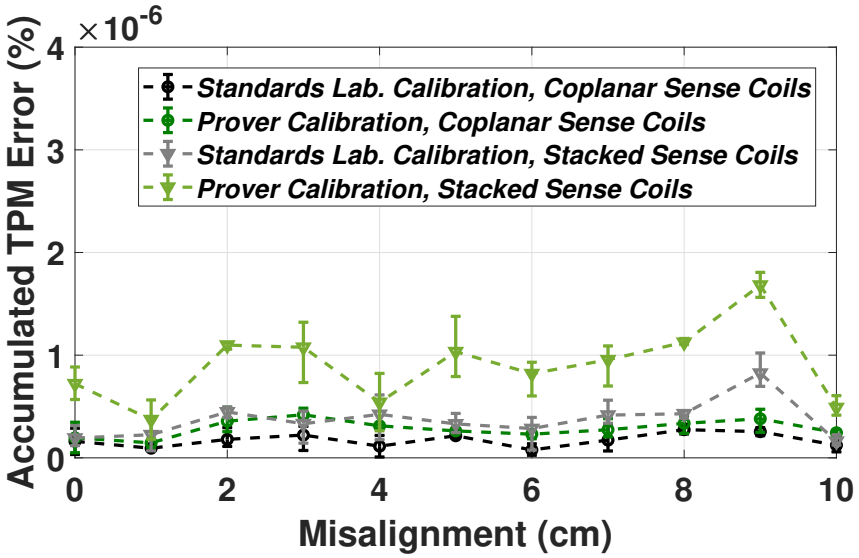

Figure 7.8. Accumulated sense-coil calibration errors are compared between coplanar (flat, low-profile) and stacked (high-profile) sense coils.

surement equipment. Prover sense coils have a fixed position 1 cm below the Rx coil; hence, the coupling coefficients between the two are invariant over misalignment. The modeled calibration errors are plotted in figure 7.8. Note that the FC-TPM errors are nearly invariant to misalignment. The configuration for the calibration of FC-TPM sense coils in energy service stations is shown in figure 7.7. The accumulated modeled errors are shown in figure 7.8, which shows that coplanar sense coils for both the provers and FC-TPM are as accurate as stacked coaxial coils.

CHAPTER 8

Conclusions and Future Work

Ensuring energy safety and security is vital, especially in transportation, pervasive in our daily lives. Wireless power transfer is an emerging technology for charging electric vehicles, which needs to be reasonable and safe to use. Decisions by stakeholders will require fine-grained information about efficiency, energy consumption, and charging safety. This is evidenced by growing efforts to standardize the accurate metering and safe operation of electric vehicle charging. This dissertation has addressed fair metering and safety concerns in wireless power transfer. An electromagnetic model-based method was developed using a small set of non-contact open-circuited sense coils that enable transfer-power measurement and foreign object detection in wireless charging space. The dissertation is concluded by presenting a summary and potential future research path.

8.1 Summary

In Chapter 2, transfer-power was defined from the Poynting vector as the real power transmitted from the Tx to the Rx coil in wireless charging space. Measurement of transfer-power imposes the cost for losses to where they are dissipated, resulting in fair metering, which penalizes stakeholders who cause losses and motivates them to improve systems. Faraday coil transfer-power measurement (FC-TPM) was presented by employing two non-contact open-circuited sense coils, electromagnetically coupled to the Tx and Rx coils. The sense coil voltages are theoretically mapped to

the Poynting vector, validating the fundamental physics of FC-TPM. The transfer-power can be reconstructed by measuring sense coil voltages, where the geometric parameters, which encapsulate the couplings between the Tx, Rx, and sense coils, are needed.

In Chapter 3, we presented an accurate FC-TPM despite geometric variations such as misalignment from the Rx coil. Multiple sense coils are employed, and their voltages are linearly combined to reconstruct the transfer-power where non-varying geometric parameters over misalignment can be derived. The coupling coefficient variations from Rx coil misalignment can be approximated by quadratics to explain the derivation. The new geometric parameters for multiple sense coils can then be calibrated in advance, which is practical for metering in charging stations without knowing misalignment. The fundamental of accurate FC-TPM by combining multiple sense coil voltages is validated over multi-dimensional variations through FEM simulations. Transfer-power was well-reconstructed over simultaneous variations of misalignment, different litz wire types, and operating frequencies.

In Chapter 4, electromagnetically thin and physically flat sense coils were presented by showing the FEM simulation results of negligible eddy current loss dissipation in the sense coils and comparable performance of a flat sense coil set to optimal sense coil geometries between the Tx and Rx coils.

In Chapter 5, FC-TPM was demonstrated in hardware using 1 kW wireless power transfer testbed, which consists of current-mode class D (CMCD) converters, Tx and Rx coils wound from litz wire, and thin sense coils. The transfer-power was reconstructed accurately within 0.1% error despite Rx coil misalignment up to 10 cm. Transfer-power is saliently different from the dc Tx input power or dc Rx output power which aggregate Tx and Rx losses.

In Chapter 6, An accurate and effective method for electromagnetic model-based foreign object detection (EM-FOD) with a wide dynamic range, which is invariant to power level and misalignment, was presented in theory, simulation, and hardware. The detection metric presented for foreign object detection using the sequent error in the Tx coil current reconstruction results from the deviation to an adverse model from an easily calibrated, normal electromagnetic model.

In Chapter 7, a calibration-transfer strategy was presented using low-profile coplanar sense coils to enable the practical deployment of FC-TPM, an accurate and trustworthy measurement of the energy that is transferred to electric vehicles through wireless power transfer. Coplanar sense coils for prover transfer standards overcome sensitivity to the environment and mechanical stress, which is a weakness in transfer-calibration using calibrated receiver coils.

8.2 Future Work

The accurate electromagnetic physics model of wireless power transfer was presented in this dissertation to measure the power and detect foreign objects. Future research can include accurate FC-TPM over all multi-dimensional variations, including other types of charging geometries [17; 117; 118] with corresponding sense coil placement optimization. In addition, the results of this dissertation can open the active research area that FC-TPM can be extended to include magnetic cores where the eddy currents in the magnetic cores can be modeled as a single winding coupled to the rest of the coils. The variations of magnetic geometries due to the cores can be approximated by the polynomials, where the same fundamental of using multiple sense coils can be utilized. One can also explore the impact of the core shape on standardization and calibration's universality.

The fundamental of the electromagnetic physics model to reconstruct the target information can be potentially expanded to detect various abnormal or defective objects that are not included in normal space. A sentinel can be created using a sparse electromagnetic measurement to recover high fidelity information for safety and security in energy systems, which can be modeled as electromagnetic windings. A small number of sensors sample the electromagnetic field to reconstruct the information for the diagnostics and prognostics of comprehensive electromagnetic energy systems. The particular applications in large-scale energy systems can include: (i) fusion energy (e.g., superconducting magnets used for fusion reactors); (ii) medicine (e.g., electromagnets for Magnetic Resonance Imaging (MRI) and Nuclear Magnetic Resonance (NMR)); (iii) electri-

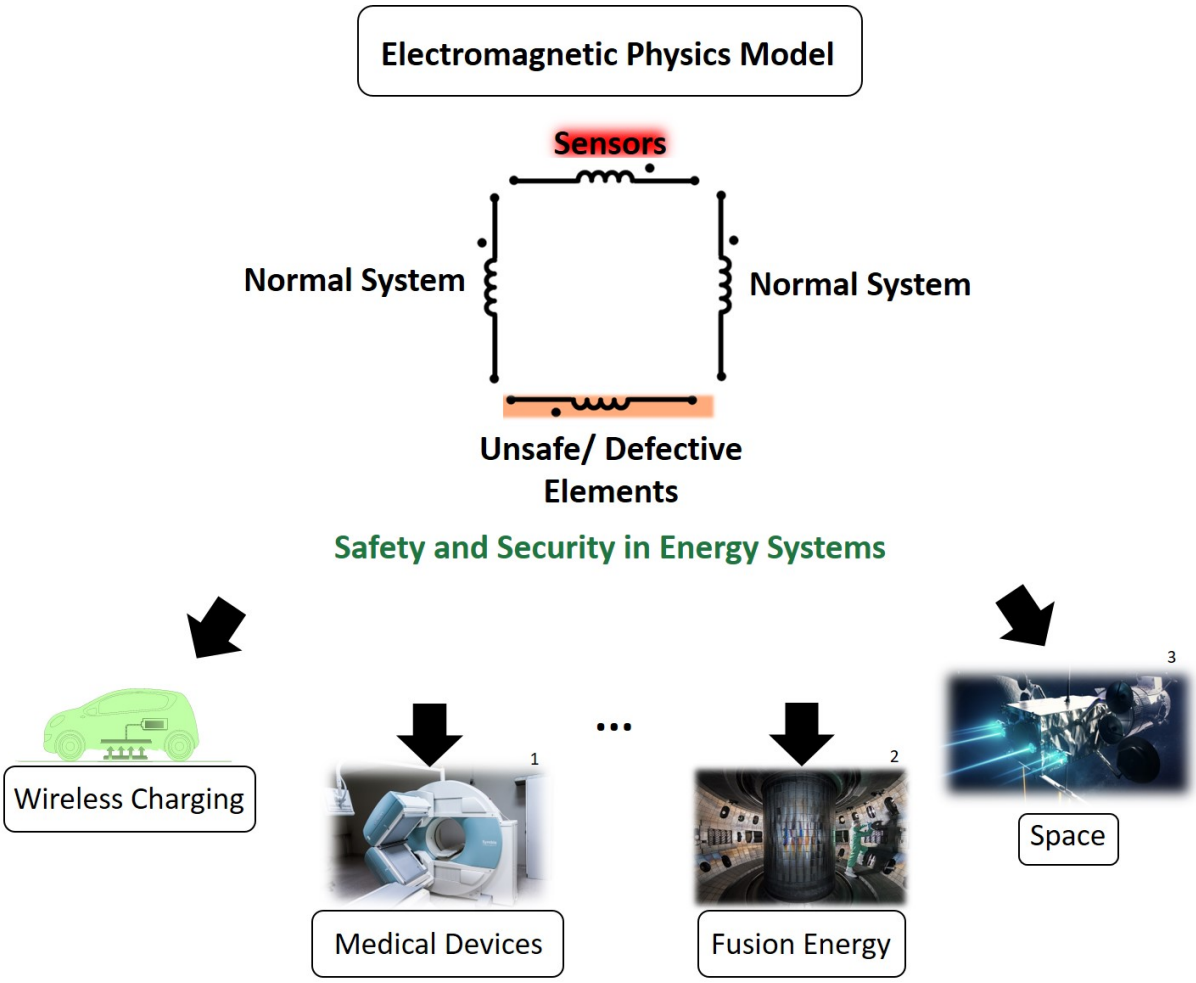

Figure 8.1. The sparse electromagnetic measurement with the physics model can be used for diagnostics and prognostics of electromagnetic energy systems. Photo credits 1: Michal Jarmoluk from Pixabay; 2:© ITER Organization, http://www.iter.org/; 3:Artist's rendering of the Power and Propulsion Element and the Habitation and Logistics Outpost (HALO) in lunar orbit, NASA's Lunar Exploration Program Overview, p24, Sep, 2020.

fied transportations (e.g., Maglev, autonomous underwater vehicles (AUVs), and unmanned aerial vehicles (UAV)); and (iv) Space (e.g., electromagnetic thrusters), as illustrated in Fig. 8.1.

APPENDIX A

List of Variables

α_{ij} Linear coefficient for i and j pair of sense coils in FC-TPM

$\gamma_{_R}$ Factor of external field from receiver interacting with self-field of transmitter

$\gamma_{_T}$ Factor of external field from transmitter interacting with self-field of receiver

κ_{ij} Geometric coupling coefficient from transfer-power to pairwise-product of sense coil voltages i and j

ω Angular frequency

$d_{X:Y}$ Vertical distance between coils X and Y

I_X Coil X current

$k_{X:Y}$ Coupling coefficient between coils X and Y

L_X Coil X self-inductance

$M_{X:Y}$ Mutual inductance between coils X and Y

$P_{\text{d,Rx}}$ Rx coil heat dissipation

$P_{\text{d,Tx}}$ Tx coil heat dissipation

P_{Rx} Rx coil terminal power

P_{Transfer} Transfer-power

$P_{\text{Tx:Rx}}$ Principal transfer-power

P_{Tx} Tx coil terminal power

R_R Rx coil winding resistance with no external field

R_T Tx coil winding resistance with no external field

r_X Radius of coil X

$R_{R:t}$ Eddy current resistance on Tx winding from Rx magnetic field, reflected to Rx winding

$R_{T:r}$ Eddy current resistance on Rx winding from Tx magnetic field, reflected to Tx winding

V_X Coil X terminal voltage

x Rx coil lateral misalignment

APPENDIX B

Derivation of Poynting Vector in Wireless Power Transfer

The real part of the time-averaged complex Poynting vector $\vec{S}$ only has the $\hat{z}$ component, as shown in (2.5),

$$\begin{aligned} \mathrm{Re}\{\vec{S}\} &= \mathrm{Re}\{S_z\} \\ &= \hat{z}\ \frac{3\mu_0 A^2}{16\pi^2 r^5}\sin 2\theta \sin\theta\ \ \mathrm{Re}\left\{j\omega I_R I_T^*\right\}. \end{aligned} \tag{B.1}$$

The transfer-power P_{Transfer} is the average power, which is calculated from (2.1), applying the surface integral to (2.5) over the infinite plane $\mathcal{P}$.

$$\begin{aligned} P_{\text{Transfer}} &= \iint_S S\vec{ds} \\ &= \mathrm{Re}\{j\omega I_R I_T^*\}\int_0^{\infty}\int_0^{2\pi}\frac{3\mu_0 A^2}{16\pi^2 r^5}2\sin^2\theta\cos\theta\, d\varphi\,(\rho\, d\rho) \\ &= \mathrm{Re}\{j\omega I_R I_T^*\}\frac{3\mu_0 A^2}{4\pi}\int_0^{\frac{\pi}{2}}\frac{1}{\sqrt{(z^2\tan^2\theta+z^2)^5}}\sin^2\theta\cos\theta\, z\tan\theta\,\frac{z}{\cos^2\theta}\,d\theta, \end{aligned} \tag{B.2}$$

where

$$\begin{aligned} \rho &= z\tan\theta, \\ d\rho &= \frac{z}{\cos^2\theta}\,d\theta. \end{aligned} \tag{B.3}$$

Equation (B.2) can be simplified further

$$
\begin{aligned}
P_{\text{Transfer}} &= \mathrm{Re}\{j\omega I_R I_T^*\}\frac{3\mu_0 A^2}{4\pi}\int_0^{\frac{\pi}{2}} \frac{1}{z^3}\cos^5\theta\sin^2\theta\cos\theta\,\frac{\sin\theta}{\cos\theta}\frac{1}{\cos^2\theta}\,d\theta \\
&= \mathrm{Re}\{j\omega I_R I_T^*\}\frac{3\mu_0 A^2}{4\pi z^3}\int_0^{\frac{\pi}{2}} \cos^3\theta\sin^3\theta\,d\theta \\
&= \mathrm{Re}\{j\omega I_R I_T^*\}\frac{3\mu_0 A^2}{4\pi z^3}\frac{1}{8}\int_0^{\frac{\pi}{2}} \sin^3 2\theta\,d\theta \\
&= \mathrm{Re}\{j\omega I_R I_T^*\}\frac{3\mu_0 A^2}{4\pi z^3}\frac{1}{8}\int_0^{\frac{\pi}{2}} (1-\cos^2 2\theta)(\sin 2\theta)\,d\theta \\
&= \mathrm{Re}\{j\omega I_R I_T^*\}\frac{3\mu_0 A^2}{4\pi z^3}\frac{1}{8}\int_0^{\pi} (1-\cos^2\alpha)(\sin\alpha)\,\frac{1}{2}d\alpha \\
&= \mathrm{Re}\{j\omega I_R I_T^*\}\frac{3\mu_0 A^2}{4\pi z^3}\frac{1}{16}\int_1^{-1} (1-T^2)(-dT) \\
&= \mathrm{Re}\{j\omega I_R I_T^*\}\frac{\mu_0 A^2}{\pi z^3}\frac{1}{16}.
\end{aligned}
\tag{B.4}
$$

It is worth noting that the Poynting vector plane is chosen as $z = \frac{d_{T:R}}{2}$, and therefore (B.4) is

$$
P_{\text{Transfer}} = \mathrm{Re}\left\{ j\omega\,\frac{\mu_0 A^2}{2\pi d_{T:R}^3} I_R I_T^* \right\}. \tag{B.5}
$$

APPENDIX C

Steps for Obtaining the Winding Resistances and Electromagnetic Parameters

(a) R_T and R_R: The effective winding resistance R_{T} of the Tx coil can be calculated when the Rx coil is removed. The input power P_{Tx} is $\mathrm{Re}\{I_T^* I_T\} R_T$, which is the ohmic loss in the Tx coil. The winding resistance R_T can through the current I_T. Similarly, the winding resistance R_{R} of the Rx coil can also be calculated when the Tx coil is removed.

(b) $R_{T:r}$, $R_{R:t}$: $R_{T:r}$, and $R_{R:t}$ can be calculated when one coil is open-circuited, while the other coil is driven. If the Tx coil is driven by I_T and the Rx coil is open-circuited (I_R=0), the eddy current loss in the Rx coil $P_{\text{Loss,eddy(Rx)}}$ can be derived from (2.26) resulting in

$$P_{\text{Loss,eddy(Rx)}} = P_{\text{Tx}} - \mathrm{Re}\left\{I_T^* I_T\right\} R_T. \tag{C.1}$$

Note that R_T was obtained previously; so $R_{T:r}$ can be calculated

$$R_{T:r} = \frac{P_{\text{Loss,eddy(Rx)}}}{\mathrm{Re}\left\{I_T^* I_T\right\}}. \tag{C.2}$$

Similarly, $R_{R:t}$ can be obtained when the Rx is driven by I_R and the Tx coil is open-circuited ($I_T = 0$)

$$R_{R:t} = \frac{P_{\text{Loss,eddy(Tx)}}}{\mathrm{Re}\left\{I_R^* I_R\right\}}. \tag{C.3}$$

(c) γ_T, γ_R: γ_T, and γ_R can be obtained when both the Tx and Rx currents are in phase, resulting in zero principal transfer-power ($P_{\text{Tx:Rx}}$=0), as discussed in Section 2.2.2. $\gamma_{T,R}$ can be extracted from the the input and output power in (2.26) and (2.27)

$$\gamma_R = \frac{P_{\text{Tx}} - \text{Re}\left\{I_T^* I_T\right\} R_T - \text{Re}\left\{I_T^* I_T\right\} R_{T:r}}{\text{Re}\left\{I_T^* I_R\right\} R_T}, \tag{C.4}$$

$$\gamma_T = \frac{P_{\text{Rx}} - \text{Re}\left\{I_R^* I_R\right\} R_R - \text{Re}\left\{I_R^* I_R\right\} R_{R:t}}{\text{Re}\left\{I_R^* I_T\right\} R_R}. \tag{C.5}$$

APPENDIX D

A Quadratic Approximation for the Mutual Inductance Over Lateral Misalignment

This Appendix is worked by Xiaofan Cui, who is the co-author of the published work [95].[1]

From Grover [56], the mutual inductance ($M_{T:R}$) of two coils consisting of circular filaments, which are laterally misaligned by x is

$$M_{T:R} = \frac{2\mu_0\sqrt{r_{_T} r_{_R}}}{\pi} \int_0^{\pi} \frac{1 - \frac{x}{r_R}\cos\varphi}{k\sqrt{V^3}} \Psi(k)\, d\varphi, \tag{D.1}$$

where

$$\alpha = \frac{r_{_R}}{r_{_T}},\ \beta = \frac{d_{T:R}}{r_{_T}},\ V = \sqrt{1 + \frac{x^2}{r_{_R}^2} - 2\frac{x}{r_{_R}}\cos\varphi}, \tag{D.2}$$

$$k^2 = \frac{4\alpha V}{(1+\alpha V)^2 + \beta^2},\ \Psi(k) = \left(1 - \frac{k^2}{2}\right) F(k) - E(k), \tag{D.3}$$

$$F(k) = \int_0^{\frac{\pi}{2}} \frac{d\theta}{\left(1 - k^2\sin^2\theta\right)^{1/2}},\ E(k) = \int_0^{\frac{\pi}{2}} \left(1 - k^2\sin^2\theta\right)^{1/2} d\theta. \tag{D.4}$$

r_T and r_R are the radii of the coils, $d_{T:R}$ is the vertical distance between two coils, x is the lateral misalignment, and k parameterizes the elliptic integrals.

We assume that the normalized misalignment $\gamma \triangleq x/r_{_R} \ll 1$. This enables us to approximate

[1] S. Y. Chu, X. Cui and A. Avestruz, "Accurate Transfer-Power Measurement for Wireless Charging of Electric Vehicles Under Misalignment," 2018 IEEE PELS Workshop on Emerging Technologies: Wireless Power Transfer (Wow), Montreal, QC, Canada, 2018, pp. 1-6.

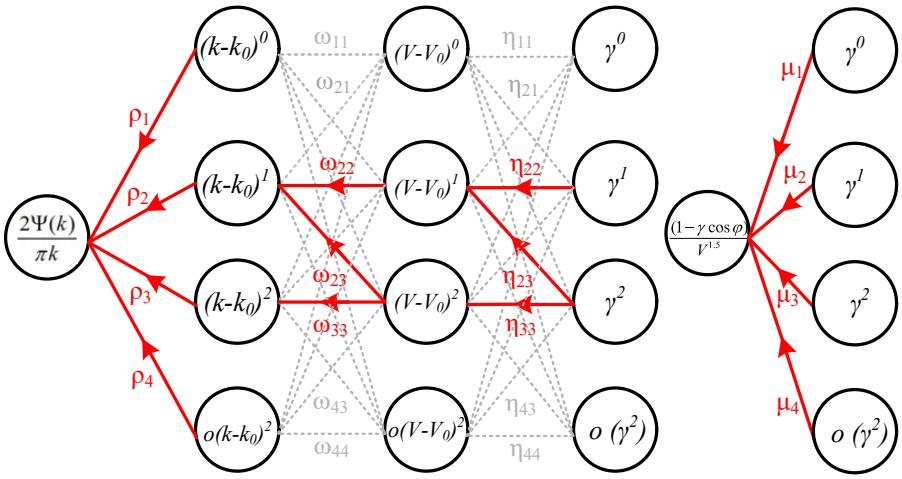

Figure D.1. Taylor expansion of the mutual inductance to the misalignment.

the mutual inductance $M_{T:R}$ by a polynomial function of the normalized misalignment γ through Taylor expansion.

We first express $M_{T:R}$ as

$$M_{T:R} = \mu_0 \sqrt{r_T r_R} \int_0^{\pi} \underbrace{\left(1 - \frac{x}{r_R}\cos\varphi\right) V^{-\frac{3}{2}}}_{\text{A}} \times \underbrace{\frac{2\Psi(k)}{\pi k}}_{\text{B}} d\varphi. \tag{D.5}$$

The Taylor expansion of A in (D.5) can be expressed as

$$(1 - \gamma\cos\varphi)V^{-\frac{3}{2}} = \mu_1 + \mu_2\gamma + \mu_3\gamma^2 + o(\gamma^2), \tag{D.6}$$

where

$$\mu_1 = 1, \quad \mu_2 = \frac{1}{2}\cos\varphi, \quad \mu_3 = \frac{9}{8}\cos^2\varphi - \frac{3}{4}. \tag{D.7}$$

The Taylor expansion of B in (D.5) can be performed in three steps. The first step expands $2\Psi(k)/(\pi k)$ as a function of k, which is illustrated in the first layer of Fig. D.1.

$$\frac{2\Psi(k)}{\pi k} = \rho_1 + \rho_2(k - k_0) + \rho_3(k - k_0)^2 + o\left((k - k_0)^2\right), \tag{D.8}$$

where

$$\rho_1 = \frac{2-k_0^2}{\pi k_0}F(k_0) - \frac{2}{\pi k_0}E(k_0), \tag{D.9}$$

$$\rho_2 = -\frac{2}{\pi k_0^2}F(k_0) + \frac{2-k_0^2}{\pi(1-k_0^2)k_0^2}E(k_0), \tag{D.10}$$

$$\rho_3 = \frac{(5k_0^4-9k_0^2+4)}{2\pi(k_0^2-1)^2k_0^3}F(k_0) - \frac{(3k_0^4-9k_0^2+4)}{2\pi(k_0^2-1)^2k_0^3}E(k_0), \tag{D.11}$$

$$k_0 = \sqrt{\frac{4\alpha}{(1+\alpha)^2+\beta^2}}. \tag{D.12}$$

The following two equations are useful for deriving (D.8):

$$\frac{\mathrm{d}\,F(k)}{\mathrm{d}\,k} = \frac{E(k)}{k(1-k^2)} - \frac{F(k)}{k}, \tag{D.13}$$

$$\frac{\mathrm{d}\,E(k)}{\mathrm{d}\,k} = \frac{E(k)-F(k)}{k}. \tag{D.14}$$

The second step expands k as a function of V, which is illustrated in the second layer of Fig. D.1.

$$k = k_0 + \omega_{22}(V-V_0) + \omega_{23}(V-V_0)^2 + o\left((V-V_0)^2\right), \tag{D.15}$$

where

$$\omega_{22} = \frac{\alpha^{\frac{1}{2}}(1-\alpha^2+\beta^2)}{\left((1+\alpha)^2+\beta^2\right)^{\frac{3}{2}}} \tag{D.16}$$

$$\omega_{23} = \frac{\alpha^{\frac{1}{2}}\left((1+\alpha)^2(3\alpha^2-6\alpha-1) - 2\beta^2(5\alpha^2+4\alpha+1) - \beta^4\right)}{4((1+\alpha)^2+\beta^2)^{\frac{5}{2}}} \tag{D.17}$$

$$\omega_{33} = \omega_{22}^2, \tag{D.18}$$

$$V_0 = 1. \tag{D.19}$$

The third step expands V as a function of γ, which is illustrated in the third layer of Fig. D.1.

$$V = V_0 + \eta_{22}\gamma + \eta_{23}\gamma^2 + o\left(\gamma^2\right), \tag{D.20}$$

where

$$\eta_{22} = -\cos\varphi, \tag{D.21}$$

$$\eta_{23} = \frac{1}{2}\sin^2\varphi, \tag{D.22}$$

$$\eta_{33} = \eta_{22}^2. \tag{D.23}$$

Through Fig. D.1, the Taylor expansion of B in (D.5) is

$$\frac{2\Psi(k)}{\pi k} = \rho_1 + \rho_2\omega_{22}\eta_{22}\,\gamma + \left(\rho_2\omega_{22}\eta_{23} + \rho_2\omega_{23}\eta_{33} + \rho_3\omega_{33}\eta_{33}\right)\gamma^2 + o\left(\gamma^2\right). \tag{D.24}$$

From (D.5), (D.6) and (D.24), we can extract the function that is a quadratic approximation $M_{T:R}$. Fig. D.2 shows that the expression for mutual inductance in Grover can be well-approximated by a quadratic function.

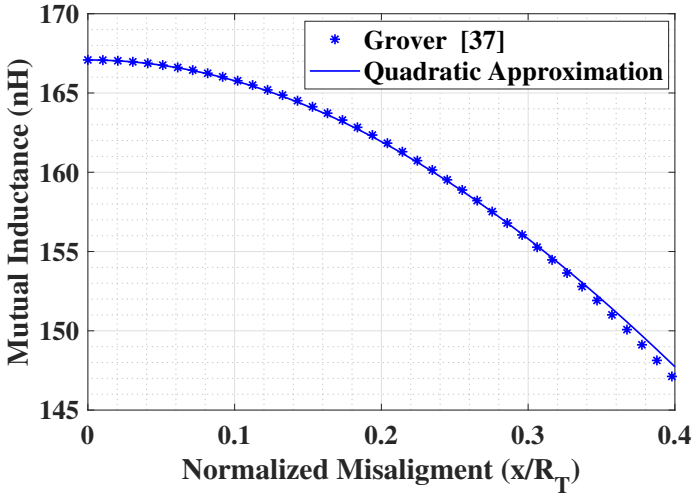

Figure D.2. The expression for the mutual inductance of circular filaments in Grover can be well-approximated by a quadratic function when the misalignment distance is not too large relative to the radii of the coils.

APPENDIX E

Schematics and Layout

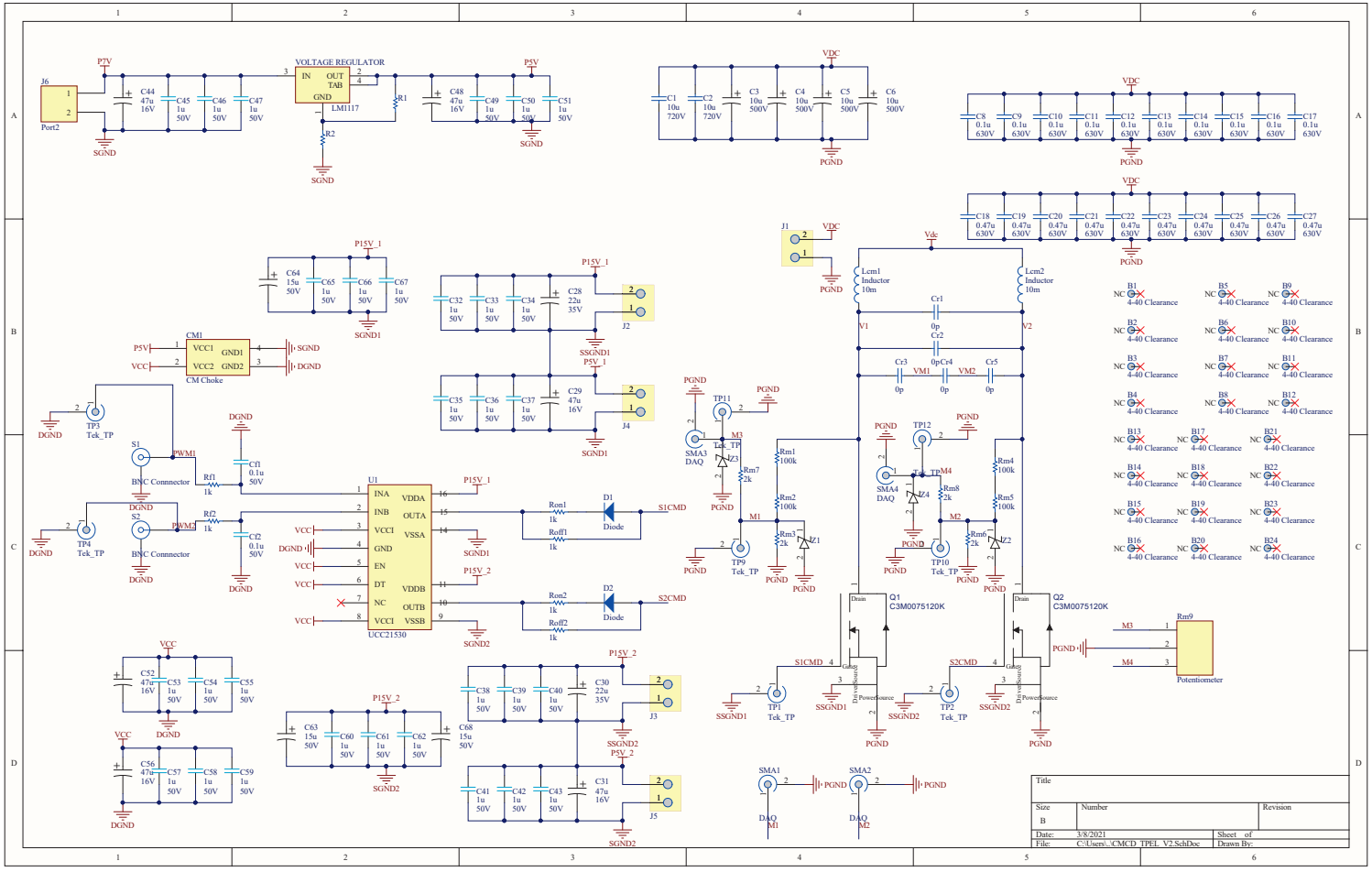

Figure .1. Schematic for CMCD converter

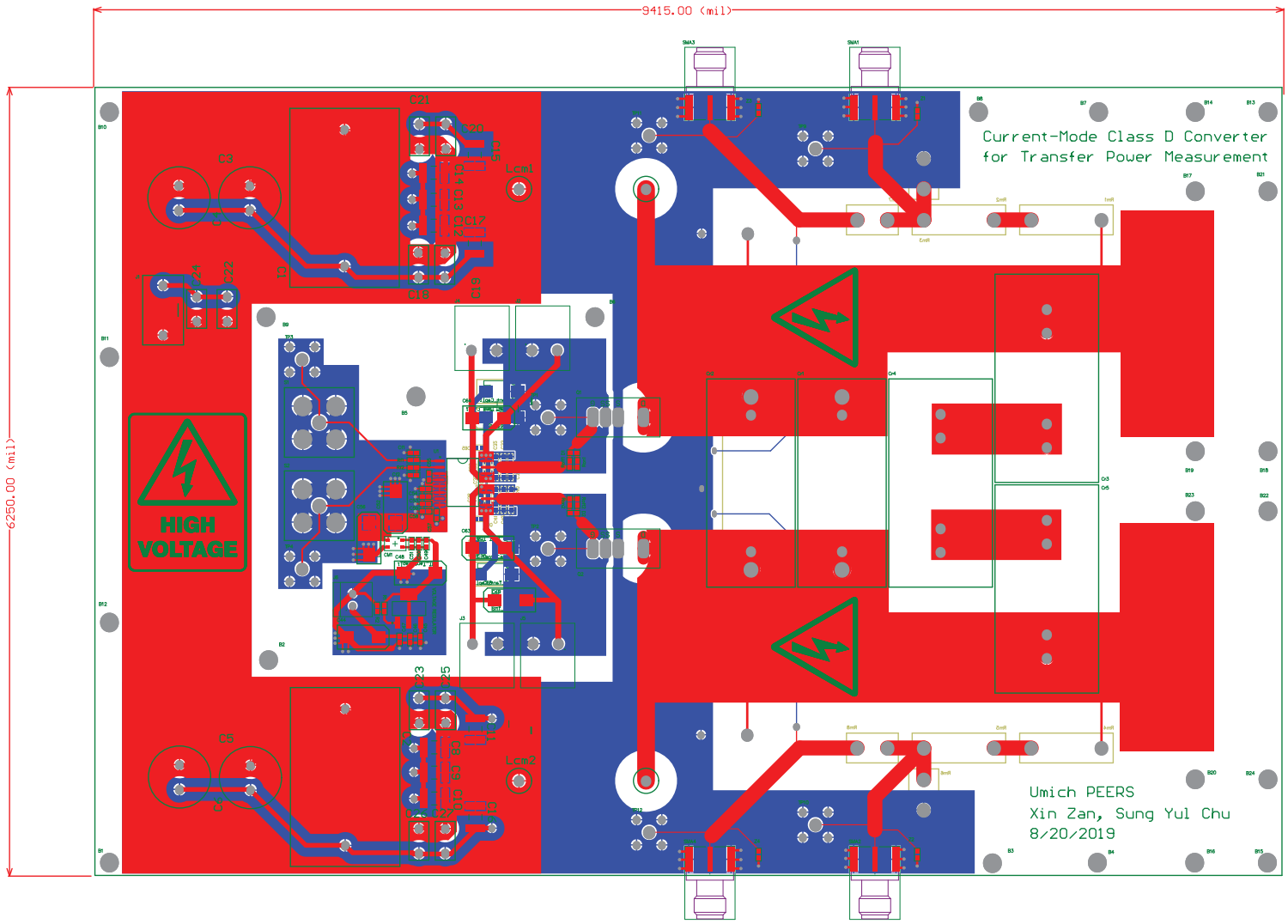

Figure .2. PCB layout for CMCD converter

BIBLIOGRAPHY

[1] T. Butcher, "Back to basics: Weights and Measures week 2018," *Taking Measure blog, NIST*, March 2018.

[2] J. Huh, S. W. Lee, W. Y. Lee, G. H. Cho, and C. T. Rim, "Narrow-width inductive power transfer system for online electrical vehicles," *IEEE Transactions on Power Electronics*, vol. 26, pp. 3666–3679, Dec 2011.

[3] G. A. Covic and J. T. Boys, "Inductive power transfer," *Proceedings of the IEEE*, vol. 101, pp. 1276–1289, June 2013.

[4] Chwei-Sen Wang, O. H. Stielau, and G. A. Covic, "Design considerations for a contactless electric vehicle battery charger," *IEEE Transactions on Industrial Electronics*, vol. 52, no. 5, pp. 1308–1314, 2005.

[5] S. Y. Choi, B. W. Gu, S. Y. Jeong, and C. T. Rim, "Advances in wireless power transfer systems for roadway-powered electric vehicles," *IEEE Journal of Emerging and Selected Topics in Power Electronics*, vol. 3, pp. 18–36, March 2015.

[6] C. C. Mi, G. Buja, S. Y. Choi, and C. T. Rim, "Modern advances in wireless power transfer systems for roadway powered electric vehicles," *IEEE Transactions on Industrial Electronics*, vol. 63, pp. 6533–6545, Oct 2016.

[7] S. Li and C. C. Mi, "Wireless power transfer for electric vehicle applications," *IEEE Journal of Emerging and Selected Topics in Power Electronics*, vol. 3, pp. 4–17, March 2015.

[8] A. Daga, J. M. Miller, B. R. Long, R. Kacergis, P. Schrafel, and J. Wolgemuth, "Electric fuel pumps for wireless power transfer: Enabling rapid growth in the electric vehicle market," *IEEE Power Electronics Magazine*, vol. 4, pp. 24–35, June 2017.

[9] C. Wang, O. H. Stielau, and G. A. Covic, "Design considerations for a contactless electric vehicle battery charger," *IEEE Transactions on Industrial Electronics*, vol. 52, pp. 1308–1314, Oct 2005.

[10] M. Pinuela, D. C. Yates, S. Lucyszyn, and P. D. Mitcheson, "Maximizing dc-to-load efficiency for inductive power transfer," *IEEE Transactions on Power Electronics*, vol. 28, pp. 2437–2447, May 2013.

[11] S. Y. R. Hui, W. Zhong, and C. K. Lee, "A critical review of recent progress in mid-range wireless power transfer," *IEEE Transactions on Power Electronics*, vol. 29, pp. 4500–4511, Sep. 2014.

[12] W. Zhang and C. C. Mi, "Compensation topologies of high-power wireless power transfer systems," *IEEE Transactions on Vehicular Technology*, vol. 65, pp. 4768–4778, June 2016.

[13] T. Kan, T. Nguyen, J. C. White, R. K. Malhan, and C. C. Mi, "A new integration method for an electric vehicle wireless charging system using LCC compensation topology: Analysis and design," *IEEE Transactions on Power Electronics*, vol. 32, pp. 1638–1650, Feb 2017.

[14] W. X. Zhong and S. Y. R. Hui, "Maximum energy efficiency tracking for wireless power transfer systems," *IEEE Transactions on Power Electronics*, vol. 30, pp. 4025–4034, July 2015.

[15] J. M. Miller, O. C. Onar, and M. Chinthavali, "Primary-side power flow control of wireless power transfer for electric vehicle charging," *IEEE Journal of Emerging and Selected Topics in Power Electronics*, vol. 3, no. 1, pp. 147–162, 2015.

[16] V. P. Galigekere, J. Pries, O. C. Onar, G. Su, S. Anwar, R. Wiles, L. Seiber, and J. Wilkins, "Design and implementation of an optimized 100 kW stationary wireless charging system for EV battery recharging," in *2018 IEEE Energy Conversion Congress and Exposition (ECCE)*, pp. 3587–3592, 2018.

[17] J. Pries, V. P. N. Galigekere, O. C. Onar, and G. Su, "A 50-kW three-phase wireless power transfer system using bipolar windings and series resonant networks for rotating magnetic fields," *IEEE Transactions on Power Electronics*, vol. 35, no. 5, pp. 4500–4517, 2020.

[18] A. Pevere, R. Petrella, C. C. Mi, and Shijie Zhou, "Design of a high efficiency 22 kW wireless power transfer system for EVs fast contactless charging stations," in *2014 IEEE International Electric Vehicle Conference (IEVC)*, pp. 1–7, 2014.

[19] A. Ridge, K. K. Ahamad, R. McMahon, and J. Miles, "Development of a 50 kW wireless power transfer system," in *2019 IEEE PELS Workshop on Emerging Technologies: Wireless Power Transfer (WoW)*, pp. 406–409, 2019.

[20] H. Takanashi, Y. Sato, Y. Kaneko, S. Abe, and T. Yasuda, "A large air gap 3 kW wireless power transfer system for electric vehicles," in *2012 IEEE Energy Conversion Congress and Exposition (ECCE)*, pp. 269–274, 2012.

[21] O. C. Onar, S. L. Campbell, L. E. Seiber, C. P. White, and M. Chinthavali, "A high-power wireless charging system development and integration for a Toyota Rav4 electric vehicle," in *2016 IEEE Transportation Electrification Conference and Expo (ITEC)*, pp. 1–8, 2016.

[22] F. Y. Lin, S. Kim, G. A. Covic, and J. T. Boys, "Effective coupling factors for series and parallel tuned secondaries in IPT systems using bipolar primary pads," *IEEE Transactions on Transportation Electrification*, vol. 3, no. 2, pp. 434–444, 2017.

[23] A. Zaheer, H. Hao, G. A. Covic, and D. Kacprzak, "Investigation of multiple decoupled coil primary pad topologies in lumped IPT systems for interoperable electric vehicle charging," *IEEE Transactions on Power Electronics*, vol. 30, no. 4, pp. 1937–1955, 2015.

[24] M. Budhia, J. T. Boys, G. A. Covic, and C. Huang, "Development of a single-sided flux magnetic coupler for electric vehicle IPT charging systems," *IEEE Transactions on Industrial Electronics*, vol. 60, no. 1, pp. 318–328, 2013.

[25] M. Budhia, G. A. Covic, and J. T. Boys, "Design and optimization of circular magnetic structures for lumped inductive power transfer systems," *IEEE Transactions on Power Electronics*, vol. 26, pp. 3096–3108, Nov 2011.

[26] R. Bosshard, J. W. Kolar, J. Mühlethaler, I. Stevanović, B. Wunsch, and F. Canales, "Modeling and η-α-pareto optimization of inductive power transfer coils for electric vehicles," *IEEE Journal of Emerging and Selected Topics in Power Electronics*, vol. 3, pp. 50–64, March 2015.

[27] C. R. Sullivan and L. Beghou, "Design methodology for a high-Q self-resonant coil for medical and wireless-power applications," in *2013 IEEE 14th Workshop on Control and Modeling for Power Electronics (COMPEL)*, pp. 1–8, June 2013.

[28] J. P. K. Sampath, A. Alphones, and H. Shimasaki, "Coil design guidelines for high efficiency of wireless power transfer (wpt)," in *2016 IEEE Region 10 Conference (TENCON)*, pp. 726–729, 2016.

[29] J. Pries, V. P. Galigekere, O. C. Onar, G. Su, R. Wiles, L. Seiber, J. Wilkins, S. Anwar, and S. Zou, "Coil power density optimization and trade-off study for a 100kW electric vehicle IPT wireless charging system," in *2018 IEEE Energy Conversion Congress and Exposition (ECCE)*, pp. 1196–1201, 2018.

[30] L. Percebon, D. Kuerschner, and S. Mathar, "Characterisation of factors influencing the magnetic leakage field of a 7 kW wireless electric vehicle charging system," in *2016 IEEE PELS Workshop on Emerging Technologies: Wireless Power Transfer (WoW)*, pp. 145–151, Oct 2016.

[31] J. Kim, J. Kim, S. Kong, H. Kim, I. Suh, N. P. Suh, D. Cho, J. Kim, and S. Ahn, "Coil design and shielding methods for a magnetic resonant wireless power transfer system," *Proceedings of the IEEE*, vol. 101, pp. 1332–1342, June 2013.

[32] M. Mohammad, E. T. Wodajo, S. Choi, and M. E. Elbuluk, "Modeling and design of passive shield to limit EMF emission and to minimize shield loss in unipolar wireless charging system for EV," *IEEE Transactions on Power Electronics*, vol. 34, no. 12, pp. 12235–12245, 2019.

[33] O. C. Onar, G. Su, E. Asa, J. Pries, V. Galigekere, L. Seiber, C. White, R. Wiles, and J. Wilkins, "20-kW bi-directional wireless power transfer system with energy storage system connectivity," in *2020 IEEE Applied Power Electronics Conference and Exposition (APEC)*, pp. 3208–3214, 2020.

[34] IEA, "Global EV Outlook 2019: Scaling-up the transition to electric mobility," *IEA 2019*, May 2019.

[35] T. Covert, M. Greenstone, and C. R. Knittel, "Will we ever stop using fossil fuels?," *Journal of Economic Perspectives*, vol. 30, pp. 117–38, February 2016.

[36] EIA, "Electric Power Annual 2018," *U.S. Energy Information Administration*, p. 21, Oct 2019.

[37] R. Cherif, F. Hasanov, and A. Pande, "Riding the energy transition: Oil beyond 2040," *IMF Working Paper*, May 2017.

[38] T. Bohn, "Scalable electric submeter challenges for electric vehicle charging; low level ac to dc extreme fast charging for commercial vehicles," in *2019 IEEE Transportation Electrification Conference and Expo (ITEC)*, June 2019.

[39] T. Minami, I. Tabuchi, R. Tanaka, and Y. Tsuruda, "Development of a real-time power and impedance sensor for wireless power transfer systems," in *2015 IEEE Wireless Power Transfer Conference (WPTC)*, pp. 1–3, May 2015.

[40] M. Zucca, O. Bottauscio, S. Harmon, R. Guilizzoni, F. Schilling, M. Schmidt, P. Ankarson, T. Bergsten, K. Tammi, P. Sainio, J. B. Romero, E. L. Puyal, L. Pichon, F. Freschi, V. Cirimele, P. Bauer, J. Dong, A. Maffucci, S. Ventre, N. Femia, G. Di Capua, N. Kuster, and I. Liorni, "Metrology for inductive charging of electric vehicles (MICEV)," in *2019 AEIT International Conference of Electrical and Electronic Technologies for Automotive (AEIT AUTOMOTIVE)*, pp. 1–6, 2019.

[41] J. H. Spreen, "Electrical terminal representation of conductor loss in transformers," *IEEE Transactions on Power Electronics*, vol. 5, pp. 424–429, Oct 1990.

[42] D. R. Zimmanck and C. R. Sullivan, "Efficient calculation of winding-loss resistance matrices for magnetic components," in *2010 IEEE 12th Workshop on Control and Modeling for Power Electronics (COMPEL)*, pp. 1–5, June 2010.

[43] S. Y. Jeong, H. G. Kwak, G. C. Jang, S. Y. Choi, and C. T. Rim, "Dual-purpose nonoverlapping coil sets as metal object and vehicle position detections for wireless stationary EV chargers," *IEEE Transactions on Power Electronics*, vol. 33, pp. 7387–7397, Sep. 2018.

[44] V. X. Thai, G. C. Jang, S. Y. Jeong, J. H. Park, Y. S. Kim, and C. T. Rim, "Symmetric sensing coil design for the blind-zone free metal object detection of a stationary wireless electric vehicles charger," *IEEE Transactions on Power Electronics*, vol. 35, no. 4, pp. 3466–3477, 2020.

[45] SAE, *Wireless Power Transfer for Light-Duty Plug-In/ Electric Vehicles and Alignment Methodology*, May 2016.

[46] J. Kong, *Electromagnetic Wave Theory*. A Wiley-Interscience publication, Wiley, 1986.

[47] Y. Guo, J. Li, X. Hou, X. Lv, H. Liang, J. Zhou, and H. Wu, "Poynting vector analysis for wireless power transfer between magnetically coupled coils with different loads," in *Scientific Reports*, 2017.

[48] D. Cheng, *Field and Wave Electromagnetics*. The Addison-Wesley series in electrical engineering, Addison-Wesley Publishing Company, 1989.

[49] Y. Liu and A. P. Hu, "Study of power flow in an IPT system based on Poynting vector analysis," *Energies*, vol. 11, no. 1, 2018.

[50] D. Vyroubal, "Impedance of the eddy-current displacement probe: the transformer model," *IEEE Transactions on Instrumentation and Measurement*, vol. 53, pp. 384–391, April 2004.

[51] J. García-Martín, J. Gómez-Gil, and E. Vázquez-Sánchez, "Non-destructive techniques based on eddy current testing," *Sensors*, vol. 11, no. 3, pp. 2525–2565, 2011.

[52] A. V. Oppenheim and R. W. Schafer, *Discrete-Time Signal Processing*. Upper Saddle River, NJ, USA: Prentice Hall Press, 3rd ed., 2009.

[53] T. Radil, P. M. Ramos, and A. Cruz Serra, "New spectrum leakage correction algorithm for frequency estimation of power system signals," *IEEE Transactions on Instrumentation and Measurement*, vol. 58, pp. 1670–1679, May 2009.

[54] Y. Gao, A. Ginart, K. B. Farley, and Z. T. H. Tse, "Misalignment effect on efficiency of wireless power transfer for electric vehicles," in *2016 IEEE Applied Power Electronics Conference and Exposition (APEC)*, pp. 3526–3528, 2016.

[55] S. Babic, F. Sirois, C. Akyel, and C. Girardi, "Mutual inductance calculation between circular filaments arbitrarily positioned in space: Alternative to Grover's formula," *IEEE Transactions on Magnetics*, vol. 46, pp. 3591–3600, Sep. 2010.

[56] F. Grover, *Inductance Calculations*. Dover Books on Electrical Engineering, Dover Publications, 2013.

[57] A. C. Cameron and F. A. Windmeijer, "An R-squared measure of goodness of fit for some common nonlinear regression models," *Journal of Econometrics*, vol. 77, no. 2, pp. 329 – 342, 1997.

[58] K. P. Murphy, *Machine Learning: A Probabilistic Perspective*. MIT press, 2012.

[59] M. Q. Nguyen, Z. Hughes, P. Woods, Y. Seo, S. Rao, and J. . Chiao, "Field distribution models of spiral coil for misalignment analysis in wireless power transfer systems," *IEEE Transactions on Microwave Theory and Techniques*, vol. 62, no. 4, pp. 920–930, 2014.

[60] W. Wu and Q. Fang, "Design and simulation of printed spiral coil used in wireless power transmission systems for implant medical devices," in *2011 Annual International Conference of the IEEE Engineering in Medicine and Biology Society*, pp. 4018–4021, 2011.

[61] Z. Luo and X. Wei, "Analysis of square and circular planar spiral coils in wireless power transfer system for electric vehicles," *IEEE Transactions on Industrial Electronics*, vol. 65, no. 1, pp. 331–341, 2018.

[62] J. Acero, C. Carretero, I. Lope, R. Alonso, Lucia, and J. M. Burdio, "Analysis of the mutual inductance of planar-lumped inductive power transfer systems," *IEEE Transactions on Industrial Electronics*, vol. 60, no. 1, pp. 410–420, 2013.

[63] M. Budhia, G. A. Covic, and J. T. Boys, "Design and optimization of circular magnetic structures for lumped inductive power transfer systems," *IEEE Transactions on Power Electronics*, vol. 26, no. 11, pp. 3096–3108, 2011.

[64] M. Teng, W. Chenyang, W. Kai, and L. Ping, "Design of multilayer flat spiral inductive coil for wireless power transfer," in *2016 IEEE 5th Global Conference on Consumer Electronics*, pp. 1–2, 2016.

[65] Z. Luo and X. Wei, "Analysis of square and circular planar spiral coils in wireless power transfer system for electric vehicles," *IEEE Transactions on Industrial Electronics*, vol. 65, pp. 331–341, Jan 2018.

[66] G. L. Harris and L. Eason, "NIST HB 105-3, Specifications and tolerances for reference standards and field standard weights and measures, 3. specifications and tolerances for graduated neck type volumetric field standards," *Handbook (NIST HB)-105-3 2009*, Feb. 2010.

[67] G. L. Harris and V. R. Miller, "NISTIR 7383, Selected procedures for volumetric calibrations," *NIST Interagency/Internal Report (NISTIR)*, May 2019.

[68] X. Nan and C. R. Sullivan, "An equivalent complex permeability model for litz-wire windings," *IEEE Transactions on Industry Applications*, vol. 45, no. 2, pp. 854–860, 2009.

[69] A. Delgado, G. Salinas, J. A. Oliver, J. A. Cobos, and J. Rodriguez-Moreno, "Equivalent conductor layer for fast 3-d finite element simulations of inductive power transfer coils," *IEEE Transactions on Power Electronics*, vol. 35, no. 6, pp. 6221–6230, 2020.

[70] A. Stadler and C. Gulden, "Copper losses of litz-wire windings due to an air gap," in *2013 15th European Conference on Power Electronics and Applications (EPE)*, pp. 1–7, 2013.

[71] S. Boyd and L. Vandenberghe, *Convex Optimization*. USA: Cambridge University Press, 2004.

[72] D. P. Bertsekas, *Constrained Optimization and Lagrange Multiplier Methods*. Academic press, 2014.

[73] T. Negishi, "Welfare economics and existence of an equilibrium for a competitive economy," *Metroeconomica*, vol. 12, pp. 92–97, 1960.

[74] K.-H. Chang, "Chapter 5 - multiobjective optimization and advanced topics," in *Design Theory and Methods Using CAD/CAE* (K.-H. Chang, ed.), pp. 325–406, Boston: Academic Press, 2015.

[75] M. A. Prelee and D. L. Neuhoff, "Multidimensional Manhattan sampling and reconstruction," *IEEE Transactions on Information Theory*, vol. 62, no. 5, pp. 2772–2787, 2016.

[76] X. Zan and A. Avestruz, "27.12 MHz bi-directional wireless power transfer using current-mode class D converters with phase-shift power modulation," in *2018 IEEE PELS Workshop on Emerging Technologies: Wireless Power Transfer (WoW)*, pp. 1–6, June 2018.

[77] X. Zan and A. Avestruz, "Performance comparisons of synchronous and uncontrolled rectifiers for 27.12 MHz wireless power transfer using CMCD converters," in *2018 IEEE Energy Conversion Congress and Exposition (ECCE)*, pp. 2448–2455, Sep. 2018.

[78] X. Zan and A. Avestruz, "100 MHz wireless power transfer for lightweight UAVs and agile robots," in *2020 IEEE Applied Power Electronics Conference and Exposition (APEC)*, pp. 1655–1661, 2020.

[79] L. Gu, Z. Tong, W. Liang, and J. Rivas-Davila, "A multiresonant gate driver for high-frequency resonant converters," *IEEE Transactions on Industrial Electronics*, vol. 67, no. 2, pp. 1405–1414, 2020.

[80] C. R. Sullivan and R. Y. Zhang, "Analytical model for effects of twisting on litz-wire losses," in *2014 IEEE 15th Workshop on Control and Modeling for Power Electronics (COMPEL)*, pp. 1–10, 2014.

[81] D. Barth, B. Klaus, and T. Leibfried, "Litz wire design for wireless power transfer in electric vehicles," in *2017 IEEE Wireless Power Transfer Conference (WPTC)*, pp. 1–4, 2017.

[82] C. Utschick, C. Merz, and C. Som, "Ac loss behavior of wireless power transfer coils," in *2019 IEEE Wireless Power Transfer Conference (WPTC)*, pp. 120–125, 2019.

[83] A. Roßkopf, E. Bär, and C. Joffe, "Influence of inner skin- and proximity effects on conduction in litz wires," *IEEE Transactions on Power Electronics*, vol. 29, no. 10, pp. 5454–5461, 2014.

[84] J. Ferreira, "Analytical computation of ac resistance of round and rectangular litz wire windings," *IEE Proceedings B (Electric Power Applications)*, vol. 139, pp. 21–25(4), January 1992.

[85] V. Väisänen, J. Hiltunen, J. Nerg, and P. Silventoinen, "Ac resistance calculation methods and practical design considerations when using litz wire," in *IECON 2013 - 39th Annual Conference of the IEEE Industrial Electronics Society*, pp. 368–375, 2013.

[86] R. W. Erickson and D. Maksimovic, *Fundamentals of Power Electronics*. Springer, 2nd ed., 2001.

[87] H. W. Ott, *Noise Reduction Techniques in Electronic Systems*. Wiley, 1988.

[88] S. Y. Chu and A. Avestruz, "A new calibration strategy for transfer-power measurement of wireless charging of electric vehicles," in *2019 IEEE Transportation Electrification Conference and Expo (ITEC)*, June 2019.

[89] X. Zan, Z. Guo, and A. Avestruz, "Inductive wireless power transfer at 100 MHz with wide load range and constant output current," in *2019 IEEE Energy Conversion Congress and Exposition (ECCE)*, pp. 4967–4975, Sep. 2019.

[90] R. Muñiz, J. Díaz, F. Nuño, M. J. Prieto, and A. M. Pernía, "A smart power meter to recharge electric vehicles in communal parking areas," *IEEE Internet of Things Journal*, vol. 6, no. 2, pp. 3448–3454, 2019.

[91] A. Muharam, M. Pratama, K. Ismail, S. Kaleg, M. R. Kurnia, and A. Hapid, "A development of smart metering infrastructure for electric vehicle charging point," in *2016 International Conference on Sustainable Energy Engineering and Application (ICSEEA)*, pp. 27–33, 2016.

[92] L. Qiao, X. Liu, and B. Jiang, "Design and implementation of the smart meter in vehicle-to-grid," in *2011 4th International Conference on Electric Utility Deregulation and Restructuring and Power Technologies (DRPT)*, pp. 618–621, 2011.

[93] T. Butcher, L. Crown, and R. Harshman, "Specifications, tolerances, and other technical requirements for weighing and measuring devices (nist hb44, 2018 ed)," 2017-11-17 2017.

[94] S. Y. Chu and A. Avestruz, "Transfer-power measurement: A non-contact method for fair and accurate metering of wireless power transfer in electric vehicles," in *2017 IEEE 18th Workshop on Control and Modeling for Power Electronics (COMPEL)*, pp. 1–8, July 2017.

[95] S. Y. Chu, X. Cui, and A. Avestruz, "Accurate transfer-power measurement for wireless charging of electric vehicles under misalignment," in *2018 IEEE PELS Workshop on Emerging Technologies: Wireless Power Transfer (WoW)*, pp. 1–6, June 2018.

[96] J. Poon, P. Jain, I. C. Konstantakopoulos, C. Spanos, S. K. Panda, and S. R. Sanders, "Model-based fault detection and identification for switching power converters," *IEEE Transactions on Power Electronics*, vol. 32, pp. 1419–1430, Feb 2017.

[97] L. Xiang, Z. Zhu, J. Tian, and Y. Tian, "Foreign object detection in a wireless power transfer system using symmetrical coil sets," *IEEE Access*, pp. 1–1, 2019.

[98] Y. Zhang, B. Yu, K. Wang, Y. Wang, and Y. Yang, "Metal foreign object detection in electric vehicle wireless power transmission," in *2020 IEEE International Conference on Information Technology,Big Data and Artificial Intelligence (ICIBA)*, vol. 1, pp. 696–701, 2020.

[99] T. Sun and C. Qi, "Design of metal object detection coil set with positioning function for WPT system," in *IECON 2020 The 46th Annual Conference of the IEEE Industrial Electronics Society*, pp. 3884–3888, 2020.

[100] K. Maikawa and T. Imazu, "Contactless electricity supply device with foreign object detector," U.S. Patent 9 553 636 , Jan. 2017.

[101] S. Y. Jeong, V. X. Thai, J. H. Park, and C. T. Rim, "Self-inductance-based metal object detection with mistuned resonant circuits and nullifying induced voltage for wireless EV chargers," *IEEE Transactions on Power Electronics*, vol. 34, pp. 748–758, Jan 2019.

[102] S. Fukuda, H. Nakano, Y. Murayama, T. Murakami, O. Kozakai, and K. Fujimaki, "A novel metal detector using the quality factor of the secondary coil for wireless power transfer systems," in *2012 IEEE MTT-S International Microwave Workshop Series on Innovative Wireless Power Transmission: Technologies, Systems, and Applications*, pp. 241–244, May 2012.

[103] N. Kuyvenhoven, C. Dean, J. Melton, J. Schwannecke, and A. E. Umenei, "Development of a foreign object detection and analysis method for wireless power systems," in *2011 IEEE Symposium on Product Compliance Engineering Proceedings*, pp. 1–6, Oct 2011.

[104] J. Patino, S. N. Thekkevalappil, and S. Sibecas, "Energy transfer optimization by detecting and mitigating magnetic saturation in wireless charging with foreign object detection," U.S. Patent 9 819 232 , Nov. 2017.

[105] M. Singh, "Apparatus, system, and method for detecting a foreign object in an inductive wireless power transfer system based on input power," U.S. Patent 9 555 3485 , Jan. 2017.

[106] Z. N. Low, J. J. Casanova, P. H. Maier, J. A. Taylor, R. A. Chinga, and J. Lin, "Method of load/fault detection for loosely coupled planar wireless power transfer system with power delivery tracking," *IEEE Transactions on Industrial Electronics*, vol. 57, pp. 1478–1486, April 2010.

[107] H. Dorairaj, R. Kumar, and S. Ganguly, "Foreign object detection in inductive coupled devices," U.S. Patent 8 575 944 , Nov. 2013.

[108] S. Huang, J. Su, S. Dai, C. Tai, and T. Lee, "Enhancement of wireless power transmission with foreign-object detection considerations," in *2017 IEEE 6th Global Conference on Consumer Electronics (GCCE)*, pp. 1–2, 2017.

[109] Y. Lu and M. J. Higgins-Luthman, "Object detection and tracking system," U.S. Patent 8 027 029 , Sep. 2011.

[110] T. Poguntke, P. Schumann, and K. Ochs, "Radar-based living object protection for inductive charging of electric vehicles using two-dimensional signal processing," *Wireless Power Transfer*, vol. 4, no. 2, p. 88–97, 2017.

[111] T. Sonnenberg, A. Stevens, A. Dayerizadeh, and S. Lukic, "Combined foreign object detection and live object protection in wireless power transfer systems via real-time thermal camera analysis," in *2019 IEEE Applied Power Electronics Conference and Exposition (APEC)*, pp. 1547–1552, 2019.

[112] D. Bell and M. A. Leabman, "Systems and methods of object detection in wireless power charging systems," U.S. Patent 10 291 056 , May. 2019.

[113] A. Azad, V. Kulyukin, and Z. Pantic, "Misalignment tolerant DWPT charger for EV roadways with integrated foreign object detection and driver feedback system," in *2019 IEEE Transportation Electrification Conference and Expo (ITEC)*, pp. 1–5, 2019.

[114] M. Ote, S. Jeong, and M. M. Tentzeris, "Foreign object detection for wireless power transfer based on machine learning," in *2020 IEEE Wireless Power Transfer Conference (WPTC)*, pp. 476–479, 2020.

[115] C. R. Sullivan, "Computationally efficient winding loss calculation with multiple windings, arbitrary waveforms, and two-dimensional or three-dimensional field geometry," *IEEE Transactions on Power Electronics*, vol. 16, pp. 142–150, Jan 2001.

[116] J. Barton, T. G. Butcher, L. D. Crown, R. A. Harshman, G. D. Lee, and D. A. Olson, "Specifications, tolerances, and other technical requirements for weighing and measuring devices," *Handbook (NIST HB)-44 2019*, Nov. 2018.

[117] G. R. Nagendra, G. A. Covic, and J. T. Boys, "Determining the physical size of inductive couplers for IPT EV systems," *IEEE Journal of Emerging and Selected Topics in Power Electronics*, vol. 2, no. 3, pp. 571–583, 2014.

[118] F. Y. Lin, G. A. Covic, and J. T. Boys, "Evaluation of magnetic pad sizes and topologies for electric vehicle charging," *IEEE Transactions on Power Electronics*, vol. 30, no. 11, pp. 6391–6407, 2015.